Dynamic Modeling and Control of Free-Flying Space Robots

Author:
Shi, Lingling

Publication Date:
2017

DOI:
https://doi.org/10.26190/unsworks/19752

Dynamic Modeling and Control of Free-Flying Space Robots

Lingling Shi

A thesis in fulfilment of the requirements for the degree of
Doctor of Philosophy

School of Mechanical and Manufacturing Engineering

University of New South Wales

Australia

June 2017

PLEASE TYPE

THE UNIVERSITY OF NEW SOUTH WALES
Thesis/Dissertation Sheet

Surname or Family name: Shi

First name: Lingling | Other name/s:

Abbreviation for degree as given in the University calendar: PhD

School: School of Mechanical and Manufacturing Engineering | Faculty: Engineering

Title: Dynamic modeling and control of free-flying space robots

Abstract 350 words maximum: (PLEASE TYPE)

Free-Flying Space Robots (FFSRs) have the potential to assemble large space structures in orbit autonomously or telerobotically instead of time-consuming, risky and expensive astronaut Extra Vehicular Activities (EVA). However, dynamic coupling between the space manipulator and the spacecraft base can introduce modeling and control problems distinguished from fix-base robots. In this thesis, systematic modelling and control approaches for an FFSR are presented. Before proceeding to a complex on-orbit assembly case where FFSRs are used, a simple on-orbit assembly case, i.e. a deploying spacecraft is first analyzed. The subsequent chapters then investigate modelling, motion control and force control of an FFSR.

A robust controller is developed for a deploying spacecraft based on the twisting algorithm to control its attitude despite the substantial inertia change caused by structural reconfiguration. The controller delivers smooth control toques which are perfectly practical for the control of Reaction Wheels (RWs) and is able to steer the satellite to the desired orientation with reduced settling times.

In the on-orbit assembly case where FFSRs are used, a comprehensive dynamic model for a reaction-wheel actuated FFSR is first presented. The reformulated model incorporates the contribution of reaction-wheel momentum to the entire system. Based on the decoupled form of the model, two types of robust controllers are developed to implement coordinated control of both the space manipulator and the spacecraft. The control methodologies are applied for both the approaching phase and post-capture phase. It is shown that the controllers successfully achieve motion control for each sub-channel of the system, including the attitude states and manipulator motion states.

To implement target capture, a new control-oriented model structure for an FFSR is proposed. The developed model allows simultaneous end-effector motion/force control and active base attitude control. Hybrid motion and force control method is extended to enforce the FFSR tracking a desired trajectory of contact force which incorporates the consistent motion between FFSR's end-effector and the floating target. Meanwhile, attitude control of the spacecraft is achieved by taking the constraint forces from the articulated joint as disturbances.

All the control approaches are verified through numerical simulations in each corresponding chapter.

FOR OFFICE USE ONLY | Date of completion of requirements for Award:

Originality Statement

'I hereby declare that this submission is my own work and to the best of my knowledge it contains no materials previously published or written by another person, or substantial proportions of material which have been accepted for the award of any other degree or diploma at UNSW or any other educational institution, except where due acknowledgement is made in the thesis. Any contribution made to the research by others, with whom I have worked at UNSW or elsewhere, is explicitly acknowledged in the thesis. I also declare that the intellectual content of this thesis is the product of my own work, except to the extent that assistance from others in the project's design and conception or in style, presentation and linguistic expression is acknowledged.'

Signed ....

Date ....

Copyright Statement

Authenticity Statement

'I certify that the Library deposit digital copy is a direct equivalent of the final officially approved version of my thesis. No emendation of content has occurred and if there are any minor variations in formatting, they are the result of the conversion to digital format.'

Signed ....

Date ....

Abstract

Free-Flying Space Robots (FFSRs) have the potential to assemble large space structures in orbit autonomously or telerobotically instead of time-consuming, risky and expensive astronaut Extra Vehicular Activities (EVA). However, dynamic coupling between the space manipulator and the spacecraft base can introduce modelling and control problems distinguished from fix-base robots. In this thesis, systematic modelling and control approaches for an FFSR are presented. Before proceeding to a complex on-orbit assembly case where FFSRs are used, a simple on-orbit assembly case, i.e. a deploying spacecraft is first analyzed. The subsequent chapters then investigate modeling, motion control and force control of an FFSR.

A robust controller is developed for a deploying spacecraft based on the twisting algorithm to control its attitude despite the substantial inertia change caused by structural reconfiguration. The controller delivers smooth control torques which are perfectly practical for the control of Reaction Wheels (RWs) and is able to steer the satellite to the desired orientation with reduced settling times.

In the on-orbit assembly case where FFSRs are used, a comprehensive dynamic model for a reaction-wheel actuated FFSR is first presented. The reformulated model incorporates the contribution of reaction-wheel momentum to the entire system. Based on the decoupled form of the model, two types of robust controllers are developed to implement coordinated control of both the space manipulator and the spacecraft in the presence of system uncertainties. The control methodologies can be applied for both the approaching phase and post-capture phase. It is shown that the controllers successfully achieve motion control for each sub-channel of the system, including the attitude states and manipulator motion states.

To implement target capture, a new control-oriented model structure for

an FFSR is proposed. The developed model allows simultaneous end-effector motion/force control and active base attitude control. Hybrid motion and force control method is extended to enforce the FFSR to track a desired trajectory of contact force which incorporates the consistent motion between FFSR's end-effector and the floating target. Meanwhile, attitude control of the spacecraft is achieved by taking the constraint forces from the articulated joint as disturbances.

All the control approaches are verified through numerical simulations in each corresponding chapter.

Publications

The following papers are under review or have been published during the production of this thesis.

Journal

1. **Lingling Shi**, Nathan Kinkaid and Jay Katupitiya. Robust control for satellite attitude regulation during on-orbit assembly. *IEEE Transactions on Aerospace and Electronic Systems*, 52(1): 49-59, 2016.

2. Hiranya S. Jayakody, **Lingling Shi**, Jay Katupitiya, and Nathan Kinkaid. Robust adaptive coordination controller for a spacecraft equipped with a robotic manipulator. *Journal of Guidance, Control and Dynamics*, 39 (12), 2699-2711, 2016.

3. **Lingling Shi**, Jayantha Katupitiya, and Nathan Kinkaid. Simultaneous force-torque control by an on-orbit space robot. *IEEE Transactions on Aerospace and Electronic Systems*. (under revision)

4. **Lingling Shi**, Sharmila Kayastha, and Jayantha Katupitiya. Robust coordinated control of a dual-arm space robot. *Acta Astronautica*. (sent to production)

Conference

1. **Lingling Shi**, Hiranya S. Jayakody, Nathan Kinkaid and Jay Katupitiya. Attitude regulation of a free-flying space robot during contact operations. In *IEEE Aerospace Conference*, Big Sky, USA, March 2016.

2. **Lingling Shi**, Jay Katupitiya and Nathan Kinkaid. Robust attitude controller for a spacecraft equipped with a robotic manipulator. In *American Control Conference*, Boston, USA, July 2016.

Dedicated to

my parents,

Yanshu Pei and Dexiang Shi.

Acknowledgements

I firstly wish to express my sincere gratitude to my both supervisors: Associate Professor Jayantha Katupitiya and Dr. Nathan Kinkaid. Thanks for providing invaluable insights, support and guidance throughout my research. For each meeting, they create a relaxing atmosphere while providing professional suggestions. Their respect to my own opinions and encouragement to proceed with novel ideas would be beneficial for my whole life. I also wish to thank Dr. Mark Whitty who has been the chair for my annual reviews for providing suggestions for my research.

Thanks also goes to my colleagues in the mechatronics group. Thank you Dr. Scarlett Liu, who was the only female in the group besides me at the start of my PhD career, for your encouragement and company both in research and private life. Thank you Dr. Hiranya Jayakody for giving advices on my research, tutorials and collaborative papers. Thank you Sharmila Kayastha for insightful discussion on the topic and collaboration on a journal paper. Thank you Dr. Steven Lin for reviewing my thesis and providing detail suggestions. Thank you Javad Taghia for being my neighbour in the office and always available to suggest solutions of technical or trivial problems. Thank you Dr. Penglei Dai for your patience to chat with me and exemplify with continuous endeavour and optimistic attitude. Thank you Annie Wang for always being by my side and supporting me in every aspect. Thank you Qifan Tan for reviewing part of my thesis and giving detail feedback. Thank you Dr. Michael Woods, Dr. Stanley Lam, Julie Tang, and Shilong Liu for your help. You make my life in UNSW memorable.

My special thanks must be given to my parents. Without their unconditional love and support, I will not have the opportunity to explore my research interest and enrich my life experience. My love also goes to my younger brother, who is

now in university persuing a bachelor's degree. Though he is six years younger, he always encourages me and cheers me up by relieving the burden of supporting the whole family.

Finally, my deep gratitude and love goes to my fiance, Minghe Shan who is a PhD candidate in Delft University of Technology. Despite the long distance relationship having lasted more than three years, he comforts and supports me with love any time I feel depressed. Thank you for standing behind me for six years and always indicating me a bright future.

Contents

List of Figures

List of Tables

List of Abbreviations

EVA	Extra Vehicular Activities
FFSR	Free-Flying Space Robot
RW	Reaction Wheel
CM	Center of Mass
w.r.t.	with respect to
PI	Proportional-Integral
SMC	Sliding Mode Control
HOSMC	Higher Order Sliding Mode Control
TASMC	Twisting-Algorithm-based SMC
SQC2S	Smoothed Quasi-Continuous Second-Order SMC
CIMSMC	Constant Inertia Matrix -based Twisting Algorithm SMC
TVIMSMC	Time-Varying Inertia Matrix -based Twisting Algorithm SMC
AVSC	Adaptive Variable Structure Control
MIMO	Multiple-Input Multiple-Output
SISO	Single-Input Single-Output
CSMC	Smoothed SMC controller with constant gain
ASMC	Smoothed SMC controller with adaptive gain

List of Symbols

Coordinate Frames

Symbol	Description
Σ_i	Link frame
Σ_{wi}	i^{th} reaction-wheel frame
ΣB	Body/Base frame
ΣB_1	Reference half coordinate frame of the deploying satellite
ΣB_2	Trailing half coordinate frame of the deploying satellite
ΣG	Space robot frame
ΣI	Inertial frame
ΣO	Orbit frame
ΣT	Target frame

Symbol	Description	Units
α	Attitude angle of the spacecraft base along roll axis	rad
β	Attitude angle of the spacecraft base along pitch axis	rad
$\boldsymbol{A}_F$	Inertia matrix of the space robot model subject to external contact forces	
$\boldsymbol{A}_J$	Inertia matrix of the space manipulator model	

$\boldsymbol{B}_{F}$	Nonlinear terms of the space robot model subject to external contact forces	
$\boldsymbol{B}_{J}$	Nonlinear terms of the space manipulator model	
$\boldsymbol{F}_e$	Contact forces between the EE and the target	N
$\boldsymbol{J}_{FJ}$	Jacobian transpose of the space manipulator model	
$\boldsymbol{J}_{F}$	Jacobian transpose of space robot model subject to external contact forces	
$\boldsymbol{r}_0$	Position of CM of the base	m
$\boldsymbol{r}_e$	Position of the EE	m
$\boldsymbol{r}_g$	Position of CM of the FFSR	m
$\boldsymbol{r}_t$	Position of CM of the target	m
$\bar{\boldsymbol{\delta}}$	Additional buffer of SQC2S	
$\bar{\boldsymbol{\Lambda}}$	Positive-definite matrix in the sliding surface of SQC2S	
$\bar{\boldsymbol{B}}$	Intensity of local Earth's magnetic field	N/kg
$\bar{\boldsymbol{H}}$	Actual value of RW angular momentum	Nms
$\bar{\boldsymbol{H}}_N$	Desired nominal value of RW angular momentum	Nms
$\bar{\boldsymbol{M}}$	Magnetic moment vector	Am^2
$\bar{\boldsymbol{s}}$	Sliding surface of SQC2S	
$\boldsymbol{\delta}_f$	Additional buffer of TASMC	
$\hat{\boldsymbol{J}}$	Upper bound of the inertia matrix of the satellite	
$\boldsymbol{\Lambda}$	Positive-definite matrix in the sliding surface of TASMC	
$\boldsymbol{\Lambda}_r$	Positive-definite matrix in the sliding surface of boundary layer SMC	
$\boldsymbol{\omega}$	Inertial angular velocity of the satellite	rad/s

$\boldsymbol{\omega}_e$	Angular velocity of the EE	rad/s
$\boldsymbol{\Omega}_i$	Angular velocity of the i^{th} RW w.r.t. the satellite	rad/s
$\boldsymbol{\omega}_t$	Angular velocity of the target	rad/s
$\boldsymbol{\omega}_B$	Angular velocity of the spacecraft base	rad/s
$\boldsymbol{\omega}_{ob}$	Angular velocity of the satellite w.r.t. the orbit frame	rad/s
$\boldsymbol{\Phi}_M$	$\boldsymbol{\Phi}_M = [\phi_1, \phi_2, \cdots, \phi_n]^T$, joint angles of the manipulator	rad
$\boldsymbol{\Phi}_W$	$\boldsymbol{\Phi}_W = [\phi_{w1}, \phi_{w2}, \phi_{w3}]^T$, rotation angles of the RWs	rad
$\boldsymbol{\tau}$	$\boldsymbol{\tau} = [\boldsymbol{\tau}_J, \boldsymbol{\tau}_w^T]^T$, control torques, including joint torques and RW torques	Nm
$\boldsymbol{\tau}^\star$	Introduced virtual torque	Nm
$\boldsymbol{\tau}_a$	Aerodynamic disturbance torque	Nm
$\boldsymbol{\tau}_e$	External torques applied to the EE by the target	Nm
$\boldsymbol{\tau}_g$	Gravity-gradient torque	Nm
$\boldsymbol{\tau}_t$	External torques applied on the target	Nm
$\boldsymbol{\tau}_w$	Reaction-wheel torques	Nm
$\boldsymbol{\tau}_B$	Command control torques for three axes of the body frame	Nm
$\boldsymbol{\tau}_F$	$\boldsymbol{\tau}_F = [\boldsymbol{\tau}_J^T, \widetilde{\boldsymbol{\tau}}_B^T]^T$, control torques, including joint torques and introduced attitude control torques	Nm
$\boldsymbol{\tau}_J$	Joint torques	Nm
$\boldsymbol{\tau}_{tf}$	Tumbling torques generated by possible bias contact forces	Nm
$\boldsymbol{\tau}_u$	Unloading torque	Nm
$\boldsymbol{\varepsilon}$	Vector component of satellite quaternion parameters, $\boldsymbol{\varepsilon} = [q_{b1}, q_{b2}, q_{b3}]^T$	

$\boldsymbol{\varepsilon}_t$	Vector component of quaternion parameters of the target, $\boldsymbol{\varepsilon} = [q_{t1}, q_{t2}, q_{t3}]^T$	
$\widetilde{\boldsymbol{\tau}}_B$	Introduced attitude control torques, $\widetilde{\boldsymbol{\tau}}_B = -\boldsymbol{\tau}_w - \boldsymbol{\omega}_B \times \int \boldsymbol{\tau}_w dt$	Nm
$\widetilde{\boldsymbol{A}}$	Inertia matrix in space robot dynamic equation for the inertial-space control	
$\widetilde{\boldsymbol{B}}$	Nonlinear terms in space robot dynamic equation for the inertial-space control	
$\widetilde{\boldsymbol{e}}_1$	Motion tracking error at position level in the inertial space	
$\widetilde{\boldsymbol{e}}_2$	Motion tracking error at velocity level in the inertial space	
$\boldsymbol{A}$	Inertia matrix in space robot dynamic equation for the joint-space control	
$\boldsymbol{A}_w$	Configuration matrix of the reaction-wheel cluster	
$\boldsymbol{B}$	Nonlinear terms in space robot dynamic equation for the joint-space control	
$\boldsymbol{D}$	Disturbance torque	Nm
$\boldsymbol{e}_1$	Motion tracking error at position level in the joint space	
$\boldsymbol{e}_2$	Motion tracking error at velocity level in the joint space	
$\boldsymbol{H}_B$	Total angular momentum of the entire deploying satellite	Nms
$\boldsymbol{I}_i$	Inertia matrix of link i	kgm^2
$\boldsymbol{I}_t$	Inertia matrix of the target	$\mathrm{kg} \cdot \mathrm{m}^2$
$\boldsymbol{J}$	Inertia matrix of the entire deploying satellite	$\mathrm{kg} \cdot \mathrm{m}^2$
$\boldsymbol{J}_{wi}$	Inertia matrix of the i^{th} RW	$\mathrm{kg} \cdot \mathrm{m}^2$
$\boldsymbol{k}_r$	Adaptive gain of ASMC	
$\boldsymbol{P}_e$	Position of the end-effector	m

$\boldsymbol{q}$	Quaternion parameters of the satellite, $\boldsymbol{q} = [q_{b1}, q_{b2}, q_{b3}, q_{b4}]^T$	
$\boldsymbol{q}_r$	$\boldsymbol{q}_r = [\boldsymbol{\Phi}_M^T, \boldsymbol{\Phi}_S^T]^T$, generalized coordinates for space robot, including joint angles and spacecraft attitude	rad
$\boldsymbol{q}_t$	Quaternion parameters of the target, $\boldsymbol{q}_t = [q_{t1}, q_{t2}, q_{t3}, q_{t4}]^T$	
$\boldsymbol{q}_{rd}$	Desired state vector of $\boldsymbol{q}_r$	rad
$\boldsymbol{R}_a^t$	Rotation matrix from the inertial frame to the target frame	
$\boldsymbol{r}_g$	Position of the space robot centroid	m
$\boldsymbol{R}_o^b$	Rotation matrix from the orbit frame to the body frame	
$\boldsymbol{R}_{wi}^b$	Rotation matrix from the i^{th} RW frame to the body frame	
$\boldsymbol{s}$	Sliding surface of TASMC	
$\boldsymbol{S}(\cdot)$	Skew-symmetric matrix	
$\boldsymbol{T}$	External control torque	Nm
$\boldsymbol{U}$	Introduced control torques, $\boldsymbol{U} = -\boldsymbol{\tau}_B - \boldsymbol{\omega} \times \int \boldsymbol{\tau}_B dt$	Nm
$\boldsymbol{v}$	Orbital velocity of the satellite	m/s
$\boldsymbol{v}_e$	Linear velocity of the EE	m/s
$\boldsymbol{X}$	$\boldsymbol{X} = [\boldsymbol{\Phi}_S^T, \boldsymbol{P}_e^T]^T$, control variable of the space robot in the inertial space, including spacecraft attitude and end-effector position	
$\boldsymbol{X}_d$	Desired state vector of $\boldsymbol{X}$	
$\boldsymbol{\Phi}_S$	$\boldsymbol{\Phi}_S = [\alpha, \beta, \gamma]^T$, attitude of the spacecraft base	rad
δ	Indentation in the contact	N
$\Delta\bar{\boldsymbol{H}}$	Excessive angular momentum of RWs	Nms

η	Scalar component of satellite quaternion parameters, $\eta = q_{b4}$	
η_t	Scalar component of quaternion parameters of the target, $\eta_t = q_{t4}$	
γ	Attitude angle of the spacecraft base along yaw axis	rad
ρ_a	Atmosphere density	kg/m^3
f_n	Normal contact force	N
i_o	Orbit inclination	rad
k_δ	Contact stiffness	N/m
$K_{_M}$	Unloading control gain	
N_w	Number of reaction wheels	
t_o	Cruise time from ascending node	s
ω_o	Orbit angular velocity	rad/s

Subscripts

Symbol	**Description**
${}^a\{\cdot\}$	Variable expressed in the inertial frame
${}^b\{\cdot\}$	Variable expressed in the body frame
${}^o\{\cdot\}$	Variable expressed in the orbit frame
${}^t\{\cdot\}$	Variable expressed in the target frame
${}^w\{\cdot\}$	Variable expressed in the reaction-wheel frame

Chapter 1

Introduction

Space structures are expected to increase in size in the future, on the order of hundreds of meters to kilometres, in order to enlarge their application capabilities. To ensure efficient transportation of such space structures, they may be transported in a compact form so that launch vehicle payload volume can be efficiently utilized. After arriving in orbit, the space structures will be assembled.

To date, such on-orbit servicing operations are performed with robotic, telerobotic arms and/or astronaut's Extra Vehicular Activities (EVA). For example, the well known Space Station Remote Manipulator System (SSRMS) equipped onboard the International Space Station (ISS), controlled by the astronauts stationed in ISS, carries out delicate assembly and service tasks with the assistance of Dextre - the Special Purpose Dextrous Manipulator (SPDM) [1, 2]. However, this type of robot setups have workspace limited to the vicinity of the spacecraft and depend on the availability of astronaut. A solution to such problems can be provided by employing Free-Flying Space Robots (FFSRs), where the manipulator is mounted on a small-scale spacecraft. The FFSR has the freedom to visit and move around target space structures and can perform tasks autonomously or telerobotically, removing the risky astronaut's EVA, reducing costs while at the same time implementing more precise motions.

However, for FFSRs, since the robot arms are generally mounted on a base of comparable size, their approaching motions to a target (e.g. an assembling base or a structural component) and inevitable physical contact with another object will disturb the attitude of the supporting base in microgravity environment. The attitude deviations must be brought under control to maintain communication with ground stations and to keep the onboard solar panels in correct orientation for energy accumulation. Simultaneously, the generated contact forces and/or the end-effector motion have to be considered and controlled so that structural components will be successfully assembled and not lost or damaged.

In this thesis, first, a basic and simple example for on-orbit assembly case, i.e. spacecraft deployment, is considered. Modeling and robust control methods of a deploying spacecraft are proposed taking into account the substantial change in its inertia. Instead of fuel-consuming thrusters, electrically powered Reaction Wheels (RWs) are chosen to generate attitude control torques, which can reduce the need of fuel carried onboard the spacecraft. Further, a more complicated on-orbit assembly case which utilizes FFSRs is investigated. Systematic control approaches are proposed to meet motion and force specifications of an FFSR required for the space tasks. The developed two types of coordination controllers can achieve robust control of both the spacecraft attitude and its end-effector motion. In addition, control laws are developed to track a desired force trajectory, distinguished from the controllers developed by the predecessors which are aimed at maintaining a contact between the end-effector and the target.

In this chapter, the background of the presented work and the motivation inspired by the research gap are first presented. Then the objectives of this thesis in alignment with the motivation are explained. The thesis contributions are claimed in the following section. The last section outlines the thesis organization.

1.1 Background and Motivation

A practical on-orbit assembly space mission by FFSRs has not been experimentally validated yet. Figure 1.1 presents some examples of on-orbit servicing technology demonstration missions that have been launched or are currently in development stage. The missions are able to give insight into FFSR operations but without providing complete solutions to the problems that need to be solved in a potentially

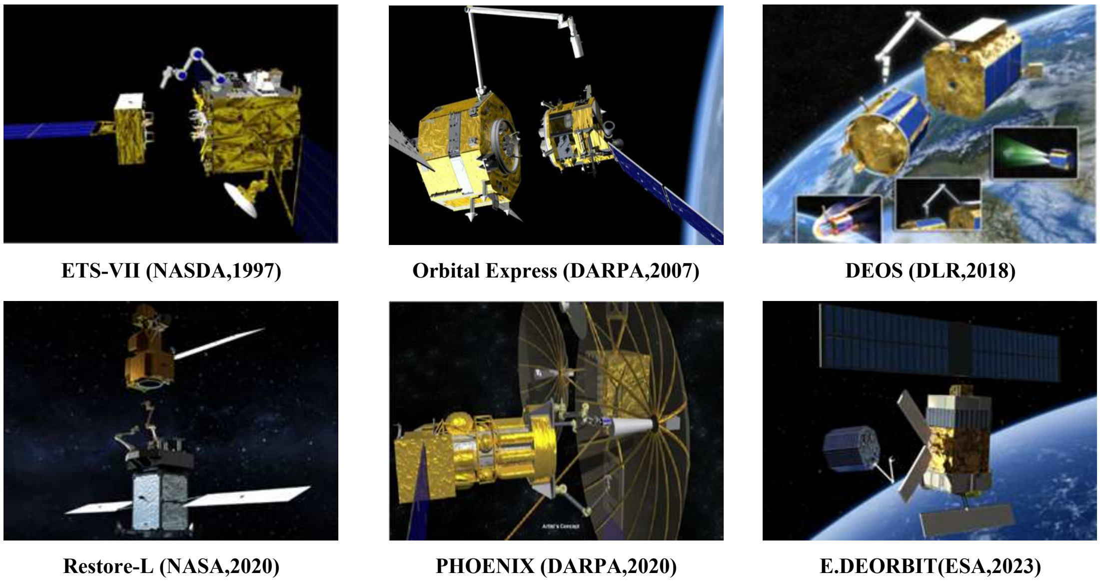

Figure 1.1: On-orbit servicing missions [3–8]

complicated space operation, e.g., none of the above missions have proved robust control of the space manipulator motion or successful force tracking performance with active spacecraft attitude regulation.

A space robot operation generally includes four phases as shown in Figure 1.2. In the observing and planning phase, the space robot characterizes the target motion and its physical properties and accordingly determines when and how to capture the target. Then for the second phase, the space robot approaches its end-effector to the target following the reference path determined in the first phase. The third phase corresponds to target capture when physical connection between the chaser FFSR and the client target is established. After that, the space robot will control its manipulator motion to manipulate the target and stabilize the entire system. Such operations contribute to the fourth phase - post-capture phase. Since the first phase is beyond the thesis scope, it is not further discussed in the following.

The approaching phase and post-capture phase require coordinated motion control of the spacecraft base and the space manipulator despite the coupling dynamics between them. Several work have proposed control laws by taking advantage of symmetric and positive definite property of the inertia matrix in the space robot model [10–12]. However, such a model was developed based on the assumption that external torques are provided by thrusters to regulate the

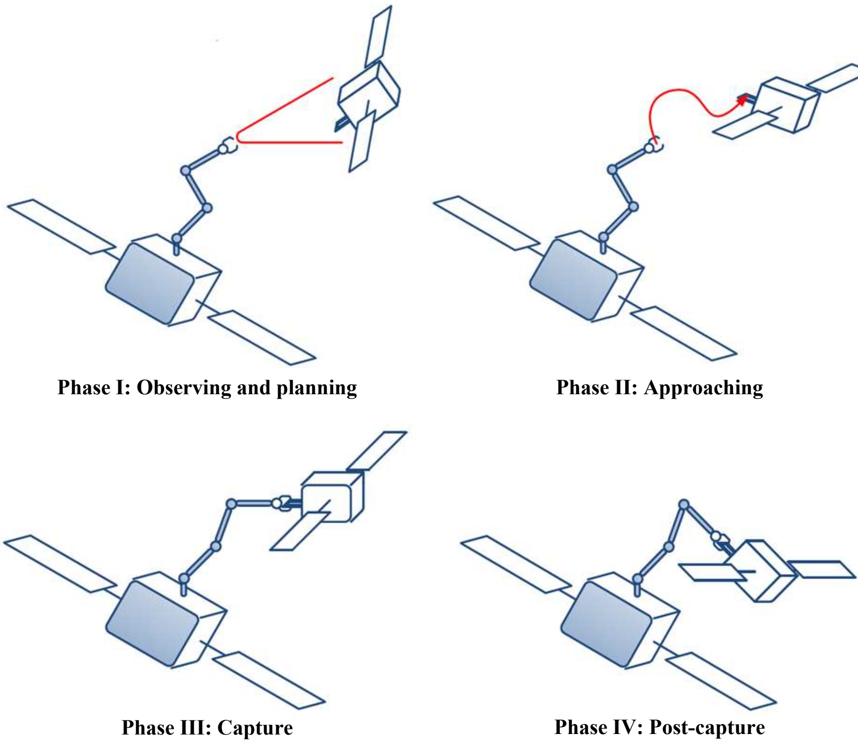

Figure 1.2: Four phases of FFSR operation [9]

spacecraft attitude. When considering using RWs which generate internal regulation torques, the model cannot accurately describe the space robot features in that its derivation does not account for the momentum of RWs. Actually, the involvement of RW momentum results in loss of advantageous properties (the inertia matrix is symmetric and positive definite) of the conventional space robot model, and as a result the above-mentioned controllers cannot be used. Furthermore, few literatures have focused on fast control of a space robot. Whereas, the application of RWs makes the abundant availability of solar energy to provide an opportunity to implement robust, faster attitude controllers. Time-optimal reorientation of a single spacecraft without extended robot arms was studied in [13–15]. Such a single rigid spacecraft has a dynamic model much simpler than an FFSR. In contrast, strong system nonlinearities, multiple input-torques, practical uncertainties and existing space disturbances complicate the process of controller design of FFSRs. Therefore, how to formulate the space robot model taking into account of the contribution of RWs to the angular momentum of the entire system and further to develop robust controllers that can achieve fast coordination of spacecraft base and space manipulator motions have become important issues that need to be resolved.

Performing capture of a target by an FFSR is one of the most challenging and risky operations for spacecraft since physical contact between the robot end-effector and the target is inevitable. Implementation of target capture intrinsically requires that a space robot to provide appropriate forces to either grasp the target or comply with the target motion, in addition to achieving its predetermined position. The floating feature of the system (the chaser FFSR plus the client target) makes accurate force control a sophisticated task. Despite fundamental research of target capture having been conducted, many researchers dealt with how to control the motion of an FFSR in order to maintain a contact between the robot manipulator and target [16–19]. However, tracking a desired force may be required for potential on-orbit assemble tasks, such as in-space screw-driving. If adopting the unified model of a space robot as established for the approaching phase or the post-capture phase, force tracking can be achieved, but a desired orientation of the spacecraft cannot be guaranteed. Therefore, a control-oriented space robot model with new structure needs to be established and also controllers which can track the desired contact force trajectory as well as regulate spacecraft attitude remain to be developed.

1.2 Objectives

The overall aims of the presented work can be categorised as: firstly, developing modeling and control methods of a deploying spacecraft which is a simple case of on-orbit assembly; secondly, developing systematic control approaches to deal with motion and force control of an FFSR for target capture operation which represents a general task in on-orbit assembly mission by FFSRs. Specifically, the objectives include:

- Establish kinematic and dynamic model for a deploying spacecraft and an FFSR which utilizes RWs to provide attitude regulation torques;
- Develop robust attitude controllers for the deploying spacecraft which can accommodate substantial inertia changes caused by structural reconfiguration;

- Develop coordination controllers for an FFSR to simultaneously control the spacecraft attitude and its manipulator motion required in the approaching or post-capture phase;

- Develop force control strategies for an FFSR to achieve contact force tracking in a target capture operation while regulating the spacecraft attitude.

1.3 Contributions

This thesis is developed on the idea that a fundamental knowledge of kinematics and dynamics of the spacecraft is a prerequisite in designing effective control algorithms. Therefore, the emphasis is initially placed in the establishment of spacecraft model and then proceeded with developing effective controllers. The thesis contributions include:

- A Twisting Algorithm -based Sliding Mode Controller (TASMC) is developed to maintain the attitude of a deploying spacecraft, i.e. when a spacecraft unfolds itself. The controller has the capability to accommodate the substantial inertia change which can reach an amplitude of 10^4 kg $\cdot$ m^2. Also, the controller eliminates the chattering effect of the conventional sliding mode control method and thus delivers smooth control torques which are perfectly practical for the control of RWs. Taking reaction-wheel torque saturation and speed saturation into account, simulation results reveal that the proposed controller is able to steer the satellite to the desired orientation with smaller settling time in comparison to the controllers proposed in previous literature when consuming comparable energy.

- A comprehensive dynamic model for a reaction-wheel actuated FFSR is presented. The reformulated model incorporates the contribution of reaction-wheel momentum to the entire system. Further the derived Multiple-Input Multiple-Output (MIMO) system model is decoupled into multiple single-input sub-channels using a diagonalization method, in order to prepare for development of robust coordination controllers.

- Two types of coordination controller are developed to control the space manipulator motion and the spacecraft attitude at the same time, i.e. the Smoothed Sliding Mode Controller and the Adaptive Variable Structure Controller (AVSC). Both controllers are robust to system uncertainties when following the reference end-effector path. The application of the AVSC method proposed in [20] achieves improvement of settling times in set-point/attitude regulation case.

- A control-oriented model structure for an FFSR in contact with a target is proposed. Separate models for the space manipulator and the spacecraft base are established to form basis for separate contact-force control and base attitude control. The reaction torque applying from the first joint to the base is considered as a disturbance. Such a framework of the model makes simultaneous end-effect motion/force control and base attitude control achievable.

- Hybrid motion and force control method is extended to enforce the FFSR to track a desired trajectory of contact force. The developed force controller incorporates the consistent motion between FFSR's end-effector and the tumbling floating target. Two simulation examples, including an FFSR-Target contact example and a specific on-orbit screw-driving example demonstrate that the controller can present accurate force tracking performance. Meanwhile, by using a separate attitude controller, spacecraft attitude is successfully regulated in the presence of disturbance coming from the manipulator motion and the contact forces.

1.4 Thesis Organization

The thesis is organized into six chapters.

Chapter 2 provides a literature review related to dynamic modeling and control of FFSR systems, including space robot modeling, coordination control and force control.

Chapter 3 establishes model of a reaction-wheel actuated deploying spacecraft and proposes a robust attitude control method. The solution is derived from the viewpoint of substantial inertia change of the spacecraft instead of analyzing the problem in a way of multi-body dynamics.

Chapter 4 presents a comprehensive dynamic model for a reaction-wheel actuated space robot and introduces two types of robust controllers that can maintain the attitude of the spacecraft as required when its manipulator is following the prescribed trajectory.

Chapter 5 reformulates the dynamic model of an FFSR in a control-oriented framework and presents a hybrid controller to track the designated motion of FFSR while ensuring a desired contact force. The spacecraft attitude is simultaneously regulated using RWs. Post-capture stabilization is also discussed, which is realized by adopting the Smooth Sliding Mode Controller developed in Chapter 4.

Chapter 6 concludes this thesis and suggests some directions for future research.

Chapter 2

Literature Review

This chapter reviews the past and present researches related to the problem of dynamic modeling and control of space robotic systems. The aim of this chapter is to identify what has been done in the previously published literature and thus lay a foundation for the thesis to fill the determined gap by proposing innovative modeling and control methods.

Section 2.1 presents space robot modeling techniques by first introducing the widely used methods for ground-based multi-body systems and then proceeding with modeling approaches developed for space robotic systems. Section 2.2 addresses control methods of the space robot motion which make approaching of a space robot end-effector to a target achievable. Section 2.3 introduces force control methods to deal with contact forces during the capture phase of a space task. Section 2.4 closes this chapter by clarifying that the objectives of the thesis are yet to be achieved based on the literature survey in above sections.

2.1 Space Robot Modeling

The challenge of creating a space environment validation makes a fully reliable space robot model to be essential in developing effective control algorithms. The loss of gravity results in coupled dynamics in space robot since the space manipulator motion disturbs the floating base, complicating modeling of a space robot in comparison to that of a ground-based robot. Despite this discrepancy, the multi-body dynamics used for fixed-base robots undoubtedly founds a basis for space robot exploration. To this end, the conventional dynamic modeling methods for ground-based robot is first introduced in this section and techniques progressing conventional modeling methods to space robot are followed.

2.1.1 Ground Robot Dynamics

Fixed-base robot dynamics has drawn much research interests, among which Newton-Euler method [21], Lagrangian formulations [22] and Kane's method [23] are the main approaches that can be extended to the dynamic modeling of space robotic systems [24]. Other methods, such us D'Alembert principle [25], Hamilton's method [26], Boltzmann-Hamel method [27], and Gibbs equations [28] are not enthusiastically utilized by the analysts for their specific drawbacks [29]. Considering the application to space robot dynamic modeling, the first three primarily used methods mentioned above are introduced in detail.

Newton-Euler Method

The application of Newton-Euler (NE) method to multi-body systems was pioneered in [30, 31]. The general idea is to describe an open-chain multi-body system based on its topological-tree property. For each link, the motion of its Center of Mass (CM) is selected to represent the translational motion of the link and the introduction of barycenter or augmented body concept [30, 32] can represent the rotational motion. The NE equations are coupled but easily understood and the recursive NE method is commonly used to obtain required torques. However, the constraint forces which appear in the course of the derivation of NE equations cannot be eliminated and thus direct input-output equations cannot be obtained especially for a robot with high degrees of freedom.

Lagrangian Method

Lagrangian method eliminates the problem of introduction of non-contributing constraint forces/torques [33]. Instead, it analyzes the robot dynamics by building a relationship of the kinetic energy and potential energy with the generalized forces.

This method is derived based on the principle of virtual work. According to the Lagrarian formation, it is very clear to get through the mathematical deriving process. Such feature popularizes the Lagrangian method in the modeling of a space robot [10, 34]. However, the Lagrangian method suffers complex computation of equations [35], especially the partial differentiation of the Lagrangian with regards to the generalized coordinates or the generalized velocities.

Kane's Method

Another popular method to establish dynamics for a robot is the Kane's method [23, 36, 37]. The method is based on new kinematic quantities, including partial velocities and partial angular velocities. Non-contributing forces or torques are eliminated by dot multiplying these quantities with available quantities, such as the inertial forces and contact forces, avoiding the problem confronted in Newton-Euler method. Also unlike Lagrangian approach, Kane's method eliminates the need to differentiate complex kinetic or potential energy and thus simplifies the formulation process. Kane's method can be applied to closed-chain robots. One drawback is that the physical meaning of this method is not as obvious as the Newton-Euler method or the Lagrangian method, which leads to less popularity of its application to space robot systems.

2.1.2 Space Robot Dynamics

Distinguished from ground-based robots, a space robot has a mobile support base. The dynamic model of a space robot has to be derived by considering the momentum of the entire system in addition to its kinematic relationship. Researchers have extended the conventional multi-body dynamic methods to space robot modeling by introducing new concepts or models.

Generalized Jacobian Matrix

As pointed by Longman *et al.* [38], the posture of the space robot end-effector does not have a closed-form solution and the solution can not be deducted without considering the history of postural change. Instead of describing the forward kinematics at position level, Umetani and Yoshida linearized the relationship between the motion rate of the space robot end-effector and that of joint variables excluding their history [39]. This forward kinematics can help to develop open-loop resolved rate control method when the spacecraft base is restricted with desired attitude.

Furthermore, to take the dynamical interaction between the manipulator arm and the spacecraft base into account, they introduced the relationship of momentum equilibrium into the kinematic formulation and proposed the concept of Generalized Jacobian Matrix (GJM) [39–41]. The GJM can be expressed as the extended manipulator Jacobian matrix which compensates disturbance to the supporting base. It reflects that the end-effector motion is not solely related to the kinematic properties of the robot, but also dependent on the robot inertia properties. When the manipulator inertia is negligible compared with its mounted base, the matrix becomes much like the inertia matrix of a fix-base case. The GJM proves to be useful to solve inverse kinematics for a free-floating space robot. However, it was illustrated that dynamic singularities exist when GJM is deficient at some configurations and the end-effector can not move in specific directions [42]. A Moore-Penrose pseudo-inverse form of the GJM was utilized to solve this problem by introducing redundancy with the sacrifice of more complex formulation in [43].

The Virtual Manipulator Method

Vafa and Dubowsky [44, 45] proposed another effective method - the Virtual Manipulator (VM) method to realize modeling and analyzing the kinematics and dynamics of space manipulator systems. The VM is an ideal kinematic chain with its base, the Virtual Base (VB) fixed to the Virtual Ground (VG). The VG lies in the center of mass of the spacecraft-manipulator system. In the case of a free-floating space robot system where no external forces act on the system, the VB will be stationary in the inertial space regardless the manipulator motions and internal constraint forces. Such feature represents the space robot system with a floating base by a system with a fixed base in the inertial space and thus algorithms developed for the ground-based robot can be applied directly to the space robot. In cases where external forces or torques are exerted on the system, the motion of the VB can be calculated based on the forces/torques. A space robot of N links and its end-effector VM is presented in Figure 2.1.

However, even it is simpler to analyze the VM than to analyze an actual space robot, especially for a free-floating case, the VM is an idealized kinematic chain and cannot be physically built and thus the VM method is not available for experimental test [46].

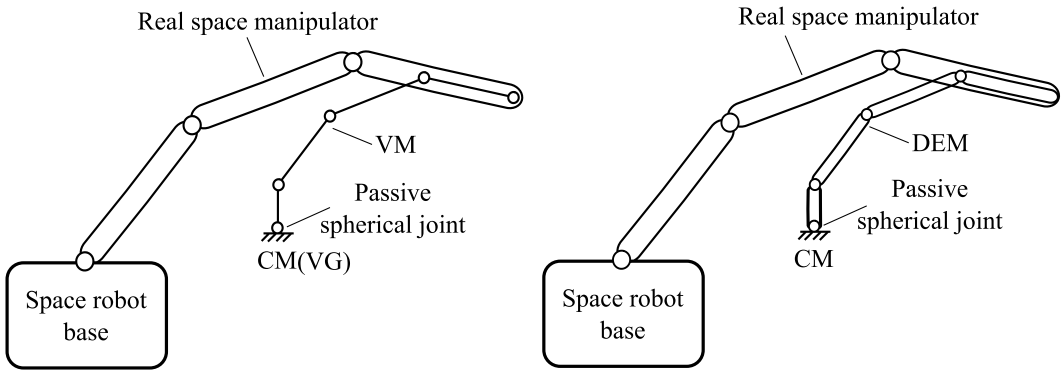

Figure 2.1: Space manipulator and its end-effector VM [44] and DEM [47]: a three-link planar robot case

Dynamically Equivalent Manipulator

The Dynamically Equivalent Manipulator (DEM) approach proposed by Liang *et al.* [47] improves the VM concept and can represent the space manipulator system both kinematically and dynamically. The DEM is a fixed-base manipulator with a passive spherical first joint, which is geometrically identical to the end-effector VM of the space manipulator. Besides, its dynamic parameters, including mass and inertia, satisfy certain algebraic equations. Under such conditions, the DEM performs identically as a given space manipulator system. A three-link planar space robot and its corresponding DEM is illustrated in Figure 2.1. The DEM can be set up physically to perform experiment validation and extended to represent a free-flying space robot with actuating reaction wheels.

2.2 Motion Control

The approaching phase requires the space robot end-effector to perform approaching motion to the target. Such manipulator motion will disturb the unrestricted spacecraft base and any motion design without provision of this reaction motion will result in task failure. If the spacecraft base is not controlled, as is the case of a free-floating space robot, the motion of the space robot will be solely determined by joint motions. Thus, the space robot kinematic and dynamic model will be finally dependent on joint angles and are of the same structure as that of the fixed-base robots. This implies that any control schemes used for ground-based robots can be adopted. However, most space missions require spacecraft attitude control so as to orient solar panels to absorb solar energy or to orient antennas to communicate with ground segments. In addition, the computational efficiency of path planning and control approaches can be improved under attitude control [48].

For a free-flying space robotic system with an attitude controlled-base, strong system nonlinearities, multiple input-torques, practical uncertainties and space disturbances make the design of its motion controller a complicate problem. The solutions in terms of this problem can be classified into two types. One type comes from the idea of minimizing or restricting the disturbance generated by the manipulator motion to the base. The other can be referred as active control of the base attitude in comparison to the first solution (passive attitude control).

2.2.1 Base Disturbance Minimization

The disturbance caused by the manipulator motion on the spacecraft base can be reduced or minimized by performing path planning for the manipulator motion.

Vafa and Dubowsky developed a tool called the Disturbance Map (DM) [49] based on the concept of VM. The DM improves understanding of the dynamic disturbance by evaluating the direction of the joint motion corresponding to mimimum or maximum disturbances. In [50], an improved version of DM, namely the Enhanced DM (EDM) was presented. The EDM can help plan the manipulator motion to reduce disturbances to the base. The authors also proposed EDM-based methods to suggest paths for a given manipulator which result in low attitude fuel consumption.

Nenchev *et al.* proposed the Reaction Null Space (RNS) concept to acquire the manipulator motion that does not disturb the spacecraft attitude when the space robot end-effector is following a predefined path [51]. The RNS was improved from the concept of Fixed-Attitude Restricted (FAR) Jacobian matrix proposed by the same authors which can be utilized to generate disturbance-free path in the joint space for free-floating space robots [52, 53]. The RNS-based approach has the advantage to decouple the manipulator dynamics from the base dynamics. However, existence of the RNS requires the availability of specific features of the space robot such as kinematic redundancy or dynamic redundancy. A composite control law based on RNS was developed in [51] to implement end-effector path tracking whilst inducing no disturbances to the flexible base. Similarly, an integrated motion controller based on the RNS concept was proposed for the Japanese Experiment Module Remote Manipulator System/Small Fine Arm (JEMRMS/SFA) on the ISS by making use of the inherent kinematic/dynamic redundancies of the system [54].

Xu and Shum proposed a concept of Coupling Factor as a measurement to characterize the degree of dynamic coupling [55]. Based on the dynamic analysis, the authors developed a simple Proportional-Derivative (PD) control scheme for regulation control, and a globally stable dynamic control scheme for tracking applications. The base exhibited both translation and rotation as the robot end-effector follows a prescribed path.

As mentioned above, and also accordng to a survey of literature on disturbance minimization on the spacecraft base [9, 56–58], it can be concluded that zero reaction can hardly be achieved for space robots without kinematic or dynamic redundancy to follow an arbitrary prescribed path. To this end, active attitude control can be utilized in coordination with manipulator motion control to avoid such problems. The examples of active base control are given in the next part.

2.2.2 Active Base Control

Some existing literature has tackled the active motion control problem by only inferring kinematic features even though some of them involved the dynamics-dependent GJM [39, 59–63]. A time-optimal control strategy was proposed based on system kinematics and momentum conservation law in [62]. The controller was designed in open-loop form. In [63], the approach to derive the required joints' motion, which makes the end-effector immune to the non-zero initial angular momentum was developed based on system kinematics. The attitude of the spacecraft control was also presented.

Later, PD-type controllers [64–66] and nonlinear controllers [67, 68] based on the space robot dynamic feature were proposed. In [65], Papadopoulos and Dubowsky developed a Transposed Jacobian (TJ) type coordination controller which can achieve control of desired orientation and position for both the end-effector and the spacecraft base. The additional control of base attitude and position enhanced the reachable workspace of the space manipulator and could achieve a favorable manipulator configuration. Such simple and intuitive TJ algorithm can be employed for highly nonlinear and complex system. Two types of nonlinear controllers were developed to control a free-flying space robot with control moment gyros in [67]. One was based on the Lyapunov's second method and the other used the exact linearization technique. In [68], the authors used separate controllers to control the rigid-body maneuver and vibration suppression of flexible arms of a space robot. For the rigid-body maneuver, on-line feedback tracking control was developed based on Lyapunov-like methodology and for the vibration suppression, Linear Quadratic Regulator (LQR) control was utilized. Two control strategies were presented in [69] for a two-arm space robot, which can compensate the flexibility excitation of the solar panels mounted on the base. One controller implements flexibility compensation task by allocating opportune joint torques whereas the other exploits thrusters' control to reduce the flexibility oscillations.

The aforementioned controllers assumed exact models which is always impractical due to imprecise dynamic features or unknown disturbances. Next the control algorithms that can overcome the problem of system uncertainties and parameter variation are presented.

A Modified Transposed Jacobian (MTJ) algorithm was developed to enhance the controller resistance to dynamic uncertainty and noise [66]. The MTJ algorithm achieved improved performance than TJ by using the stored data of previous control command and it requires reduced computational burden than model-based algorithm.

Xu *et al.* discussed adaptive control of a space robot system with an attitude controlled base both in the joint space and in the task space [70]. The authors first provided insight into linear parameterization problem of the space robot dynamic model. It was concluded that though the space robot dynamics can be linearized in the joint space, it is impossible to perform parameter linearization in the task space. Therefore, the adaptive control scheme was first developed in joint space. Then the problem of task space control was approached by making use of the proposed joint space adaptive controller and updating joint trajectory which is obtained by mapping the desired task-space trajectory with estimated dynamic parameters. Due to the unavailability of linear parameterization in task space, in most cases, the adaptive controller was developed for joint space control. The research presented in [71] defined the desired joint space variables in terms of the desired inertial space variables and inertial space error and also demonstated that the error with respect to inertial space can converge to zero based on Lyapunov method. Adaptive methods which adjust controller gains in real time were utilized at the expense of computational burden [11, 12, 72–74]. A control strategy based on a modified version of the Simple Adaptive Control theory is developed in [75] to improve the computational efficiency. Ulrich *et al.* [76] focused on the joint flexibility effects and proposed an adaptive composite controller to fix this problem. Extension of joint space control to task space control can be referred to the suggestions proposed in [70].

A robust Sliding Mode Controller (SMC) was proposed to implement a unknown-target capturing operation in [77]. The control task was achieved by first tracking the target motion and then stabilizing both the space robot and the target. The attitude error was kept small for both stages of control. To exploit the robustness of the SMC method, a second-order SMC was applied to achieve set-point position control for a space robot with one flexible link in [78]. However, SMC cannot ensure rapid spacecraft maneuvers which is a crucial requirement in space robotics when it comes to maintaining communication links, efficient solar energy harvesting and picking up targets in capture mode [79]. Time-optimal reorientation of a single spacecraft without extended robot arms was studied in [13–15]. For a single rigid spacecraft, its dynamic model is much simpler than a space robot and can be linearized if assumed as an inertially symmetric body [13], which significantly simplifies the design of the optimal controller. Few literatures have focused on time-optimal set-point control of a space robot. In [62], an optimal control approach was proposed to control the motion of a free-floating robot, whereas the attitude of the spacecraft is not controlled at a specifically predefined value and the controller requires precise model parameters.

Neural networks were also applied to achieve space robot control with the existence of system uncertainties or disturbances [80–83]. In [84], a control method based on syncretized neural network and variable structure control was proposed to track desired joint trajectories for free-floating robots without addressing attitude regulation of the platform. A Radial Basis Function (RBF) neural network was used to adaptively estimate system uncertainties and variable structure was integrated to supplement blind sections.

2.3 Force Control

During the capture phase of space tasks that involved in on-orbit assembly, physical contact between the robot manipulator and the target object is inevitable. The generated contact forces must be carefully controlled so that structural components will be successfully assembled and not lost or damaged. In addition, the spacecraft platform needs to be oriented to a desired attitude to maintain communication with a ground station and solar energy accumulation.

In the demonstration of autonomous cooperative satellite capture by ETS-VII [85], the End-Effector (EE) captured the target in a closed-contact way by forming a physical enclosure around a grapple fixture of the target before making contact. Only precise motion control was required in such a case whereas force control was not considered. The spacecraft attitude control system was not activated during this capture process to avoid excess base motion. For the Orbital Express Demonstration System, the client satellite was captured by a gripper-like EE in an open-contact way and then made to mate with the chaser satellite using electrical connectors [86]. The gripper pinched the target to prevent it from escaping without accurate force tracking.

To summarize the fundamental research of target capture that has been published, one solution to the problem is to analyze the system from the view point of momentum transfer and the other solution can be derived in terms of contact forces generated during the capture operation [87]. Examples in terms of these two methods are detailed in the following sections.

2.3.1 Momentum Transfer

Since the impact force is considered to be difficult to sense precisely, Yoshida *et al.* [88] dealt with the contact problem by figuring out the velocity relationship just before and after the contact. The solution takes advantage of momentum conservation for a free-floating space robot without sensing the contact force. The authors discussed the collision dynamics with proposing the concepts of "Extended Generalized Inertial Tensor (Ex-GIT)" and "Virtual Mass". By means of these concepts, the collision of this complicated chain problem was analyzed in a similar way of mass points collision theory which is much simpler. The authors also further investigated the impulse characteristics against collisions in various conditions in [89]. However, such analysis only focused on the moments before and after the contact instead of control of the contact force.

In [90], Nenchev and Yoshida provided further insight into the base and joint reactions against contact phenomenon. The main idea of the work is to use the dependence of the change of the two partial momenta, that of the base and the manipulator arm. With proper pre-contact configuration of the space robot the change of base partial momentum can be minimized. A post-contact controller based on the concept of RNS [91] was developed to transfer excess angular momentum from the base towards the manipulator and simultaneously to decrease the joint velocity. The discussion is essentially of theoretical interest whilst practically it is difficult to achieve the favourable momentum distribution presented in the literature.

In a similar way, by analyzing momentum distribution of the system, the authors in [92, 93] involved reaction wheels to accommodate the undesirable angular momentum for the spacecraft base. They considered minimization of the spacecraft attitude deviation as a constraint, which is represented by zero angular momentum of spacecraft base, and proposed controllers in a open-loop form to derive the required motion of reaction wheels and robot arms for both capture and post-capture phases. Some other literatures also considered minimization of the contact forces in the direction of a proper pre-contact configuration [94–98].

The above literatures, however, assume that the end-effector can follow the rotation motion of the target. To further involve a target that may have a large angular momentum, a contact/push-based control method using a cushion type damper was proposed in [99] to absorb the rotational motion. The force generated by the contact between the flexible end-effector and the target surface was utilized to decrease the angular momentum of the target. A similar method that utilized impulse control to damp a tumbling target was discussed in [100].

Instead of considering the contact forces as external force to the space robot, Shibli proposed a unified control-oriented modeling approach which allows considering the generalized constraint forces between the end-effector and the target satellite as internal forces [101, 102]. The developed approach combines the dynamics of the space robot and the target in a single framework by treating kinematic constraints at the differential level together with the constraints of linear and angular momentum. An adaptive inverse dynamic controller was developed accordingly to track motion trajectory while regulating the interaction forces.

2.3.2 Contact Force Control

Fundamental force control methods for ground-based robots can be categorized based on involvement of the relationship between the robot motion and the contact force, or the force feedback, or both of them as: (1) Methods based on the relation between position and force - stiffness control [103, 104]; (2) Methods based on the relation between velocity and force - impedance control [105] and admittance control [106]; (3) Method involving direct force and position feedback - hybrid control [107]; (4) Method involving direct position feedback - explicit force control [108]. The principles of such control algorithms were addressed by Zeng and Hemami in [109]. The authors also compared and summarized similarities and differences between these various force control methods in terms of the controlled space, measured variables, modified variables and modulated objectives, as given in Table 2.1.

Table 2.1: Various force control methods [109]

<table>
<tr><th colspan="2">Algorithm Classification</th><th>Workspace</th><th>Measured Variables</th><th>Modified Variables</th><th>Modulated Objectives</th></tr>
<tr><td colspan="2">Active stiffness control</td><td>Joint space/ Task space</td><td>Position Force</td><td>Joint displacement /position error Contact force</td><td>Stiffness matrix</td></tr>
<tr><td colspan="2">Impedance control</td><td rowspan="2">Task space</td><td>Position Velocity Force</td><td>Position and velocity error /desired trajectory Contact force</td><td>Impedance</td></tr>
<tr><td colspan="2">Admittance control</td><td>Force</td><td>Force error</td><td>Admittance</td></tr>
<tr><td rowspan="4">Hybrid control</td><td rowspan="2">Hybrid position /force</td><td>Position subspace</td><td>Position</td><td>Position error</td><td>Postion</td></tr>
<tr><td>Force subspace</td><td>Force</td><td>Force error</td><td>Force</td></tr>
<tr><td rowspan="2">Hybrid impedance</td><td>Position subspace</td><td rowspan="2">Force</td><td>Velocity error</td><td rowspan="2">Impedance</td></tr>
<tr><td>Force subspace</td><td>Force error</td></tr>
<tr><td>Explicit force control</td><td>PI,PD, PID,etc.</td><td>Task space</td><td>Force</td><td>Force error</td><td>Desired force</td></tr>
</table>

To achieve accurate force tracking performance for ground-based robot systems subjected to unknown parameters and uncertainties, fundamental force control techniques were improved by incorporating the advanced control algorithms. Such advanced force control methods include adaptive force control [110–113], robust force control [114–117] and learning algorithm-based force control [118–120].

The floating feature of the spacecraft and the target to be captured intrinsically complicate the contact force control. Therefore, when it comes to implement capture of a target by a space robot, instead of actively controlling the force trajectory, impedance control method has been progressed to apply on the space robot to maintain a contact between the space robot end-effector and the target. A survey of literature with regards to maintaining a contact in the case of space robot capturing a target using the impedance control method is presented in the following. Since hybrid motion and force control has been a basic control strategy that can be potentially extended to the space robotic systems, the principle of this method is also addressed.

Impedance Control

The underlying idea of impedance control is that the controller attempts to implement a dynamic relation between manipulator variables such as end-point position and force rather than control these variables alone [105]. This relationship is referred as mechanical impedance. By enforcing a desired mechanical impedance, the contact can be effectively handled. A basic scheme of impedance control is presented in Figure 2.2. The figure shows that the introduced input y attributed to impedance control methodology is derived based on the position and velocity error of the end-effector as well as the contact force. In combination with the inverse dynamic control law, the controller ensures a desired relationship between the desired contact forces and the end-effector displacement in task space.

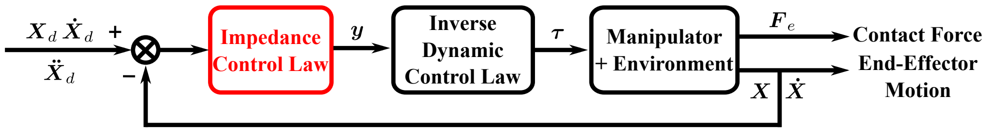

Figure 2.2: Block scheme of basic impedance control [121]

Extended from the concept of impedance control, the Object Impedance Control (OIC) method was proposed to deal with problem of multiple robot arms manipulating a common object [122]. In this method, the combination of feedforward and feedback control allows the object to behave as a reference impedance [123]. Moosavian and Papadopoulos presented the general formulation for the Multiple Impedance Control (MIC) algorithm in [124]. The MIC control law is able to enforce establishment of same designated impedance behaviour for all cooperative manipulators and the manipulated target. An example given in [123] showed that the MIC algorithm yielded improved performance over OIC in the presence of flexibility. Strategy of utilizing impedance control for contact tasks involving cooperative manipulators was also discussed in [125] and [126]. The basic idea is that the impedance was assigned between each manipulator displacement/velocity and the contact forces.

The performance of impedance controller is affected by the uncertainties in both the robot dynamic model and the environment. To overcome such shortcomings, advanced control algorithms can be incorporated [127–134]. In [128], an adaptive robust force tracking impedance control scheme was proposed. The controller implemented online estimation to obtain environment parameters and updated the reference position matching a desired force. This control scheme is useful in limited scenario because the force error may get infinite if the desired force or the environment position error is a function of complex form. A closed-loop control scheme was addressed in [129] to implement both force and impedance control of robot manipulator. The methodology is based on the replacement of robot dynamics by a target impedance which was realized using feedback and feedforward compensation of robot control variables. The controller is robust when subject to environment uncertainties but sensitive to the robot model. In [130] a neural network-based compensator served as auxiliary controllers to counteract model uncertainties and environmental disturbances. Also the referenced trajectory was modified using sensed contact force instead of environment stiffness which cannot be accurately known.

Next some examples of extending the impedance control method to the space robotic systems are given. Such examples take into account the floating feature for the space robot and the target. A simple illustration of impedance control for the ground-based robot and free-flying robot is presented in Figure 2.3. The objective for impedance-based space robot control is to maintain a contact between the space robot end-effector and the target during the capture phase.

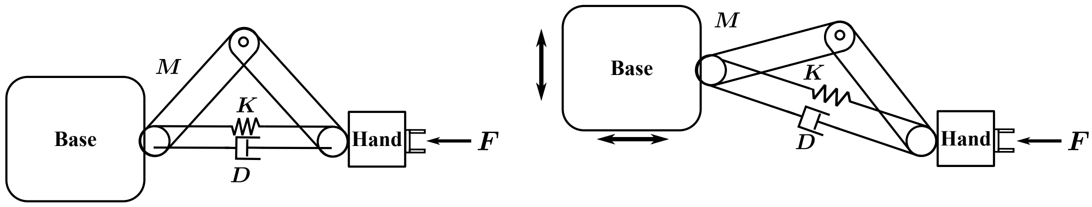

a) Conventional impedance control b) Free-flying space robots impedance control

Figure 2.3: Impedance control schematic diagram

Moosavian *et al.* utilized the MIC algorithm to manipulate space objects by including the coupling dynamics between the manipulators and the free-flying base [135]. By tuning the controller mass matrix gain, the simulation results revealed that all object levels, including the spacecraft base, the manipulators and the grasped object, could track their desired trajectory with negligible errors in the presence of contact forces and even significant disturbances. This is based on the condition that the force applied to the support base can be precisely controlled, as assumed in [136–138]. Nonetheless, in fact, it is difficult to achieve precise spacecraft base force control in that the thruster's output force is constant and only the total impulse can be controlled [139]. To this end, Nakanishi and Yoshida proposed an impedance control algorithm by controlling the end tip of the space robot as a mass-damper-spring system, which is fixed at a point in the inertial coordinate despite of the base reactive motion [140]. This method requires accurate target mass and contact stiffness though.

Other literature contributed to the impedance-control-based capture phase by investigating the practical operation environment and process. Considering that the short duration of the contact phase as a result of the unconstrained and microgravity space environment, the concept of coefficient of restitution was introduced to connect impedance control parameters with contact features [18]. Such definition enables the varible to serve as a criterion for maintaining contact [18, 19]. An open-loop impedance-based control law was constructed to achieve uni-axial force control based on the desired coefficient of restitution. In [16], impedance matching concept was proposed to optimize the regulation of impedance control for nonlinear dynamic robotic tasks in terms of system transient and steady-state response. A rigid end-effector grasping a soft material object or the opposite situation was considered in the task. Ref. [17] discussed the application of impedance matching to implement robotic capture of a non-cooperative satellite.

Hybrid Motion and Force Control

Since the end-effector position and the contact forces cannot be simultaneously controlled in a same direction, they should be controlled along different directions respectively, as suggested by the hybrid motion and force control scheme [107]. The "hybrid" technique combines the position and force information into positional data to realize position and force trajectory tracking at the same time. The concept of selection matrices were proposed to describe and analyze force-controlled and position-controlled degrees of freedom separately. A conceptual architecture of hybrid motion and force control is illustrated in Figure 2.4.

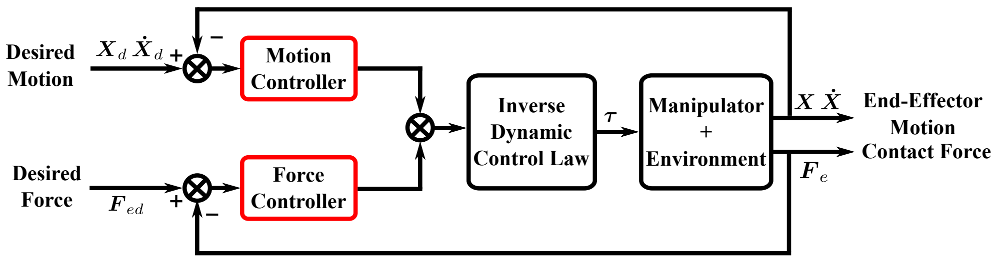

Figure 2.4: Hybrid control architecture

In the literature where this concept was proposed, the authors also applied the method to a Scheinman manipulator to verify that simultaneous force and position trajectory control can be achieved [107]. The theory has been extended to the case of multi-arm cooperating robots [141, 142]. Considering a situation where the precise information of the contact object cannot be obtained, Yoshikawa and Sudo developed an on-line estimation algorithm which can estimate the local shape of the constraint surface by using measured data on the position and force of the end-effector [143]. Such an approach can help decrease the burden on the operator of giving precise data on the constraint and make the dynamic hybrid control approach more practical. A force control method regarding flexible robot links was proposed in [144]. Further, to cope with system uncertainties as well as external disturbances, control methods that combines the hybrid control method with advanced algorithms, such as learning algorithm, sliding mode control, adaptive control, neural networks, were developed [119, 145–147].

Note that the above examples are restricted to the application of ground-based robots. When adopting the hybrid motion and force control to space missions, the space task should be planned in detail and the control mode may be required to be switched during the task.

2.4 Summary

This chapter presents a literature review of past work related to modeling and control of a space robot system. The commonly used modeling technique for a free-flying space robot is based on the Lagrangian method and incorporates the space robot kinematics which takes the floating feature of the spacecraft base into account. Whereas, such formulation always assume that external forces/torques generated by thrust jets are applied to regulate the spacecraft orientation. However, the thrusters run on fuel: a source of energy with limited availability. Also in a scenario where the spacecraft is flying in close proximity to structural components that are to be assembled, filing clusters is undesirable. When replacing thrust jets by Reaction Wheels (RWs) which utilizes sustainable electricity to provide control torques for the spacecraft base, the momentum contribution of the RWs to the space robot is seldom considered when deriving the Lagrangian equations. Therefore, control algorithm designed based on the conventional dynamics for a space robot need to be improved by first investigating the feature of the updated dynamic model which takes this aspect into account. Further, robust control methods related to rapid maneuvers of a free-flying robot was rarely discussed. For the force control required in the capture phase, many researchers dealt with maintaining a contact between the space robot and target. Solution of tracking a desired contact force and simultaneous controlling the spacecraft attitude has not been presented. The review of existing research provides a basic guide and helps innovate approaches to the thesis objectives.

Chapter 3

Robust Attitude Control of an On-Orbit Deploying Satellite

3.1 Introduction

Satellites with increasing large volume are required to be launched for carrying out space missions of higher performance. Restricted by current launch vehicle fairings, it may be impossible to launch such large and bulky structures in an assembled state [148]. As a solution, such structures will be compactly stowed in a unassembled form in space vehicles before launching and assembled or deployed in orbit. During the assembly or deployment, the reconfiguration of the satellite may cause adverse attitude deviation which can disrupt communication with ground stations and energy accumulation from the Sun. Therefore, it is important to control the spacecraft attitude for successful space operations.

The attitude control of a spacecraft for a simple specific on-orbit assembly case, i.e. spacecraft deployment is investigated in this chapter. The deploying scenario is represented by the opening of a satellite in the clamshell arrangement, as is the case of Astrium's "Snapdragon" [149, 150] spacecraft configuration shown in Figure 3.1. Such a spacecraft could be considered as a space robot with only one link mounted on its base. Assume one of the "shells" carries most of the on-board subsystems, such as the attitude control, power supply and communication subsystems. During the deployment, this reference half of the satellite will be disturbed by the motion of the other half and have to be controlled. Instead of analyzing the problem in a way of multi-body dynamics, a solution is derived from the viewpoint of substantial inertia change of the satellite when considering the spacecraft as a whole. A robust attitude controller is developed to illustrate whether such large system uncertainties will lead to system instability.

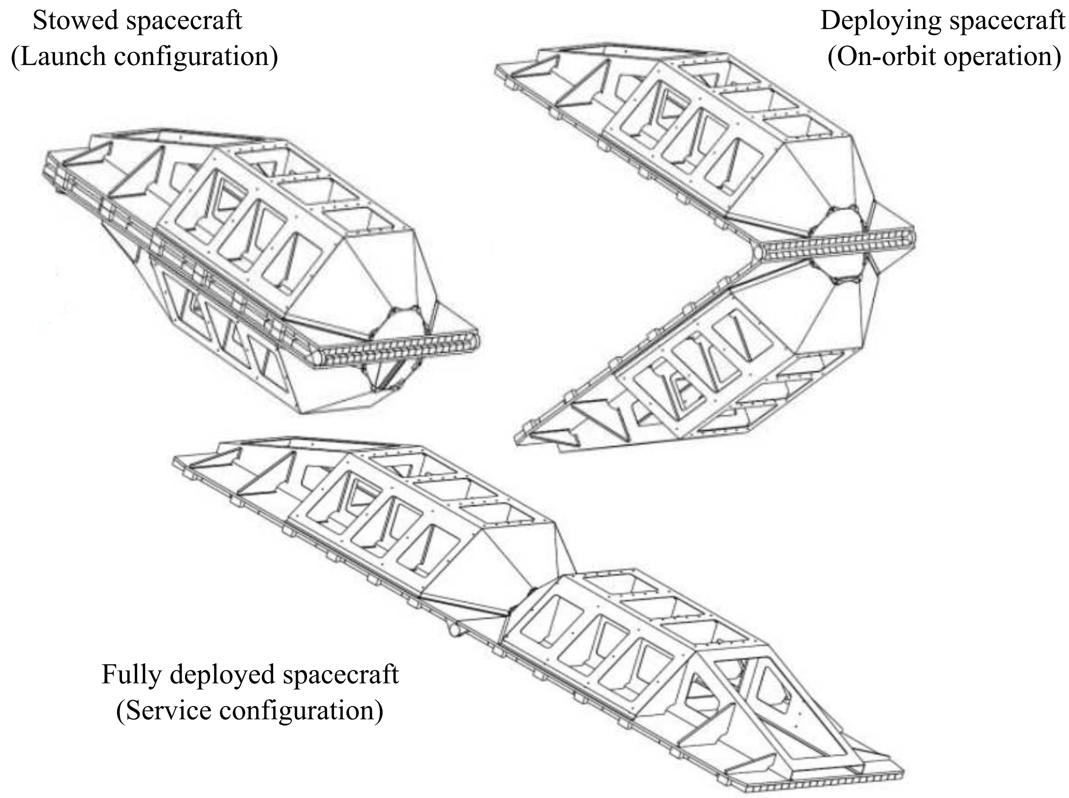

Figure 3.1: Astrium "Snapdragon" spacecraft configuration [149]

This chapter is organized with seven sections. Section 3.2 presents the mathematical model of a satellite using quaternions to represent its attitude. The large inertia change due to the deployment of the satellite is also discussed. Section 3.3 deals with problems of torque saturation and speed saturation for the Reaction Wheels (RWs) which are used to provide attitude regulation torques. In Section 3.4, a robust attitude controller is designed based on the twisting-algorithm sliding mode control method which maintains the reference half of the satellite at an appropriate orientation. Two different kinds of inertia matrices are used and compared in the controller to optimize the performance. A Smoothed Quasi-Continuous Second Order Sliding Mode Controller (SQC2S) proposed by other authors [151] which can deliver good performance in the presence of system uncertainties is chosen to make a comparison with the proposed controller. This SQC2S method is applied to the deploying satellite model in Section 3.5. Simulation results illustrating the comparison are shown in Section 3.6. Section 3.7 closes this chapter.

3.2 The Satellite Model

3.2.1 Basic Coordinate Frames

It is first necessary to clarify the coordinate frames used below to specify spacecraft attitude before proceeding to the kinematics of a three-axis-stabilized satellite. Three coordinate frames, including the body frame, the reference frame and the inertial frame, are defined as shown in Figure 3.2.

(1) *Inertial frame (ΣI).* Suppose the satellite is orbiting the Earth. The inertial frame is located at the Center of Mass (CM) of the Earth. Its Z_I axis is parallel to the Earth's rotation axis, X_I axis points towards the Vernal Equinox and the Y_I axis completes the right-handed orthogonal coordinate system.

(2) *Orbit frame (ΣO).* For a planet-orbiting satellite, the reference frame is defined as the orbit frame, in which the deploying satellite is to be attitude-stabilized. The origin of ΣO is located at the CM of the satellite and moves together with the spacecraft. The X_O axis is in the orbit plane and aligns with direction of the satellite velocity. The Z_O axis points towards the nadir. The Y_O axis is normal to the orbit plane and completes a three-axis right-handed orthogonal system.

(3) *Body frame (ΣB).* The body frame is chosen according to the physical features of the satellite. Its origin is also located at the CM of the satellite but its axes are fixed with the satellite body, each of which is defined to make it close to the corresponding orbit axis, as shown in Figure 3.2. The coordinate axes are aligned with satellite principle inertia axes.

Frame transformations are needed when expressing variables in different frames. Throughout this chapter, terms with left superscript ${}^{a}\{\cdot\}$, ${}^{o}\{\cdot\}$ and ${}^{b}\{\cdot\}$ represent

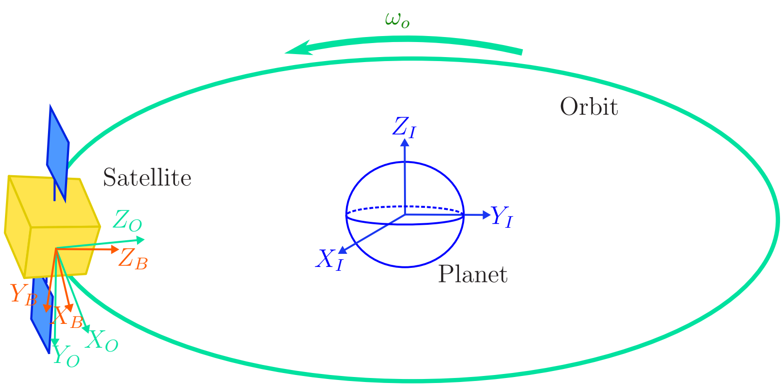

Figure 3.2: Definition of Coordinate Frames

variables expressed in the inertial frame, the orbit frame and the body frame, respectively. Let ${}^o\boldsymbol{\omega}_{io}$ be the orbit angular velocity and ${}^b\boldsymbol{\omega}_{ob}$ be the angular velocity of the satellite with respect to (w.r.t.) the orbit frame. Then the inertial angular velocity of the satellite ${}^b\boldsymbol{\omega}$ takes the form,

$$ {}^b\boldsymbol{\omega} = {}^b\boldsymbol{\omega}_{ob} + \boldsymbol{R}_o^b \, {}^o\boldsymbol{\omega}_{io}, \tag{3.1} $$

where $\boldsymbol{R}_o^b$ represents the rotation matrix from the orbit frame to the body frame. Assume the satellite is in a circular orbit. Then the orbit angular velocity ω_o is constant and ${}^o\boldsymbol{\omega}_{io} = [0, -\omega_o, 0]^T$ according to the orbit frame definition.

3.2.2 Satellite Kinematics

Euler angles, quaternion parameters, Rodrigues Parameters (RP) and Modified Rodrigues Parameters (MRP) [152] are commonly used to describe the attitude of a spacecraft. These attitude representations can transform to each other in that the spacecraft attitude is uniquely determined. Quaternions show non-singular behavior compared with Euler angles and relieve tedious calculations compared with RP or MRP. Hence, quaternions are selected to represent the satellite attitude in kinematic equations as follows.

$$ \dot{\boldsymbol{q}}_{\boldsymbol{B}} = \begin{bmatrix} \dot{\boldsymbol{\varepsilon}} \\ \dot{\eta} \end{bmatrix} = \frac{1}{2} \begin{bmatrix} \eta \boldsymbol{I}_3 + \boldsymbol{S}(\boldsymbol{\varepsilon}) \\ -\boldsymbol{\varepsilon}^T \end{bmatrix} {}^b\boldsymbol{\omega}_{ob}, \tag{3.2} $$

where $\boldsymbol{q}_B$ is the quaternion and $\boldsymbol{q}_B = [q_{b1}, q_{b2}, q_{b3}, q_{b4}]^T$; $\boldsymbol{\varepsilon}$ is a vector component of $\boldsymbol{q}_B$ and $\boldsymbol{\varepsilon} = [q_{b1}, q_{b2}, q_{b3}]^T$; η is the scalar component of $\boldsymbol{q}_B$ and $\eta = q_{b4}$; $\boldsymbol{I}_3 \in \mathbb{R}^{3\times 3}$ is an identity matrix. Based on the derivation of quaternion parameters [152], the elements of $\boldsymbol{q}_B$ are restricted by $\boldsymbol{\varepsilon}^T\boldsymbol{\varepsilon} + \eta^2 = 1$. Let $\dot{\boldsymbol{\varepsilon}} = \frac{1}{2}\Xi(\boldsymbol{q}_B)\ {}^b\boldsymbol{\omega}_{ob} = \frac{1}{2}\left[\eta\boldsymbol{I}_3 + \boldsymbol{S}(\boldsymbol{\varepsilon})\right]{}^b\boldsymbol{\omega}_{ob}$ for convenience. The notation $\boldsymbol{S}(\boldsymbol{\varepsilon})$ indicates a skew-symmetric matrix such that

$$\boldsymbol{\varepsilon}\times = \boldsymbol{S}(\boldsymbol{\varepsilon}) = \begin{bmatrix} 0 & -q_{b3} & q_{b2} \\ q_{b3} & 0 & -q_{b1} \\ -q_{b2} & q_{b1} & 0 \end{bmatrix}. \tag{3.3}$$

The notation $\boldsymbol{S}(\cdot)$ is used throughout the work to represent a skew-symmetric matrix with a formula similar to (3.3). Using quaternion parameters, $\boldsymbol{R}_o^b$ in (3.1) is expressed as [153],

$$\boldsymbol{R}_o^b = \boldsymbol{R}_o^b(\boldsymbol{q}_B) = (\eta^2 - \boldsymbol{\varepsilon}^T\boldsymbol{\varepsilon})\boldsymbol{I}_3 + 2\boldsymbol{\varepsilon}\boldsymbol{\varepsilon}^T - 2\eta\boldsymbol{S}(\boldsymbol{\varepsilon}). \tag{3.4}$$

3.2.3 Satellite Dynamics

Before introducing satellite dynamics, the type of actuators which provide attitude control torques needs to be considered in that different producing torques may result in different dynamic models for the spacecraft. Two means of producing torques for the attitude control of a spacecraft are typically used: reaction forces/torques generated by thrusters and control torques generated by momentum exchange devices. Though thrusters can provide unbounded torques, smooth control is unachievable due to the inherent impulsive nature [139]. Besides, thrusters consume limited on-board fuel and may induce contamination to on-board equipment. The second option reorients the spacecraft by transferring the undesired angular momentum of the satellite body to the internal momentum exchange devices, such as momentum wheels, Control Momentum Gyros (CMGs) and RWs, without changing the momentum of the entire system (satellite body plus momentum exchange devices). Momentum wheels primarily provide momentum bias necessary for attitude stability [154]. CMGs allow large torques but are relatively heavy and seldom used for ordinary-sized spacecraft. Therefore, RWs are preferred in this work because they can provide continuous and smooth control torques, leading to accurate attitude control and moderately fast maneuvers.

The deploying satellite is modeled as a rigid body with its deployment process represented by an inertia matrix that changes with time. This inertia change due to the opening clamshell is discussed later in Section 3.2.4. As RWs generate internal torques, the control torques must be obtained from the RWs' momentum instead of simply applying an external torque which is the case when using thrusters. The dynamic equation can be derived from the Newton-Euler formulation as,

$$\dot{\boldsymbol{H}}_B + \boldsymbol{\omega} \times \boldsymbol{H}_B = \boldsymbol{T} + \boldsymbol{D}, \tag{3.5}$$

where $\boldsymbol{T}$ is the external control torque; $\boldsymbol{D}$ represents bounded disturbances; $\boldsymbol{H}_B$ is the total angular momentum of the spacecraft with respect to origin of the inertial frame and includes two parts: angular momentum of the satellite body and angular momentum of the RWs, expressed by

$$\boldsymbol{H}_B = \left(\boldsymbol{J} - \sum_{i=1}^{N_w} \boldsymbol{J}_{wi}\right)\boldsymbol{\omega} + \sum_{i=1}^{N_w} \boldsymbol{J}_{wi}\left(\boldsymbol{\Omega}_i + \boldsymbol{\omega}\right), i = 1, 2, \cdots, N_w, \tag{3.6}$$

where $\boldsymbol{J}$ and $\boldsymbol{J}_{wi}$ represent the inertia matrix of the entire spacecraft and the i^{th} RW, respectively; N_w is the number of RWs; $\boldsymbol{\Omega}_i$ is the reaction-wheel angular velocity w.r.t. the satellite. All non-scalar variables in (3.5) are expressed in the body frame. Specifically, $\boldsymbol{J}_{wi}$ and $\boldsymbol{\Omega}_i$ are transformed from reaction-wheel-frame values ${}^w\boldsymbol{J}_{wi}$ and ${}^w\boldsymbol{\Omega}_i$ which are known *a prior* or can be directly measured, as $\boldsymbol{J}_{wi} = \boldsymbol{R}_{wi}^b\, {}^w\boldsymbol{J}_{wi}\left(\boldsymbol{R}_{wi}^b\right)^T$ and $\boldsymbol{\Omega}_i = \boldsymbol{R}_{wi}^b\, {}^w\boldsymbol{\Omega}_i$, where $\boldsymbol{R}_{wi}^b$ denotes transformation matrix from the i^{th} reaction-wheel frame to the body frame and depends on the configuration of the reaction-wheel group. Substitution of (3.6) into (3.5) returns

$$\begin{aligned}
&\left(\boldsymbol{J} - \sum_{i=1}^{N_w} \boldsymbol{J}_{wi}\right)\dot{\boldsymbol{\omega}} + \sum_{i=1}^{N_w} \boldsymbol{J}_{wi}\left(\dot{\boldsymbol{\Omega}}_i + \dot{\boldsymbol{\omega}}\right) + \dot{\boldsymbol{J}}\boldsymbol{\omega} + \\
&\boldsymbol{\omega} \times \left[\left(\boldsymbol{J} - \sum_{i=1}^{N_w} \boldsymbol{J}_{wi}\right)\boldsymbol{\omega} + \boldsymbol{J}_{wi}\left(\boldsymbol{\Omega}_i + \boldsymbol{\omega}\right)\right] = \boldsymbol{D}.
\end{aligned} \tag{3.7}$$

Let $\boldsymbol{\tau}_B = \sum_{i=1}^{N_w} \boldsymbol{J}_{wi}\dot{\boldsymbol{\Omega}}_i$ represent body axes' control torques and $\boldsymbol{U} = -\boldsymbol{\tau}_B - \boldsymbol{\omega} \times \int \boldsymbol{\tau}_B dt$. Then the dynamic equation can be rewritten as,

$$\boldsymbol{J}\dot{\boldsymbol{\omega}} + \dot{\boldsymbol{J}}\boldsymbol{\omega} + \boldsymbol{\omega} \times \boldsymbol{J}\boldsymbol{\omega} = \boldsymbol{U} + \boldsymbol{D}. \tag{3.8}$$

3.2.4 Inertia of a Deploying Satellite

During the deployment of a satellite, its inertia matrix undergoes substantial change, which results in a non-negligible term with $\dot{\boldsymbol{J}}$ in (3.8). The inertia change may cause the attitude of the satellite to deviate from its desired value and must be considered when designing an attitude controller. These large changes in inertia experienced by a satellite as it deploys itself in orbit are represented by the opening of a clamshell arrangement. This arrangement is chosen for simplicity as well as the fact that the changes in inertia are large when compared with the inertia of the "reference" half or base.

It is assumed that the body frame is aligned with the direction of principal inertia axes of the "reference" half satellite all the time, as shown in Figure 3.3. The inertia matrix of the entire spacecraft w.r.t. the changing CM is calculated based on a rough geometric feature of the deploying spacecraft by following steps: (1) Derive the inertia matrix of each half of the satellite w.r.t. CM of the entire spacecraft using Parallel Axis Theorem; (2) Transform the inertia matrix to the body frame; (4) Sum the inertia of each half. Details can be found in Appendix A.2.

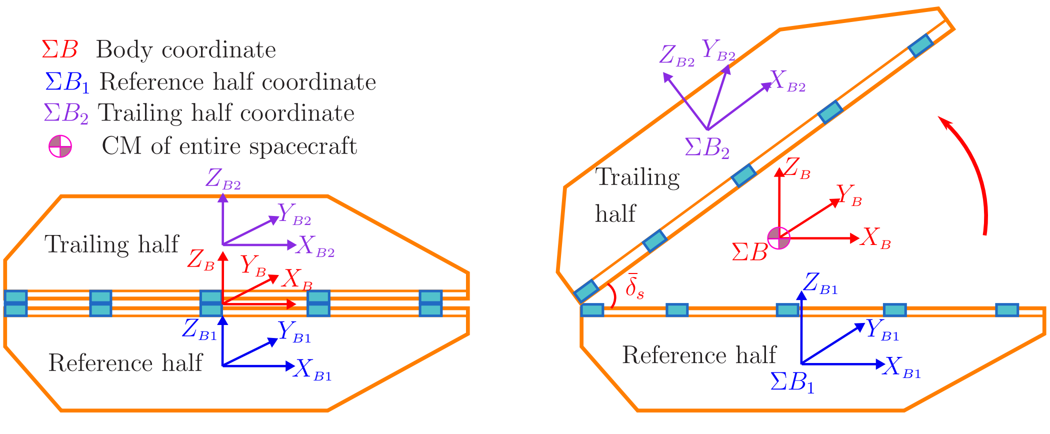

Figure 3.3: Satellite coordinate system

Since additional margin will be added to verify controller robustness, it is not necessary to get an accurate value of the inertia matrix. To simplify the derivation of the actual inertia matrix, the deploying angle $\bar{\delta}_s$ is considered as a variable which is proportional to time, i.e. the deploying rate is constant. As a result, the inertia matrix is not differentiable at the beginning and end of the deployment, which is not desirable since $\dot{\boldsymbol{J}}$ appears in the dynamic equation (3.8). Thus, a curve fitting technique is adopted to approximate the calculated inertia components, which yields smooth and differentiable functions. The final derived inertia components are presented in Figure 3.8 with solid lines.

3.2.5 Model of Disturbance Torques

The attitude system must be capable of overcoming the environmental disturbance torques that may cause the spacecraft to deviate from its desired attitude. Disturbance torques on a spacecraft mainly include aerodynamic torque, gravity-gradient torque, magnetic torque and solar radiation pressure torque. A detailed description of these orbit perturbations can be found in [155]. Since the large spacecraft cruises in Low-Earth Orbit (LEO), aerodynamic torque and gravity-gradient torque are taken into account as main disturbance torques neglecting other perturbations which are much smaller. The magnetic torque is considered as an external torque to provide unloading torques for the RWs, as described in Section 3.3.3.

Aerodynamic torque is generated by the interaction between the residual atmosphere in LEO with the spacecraft. It is a strong environmental disturbance torque for LEO spacecraft. The aerodynamic torque is given as,

$$\boldsymbol{\tau}_a = \boldsymbol{C}_a \times \boldsymbol{F}_a, \tag{3.9}$$

where $\boldsymbol{F}_a$ is the total aerodynamic force acting on the satellite and $\boldsymbol{C}_a$ is the position vector of the center of pressure about the CM of the satellite. $\boldsymbol{F}_a$ and $\boldsymbol{C}_a$ can be computed by,

$$\begin{aligned}\boldsymbol{F}_a &= -\rho_a v^2 \hat{\boldsymbol{v}} \int_{swa} \boldsymbol{n} \cdot \boldsymbol{v} \ \mathrm{d}\boldsymbol{S}, \\ \boldsymbol{C}_a &= \frac{\int_{swa} \boldsymbol{\rho} \left(\boldsymbol{n} \cdot \boldsymbol{v}\right) \ \mathrm{d}\boldsymbol{S}}{\int_{swa} (\boldsymbol{n} \cdot \boldsymbol{v}) \ \mathrm{d}\boldsymbol{S}},\end{aligned} \tag{3.10}$$

where ρ_a is the atmospheric density; $\boldsymbol{v}$ is the relative velocity between the orbital velocity of the spacecraft and the velocity of the atmosphere which rotates at approximately the same rate as the earth itself, and $\hat{\boldsymbol{v}}$ is a unit vector along the direction of $\boldsymbol{v}$; $S = \int_{swa} \boldsymbol{n} \cdot \boldsymbol{v} \ \mathrm{d}\boldsymbol{S}$ is the wetted area (area facing the flow, given by $\boldsymbol{n} \cdot \boldsymbol{v} \geq 0$) with $\boldsymbol{n}$ representing surface outward normal; $\boldsymbol{\rho}$ is the position of the acting torque on $\mathrm{d}\boldsymbol{S}$ from the spacecraft mass center. All quantities in (3.10) are expressed in the body frame. Since aerodynamic torques depend on the spacecraft configuration, a detailed derivation of aerodynamic torques for the deploying satellite is presented in Appendix A.3 based on the simplified geometric features of the spacecraft.

The Earth's gravitational force is not constant but decreases quadratically with increasing distance from the Earth's center. This gravity-gradient produces a torque due to variation of the Earths gravitational force over the satellite body. The gravity-gradient torque is given by,

$$\boldsymbol{\tau}_g = 3\omega_o^2 \ {}^b\boldsymbol{u}_e \times (\boldsymbol{J} \ {}^b\boldsymbol{u}_e), \tag{3.11}$$

where ${}^b\boldsymbol{u}_e$ is the unit vector from the spacecraft CM to nadir and ${}^b\boldsymbol{u}_e = \boldsymbol{R}_o^b \ {}^o\boldsymbol{u}_e$ with ${}^o\boldsymbol{u}_e = [0, 0, 1]^T$. Then the dominant disturbance torques suffered by the satellite become $\boldsymbol{D} = \boldsymbol{\tau}_a + \boldsymbol{\tau}_g$.

3.3 Control and Magnetic Unloading of the Reaction Wheel

According to the principle of conservation of angular momentum, an accelerating RW applies a reaction torque to the satellite in the opposite direction around its rotational axis. Though RW can provide smooth and precise control torque of the order of $0.05 - 2$ Nm [139], technically, such a device has torque and velocity limitations. When designing an attitude controller for the satellite, these limitations must be taken into consideration. In this section, the desired reaction-wheel control torques are derived based on the configuration of the reaction-wheel group. Then a current feedback controller is designed to get fast and accurate actual control torque for each RW. Momentum dumping is discussed to remove excess momentum of the RW to a predetermined limiting value.

3.3.1 Configuration of the Reaction Wheels

Three orthogonally mounted RWs, with each one's rotational axis parallel to one axis of the body frame, make up the simplest cluster to provide attitude control torques. But for the sake of redundancy, four or more RWs are always employed [156]. A commonly used pyramid-type configuration [157] is adopted to set up the reaction-wheel group and provide full 3-axis control with redundancy. Figure 3.4 (a) illustrates the configuration of one RW in the body frame. In the figure, α_{wi} represents the angle between the spin axis of the i^{th} RW and the roll-yaw $(X_B - Z_B)$ plane, and β_{wi} represents the angle between the spin axis of the i^{th} RW and Z_B axis. Set $\alpha_{w1} = \alpha_{w2} = \alpha_{w3} = \alpha_{w4} = 45°$ and $\beta_{w1} = \beta_{w2} = \beta_{w3} = \beta_{w4} = 54.74°$. Since $\sin\beta_{wi}\sin\alpha_{wi} = \sin\beta_{wi}\cos\alpha_{wi} = \cos\beta_{wi}$, $i = 1, 2, 3, 4$, RW torques are symmetrically distributed to each body axis. The configuration of the RWs is shown in Figure 3.4 (b).

As mentioned in Section 3.2.3, components of $\boldsymbol{\tau}_B$ represent control torques along three axes of the body frame. To transform between $\boldsymbol{\tau}_B$ and actual reaction-wheel control torques $\boldsymbol{\tau}_w$, configuration matrix of the reaction-wheel cluster $\boldsymbol{A}_w$ is defined as,

$$\boldsymbol{A}_w = \begin{bmatrix} \cos\alpha_w\sin\beta_w & -\cos\alpha_w\sin\beta_w & -\cos\alpha_w\sin\beta_w & \cos\alpha_w\sin\beta_w \\ \sin\alpha_w\sin\beta_w & \sin\alpha_w\sin\beta_w & -\sin\alpha_w\sin\beta_w & -\sin\alpha_w\sin\beta_w \\ \cos\beta_w & \cos\beta_w & \cos\beta_w & \cos\beta_w \end{bmatrix}.$$

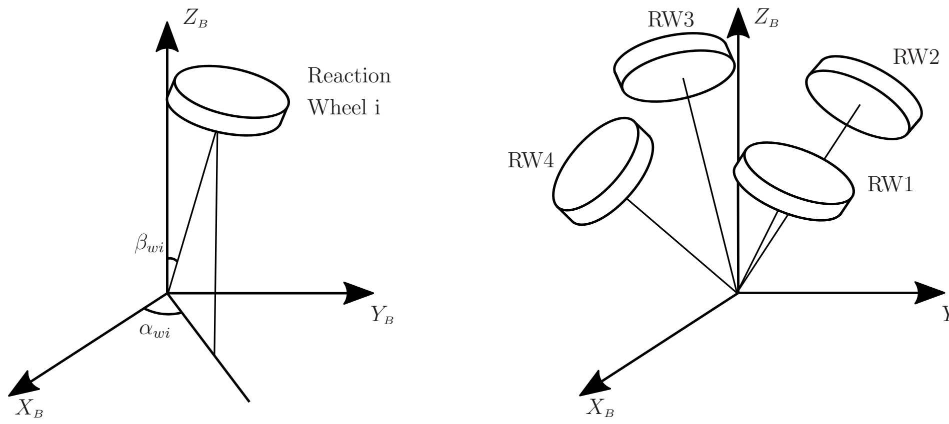

Figure 3.4: Configuration of the Reaction Wheels: (a) configuration of the i^{th} RW in the body frame, and (b) pyramid-type configuration of the RWs.

Each component of the column vector of $\boldsymbol{A}_w$ denotes RW torque contribution to X_B-, Y_B-, and Z_B- axis, respectively, indicating that $\boldsymbol{\tau}_B$ is originated from RW torques $\boldsymbol{\tau}_w$ by $\boldsymbol{\tau}_B = \boldsymbol{A}_w\ \boldsymbol{\tau}_w$. Inversely, the desired torques for RWs can be determined by multiplying the desired torques for three axes of the body frame with pseudo-inverse of the configuration matrix $\boldsymbol{A}_w^+$ as,

$$\boldsymbol{\tau}_w = \boldsymbol{A}_w^+ \boldsymbol{\tau}_B. \tag{3.12}$$

3.3.2 Reaction-Wheel Torque Control

Control torque saturation may occur in practical satellite regulation maneuvers. Therefore, the model of an armature controlled DC (Direct Current) motor which dominates the dynamics of the RW drive system is introduced and a controller to get accurate desired RW torques is designed based on the motor model. A saturation block of the input voltage for each RW is added in simulation studies.

The Laplace transform equation of the motor is given by [158],

$$\begin{aligned} I_m(s) &= \frac{-k_{me}\Omega_m(s) + V_m(s)}{L_m s + R_m}, \\ \Omega_m(s) &= \frac{k_{mt} I_m(s) - T_L(s)}{J_m s + B_m}, \end{aligned} \tag{3.13}$$

where I_m is armature current; V_m is the input voltage, R_m is the resistance; L_m

is the inductance of armature coil; k_{mt} and k_{me} represent the torque and velocity constants, respectively; Ω_m is the angular velocity of the motor and the RW attached to it; J_m is the equivalent inertia of the motor; B_m is the damping coefficient and set to be zero in this work; T_L represents the load torque and is zero as well in our case.

Since the reaction-wheel control torque is proportional to the motor current, the motor model is presented to illustrate the relationship between armature current and other electrical elements directly. By adding a feedback path from the motor current, the desired reaction-wheel control torque is compared with the actual output torque. Subsequently, a Proportional-Integral (PI) compensator is added to reduce the settling time and oscillations of the RW torque. The block diagram of this current feedback control system is shown in Figure 3.5.

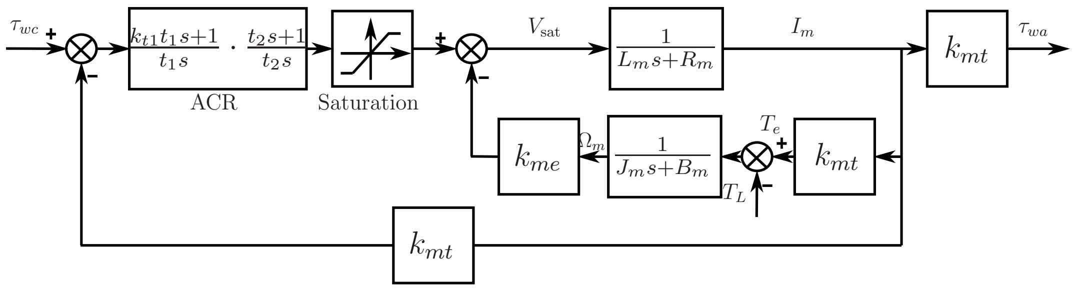

Figure 3.5: Current feedback control of the reaction-wheel torques.

3.3.3 Magnetic Unloading of the Reaction Wheel

The external disturbances can induce accumulation of angular momentum in the RWs. As a result, the RWs will reach their speed limit and finally fail to provide required torques without a momentum-dump maneuver. Two primary hardware items used to dump the RWs are magnetic torque rods and reaction thrusters. For the first option, onboard magnetic coils are used to interact with Earth's magnetic field and accordingly produce a counter torque for the spacecraft platform to realize RW unloading. The basic control equation for momentum unloading is

$$\boldsymbol{\tau}_u = -K_M \Delta \bar{\boldsymbol{H}} = \bar{\boldsymbol{M}} \times \bar{\boldsymbol{B}}, \tag{3.14}$$

where $\boldsymbol{\tau}_u$ denotes the required unloading torque generated by magnetic coils; K_M is the unloading control gain; $\Delta\bar{\boldsymbol{H}} = \boldsymbol{A}_w\left(\bar{\boldsymbol{H}} - \bar{\boldsymbol{H}}_N\right)$ is the excessive angular momentum with $\bar{\boldsymbol{H}}_N$ and $\bar{\boldsymbol{H}}$ representing the desired nominal values and actual values of RW angular momentum, respectively; $\bar{\boldsymbol{M}}$ is the desired magnetic moment vector generated by coils; $\bar{\boldsymbol{B}}$ is the intensity of local Earth's magnetic field. Though the magnetic dipole model [159] is approximate and may introduce simulation errors, it is widely used in the design phase to calculate the intensity of Earth's magnetic field $\bar{\boldsymbol{B}}$ as,

$$
{}^o\bar{\boldsymbol{B}} = \frac{\bar{\mu}}{R^3}\begin{bmatrix} -\sin(i_o)\cos(\omega_o t_o) \\ \cos(i_o) \\ -2\sin(i_o)\sin(\omega_o t_o) \end{bmatrix}, \tag{3.15}
$$

where $\bar{\mu}$ is the Earth's dipole constant ($\bar{\mu} = 7.9 \times 10^{15}$ Tm^3); R is the radius of the orbit; i_o is the orbit inclination; t_o is the cruise time from ascending node. $\bar{\boldsymbol{B}}$ should be transformed to the body frame by ${}^b\bar{\boldsymbol{B}} = \boldsymbol{R}_o^b\,{}^o\bar{\boldsymbol{B}}$.

Suppose the control magnetic dipole vector is perpendicular to Earth's magnetic field. The required magnetic moments can be expressed by,

$$
\bar{\boldsymbol{M}} = -\frac{K_M}{\bar{\boldsymbol{B}}^2}\left(\bar{\boldsymbol{B}} \times \Delta\bar{\boldsymbol{H}}\right). \tag{3.16}
$$

Substituting (3.16) into (3.14), the unloading torque is given by,

$$
\boldsymbol{\tau}_u = -\frac{K_M}{\bar{\boldsymbol{B}}^2}\left[\bar{\boldsymbol{B}}^2\Delta\bar{\boldsymbol{H}} - \bar{\boldsymbol{B}}\left(\bar{\boldsymbol{B}} \cdot \Delta\bar{\boldsymbol{H}}\right)\right]. \tag{3.17}
$$

In (3.17), $\Delta\bar{\boldsymbol{H}}$ is obtained by measuring the RWs' angular velocities and then transforming the excess RW angular momentum in the reaction-wheel frame into the body frame; K_M is obtained by trial and error to satisfy acceptable excess momentum and control moments.

It is worth mentioning that only a certain level of excess angular momentum can be unloaded using magnetic coils in low Earth orbits (the magnetic field is weak in geostationary orbit); for larger excess angular momentum, reaction thrusters are needed to dump the RWs.

3.4 Twisting Algorithm Attitude Controller

One of the prominent features of a deploying satellite is that it undergoes substantial inertia change, which brings heavy parameter uncertainty conditions for its attitude control. Sliding Mode Control (SMC) performs well in the presence of parametric uncertainties as well as internal and/or external disturbances and thus is especially applicable to this problem. Though first-order SMC can achieve performance with high accuracy, it induces high control activity which may excite vibration modes of the satellite structure and is undesirable for reaction-wheel control. Boundary layer is a popular approach to eliminate the chattering effect by changing the dynamics in a small vicinity of the sliding surface. But this modification loses the ultimate accuracy. Higher Order Sliding Mode Control (HOSMC) is developed to avoid high control activity by attaching the switching control to higher-order derivatives of actual actuator control torques [160] and can provide better accuracy than first-order SMC. In particular, the second-order SMC is widely used in the practical implementation due to potential availability of higher-order time derivatives of the sliding variable.

Section 3.4.1 presents the basic theory of conventional SMC. Then in the following sections, a Twisting-Algorithm-based Sliding Mode Controller (TASMC), which is considered to belong to the second-order SMC class, is developed to regulate the attitude of a deploying spacecraft using electrically-powered RWs. The design procedure of TASMC consists of two stages. Section 3.4.2 introduces the first stage, that is selecting sliding surfaces such that errors of the control variables will converge to the origin once arriving on the sliding manifolds in the error phase plane. For the second stage, the control law is developed in Section 3.4.3 to enforce sliding mode to reach the selected surfaces.

3.4.1 Sliding Mode Control

The overall scheme of SMC includes two phases and can be analyzed in the phase plane. For the first phase, i.e. the *reaching phase*, the system state error moves from an arbitrary initial point to a point on a predefined sliding surface at finite time.

Once it is reached, the trajectories are sliding along this surface and the *convergence phase* starts. For the convergence phase, the error dynamics is determined by the selected sliding surface and is insensitive to system uncertainties, resulting in state error convergence to the origin along the sliding surface. To illustrate the concepts of SMC, a simple second order system is presented as an example, of which the dynamic equation is

$$\ddot{x} = u + f(t), \tag{3.18}$$

where x is the system state; u is the control input; $f(t)$ is the bounded dynamics.

Theorem 3.1 Under the admissible control law, $u = -M\ \mathrm{sgn}(s) - c\dot{x}$, the system will reach and maintain at the sliding surface $s = \dot{x} + cx = 0$. M and c are positive constants, $M > |f(t)|$. The sign function sgn in the control law is defined as,

$$\mathrm{sgn}(s) = \begin{cases} -1 & \text{for } s < 0, \\ 0 & \text{for } s = 0, \\ 1 & \text{for } s > 0. \end{cases} \tag{3.19}$$

Proof Define Lyapunov function $V = \frac{1}{2}s^T s$. The reachability condition to sliding surface should be $\dot{V} = s\dot{s} < 0$. Applying the system dynamic equation (3.18), the derivative of s is

$$\dot{s} = \ddot{x} + c\dot{x} = u + f(t) + c\dot{x}. \tag{3.20}$$

Substitution of (3.20) and $u = -M\ \mathrm{sgn}(s) - c\dot{x}$ into $\dot{V}$ returns

$$\begin{aligned} \dot{V} &= s\dot{s} = s\left[u + f(t) + c\dot{x}\right] \\ &= s\left[-M\ \mathrm{sgn}(s) - c\dot{x} + f(t) + c\dot{x}\right] \\ &\leq -M|s| + |f(t)|\ |s| < -M|s| + M|s| = 0. \end{aligned} \tag{3.21}$$

Therefore, the control law drives the trajectory towards to the sliding surface. $\dot{V} = 0$ holds only when $s = 0$, which implies that once the sliding surface is reached, the trajectory will maintain on this surface. When the trajectory slides on the selecting surface, i.e. $s = \dot{x} + x \equiv 0$ which is a first-order constant linear differential equation, it subsequently converges to the origin.

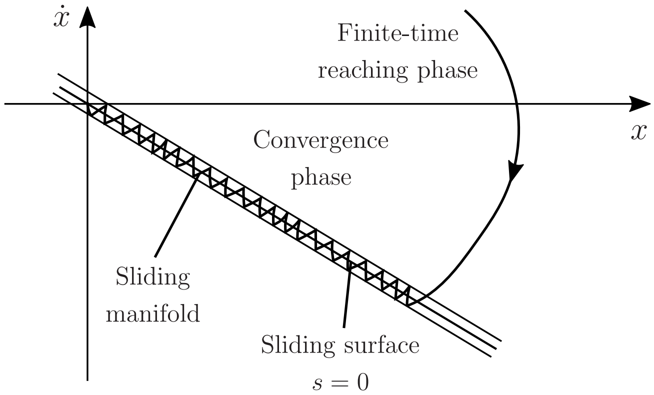

Figure 3.6: Phase plane of the second-order system.

Figure 3.6 shows the system behavior on the phase plane. At the switching line, the augmented term $-M\ \mathrm{sgn}(s)$ in the control law changes its sign and undergoes discontinuities. Practically, the imperfections of switching devices, such as a small delay [161], will induce high-frequency oscillations. Therefore, the state trajectories are actually confined to the vicinity of the switching line, of which the section is called the sliding manifold.

3.4.2 Sliding Surface

Before deriving the control law, the sliding surface is selected to deliver desired error dynamics in accordance with system performance. Assuming that during the satellite deployment, it is required to achieve and maintain an attitude at which the body frame is aligned with the orbit frame. Choose a set of sliding surfaces as,

$$\boldsymbol{s} = \boldsymbol{\omega}_{ob} + \boldsymbol{\Lambda}\boldsymbol{\varepsilon}, \tag{3.22}$$

where $\boldsymbol{s}$ is a vector, i.e. $\boldsymbol{s} = [s_x, s_y, s_z]^T$; $\boldsymbol{\omega}_{ob}$ represents the relative angular velocity between the body frame and the orbit frame which is expressed in the body frame here and afterwards; $\boldsymbol{\Lambda} \in \mathbb{R}^{3\times 3}$ is a constant symmetric positive-definite matrix.

Theorem 3.2 On the condition that the sliding surface given by (3.22) is satisfied by the proposed control law, the spacecraft attitude converges to the desired values which enforce the body frame in alignment with the orbit frame. That is if $\lim_{t\to\infty} \boldsymbol{s} = \mathbf{0}$, then $\lim_{t\to\infty} \boldsymbol{q}_B = [0\ 0\ 0\ 1]^T$ and $\lim_{t\to\infty} \boldsymbol{\omega}_{ob} = \mathbf{0}$.

Proof Select the Lyapunov function as,

$$V = \boldsymbol{\varepsilon}^T\boldsymbol{\varepsilon} + (1-\eta)^2 = 2(1-\eta) \geq 0. \tag{3.23}$$

Applying $\dot{\eta}$ from the spacecraft kinematic equation (3.2) and substituting $\boldsymbol{\omega}_{ob} = -\boldsymbol{\Lambda}\boldsymbol{\varepsilon}$ obtained from $\boldsymbol{s} = \mathbf{0}$, the derivative of V becomes,

$$\dot{V} = -2\dot{\eta} = \boldsymbol{\varepsilon}^T\ \boldsymbol{\omega}_{ob} = -\boldsymbol{\varepsilon}^T\boldsymbol{\Lambda}\boldsymbol{\varepsilon} \leq 0. \tag{3.24}$$

This implies that $\boldsymbol{\varepsilon} \to \mathbf{0}$ and $\boldsymbol{\omega}_{ob} \to \mathbf{0}$ when $\boldsymbol{s} \to \mathbf{0}$. According to the definition of quaternion parameters, it yields $\boldsymbol{q}_B \to [0\ 0\ 0\ 1]^T$, proving that the spacecraft can be oriented to and maintained at the desired attitude.

3.4.3 Attitude Regulation by Twisting Algorithm

RWs cannot operate with inputs derived from conventional first-order SMC due to the chattering effect. Without losing the superiority of suppressing the effects of system uncertainties, HOSMC based on twisting algorithm [161] can counteract the high-frequency oscillations by inserting a dynamic block, i.e. an integrator, between the system input and the discontinuous control as,

$$\dot{\underline{\boldsymbol{u}}} = \underline{\boldsymbol{v}}, \tag{3.25}$$

where $\underline{\boldsymbol{v}}$ is a new introduced discontinuous input dependent on the sliding surface and the derivative of the sliding surface which is assumed to be available. This discontinuous control input should enforce the sliding mode. The actual system input $\underline{\boldsymbol{u}}$ which is integrated from $\underline{\boldsymbol{v}}$ becomes continuous and no chattering effect will be induced.

Define a set of sliding surfaces using vector $\boldsymbol{s}$. Consider the formation

$$\ddot{\boldsymbol{s}} = \boldsymbol{F}(\boldsymbol{x}, t, \underline{\boldsymbol{u}}) - \boldsymbol{P}_0\ \mathrm{sgn}(\boldsymbol{s}) - \boldsymbol{P}_1\ \mathrm{sgn}(\dot{\boldsymbol{s}}), \tag{3.26}$$

where $\boldsymbol{x}$ represents system states; t denotes time; $\boldsymbol{F}(\boldsymbol{x}, t, \underline{\boldsymbol{u}})$ is a bounded function and $||\boldsymbol{F}(\boldsymbol{x}, t, \underline{\boldsymbol{u}})|| \leq \boldsymbol{F}_0$, $\boldsymbol{F}_0$ is a vector with positive components.

Theorem 3.3 For (3.26), if $\boldsymbol{P}_1 > \boldsymbol{F}_0$, $\boldsymbol{P}_0 > \boldsymbol{P}_1 + \boldsymbol{F}_0$, the system converges to the origin in $(\boldsymbol{s}, \dot{\boldsymbol{s}})$ subspace, that is $\boldsymbol{s} \to \boldsymbol{0}$ and $\dot{\boldsymbol{s}} \to \boldsymbol{0}$.

Proof Consider the Lyapunov function [161]

$$V = 2\sqrt{\frac{1}{2}\dot{\boldsymbol{s}}^2 + \boldsymbol{P}_0|\boldsymbol{s}|}. \tag{3.27}$$

By substituting (3.26), the time derivative of V becomes,

$$\begin{aligned}\dot{V} &= \frac{\dot{\boldsymbol{s}}\ddot{\boldsymbol{s}} + \boldsymbol{P}_0\dot{\boldsymbol{s}}\ \mathrm{sgn}(\boldsymbol{s})}{\sqrt{\frac{1}{2}\dot{\boldsymbol{s}}^2 + \boldsymbol{P}_0|\boldsymbol{s}|}} = \frac{\dot{\boldsymbol{s}}\left[\ddot{\boldsymbol{s}} + \boldsymbol{P}_0\ \mathrm{sgn}(\boldsymbol{s})\right]}{\sqrt{\frac{1}{2}\dot{\boldsymbol{s}}^2 + \boldsymbol{P}_0|\boldsymbol{s}|}} = \frac{\dot{\boldsymbol{s}}\left[\boldsymbol{F} - \boldsymbol{P}_1\ \mathrm{sgn}(\dot{\boldsymbol{s}})\right]}{\sqrt{\frac{1}{2}\dot{\boldsymbol{s}}^2 + \boldsymbol{P}_0|\boldsymbol{s}|}} \\ &= \frac{\dot{\boldsymbol{s}}\boldsymbol{F} - \boldsymbol{P}_1|\dot{\boldsymbol{s}}|}{\sqrt{\frac{1}{2}\dot{\boldsymbol{s}}^2 + \boldsymbol{P}_0|\boldsymbol{s}|}} \leq \frac{|\boldsymbol{F}|\ |\dot{\boldsymbol{s}}| - \boldsymbol{P}_1|\dot{\boldsymbol{s}}|}{\sqrt{\frac{1}{2}\dot{\boldsymbol{s}}^2 + \boldsymbol{P}_0|\boldsymbol{s}|}} \leq \frac{(\boldsymbol{F}_0 - \boldsymbol{P}_1)|\dot{\boldsymbol{s}}|}{\sqrt{\frac{1}{2}\dot{\boldsymbol{s}}^2 + \boldsymbol{P}_0|\boldsymbol{s}|}}.\end{aligned} \tag{3.28}$$

It can be inferred from (3.26) that $\dot{\boldsymbol{s}} = \boldsymbol{0}$ and $\boldsymbol{s} \neq \boldsymbol{0}$ lead to $\ddot{\boldsymbol{s}} \neq 0$, which implies $\dot{\boldsymbol{s}} = 0$ cannot maintain for finite time interval if $\boldsymbol{s} \neq 0$. Therefore, $\dot{V} < 0$ holds for trajectories not located on the origin. This demonstrates that the system motion is asymptotically stable in the subspace $(\boldsymbol{s}, \dot{\boldsymbol{s}})$ and will converge to the origin after a certain time.

Apparently, $\boldsymbol{s}$ cannot stay at zero if $\dot{\boldsymbol{s}} \neq 0$. Combining above discussions, it can be concluded that $\boldsymbol{s}$ and $\dot{\boldsymbol{s}}$ cannot remain sign-constant and they have interlacing zeros [161], as shown in Figure 3.7, which illustrates the underlying meaning of "twisting algorithm". Once arriving the origin, $\boldsymbol{s}$ and $\dot{\boldsymbol{s}}$ will stay at zero and the second order sliding mode starts.

Now the derivation of the second derivative of the sliding vector based on spacecraft kinematic and dynamic equations are given. By differentiating $\boldsymbol{s}$ defined in (3.22) twice, $\ddot{\boldsymbol{s}}$ is obtained as,

$$\ddot{\boldsymbol{s}} = \ddot{\boldsymbol{\omega}}_{ob} + \boldsymbol{\Lambda}\ddot{\boldsymbol{\varepsilon}}. \tag{3.29}$$

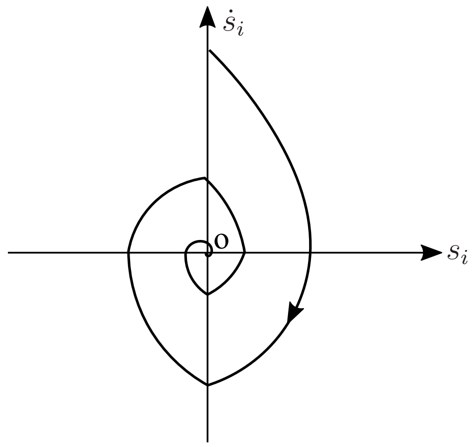

Figure 3.7: Phase portrait of twisting algorithm

Differentiating $\dot{\boldsymbol{\varepsilon}} = \frac{1}{2}\Xi(\boldsymbol{q}_B)\,\boldsymbol{\omega}_{ob}$ and replacing $\ddot{\boldsymbol{\varepsilon}}$ of (3.29) with the resulted expression returns,

$$\ddot{\boldsymbol{s}} = \ddot{\boldsymbol{\omega}}_{ob} + \frac{1}{2}\boldsymbol{\Lambda}[\dot{\Xi}(\boldsymbol{q}_B)\boldsymbol{\omega}_{ob} + \Xi(\boldsymbol{q}_B)\dot{\boldsymbol{\omega}}_{ob}]. \tag{3.30}$$

$\ddot{\boldsymbol{\omega}}_{ob}$ can be derived from (3.1) and (3.8) as,

$$\ddot{\boldsymbol{\omega}}_{ob} = \boldsymbol{J}^{-1}\dot{\boldsymbol{U}} + \boldsymbol{J}^{-1}\dot{\boldsymbol{D}} + \boldsymbol{J}^{-1}\boldsymbol{F}_1(\boldsymbol{x},t) - \boldsymbol{J}^{-1}\dot{\boldsymbol{J}}\dot{\boldsymbol{\omega}} - \boldsymbol{J}^{-1}\ddot{\boldsymbol{J}}\boldsymbol{\omega} - \boldsymbol{J}^{-1}\dot{\boldsymbol{J}}\dot{\boldsymbol{\omega}}_{ob}, \tag{3.31}$$

where $\boldsymbol{F}_1(\boldsymbol{x},t) = \left(-\boldsymbol{J}\dot{\boldsymbol{R}}_o^b\ {}^o\boldsymbol{\omega}_{io} - \boldsymbol{S}(\boldsymbol{\omega})\boldsymbol{J}\boldsymbol{\omega}\right)'$. Substitution of (3.31) into (3.30) yields,

$$\begin{aligned}\ddot{\boldsymbol{s}} =& \boldsymbol{J}^{-1}\dot{\boldsymbol{U}} + \boldsymbol{J}^{-1}\dot{\boldsymbol{D}} + \boldsymbol{J}^{-1}\boldsymbol{F}_1(\boldsymbol{x},t) - \boldsymbol{J}^{-1}\dot{\boldsymbol{J}}\dot{\boldsymbol{\omega}} \\ &- \boldsymbol{J}^{-1}\ddot{\boldsymbol{J}}\boldsymbol{\omega} - \boldsymbol{J}^{-1}\dot{\boldsymbol{J}}\dot{\boldsymbol{\omega}}_{ob} + \frac{1}{2}\boldsymbol{\Lambda}\left[\dot{\Xi}(\boldsymbol{q}_B)\boldsymbol{\omega}_{ob} + \Xi(\boldsymbol{q}_B)\dot{\boldsymbol{\omega}}_{ob}\right].\end{aligned} \tag{3.32}$$

Let $\dot{\boldsymbol{U}} = \boldsymbol{v}$, $\boldsymbol{v} = -\boldsymbol{M}_0\ \mathrm{sgn}(\boldsymbol{s}) - \boldsymbol{M}_1\ \mathrm{sgn}(\dot{\boldsymbol{s}})$, where $\boldsymbol{M}_0$ and $\boldsymbol{M}_1$ are vectors with positive components, and

$$\ddot{\boldsymbol{s}} = \boldsymbol{F}_2(\boldsymbol{x},t) - \boldsymbol{J}^{-1}\boldsymbol{M}_0\mathrm{sgn}(\boldsymbol{s}) - \boldsymbol{J}^{-1}\boldsymbol{M}_1\ \mathrm{sgn}(\dot{\boldsymbol{s}}), \tag{3.33}$$

where $\boldsymbol{F}_2(\boldsymbol{x},t) = \boldsymbol{J}^{-1}\boldsymbol{F}_1(\boldsymbol{x},t) - \boldsymbol{J}^{-1}\dot{\boldsymbol{J}}\dot{\boldsymbol{\omega}}_{ob} - \boldsymbol{J}^{-1}\ddot{\boldsymbol{J}}\boldsymbol{\omega} - \boldsymbol{J}^{-1}\dot{\boldsymbol{J}}\dot{\boldsymbol{\omega}} + \boldsymbol{J}^{-1}\dot{\boldsymbol{D}} + \frac{1}{2}\boldsymbol{\Lambda}\left[\dot{\Xi}(\boldsymbol{q}_B)\boldsymbol{\omega}_{ob} + \Xi(\boldsymbol{q}_B)\dot{\boldsymbol{\omega}}_{ob}\right]$ and $||\boldsymbol{F}_2(\boldsymbol{x},t)|| \leq \bar{\boldsymbol{F}}$. As stated in Theorem 3.3, to achieve the sliding mode, $\boldsymbol{M}_0$ and $\boldsymbol{M}_1$ must satisfy the following conditions

$$\boldsymbol{M}_1 > \boldsymbol{J}\bar{\boldsymbol{F}},\ \boldsymbol{M}_0 > \boldsymbol{J}\bar{\boldsymbol{F}} + \boldsymbol{M}_1. \tag{3.34}$$

Note that in a physical system such as a satellite, all elements of the inertia matrix are bounded. Further according to (3.32), every element of the inertia matrix must have bounded first and second derivatives to ensure complete control. The upper bound of $\boldsymbol{J}\boldsymbol{F}_2$ is

$$\begin{aligned}(\boldsymbol{J}\boldsymbol{F}_2)_{\max} =& ||\dot{\boldsymbol{S}}(\boldsymbol{\omega})||\ ||\hat{\boldsymbol{J}}||\ ||\boldsymbol{\omega}|| + ||\boldsymbol{S}(\boldsymbol{\omega})||\ \boldsymbol{J}_d\ ||\boldsymbol{\omega}|| + ||\boldsymbol{S}(\boldsymbol{\omega})||\ ||\hat{\boldsymbol{J}}||\ ||\dot{\boldsymbol{\omega}}|| \\ &+ \left(\boldsymbol{J}_d\ ||\dot{\boldsymbol{R}}_o^b|| + ||\hat{\boldsymbol{J}}||\ ||\ddot{\boldsymbol{R}}_o^b||\right)\ ||{}^o\boldsymbol{\omega}_{io}|| + \boldsymbol{J}_d\ ||\dot{\boldsymbol{\omega}}_{ob}|| + \boldsymbol{J}_{dd}\ ||\boldsymbol{\omega}|| + ||\dot{\boldsymbol{D}}|| \\ &+ \boldsymbol{J}_d\ ||\dot{\boldsymbol{\omega}}|| + \frac{1}{2}||\hat{\boldsymbol{J}}||\ \boldsymbol{\Lambda}\ ||\dot{\Xi}(\boldsymbol{q}_B)||\ ||\boldsymbol{\omega}_{ob}|| + \frac{1}{2}||\hat{\boldsymbol{J}}||\ \boldsymbol{\Lambda}\ ||\Xi(\boldsymbol{q}_B)||\ ||\dot{\boldsymbol{\omega}}_{ob}||,\end{aligned} \tag{3.35}$$

where the components of $\hat{\boldsymbol{J}}$, $\boldsymbol{J}_d$ and $\boldsymbol{J}_{dd}$ are the upper bounds, the bounds of the first derivative and the bounds of the second derivative for corresponding exact inertia matrix components respectively - i.e. $||\boldsymbol{J}|| \leq ||\hat{\boldsymbol{J}}||,\ ||\dot{\boldsymbol{J}}|| \leq \boldsymbol{J}_d,\ ||\ddot{\boldsymbol{J}}|| \leq \boldsymbol{J}_{dd}$.

Section 3.2.4 and Appendix A.2 have addressed the method to get an approximate value of $\boldsymbol{J}$, which can be used in the dynamic model for simulation. Practically, the satellite inertia matrix can be more easily obtained for the fully stowed or deployed structure. However, during the simplified deployment process or even more complicated robot on-orbit assembly operations, it may be difficult to calculate inertia components with sufficient accuracy. Therefore, two different kinds of $\hat{\boldsymbol{J}}$ are considered to be used in the controller. For the first approach, an additive buffer is introduced between $\boldsymbol{J}$ and $\hat{\boldsymbol{J}}$ to avoid unstable orientations owing to parameter uncertainty. With the assumption that the inertia matrix before and after the deployment is accurate and the error between $\boldsymbol{J}$ and $\hat{\boldsymbol{J}}$ during reconfiguration does not stay constant, a time-varying additive inertia is used (Figure 3.8). Another method is simply to take the constant bound of $\boldsymbol{J}$ as $\hat{\boldsymbol{J}}$. The constant bounds for components of $\boldsymbol{J}$ have been calculated as mentioned above and can be read from Figure 3.8. Therefore, the components of $\hat{\boldsymbol{J}}$ are shown in Table 3.1. The effect of using time-varying inertia matrix in the controller is investigated via simulation studies.

A positive constant vector $\boldsymbol{\delta}_f$ is introduced to define $\boldsymbol{M}_0$ and $\boldsymbol{M}_1$ according to the preceding inequalities (3.34) as,

$$\boldsymbol{M}_1 = \boldsymbol{J}\bar{\boldsymbol{F}} = (\boldsymbol{J}\boldsymbol{F}_2)_{\max} + \boldsymbol{\delta}_f,\ \boldsymbol{M}_0 = 2\boldsymbol{M}_1. \tag{3.36}$$

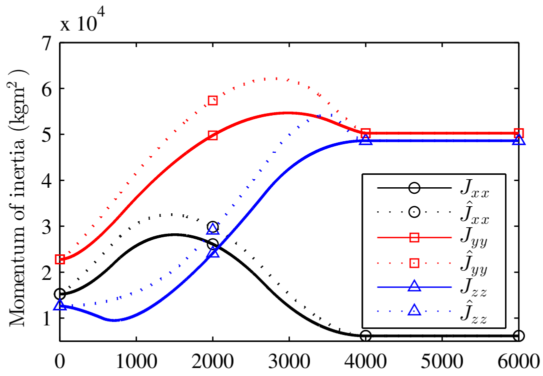

(a) Moment of inertia

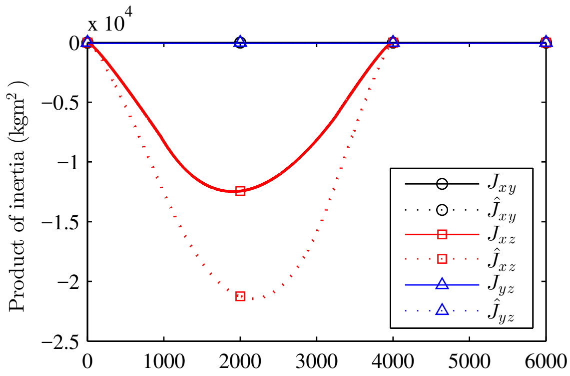

(b) Product of inertia

Figure 3.8: Components of exact inertia matrix ($\boldsymbol{J}$) and time-varying inertia matrix ($\hat{\boldsymbol{J}}$)

Table 3.1: Constant components of $\hat{\boldsymbol{J}}$ as used in the controller

component	$\hat{J}_{xx}$	$\hat{J}_{yy}$	$\hat{J}_{zz}$	$\hat{J}_{xy}$	$\hat{J}_{xz}$	$\hat{J}_{yz}$
value($\times 10^4$ kgm^2)	2.8168	5.4665	4.8620	0	-1.2477	0

The control torque can be subsequently derived by

$$\boldsymbol{U} = \int \boldsymbol{v}\, dt = \int \{-\boldsymbol{M}_0 \operatorname{sgn}(\boldsymbol{s}) - \boldsymbol{M}_1 \operatorname{sgn}(\dot{\boldsymbol{s}})\}\, dt. \tag{3.37}$$

The block diagram for the control structure is shown in Figure 3.9. As shown in the figure, the attitude and angular velocity of the spacecraft are measured. In addition, the deploying angle is measured so as to estimate the value of the inertia matrix.

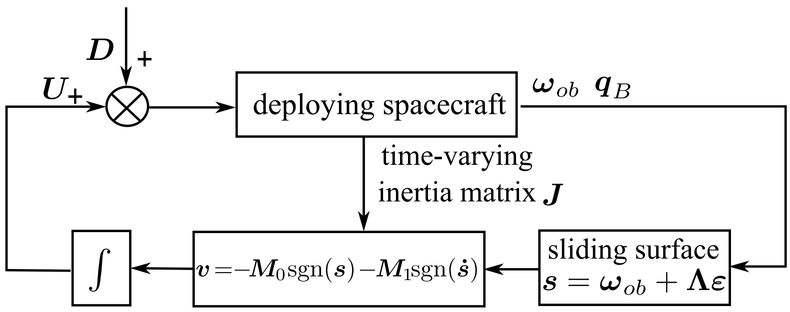

Figure 3.9: Block diagram of the control structure

3.5 Smoothed Quasi-Continuous Second-Order SMC

In literature [151], the authors compared different types of sliding mode controllers for spacecraft-attitude-tracking maneuvers, including Smoothing Model-Reference SMC (SMRSMC) [162], Smoothed Quasi-Continuous Second-Order SMC (SQC2S) and Quasi-Continuous Third-Order SMC (QC3S) [163]. Simulation results have shown that SQC2S can deliver shortest settling times as well as relatively smooth control torques compared with SMRSMC and QC3S. Thus, SQC2S is chosen to apply to the spacecraft model and make a comparison with the controller proposed in Section 3.4.

The sliding surfaces are selected the same form of the sliding vector chosen for TASMC as,

$$\bar{\boldsymbol{s}} = \boldsymbol{\omega}_{ob} + \bar{\boldsymbol{\Lambda}}\boldsymbol{\varepsilon}, \tag{3.38}$$

where $\bar{\boldsymbol{s}} = [\bar{s}_1, \bar{s}_2, \bar{s}_3]^T$; $\bar{\boldsymbol{\Lambda}} \in \mathbb{R}^{3\times 3}$ is a constant symmetric positive-definite matrix. According to Theorem 3.2, once the sliding manifold is maintained, the attitude regulation errors will converge to zero.

Define control torque $\bar{\boldsymbol{U}} = [\bar{U}_1, \bar{U}_2, \bar{U}_3]^T$. The control law can be given by [151],

$$\bar{U}_i = -k_i \frac{\dot{\bar{s}}_i + |\bar{s}_i|^{1/2}\,\mathrm{sgn}\,(\bar{s}_i)}{|\dot{\bar{s}}_i| + |\bar{s}_i|^{1/2} + \nu}, \quad i = 1, 2, 3, \tag{3.39}$$

where ν is a small positive scalar. k_i satisfies the following conditions,

$$\begin{cases} k_i > \dfrac{\psi_i\ \mathrm{sgn}(\bar{s}_i)\left(|\dot{\bar{s}}_i| + \sqrt{|\bar{s}_i|} + \nu\right)}{\dot{\bar{s}}_i\ \mathrm{sgn}(\bar{s}_i) + \sqrt{|\bar{s}_i|}}, & \text{for } \dot{\bar{s}}_i\ \mathrm{sgn}(\bar{s}_i) + \sqrt{|\bar{s}_i|} > 0, \\ k_i < \dfrac{\psi_i\ \mathrm{sgn}(\bar{s}_i)\left(|\dot{\bar{s}}_i| + \sqrt{|\bar{s}_i|} + \nu\right)}{\dot{\bar{s}}_i\ \mathrm{sgn}(\bar{s}_i) + \sqrt{|\bar{s}_i|}}, & \text{for } \dot{\bar{s}}_i\ \mathrm{sgn}(\bar{s}_i) + \sqrt{|\bar{s}_i|} < 0, \end{cases} \tag{3.40}$$

where $i = 1, 2, 3$ and $\boldsymbol{\Psi} = [\psi_1, \psi_2, \psi_3]^T = \boldsymbol{D} - \boldsymbol{S}(\boldsymbol{\omega})\boldsymbol{J}\boldsymbol{\omega} - \dot{\boldsymbol{J}}\boldsymbol{\omega} - \boldsymbol{J}\dot{\boldsymbol{R}}_o^b\,{}^o\boldsymbol{\omega}_{io} + \boldsymbol{J}\bar{\boldsymbol{\Lambda}}\dot{\boldsymbol{\varepsilon}} + (1/2)\dot{\boldsymbol{J}}\bar{\boldsymbol{s}}$.

Theorem 3.4 Under the control law stated in (3.39), the system dynamics reach and maintain on the sliding surface $\bar{\boldsymbol{s}} = \boldsymbol{0}$ in finite time.

Proof Define the Lyapunov function as,

$$V = \frac{1}{2}\bar{\boldsymbol{s}}^T \boldsymbol{J}\bar{\boldsymbol{s}}. \tag{3.41}$$

As addressed in Section 3.2.4 and illustrated in Figure 3.8, the inertia matrix of the deploying satellite is a symmetric matrix and

$$\boldsymbol{J} = \begin{bmatrix} J_{xx} & 0 & J_{xz} \\ 0 & J_{yy} & 0 \\ J_{xz} & 0 & J_{zz} \end{bmatrix},$$

with $J_{xx} > 0,\ J_{yy} > 0,\ J_{zz} > 0,\ J_{xz} \leq 0$. Specifically, $J_{xx} > |J_{xz}| = -J_{xz},\ J_{zz} > |J_{xz}| = -J_{xz}$. On these conditions, the positive property of the Lyapunov function is proved as follows.

$$\begin{aligned} V &= \frac{1}{2}\begin{bmatrix} \bar{s}_x & \bar{s}_y & \bar{s}_z \end{bmatrix}\begin{bmatrix} J_{xx} & 0 & J_{xz} \\ 0 & J_{yy} & 0 \\ J_{xz} & 0 & J_{zz} \end{bmatrix}\begin{bmatrix} \bar{s}_x \\ \bar{s}_y \\ \bar{s}_z \end{bmatrix} \\ &= \frac{1}{2}\left(J_{xx}\bar{s}_x^2 + J_{yy}\bar{s}_y^2 + J_{zz}\bar{s}_z^2 + 2J_{xz}\bar{s}_x\bar{s}_z\right) \\ &\geq \frac{1}{2}\left[J_{xx}\bar{s}_x^2 + J_{yy}\bar{s}_y^2 + J_{zz}\bar{s}_z^2 + |J_{xz}|\left(\bar{s}_x^2 + \bar{s}_z^2\right)\right] \\ &= \frac{1}{2}\left[J_{yy}\bar{s}_y^2 + \left(J_{xx} - |J_{xz}|\right)\bar{s}_x^2 + \left(J_{zz} - |J_{xz}|\right)\bar{s}_z^2\right] \\ &\geq 0. \end{aligned} \tag{3.42}$$

$V = 0$ holds true only when $\bar{\boldsymbol{s}} = \boldsymbol{0}$. The first derivative of V can be written as,

$$\dot{V} = \frac{1}{2}\bar{\boldsymbol{s}}^T\dot{\boldsymbol{J}}\bar{\boldsymbol{s}} + \frac{1}{2}\dot{\bar{\boldsymbol{s}}}^T\boldsymbol{J}\bar{\boldsymbol{s}} + \frac{1}{2}\bar{\boldsymbol{s}}^T\boldsymbol{J}\dot{\bar{\boldsymbol{s}}} = \bar{\boldsymbol{s}}^T\left(\frac{1}{2}\dot{\boldsymbol{J}}\bar{\boldsymbol{s}} + \boldsymbol{J}\dot{\bar{\boldsymbol{s}}}\right). \tag{3.43}$$

$\dot{\bar{\boldsymbol{s}}}$ is derived using (3.1), (3.2) and (3.8) as,

$$\dot{\bar{\boldsymbol{s}}} = \dot{\boldsymbol{\omega}}_{ob} + \bar{\boldsymbol{\Lambda}}\dot{\boldsymbol{\varepsilon}} = \boldsymbol{J}^{-1}\Big[\boldsymbol{U} + \boldsymbol{D} - \boldsymbol{S}(\boldsymbol{\omega})\boldsymbol{J}\boldsymbol{\omega} - \dot{\boldsymbol{J}}\boldsymbol{\omega}\Big] - \dot{\boldsymbol{R}}_o^b\, {}^o\boldsymbol{\omega}_{io} + \bar{\boldsymbol{\Lambda}}\dot{\boldsymbol{\varepsilon}}. \tag{3.44}$$

Substitution of $\dot{\bar{\boldsymbol{s}}}$ and the control law (3.39) into (3.44) returns,

$$\begin{aligned}\dot{V} &= \bar{\boldsymbol{s}}^T\left[\frac{1}{2}\dot{\boldsymbol{J}}\bar{\boldsymbol{s}} + \bar{\boldsymbol{U}} + \boldsymbol{D} - \boldsymbol{S}(\boldsymbol{\omega})\boldsymbol{J}\boldsymbol{\omega} - \dot{\boldsymbol{J}}\boldsymbol{\omega} - \boldsymbol{J}\dot{\boldsymbol{R}}_o^b\,{}^o\boldsymbol{\omega}_{io} + \boldsymbol{J}\bar{\boldsymbol{\Lambda}}\dot{\boldsymbol{\varepsilon}}\right] \\ &= \sum_{i=1}^{3}\bar{s}_i\left[\psi_i - k_i\frac{\dot{\bar{s}}_i + |\bar{s}_i|^{1/2}\,\mathrm{sgn}(\bar{s}_i)}{|\dot{\bar{s}}_i| + |\bar{s}_i|^{1/2} + \nu}\right] \\ &= \sum_{i=1}^{3}|\bar{s}_i|\left[\psi_i\,\mathrm{sgn}(\bar{s}_i) - k_i\frac{\dot{\bar{s}}_i\,\mathrm{sgn}(\bar{s}_i) + |\bar{s}_i|^{1/2}}{|\dot{\bar{s}}_i| + |\bar{s}_i|^{1/2} + \nu}\right]\end{aligned} \tag{3.45}$$

The conditions of k_i listed in (3.40) can yield

$$\psi_i\,\mathrm{sgn}(\bar{s}_i) - k_i\frac{\dot{\bar{s}}_i\,\mathrm{sgn}(\bar{s}_i) + |\bar{s}_i|^{1/2}}{|\dot{\bar{s}}_i| + |\bar{s}_i|^{1/2} + \nu} < 0, \tag{3.46}$$

which ensures $\dot{V} < 0$ when $\dot{\bar{s}}_i\,\mathrm{sgn}(\bar{s}_i) + \sqrt{|\bar{s}_i|} \neq 0$. If $\dot{\bar{s}}_i\,\mathrm{sgn}(\bar{s}_i) + \sqrt{|\bar{s}_i|} = 0$ does not hold for a finite time, the conditions of k_i are used. If $\dot{\bar{s}}_i\,\mathrm{sgn}(\bar{s}_i) + \sqrt{|\bar{s}_i|} \equiv 0$, the following equations are obtained,

$$\dot{\bar{s}}_i = \begin{cases} -\sqrt{\bar{s}_i}, & \text{for } \bar{s}_i > 0, \\ \sqrt{-\bar{s}_i}, & \text{for } \bar{s}_i \leq 0, \end{cases} \tag{3.47}$$

which indicates the system motion converges to the origin in the $(\bar{s}_i, \dot{\bar{s}}_i)$ plane along a parabola trajectory in the second quadrant or the fourth quadrant, as shown in Figure 3.10.

Hence, according to the above discussions, the system is asymptotically stable. Once the sliding surfaces $\bar{\boldsymbol{s}} = \boldsymbol{0}$ are reached, the system will slide along the surfaces.

Set

$$\begin{cases} k_i = \dfrac{(\boldsymbol{\Psi}_{\max})_i\left(|\dot{\bar{s}}_i| + \sqrt{|\bar{s}_i|} + \nu\right)}{\dot{\bar{s}}_i\,\mathrm{sgn}(\bar{s}_i) + \sqrt{|\bar{s}_i|}} + \bar{\delta}_i, & \text{for } \dot{\bar{s}}_i\,\mathrm{sgn}(\bar{s}_i) + \sqrt{|\bar{s}_i|} > 0, \\ k_i = \dfrac{(\boldsymbol{\Psi}_{\max})_i\left(|\dot{\bar{s}}_i| + \sqrt{|\bar{s}_i|} + \nu\right)}{\dot{\bar{s}}_i\,\mathrm{sgn}(\bar{s}_i) + \sqrt{|\bar{s}_i|}} - \bar{\delta}_i, & \text{for } \dot{\bar{s}}_i\,\mathrm{sgn}(\bar{s}_i) + \sqrt{|\bar{s}_i|} < 0, \end{cases} \tag{3.48}$$

with a small positive scalar $\bar{\delta}_i$, which can satisfy the inequalities of (3.40). The

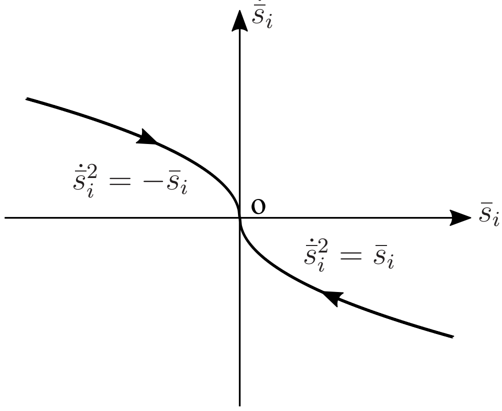

Figure 3.10: Trajectory of system dynamics for $\dot{\bar{s}}_i \ \mathrm{sgn}(\bar{s}_i) + \sqrt{|\bar{s}_i|} \equiv 0$

upper bound of $\boldsymbol{\Psi}$ is obtained as,

$$\begin{aligned}\boldsymbol{\Psi}_{\max} \leq ||\boldsymbol{\Psi}|| = & ||\boldsymbol{D}|| + ||\boldsymbol{S}(\boldsymbol{\omega})|| \ ||\boldsymbol{J}|| \ ||\boldsymbol{\omega}|| + ||\boldsymbol{J}|| \ ||\dot{\boldsymbol{R}}_o^b|| \ ||{}^o\boldsymbol{\omega}_{io}|| + ||\dot{\boldsymbol{J}}|| \ ||\boldsymbol{\omega}|| \\ & + ||\boldsymbol{J}|| \ \bar{\boldsymbol{\Lambda}} \ ||\dot{\boldsymbol{\varepsilon}}|| + \frac{1}{2}||\dot{\boldsymbol{J}}||(\boldsymbol{\omega}_{ob} + \bar{\boldsymbol{\Lambda}}\boldsymbol{\varepsilon}),\end{aligned} \tag{3.49}$$

Replacing $\boldsymbol{\Psi}_{\max}$ with $||\boldsymbol{\Psi}||$ in (3.48) for the simulation model guarantees the system stability.

3.6 Simulation

The orbit in which the spacecraft is cruising determines the orbit angular velocity and environmental disturbance torques. Therefore, the orbital parameters are given in Table 3.3. An initial attitude error represented by Euler angles is defined as $[\phi_0, \theta_0, \psi_0] = [5°, 3°, -5°]^T$. The satellite implements its deployment from $t = 0$ to $t = 4000$s ($\approx$ 0.71 orbit period). Saturated voltage for the RW-attached motor is $V_{\max} = 12$ V. For simulation models based on different control strategies, a same time-varying inertia matrix calculated in Section 3.2.4 and Appendix A.1 is used in the dynamic model to simulate the situation that the spacecraft unfolds itself. Dominant environmental disturbance torques, i.e. gravity gradient torque and aerodynamic torques calculated as in Section 3.2.5, are applied to the spacecraft. Torque saturation and magnetic unloading of the RWs, as presented in Section 3.3, are taken into account in the simulation model. Motor specifications included in

Table 3.2: Specifications of motor

Parameter	Value	Parameter	Value
Resistance R, Ω	1.3	Inductance L, mH	0.1
Damping coefficient B, Ns/m	0	Load torque T_L, N	0
Torque constant k_{mt}, Nm/A	0.031	Velocity constant k_{me}, V/rad/s	0.031
Moment of inertia J_m, $\text{kg}\cdot\text{m}^2$	3.67×10^{-3}	Maximum motor voltage, V	12

Table 3.3: Orbit parameters

Inclination i_o, degrees	Altitude h_o, km	Right Ascension Ω_o, degrees	Period T_o, s	Orbital Angular Rate ω_o, rad/s
83	470	15.7	5670	0.0011

Figure 3.5 are listed in Table 3.2. Finally, the magnetic unloading control gain K_M (see (3.17)) is determined as $K_M = 0.001$ by trial and error, which keeps the accumulated angular momentum of RWs within $|\bar{H}_i| \leq 30$ Nms and ensures limited magnetic moments $|\bar{M}_i| \leq 400$ Am^2, as shown in Figure 3.11.

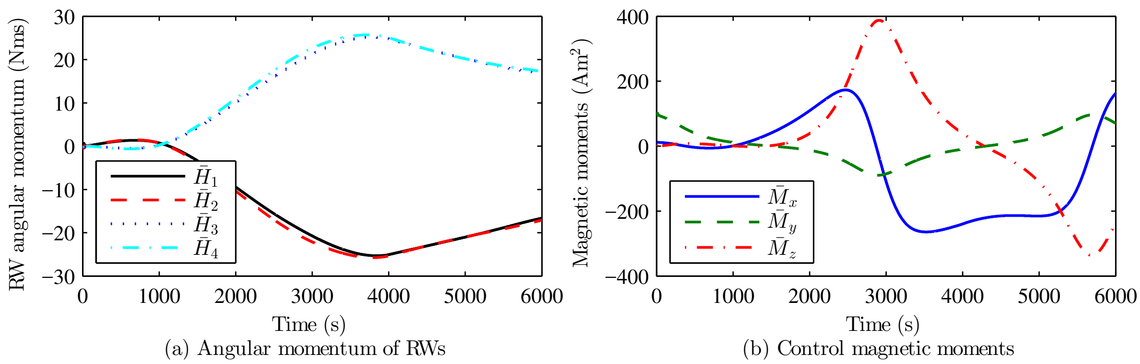

Figure 3.11: Accumulated RW angular momentum and magnetic moments

Different kinds of controllers have been tested and compared to regulate the deploying satellite to its desired orientation. The simulation mainly comprises three parts: 1) Comparison between conventional first order SMC and Twisting-Algorithm -based SMC (TASMC, constant inertia matrix is used in the controller, the constant components are listed in Table 3.1); 2) Comparison between Constant Inertia

Matrix -based TASMC (CIMSMC) and Time-Varying Inertia Matrix -based TASMC (TVIMSMC); 3) Comparison between TASMC and SQC2S proposed in [151]. All the simulations are based on the same conditions previously mentioned.

The strategy to save energy always plays an important role in space missions due to limited onboard fuel or valuable electrical energy transformed from solar energy and thus energy consumption of RWs is calculated and compared. Attitude regulation errors, angular velocity of the satellite, RW control torques and total energy consumption of each RW under different controllers are shown in Figure 3.12 - Figure 3.15.

First, conventional SMC and TASMC with constant inertia matrix (CIMSMC) are compared. Figure 3.12 (a), (b) and Figure 3.13 (a), (b) show that both controllers achieve steady state in the controlled variables. However, the control torques based on conventional first-order SMC (Figure 3.14 (a)) exhibit unacceptable chattering while the control torques based on CIMSMC (Figure 3.14 (b)) are continuous and smooth. As shown in Figure 3.15 (a) and Figure 3.15 (b), the RWs based on conventional SMC consumes much more energy due to high-frequency switching of the control signal. This level of energy drain is undoubtedly undesirable.

As referred to Section 3.4, whether it is necessary to use a time-varying inertia matrix in the controller is examined using simulations, for there is a substantial inertia change which can reach the amplitude of 10^4 kgm^2 during the deployment process. For CIMSMC, the constant bound of satellite inertia matrix $\hat{\boldsymbol{J}}$ is used in the controller, of which the components are listed in Table 3.1. Instead, for TVIMSMC, a time-varying inertia matrix, which has an additive surplus to the actual satellite inertia matrix as shown in Figure 3.8, is used in the controller. Figure 3.12 - Figure 3.15 (c) present the simulation results under TVIMSMC. Compared with the performance of CIMSMC (Figure 3.12 - Figure 3.15 (b)), TVIMSMC achieves regulation of the satellite to the steady state during deployment subjected to initial deviations as well as external disturbances, without a significant difference between the two. Therefore, a constant bound of the satellite inertia matrix can be used in the sliding mode controller instead of a time-varying inertia matrix, even when the satellite undergoes substantial inertia change during its deployment. In this respect, the robustness of SMC to uncertainty parameters is well-demonstrated.

The performance of SQC2S and TASMC (CIMSMC) can now be compared. For SQC2S as described in Section 3.5, the selection of ν is very important. It should not be set too small because the smooth properties of SQC2S will be lost and the controller becomes essentially Quasi-Continuous Second-Order SMC (QC2S) [151]. Set $\nu = 0.1$ after simulating the program with various values. In the expressions of sliding surfaces, the positive matrix $\mathbf{\Lambda}$ of CIMSMC in (3.22) is set the same value as $\bar{\mathbf{\Lambda}}$ of SQC2S in (3.38) with $\Lambda_i = \bar{\Lambda}_i = 0.1, i = 1, 2, 3$. The additional buffer $\bar{\delta}_i$ in equation (3.48) has an important effect on the performance of SQC2S. When it is set to be a smaller value, smooth control torques can be achieved resulting in degraded state errors during the regulation, as illustrated in Figure 3.12 - Figure 3.14 (d). If it is set to a large value, state errors get smaller with shorter response times, whereas, the control torques then do not exhibit smoothness, as illustrated in Figure 3.12 - Figure 3.14 (e). In contrast to this, the buffer $\boldsymbol{\delta}_f$ in (3.36) does not weigh so much in the performance of CIMSMC after testing the controller with different values of $\boldsymbol{\delta}_f$. As illustrated by Figure 3.12 (b), (d) and Figure 3.15 (b), (d), CIMSMC achieves faster response when consuming comparable energy as SQC2S. On the other hand, if the control torques of SQC2S are increased to reduce the settling times to a comparable level as CIMSMC, as shown in Figure 3.12 (b), (e), the control torques present undesirable chattering effect and subsequently more energy are consumed, as shown in Figure 3.14 (e) and Figure 3.15 (e).

3.7 Summary

In this chapter, the problem of maintaining the attitude of a spacecraft during its on-orbit deployment was discussed. The kinematic model of the spacecraft was introduced with quaternion parameters representing its attitude. Since electrical-powered Reaction Wheels (RWs) were selected to generate internal attitude regulation torques, the dynamic model of the spacecraft was established based on Newton-Euler method which derived the desired torques for RWs from the expression of their angular momentum. Practical problems that may be induced when using RWs, including torque saturation and speed saturation were analyzed. A second order Sliding Mode Controller (SMC), i.e. Twisting Algorithm -based Sliding Mode Controller (TASMC) was developed and applied to the deploying satellite model. Specifically, two kinds of inertia matrix were discussed which can be used in the controller - one is an inertia matrix with constant components; the other is a variable inertia matrix, both of which were designed via calculation of the inertia change that occurs as a result of the satellite's structural reconfiguration. Simulation results have shown that TASMC eliminates the chattering effect of conventional SMC. Compared with Smoothed Quasi-Continuous Second Order Sliding Mode Controller (SQC2S), when consuming comparable energy, the proposed controller delivers smooth control torques which are perfectly practical for the control of RWs, and is able to steer the satellite to the desired orientation with smaller settling time. The developed control algorithm lays a firm foundation to further the research to achieve high accuracy tracking operations.

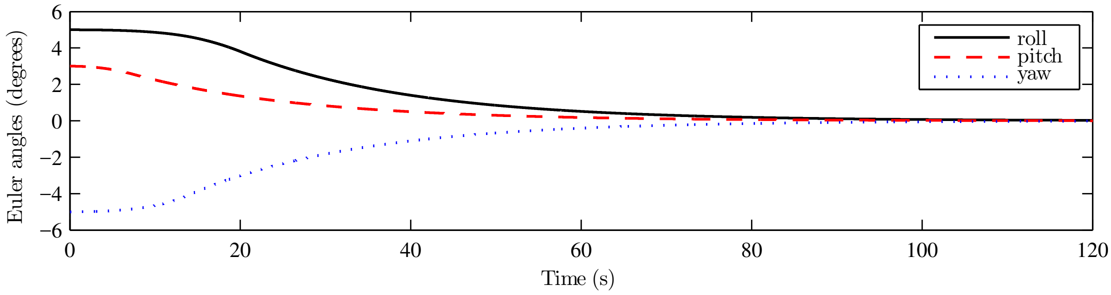

(a) Conventional first-order SMC

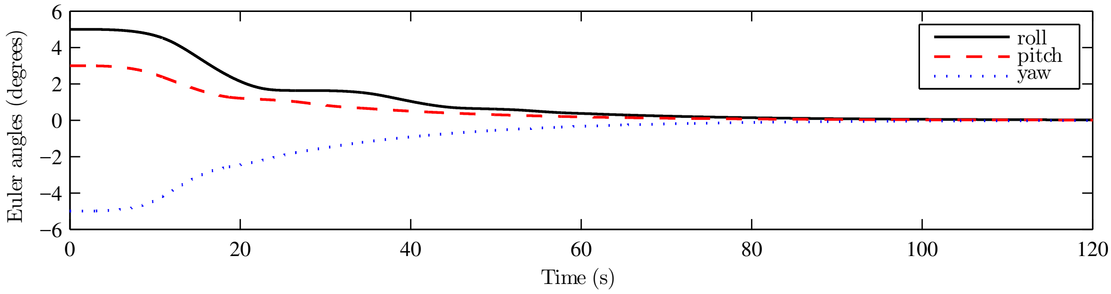

(b) CIMSMC

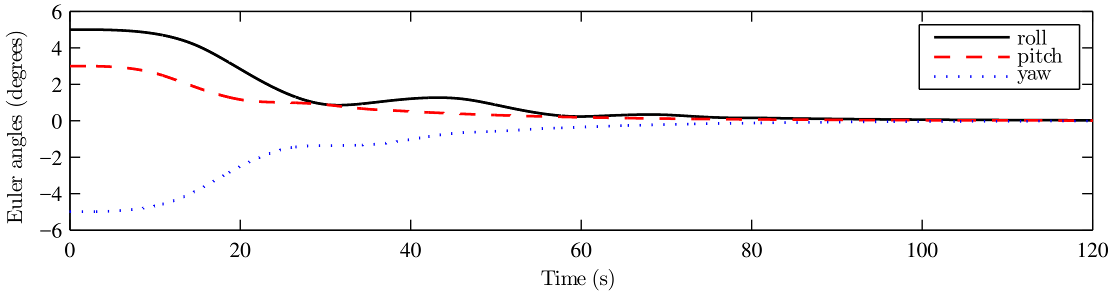

(c) TVIMSMC

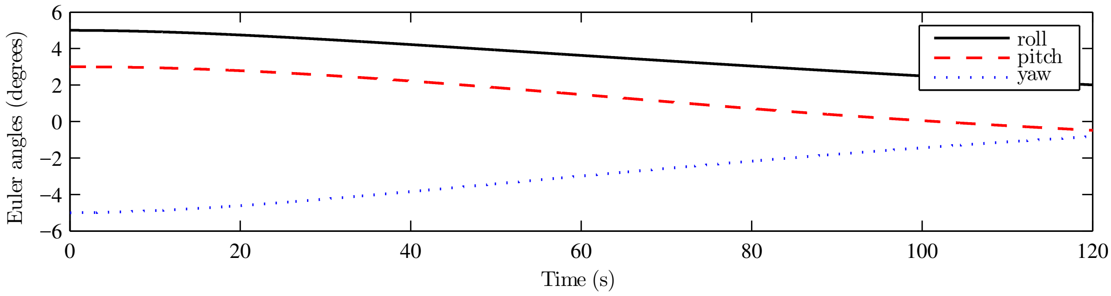

(d) SQC2S with smaller $\bar{\delta}$

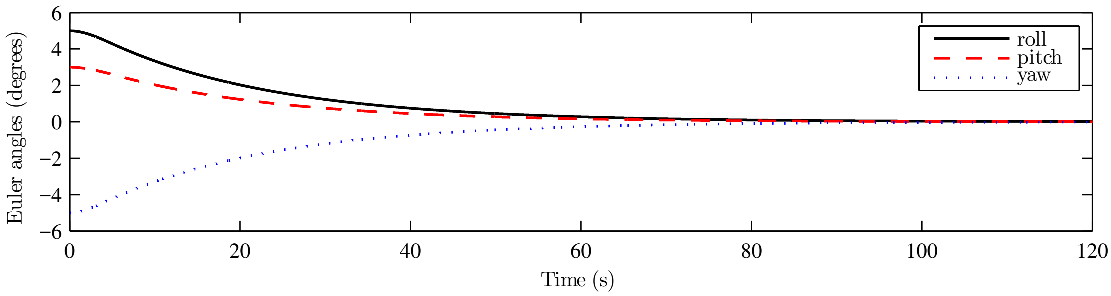

(e) SQC2S with larger $\bar{\delta}$

Figure 3.12: Attitude regulation errors under different kinds of controllers

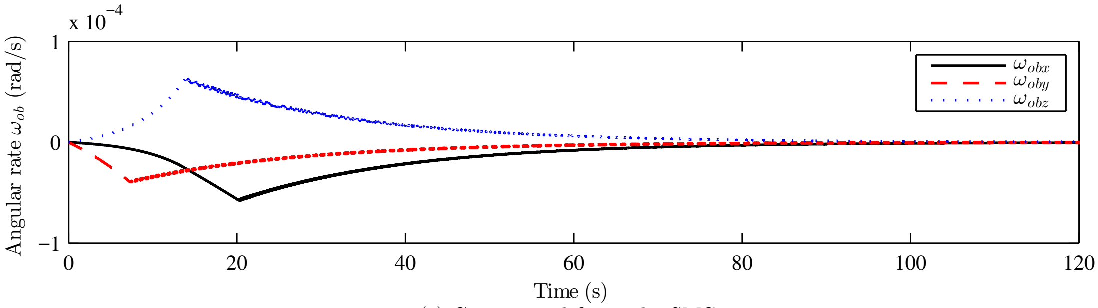

(a) Conventional first-order SMC

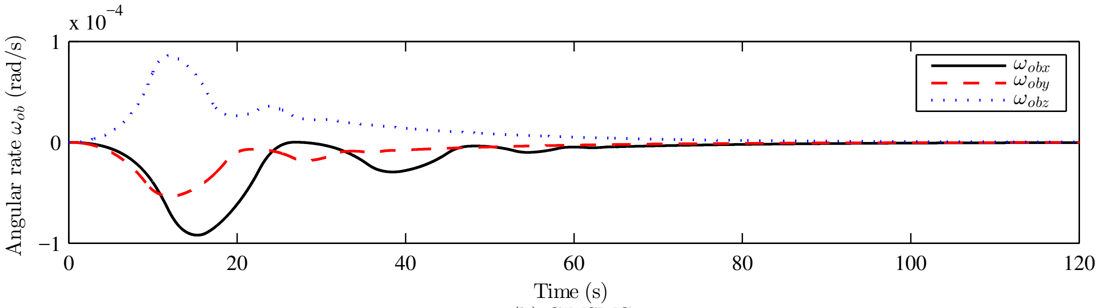

(b) CIMSMC

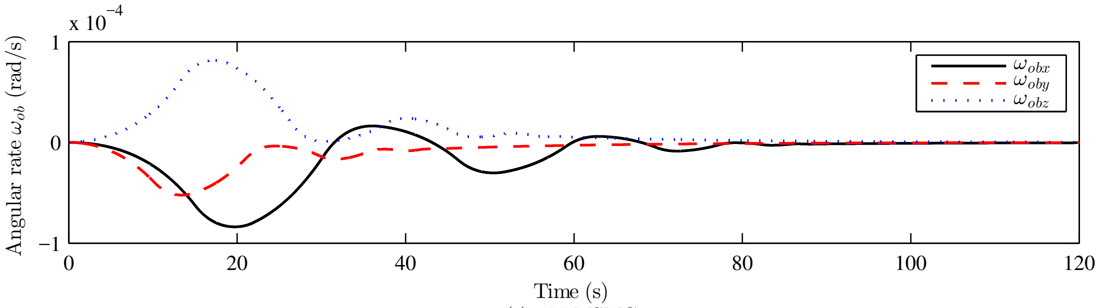

(c) TVIMSMC

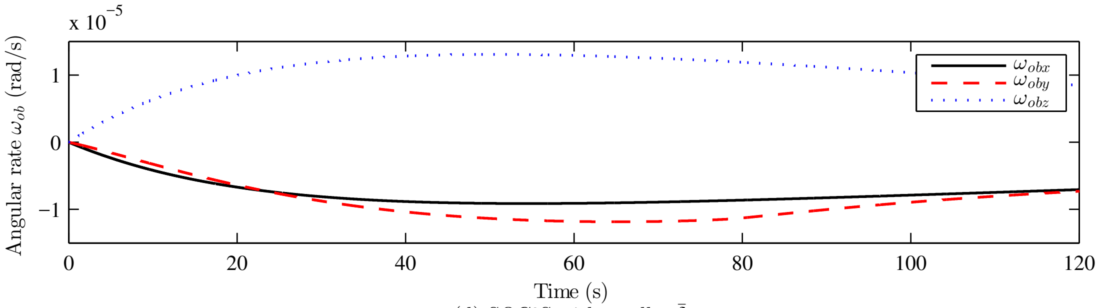

(d) SQC2S with smaller $\bar{\delta}$

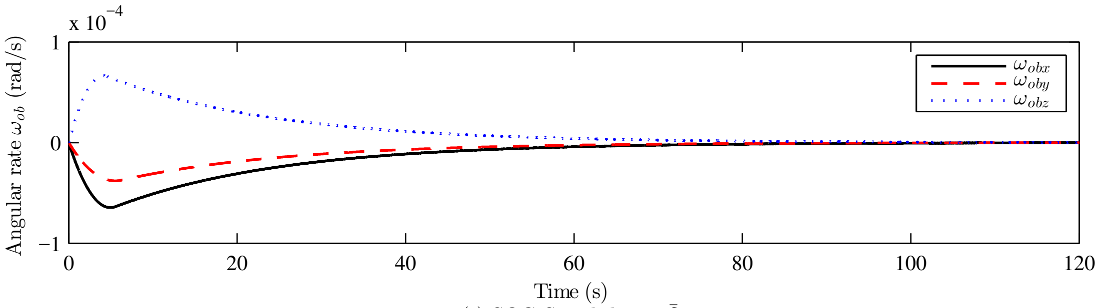

(e) SQC2S with larger $\bar{\delta}$

Figure 3.13: Angular velocity of the satellite $\boldsymbol{\omega}_{ob}$ under different kinds of controllers

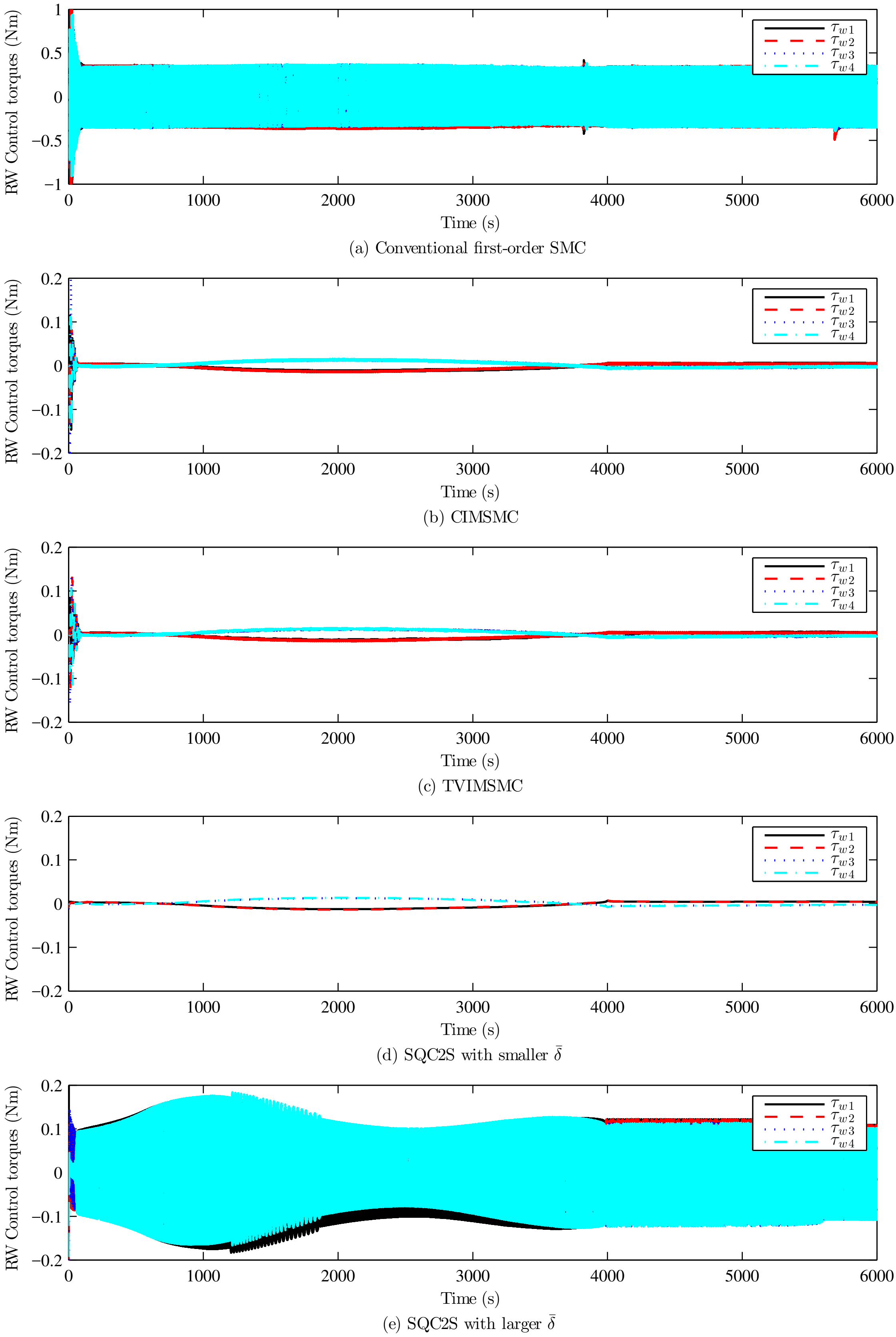

Figure 3.14: Control outputs of the RWs under different kinds of controllers

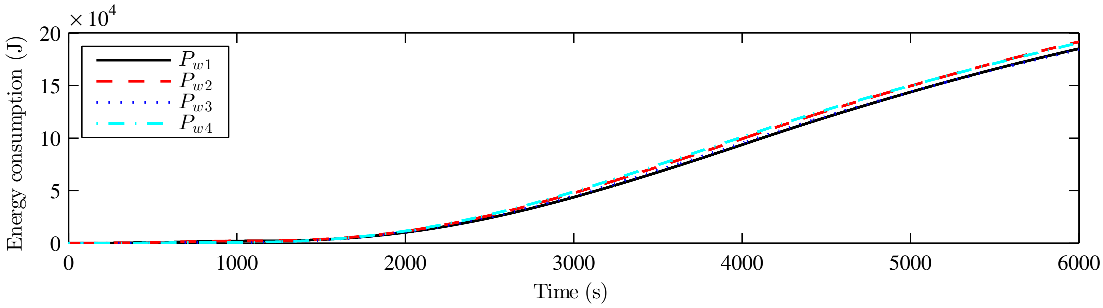

(a) Conventional first-order SMC

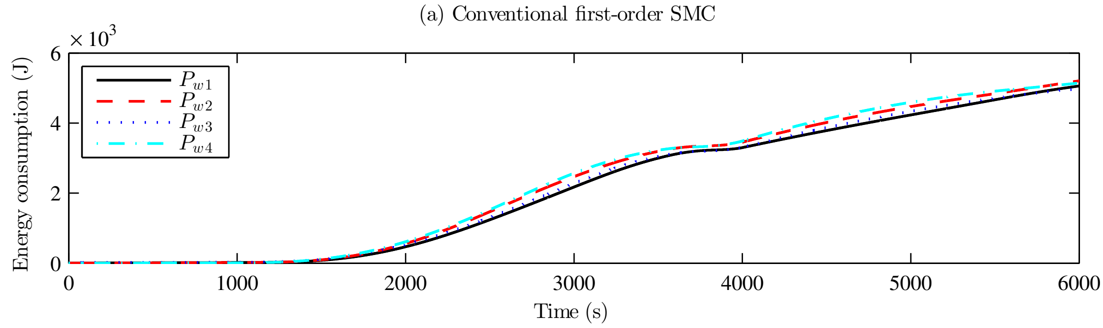

(b) CIMSMC

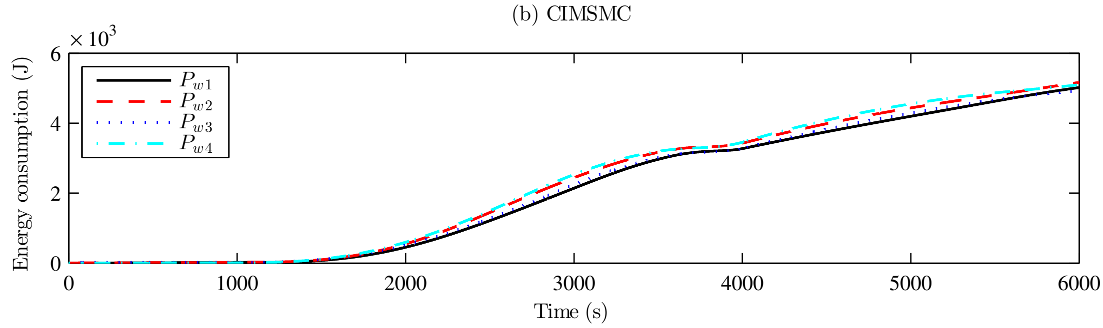

(c) TVIMSMC

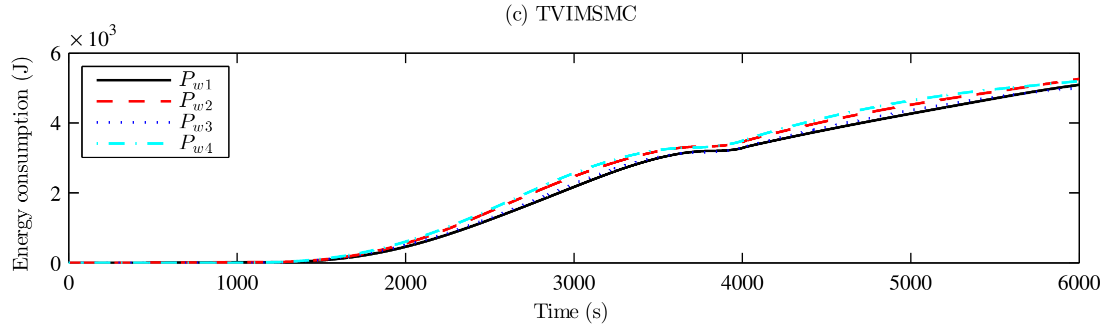

(d) SQC2S with smaller $\bar{\delta}$

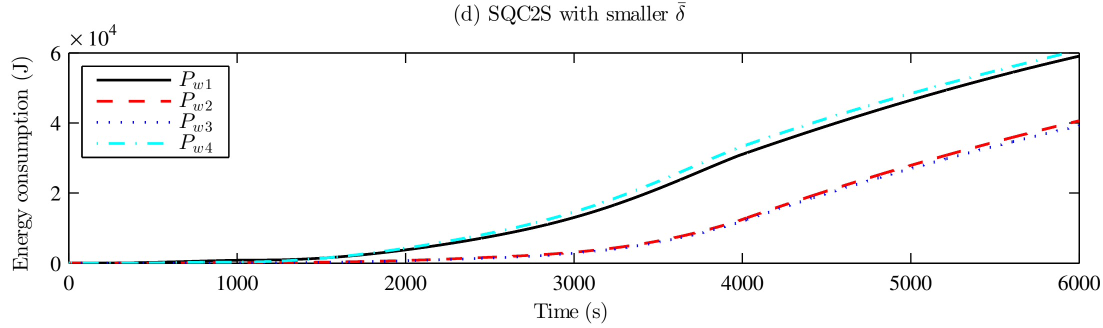

(e) SQC2S with larger $\bar{\delta}$

Figure 3.15: Energy consumption under different kinds of controllers

Chapter 4

Motion Control of a Space Robot

4.1 Introduction

Previously, in Chapter 3, a simple specific in-space assembly case, that is spacecraft deployment, was addressed. When extending to a more general on-orbit assembly mission, sophisticated space structures are assembled using Free-Flying Space Robots (FFSRs). An FFSR has one or more robotic manipulators mounted on a base of comparable size. Such a system can perform tasks autonomously or telerobotically, removing the astronaut's risky Extra Vehicular Activities (EVA), reducing costs while at the same time implementing more precise motions. The scenario of on-orbit construction of a large space structure by robotic teams is illustrated in Figure 4.1.

One major characteristic of space robots which distinguishes them from ground-fixed ones is the lack of a fixed base [39]. In the micro-gravity environment, the approaching motions of the space manipulator to a target induce undesirable disturbances to the spacecraft base. The disturbances will lead to undesired change of spacecraft attitude, potentially disrupting communication and solar energy collection processes as a result. Moreover, the robot end-effector may miss the target and fail the mission without provision of base motion. Therefore, control of both the spacecraft attitude and the manipulator motion, which takes coupling effects between the manipulator and its floating base into account, become essential for successful space operations.

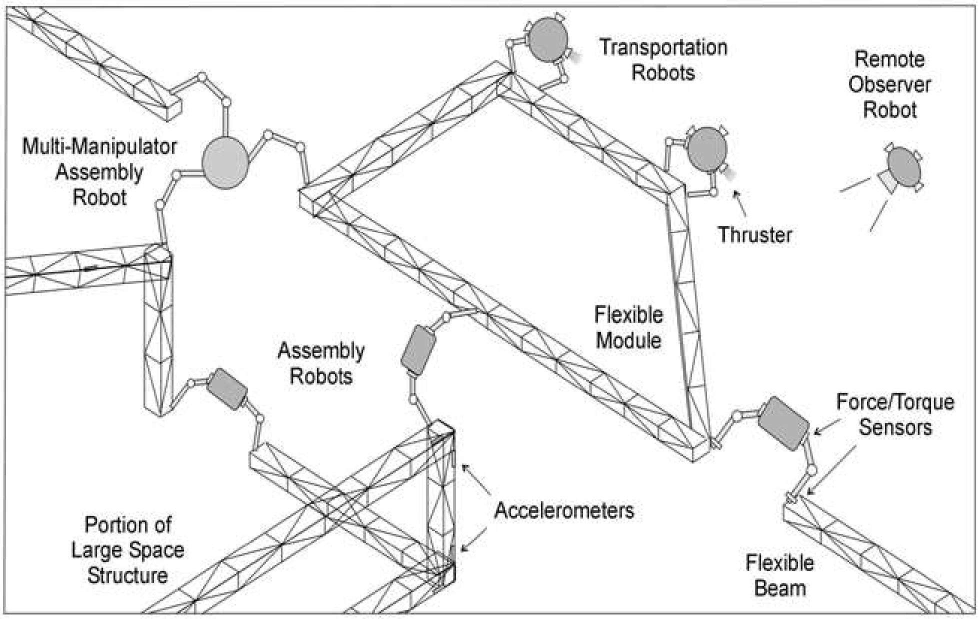

Figure 4.1: On-orbit construction of large space structures by robotic teams [164]

This chapter presents a comprehensive dynamic model for a Reaction-Wheel (RW) actuated space robot and a robust controller that can maintain the attitude of the spacecraft as required while its manipulator follows the prescribed trajectory. Note that in the context, robust controller refers to a controller that is not sensitive to uncertainties. Unlike previous work, this chapter reformulates the dynamic equation of an FFSR by taking into account the contribution of RWs to the angular momentum of the entire system when using the law of conservation of momentum. Given strong nonlinearities and multiple inputs of the system, diagonalization is first used to transform the strongly coupled problem into multiple single-input problems by introducing virtual torques. The virtual torques are later solved to obtain actual RW torques and joint torques. When involving system uncertainties, the defined virtual torque is accurately associated with the actual torque using nominal value of the uncertain inertia matrix in order to guarantee the stability of the original system. Smoothed sliding mode controllers are designed for each single-input system based on Lyapunov method provided that the bounds of uncertainties can be estimated.

In addition, a novel control method - Adaptive Variable Structure Control (AVSC) developed in [20], is applied to the space robot model to achieve fast set-point tracking and spacecraft attitude regulation. Unlike Sliding Mode Control

(SMC), the AVSC method is able to drive the error states to the origin of the error phase plane in a parabola-like trajectory rather than restrict them to a predefined sliding manifold, by tuning the control gain in real time. Such convergence in a more natural parabolic trajectory reduces the settling time of the system.

The chapter is organized into six sections. Section 4.2 systematically formulates the kinematic and dynamic equations of an FFSR based on angular momentum conservation law and Lagrangian dynamics. In Section 4.3, decoupling of this Multiple-Input Multiple-Output (MIMO) system into several single-input systems is performed before proceeding to the controller design. Then smooth SMC scheme is used for each decoupled sub-channel to finally implement spacecraft attitude regulation and simultaneous manipulator trajectory tracking in the joint space. Estimation of the bounds of the system uncertainties is elaborated in this section. Section 4.4 presents the methodology of AVSC and its application to space robots. Section 4.5 outlines the ways of space robot control in the task space. The performance of the proposed controllers is verified using a three-link space manipulator model in Section 4.6. Section 4.7 concludes this chapter.

4.2 Space Robot Model

4.2.1 Assumptions

As a typical operation in on-orbit assembly, the scenario is assumed as the space robot performs an approaching motion to a target structural component. An FFSR model which consists a mobile base and a robotic manipulator is used. Detailed assumptions are clarified as follows.

1. The manipulator comprises n rigid links connected by revolute joints, as shown in Figure 4.2. Then the robot is considered as a serial chain composed of $n+1$ rigid bodies, with $i = 0$ representing the spacecraft base and $i = 1$ to n representing the links.

2. As a result of Assumption 1, the space robot has $n + 6$ Degrees of Freedom (DOF) among which n DOF originates from the manipulator motion and 6

DOF denotes the spacecraft attitude and its translation. The n joint motors generate torques to control the arm motion. For simplicity, three orthogonally mounted RWs generate regulation torques along roll, pitch and yaw axes in the FFSR base frame; whereas translation of the spacecraft base is not controlled.

3. Since the operations are performed in close proximity and in short time compared with orbital radius and orbital period, the effects of orbital mechanics are neglected. In addition throughout the approaching operation, the target stays within the workspace of FFSR by setting an appropriate initial configuration for the space robot. As a result, no singular configuration is directed.

4. Thrusters are not fired during the operation and negligible external forces/torques act on the system. Therefore, linear and angular momentum conservation hold true throughout the approaching motion.

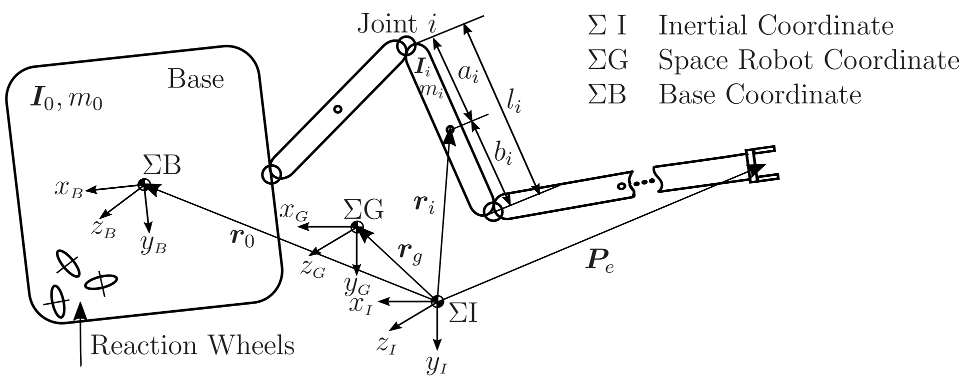

Figure 4.2: Space robot model

The symbols appearing in Figure 4.2 are defined as follows. Vectors or matrices without any indicated superscripts can mean variables with reference to the inertial frame or those that can be transformed into the inertial frame.

$\boldsymbol{r}_g \in \mathbb{R}^3$ position vector of Center of Mass (CM) of the FFSR

$\boldsymbol{r}_0 \in \mathbb{R}^3$ position vector of CM of the base

$\boldsymbol{r}_i \in \mathbb{R}^3$ position vector of CM of link i

$\boldsymbol{P}_e \in \mathbb{R}^3$ position vector of the end-effector

$a_i \in \mathbb{R}^1$ length from joint i to CM of link i

$b_i \in \mathbb{R}^1$ length from CM of link i to joint $i+1$

$l_i \in \mathbb{R}^1$ length of link i

$\boldsymbol{I}_0 \in \mathbb{R}^{3\times 3}$ inertia matrix of the spacecraft base

$\boldsymbol{I}_i \in \mathbb{R}^{3\times 3}$ inertia matrix of link i

$m_0 \in \mathbb{R}^1$ mass of the spacecraft base

$m_i \in \mathbb{R}^1$ mass of link i

4.2.2 Space Robot Kinematics

As pointed out by [38, 44], the end-effector motion of an FFSR depends on the history of manipulator motion. As a result, it is difficult to solve the inverse kinematics problem. Instead, by representing the kinematics at motion rate level, the inverse kinematics can be solved analytically [39].

Let $\boldsymbol{P}_e \in \mathbb{R}^{3\times 1}$ denote the position of the end-effector (orientation of the end-effector is not considered in this chapter), $\boldsymbol{\Phi}_S = [\alpha, \beta, \gamma]^T$ represent the attitude of the spacecraft base, $\boldsymbol{\Phi}_M = [\phi_1, \phi_2, \cdots, \phi_n]^T$ represent joint angles of the manipulator. Since the motion of the RWs has no explicit influence on the end-effector trajectory, the end-effector motion is intuitively determined by two parts, that is the spacecraft attitude motion and the manipulator motion, as,

$$\dot{\boldsymbol{P}}_e = \boldsymbol{J}_S \dot{\boldsymbol{\Phi}}_S + \boldsymbol{J}_M \dot{\boldsymbol{\Phi}}_M + \dot{\boldsymbol{r}}_g, \tag{4.1}$$

where $\boldsymbol{J}_S \in \mathbb{R}^{3\times 3}$, $\boldsymbol{J}_M \in \mathbb{R}^{3\times n}$ is a base part and a manipulator part of the extended Jacobian matrix of the space robot; $\boldsymbol{r}_g$ is the position of the space robot centroid. Assuming stationary initial condition, linear momentum of the space robot will remain at zero since there are no external forces applied, i.e. $\dot{\boldsymbol{r}}_g \equiv \boldsymbol{0}$. This linearized transformation shows that the motion rate of the end-effector $\dot{\boldsymbol{P}}_e$ in the task space can be resolved into that of $\dot{\boldsymbol{\Phi}}_S$ and $\dot{\boldsymbol{\Phi}}_M$ in the configuration space. Derivation of the above kinematic equation is detailed in Appendix B.2.

4.2.3 Space Robot Dynamics

In this section, the space robot dynamic equation is derived by first discussing the dynamic constraints of the system based on angular momentum conservation law and then using the Lagrangian formulation.

Unlike external actuators such as thrusters, RWs act as an internal component of the small space robot. Accordingly, their angular momentum forms an important part of the momentum of the entire system. Instead of representing the system angular momentum only by using spacecraft base and manipulator motion, it is necessary to add a term to incorporate the contribution of RWs as,

$$\boldsymbol{H}_0 = \boldsymbol{H}_S \dot{\boldsymbol{\Phi}}_S + \boldsymbol{H}_M \dot{\boldsymbol{\Phi}}_M + \boldsymbol{H}_W \dot{\boldsymbol{\Phi}}_W, \tag{4.2}$$

where $\boldsymbol{H}_0$ is the angular momentum of the entire system with respect to the origin of the inertial coordinate and $\boldsymbol{H}_0 \equiv \mathbf{0}$ holds true under the assumption of stationary initial state since RWs generate internal control torques; $\boldsymbol{\Phi}_W$ represents the rotation angles of the RWs with respect to the spacecraft base; $\boldsymbol{H}_S \in \mathbb{R}^{3\times 3}$, $\boldsymbol{H}_M \in \mathbb{R}^{3\times n}$ and $\boldsymbol{H}_W \in \mathbb{R}^{3\times 3}$ denote a base part, a manipulator part and a reaction-wheel part of the inertia matrix of the system with respect to the inertial frame, respectively. Rewriting (4.2) to express spacecraft attitude by using manipulator motion and RW motion results in,

$$\dot{\boldsymbol{\Phi}}_S = \boldsymbol{H}_{ms} \dot{\boldsymbol{\Phi}}_M + \boldsymbol{H}_{ws} \dot{\boldsymbol{\Phi}}_W, \tag{4.3}$$

where $\boldsymbol{H}_{ms} \in \mathbb{R}^{3\times n}$ and $\boldsymbol{H}_{ws} \in \mathbb{R}^{3\times 3}$ are coefficient matrices.

Consider (4.3) as a set of constraint equations and select $\boldsymbol{\Phi} = [\boldsymbol{\Phi}_M^T, \boldsymbol{\Phi}_W^T]^T$ as generalized coordinates. According to Lagrangian formulation, the required torques can be derived as,

$$\frac{d}{dt}\left(\frac{\partial \mathscr{L}}{\partial \dot{\phi}_i}\right) - \frac{\partial \mathscr{L}}{\partial \phi_i} = \tau_i, \quad i = 1, 2, \cdots, n, w1, w2, w3, \tag{4.4}$$

where $\tau_i, i = 1, 2, \cdots, n$ denotes joint torque and $\tau_{w1}, \tau_{w2}, \tau_{w3}$ denote RW torques along roll, pitch and yaw axes, respectively. The canonical form of (4.4) becomes,

$$\boldsymbol{H}\ddot{\boldsymbol{\Phi}} + \boldsymbol{C}\dot{\boldsymbol{\Phi}} = \boldsymbol{\tau}, \tag{4.5}$$

where $\boldsymbol{H} \in \mathbb{R}^{(n+3)\times(n+3)}$ is symmetric and positive definite, $\boldsymbol{C} \in \mathbb{R}^{(n+3)\times(n+3)}$ includes nonlinear terms and $\boldsymbol{\tau} = [\tau_1, \cdots, \tau_n, \tau_{w1}, \tau_{w2}, \tau_{w3}]^T$. The derivation of (4.5) is detailed in Appendix B.3.

The attitude of the space robot base and the manipulator motion are aimed to be controlled. According to (4.3), the RWs' motion can be expressed using the above-mentioned motions. Therefore, $\boldsymbol{\Phi} = [\boldsymbol{\Phi}_M^T, \boldsymbol{\Phi}_W^T]^T$ in (4.5) is transformed to a new practically meaningful vector $\boldsymbol{q} = [\boldsymbol{\Phi}_M^T, \boldsymbol{\Phi}_S^T]^T$ as,

$$\dot{\boldsymbol{\Phi}} = \begin{bmatrix} \dot{\boldsymbol{\Phi}}_M \\ \dot{\boldsymbol{\Phi}}_W \end{bmatrix} = \begin{bmatrix} \boldsymbol{I}_N & \boldsymbol{O}_N \\ -\boldsymbol{H}_{ws}^{-1}\boldsymbol{H}_{ms} & \boldsymbol{H}_{ws}^{-1} \end{bmatrix} \begin{bmatrix} \dot{\boldsymbol{\Phi}}_M \\ \dot{\boldsymbol{\Phi}}_S \end{bmatrix} = \boldsymbol{N}\dot{\boldsymbol{q}}, \tag{4.6}$$

where $\boldsymbol{I}_N \in \mathbb{R}^{n\times n}$ is an identity matrix; $\boldsymbol{O}_N \in \mathbb{R}^{3\times 3}$ is a zero matrix; and

$$\boldsymbol{N} = \begin{bmatrix} \boldsymbol{I}_N & \boldsymbol{O}_N \\ -\boldsymbol{H}_{ws}^{-1}\boldsymbol{H}_{ms} & \boldsymbol{H}_{ws}^{-1} \end{bmatrix}.$$

Substituting (4.6) and $\ddot{\boldsymbol{\Phi}} = \boldsymbol{N}\ddot{\boldsymbol{q}} + \dot{\boldsymbol{N}}\dot{\boldsymbol{q}}$ into (4.5), the final dynamic equation with $\boldsymbol{q}$ as the variable can be obtained as,

$$\boldsymbol{A}(\boldsymbol{q})\ddot{\boldsymbol{q}} + \boldsymbol{B}(\boldsymbol{q}, \dot{\boldsymbol{q}})\dot{\boldsymbol{q}} = \boldsymbol{\tau}, \tag{4.7}$$

where $\boldsymbol{A} = \boldsymbol{H}\boldsymbol{N}$ and $\boldsymbol{B} = \boldsymbol{H}\dot{\boldsymbol{N}} + \boldsymbol{C}\boldsymbol{N}$. It is worth noting that this vector transformation results in the loss of an advantageous property of the original inertia matrix as $\boldsymbol{H}$, i.e., $\boldsymbol{A}$ is neither symmetric nor positive definite. Consequently, a control scheme based on the aforementioned matrix features, as done by most previous literature, is no longer valid.

Set the desired state vector as $\boldsymbol{q}_d$ and define a state error vector $\boldsymbol{e}$ as $\boldsymbol{e}_1 = \boldsymbol{q} - \boldsymbol{q}_d$, $\boldsymbol{e}_2 = \dot{\boldsymbol{q}} - \dot{\boldsymbol{q}}_d$, $\boldsymbol{e} = [\boldsymbol{e}_1^T, \boldsymbol{e}_2^T]^T$. Rearrange the dynamic equation (4.7) in state-space form as,

$$\dot{\boldsymbol{e}}_1 = \boldsymbol{e}_2, \tag{4.8}$$

$$\dot{\boldsymbol{e}}_2 = -\boldsymbol{A}^{-1}(\boldsymbol{e})\boldsymbol{B}(\boldsymbol{e})\left(\boldsymbol{e}_2 + \dot{\boldsymbol{q}}_d\right) - \ddot{\boldsymbol{q}}_d + \boldsymbol{A}^{-1}(\boldsymbol{e})\boldsymbol{\tau}. \tag{4.9}$$

4.3 Sliding Mode Controller

The system aims at controlling the spacecraft attitude at the desired attitude and performing successful trajectory tracking in joint space. Specifically, as illustrated by (4.8) and (4.9), the system has $n+3$ outputs as described by the tracking error $\boldsymbol{e}_1$ and $n+3$ inputs represented by $\boldsymbol{\tau}$. The strong nonlinearities and existing system uncertainties of this MIMO system complicate the controller design. SMC has the ability to cope with nonlinear systems that are affected by disturbances or parametric uncertainties, as addressed in [165], and can be applied. However, before considering the controller design, it is necessary to convert the system model to multiple single-input subsystems. Such transformation makes it intuitive to independently determine the input entries, which can satisfy the sufficient conditions for reachability of sliding mode. Therefore, Section 4.3.2 decouples the system using a diagonalization method which is established based on the sliding surface presented in Section 4.3.1. Section 4.3.3 develops the boundary layer SMC controller for each single-input subsystem.

4.3.1 Sliding Surface

An appropriate sliding surface vector should be selected to ensure the tracking error vector converges to zero once the sliding mode is reached. Define the surface function as [165],

$$\boldsymbol{\sigma}(\boldsymbol{e}) = \left(\frac{d}{dt} + \boldsymbol{\Lambda}_r\right)^{p-1} \boldsymbol{e}_1 = \dot{\boldsymbol{e}}_1 + \boldsymbol{\Lambda}_r \boldsymbol{e}_1 = \boldsymbol{S}\ \boldsymbol{e}, \tag{4.10}$$

where p is the system order and $p = 2$ in this case; $\boldsymbol{S} \in \mathbb{R}^{(n+3)\times[2(n+3)]}$ is defined as,

$$\boldsymbol{S} = \begin{bmatrix} \boldsymbol{\Lambda}_r & \boldsymbol{I} \end{bmatrix} = \begin{bmatrix} \lambda_{r1} & & & & 1 & & & \\ & \lambda_{r2} & & & & 1 & & \\ & & \cdots & & & & \cdots & \\ & & & \lambda_{r,n+3} & & & & 1 \end{bmatrix}.$$

$\boldsymbol{\Lambda}_r \in \mathbb{R}^{(n+3)\times(n+3)}$ is a diagonal matrix with positive scalars λ_{ri} as entries, and $\boldsymbol{I} \in \mathbb{R}^{(n+3)\times(n+3)}$ is an identity matrix. When the sliding surface is reached and maintained, a set of constant-coefficient linear differential equations $\sigma_i = \dot{e}_i + \lambda_{ri} e_i \equiv 0, i = 1, 2, \cdots, n+3$ are obtained. The unique solution of each equation is $e_i = 0$, which indicates that the tracking error $\boldsymbol{e}$ can converge to zero.

4.3.2 System Decoupling

If applying SMC method directly to the original system, inconsistent solutions for the switched control gains may be derived by using a simple Lyapunov function. Instead, a decoupled system allows independent selection of switched control gains in conjunction with an intuitive choice of Lyapunov function. Therefore, the system inputs are better to be decoupled before utilizing SMC method.

To reflect practical scenarios, system uncertainties should be included (i.e., matrix $\boldsymbol{A}$ and $\boldsymbol{B}$ are not exactly known). Assume $\hat{\boldsymbol{A}} = \boldsymbol{A} + \Delta\boldsymbol{A}$, where $\hat{\boldsymbol{A}}$ denotes the nominal value of $\boldsymbol{A}$ and $\Delta\boldsymbol{A}$ represents the uncertainty. Rewrite (4.8) and (4.9) in a regular form as,

$$\dot{\boldsymbol{e}} = \begin{bmatrix} \boldsymbol{e}_2 \\ -\boldsymbol{A}^{-1}\boldsymbol{B}\left(\boldsymbol{e}_2 + \dot{\boldsymbol{q}}_d\right) - \ddot{\boldsymbol{q}}_d \end{bmatrix} + \begin{bmatrix} \boldsymbol{O} \\ \boldsymbol{A}^{-1} \end{bmatrix} \boldsymbol{\tau} = \boldsymbol{f}'(\boldsymbol{e}, t) + \boldsymbol{g}(\boldsymbol{e})\boldsymbol{\tau}, \tag{4.11}$$

where $\boldsymbol{O} \in \mathbb{R}^{(n+3)\times(n+3)}$ is a zero matrix,

$$\boldsymbol{f}'(\boldsymbol{e}, t) = \begin{bmatrix} \boldsymbol{e}_2 \\ -\boldsymbol{A}^{-1}\boldsymbol{B}\left(\boldsymbol{e}_2 + \dot{\boldsymbol{q}}_d\right) - \ddot{\boldsymbol{q}}_d \end{bmatrix},$$

$$\boldsymbol{g}(\boldsymbol{e}) = \begin{bmatrix} \boldsymbol{O} \\ \boldsymbol{A}^{-1} \end{bmatrix}.$$

Now, construct a virtual torque $\boldsymbol{\tau}^{\star}$ via a transformation from the actual torque $\boldsymbol{\tau}$ according to a diagonalization method [166]. It should be mentioned that the practical controller $\boldsymbol{\tau}$ which originates from the calculated virtual torque $\boldsymbol{\tau}^{\star}$ must be deterministic to guarantee the stability of the original system. Accordingly, $\boldsymbol{\tau}^{\star}$ is designed using nominal value of $\boldsymbol{A}$ as,

$$\boldsymbol{\tau}^{\star} = \left[\frac{\partial \boldsymbol{\sigma}}{\partial \boldsymbol{e}} \hat{\boldsymbol{g}}(\boldsymbol{e})\right] \boldsymbol{\tau} = \left\{ \begin{bmatrix} \boldsymbol{\Lambda}_r & \boldsymbol{I} \end{bmatrix} \begin{bmatrix} \boldsymbol{O} \\ \hat{\boldsymbol{A}}^{-1} \end{bmatrix} \right\} \boldsymbol{\tau} = \hat{\boldsymbol{A}}^{-1} \boldsymbol{\tau}. \tag{4.12}$$

Replacing $\boldsymbol{\tau}$ with $\boldsymbol{\tau} = \hat{\boldsymbol{A}} \boldsymbol{\tau}^{\star} = (\boldsymbol{A} + \Delta \boldsymbol{A})\, \boldsymbol{\tau}^{\star}$ in (4.9) produces (suppressing t and $\boldsymbol{e}$ arguments),

$$\dot{\boldsymbol{e}}_2 = -\boldsymbol{A}^{-1} \boldsymbol{B} \left(\boldsymbol{e}_2 + \dot{\boldsymbol{q}}_d\right) - \ddot{\boldsymbol{q}}_d + \boldsymbol{A}^{-1} \left(\boldsymbol{A} + \Delta \boldsymbol{A}\right) \boldsymbol{\tau}^{\star} = \boldsymbol{f}(\boldsymbol{e}, t) + \boldsymbol{\tau}^{\star} + \boldsymbol{h}(\boldsymbol{e}, t), \tag{4.13}$$

where $\boldsymbol{f}(\boldsymbol{e}, t) = -\boldsymbol{A}^{-1} \boldsymbol{B} \left(\boldsymbol{e}_2 + \dot{\boldsymbol{q}}_d\right) - \ddot{\boldsymbol{q}}_d$ is the known plant, and $\boldsymbol{h}(\boldsymbol{e}, t) = \boldsymbol{A}^{-1} \Delta \boldsymbol{A} \boldsymbol{\tau}^{\star}$ represents the system uncertainties as a whole. Equation (4.13) shows the coefficient of $\boldsymbol{\tau}^{\star}$ is a constant. Thus, the transformation from a complicated MIMO problem to $n + 3$ single-input controller design tasks is completed.

4.3.3 Controller Design

Convergence Condition

Select Lyapunov function as,

$$V = \frac{1}{2} \boldsymbol{\sigma}^T \boldsymbol{\sigma}, \tag{4.14}$$

which satisfies $V \geq 0$ when $\boldsymbol{\sigma} \neq 0$. Define the control torque of each sub-channel as,

$$\begin{cases} \tau_i^{\star} < \{-(f_i + \lambda_{ri} e_{2i} + h_i)\}_{\min}, & \sigma_i > 0 \\ \tau_i^{\star} > \{-(f_i + \lambda_{ri} e_{2i} + h_i)\}_{\max}, & \sigma_i < 0 \end{cases} \quad i = 1, \cdots, n + 3. \tag{4.15}$$

Theorem 4.1 Under the control law stated in (4.15), the system dynamics reaches and maintains on the sliding surface $\boldsymbol{\sigma}(\boldsymbol{e}) = 0$ in finite time.

Proof Differentiate sliding surface function as an initial step to get the derivative of Lyapunov function. Combining the derivative of (4.10) with (4.8) and (4.13), the derivative of the sliding surface can be expressed by,

$$\begin{aligned}\dot{\boldsymbol{\sigma}} &= \frac{\partial \boldsymbol{\sigma}}{\partial \boldsymbol{e}}\dot{\boldsymbol{e}} = \frac{\partial \boldsymbol{\sigma}}{\partial \boldsymbol{e}}\begin{bmatrix} \dot{\boldsymbol{e}}_1 \\ \dot{\boldsymbol{e}}_2 \end{bmatrix} = \boldsymbol{S}\begin{bmatrix} \boldsymbol{e}_2 \\ \boldsymbol{f}(\boldsymbol{e},t) + \boldsymbol{h}(\boldsymbol{e},t) + \boldsymbol{\tau}^\star \end{bmatrix} \\ &= \begin{bmatrix} \lambda_{r1}e_{21} + f_1 + h_1 + \tau_1^\star \\ \lambda_{r2}e_{22} + f_2 + h_2 + \tau_2^\star \\ \vdots \\ \lambda_{r,n+3}e_{2,n+3} + f_{n+3} + h_{n+3} + \tau_{n+3}^\star \end{bmatrix}.\end{aligned} \tag{4.16}$$

Subsequently, the derivative of Lyapunov function (4.14) is

$$\dot{V} = \boldsymbol{\sigma}^T\dot{\boldsymbol{\sigma}} = \sum_{i=1}^{n+3}\sigma_i(\lambda_{ri}e_{2i} + f_i + h_i + \tau_i^\star). \tag{4.17}$$

When $\tau_i^\star$ satisfies the conditions listed in (4.15), $\dot{V} < 0$ turns out to be true for $\boldsymbol{\sigma}(\boldsymbol{e}) \neq 0$. This ensures that the trajectory of system dynamics converges and maintains on the sliding surface $\boldsymbol{\sigma}(\boldsymbol{e}) = 0$ in finite time.

Handling the Bounds of Uncertainties

To get a regular form of SMC controller and progressively eliminate the chattering effect, it is assumed that the bounds of uncertain matrices $\boldsymbol{A}$ and $\boldsymbol{B}$ can be estimated. Actually, based on the derivation in Section 4.2 and Appendix A.3, $\boldsymbol{A}$ and $\boldsymbol{B}$ are determined by physical parameters of the space robot which have practical limits, and the motion parameters of the spacecraft. Therefore in practice, before applying the controller to an actual spacecraft, simulation studies are always needed to assess the limits of the matrices according to the desired and available motion, as illustrated in [151].

Several positive scalars, including $\bar{\pi}$, $\bar{a}_1$, $\bar{a}_2$, $\bar{b}_1$, $\bar{b}_2$, $\bar{c}_1$, and $\bar{c}_2$, are introduced to define the bounds of system uncertainties as follows:

$$
\begin{aligned}
&||\boldsymbol{A}-\hat{\boldsymbol{A}}||=||\boldsymbol{\Delta A}||\leq\bar{\pi}||\hat{\boldsymbol{A}}||,\\
&\bar{a}_1||\hat{\boldsymbol{A}}||\leq||\boldsymbol{A}||\leq\bar{a}_2||\hat{\boldsymbol{A}}||,\\
&\bar{b}_1||\hat{\boldsymbol{B}}||\leq||\boldsymbol{B}||\leq\bar{b}_2||\hat{\boldsymbol{B}}||,\\
&\bar{c}_1||\hat{\boldsymbol{A}}^{-1}||\leq||\boldsymbol{A}^{-1}||\leq\bar{c}_2||\hat{\boldsymbol{A}}^{-1}||,
\end{aligned}
\tag{4.18}
$$

where $\boldsymbol{A}$ and $\boldsymbol{B}$ are actual values of the matrices, while $\hat{\boldsymbol{A}}$ and $\hat{\boldsymbol{B}}$ are their nominal values. Then the nominal values and bounds of matrices or vectors involved in (4.15) can be obtained. For the vector $\boldsymbol{f}(\boldsymbol{e},t)$, only the uncertain part $\bar{\boldsymbol{f}}=-\boldsymbol{A}^{-1}\boldsymbol{B}(\boldsymbol{e}_2+\dot{\boldsymbol{q}}_d)$ is considered since the desired acceleration of joint displacements and base attitude $\ddot{\boldsymbol{q}}_d$ is given.

$$
\begin{aligned}
\hat{\bar{\boldsymbol{f}}}\quad&=-\hat{\boldsymbol{A}}^{-1}\hat{\boldsymbol{B}}(\boldsymbol{e}_2+\dot{\boldsymbol{q}}_d),\\
\hat{\boldsymbol{h}}\quad&=\hat{\boldsymbol{A}}^{-1}\boldsymbol{\Delta A}\boldsymbol{\tau}^\star=0,\\
||\bar{\boldsymbol{f}}||\quad&=||-\boldsymbol{A}^{-1}\boldsymbol{B}(\boldsymbol{e}_2+\dot{\boldsymbol{q}}_d)||\\
&\leq||\boldsymbol{A}^{-1}||\;||\boldsymbol{B}||\;||\boldsymbol{e}_2+\dot{\boldsymbol{q}}_d||\\
&\leq\bar{c}_2||\hat{\boldsymbol{A}}^{-1}||\bar{b}_2||\hat{\boldsymbol{B}}||\;||\boldsymbol{e}_2+\dot{\boldsymbol{q}}_d||\\
&=\bar{b}_2\bar{c}_2||\hat{\boldsymbol{A}}^{-1}||\;||\hat{\boldsymbol{B}}||\;||\boldsymbol{e}_2+\dot{\boldsymbol{q}}_d||=\boldsymbol{f}^\star,\\
||\boldsymbol{h}||\quad&=||\boldsymbol{A}^{-1}\boldsymbol{\Delta A}\boldsymbol{\tau}^\star||=||\boldsymbol{A}^{-1}\boldsymbol{\Delta A}\hat{\boldsymbol{A}}^{-1}\boldsymbol{\tau}||\\
&\leq\bar{c}_2||\hat{\boldsymbol{A}}^{-1}||\bar{\pi}||\hat{\boldsymbol{A}}||\;||\hat{\boldsymbol{A}}^{-1}||\boldsymbol{\tau}_{\max}\\
&=\bar{c}_2\bar{\pi}||\hat{\boldsymbol{A}}^{-1}||\;||\hat{\boldsymbol{A}}||\;||\hat{\boldsymbol{A}}^{-1}||\boldsymbol{\tau}_{\max}=\boldsymbol{h}^\star.
\end{aligned}
\tag{4.19}
$$

Joint torques or RW torques are bounded in practical implementation, i.e. $\tau_{i\min}\leq\tau_i\leq\tau_{i\max}, i=1,2,\cdots,n+3$ with negative limit $\tau_{i\min}$ and positive limit $\tau_{i\max}$.

Now the difference between actual value of the vector and its nominal value can be given by,

$$
\begin{aligned}
||\bar{\boldsymbol{f}}-\hat{\bar{\boldsymbol{f}}}||\quad&\leq\boldsymbol{f}^\star+||\hat{\boldsymbol{A}}^{-1}\hat{\boldsymbol{B}}(\boldsymbol{e}_2+\dot{\boldsymbol{q}}_d)||\\
&\leq\boldsymbol{f}^\star+||\hat{\boldsymbol{A}}^{-1}||\;||\hat{\boldsymbol{B}}||\;||\boldsymbol{e}_2+\dot{\boldsymbol{q}}_d||\\
&=\left(\bar{b}_2\bar{c}_2+1\right)||\hat{\boldsymbol{A}}^{-1}||\;||\hat{\boldsymbol{B}}||\;||\boldsymbol{e}_2+\dot{\boldsymbol{q}}_d||=\boldsymbol{f}^{\star\star},\\
||\boldsymbol{h}-\hat{\boldsymbol{h}}||\quad&=||\boldsymbol{h}||\leq\boldsymbol{h}^\star.
\end{aligned}
\tag{4.20}
$$

Smoothed Sliding Mode Controller

According to (4.16), the condition $\dot{\boldsymbol{\sigma}} = 0$ gives an estimation of the equivalent control $\boldsymbol{\tau}^{\star}_{eq}$ as,

$$\tau^{\star}_{eqi} = -\lambda_{ri} e_{2i} - \hat{f}_i - \hat{h}_i = -\lambda_{ri} e_{2i} + \ddot{q}_{di} - \hat{\hat{f}}_i - \hat{h}_i, \quad i = 1, 2, \cdots, n+3. \tag{4.21}$$

To get a non-positive value of $\dot{V}$ despite the existing system uncertainties, $\boldsymbol{\tau}^{\star}$ can be augmented by adding another term $-\boldsymbol{k}_r \operatorname{sgn}(\boldsymbol{\sigma})$ to $\boldsymbol{\tau}^{\star}_{eq}$ which is discontinuous across the sliding surface but is required to ensure the sliding condition $\boldsymbol{\sigma} = 0$. $\boldsymbol{k}_r \in \mathbb{R}^{(n+3)\times(n+3)}$ is a diagonal matrix with positive scalar k_{ri} as entries. k_{ri} is the adaptive gain and determined as $k_{ri} = f^{\star\star}_i + h^{\star}_i + \alpha_{ri}$ with a positive vector $\boldsymbol{\alpha}_r = [\alpha_{r1}, \alpha_{r2}, \cdots, \alpha_{r,n+3}]^T$. Therefore, the augmented control effort $\boldsymbol{\tau}^{\star}$ is,

$$\tau^{\star}_i = -\lambda_{ri} e_{2i} + \ddot{q}_{di} - \hat{\hat{f}}_i - \hat{h}_i - (f^{\star\star}_i + h^{\star}_i + \alpha_{ri}) \operatorname{sgn}(\sigma_i), \quad i = 1, 2, \cdots, n+3. \tag{4.22}$$

The discontinuous term presents an intuitive feedback control strategy, that is when the surface error σ_i is negative, $-k_{ri} \operatorname{sgn}(\sigma_i)$ generates a torque to push back strongly in the positive direction (and conversely). It is observed that the control effort is associated with the extent of system uncertainties, which implies the need to explore how much uncertainty can be managed when considering torque saturation in practice. This aspect is investigated using simulations in Section 4.6.

Theorem 4.2 The control input stated in (4.22) enforces the system dynamics to the sliding surface $\boldsymbol{\sigma}(\boldsymbol{e}) = 0$.

Proof Substituting (4.22) into the derivative of the Lyapunov function (4.17) returns,

$$
\begin{aligned}
\dot{V} &= \sum_{i=1}^{n+3} \sigma_i \left(\lambda_{ri} e_{2i} + f_i + h_i + \tau_i^\star \right) \\
&= \sum_{i=1}^{n+3} \sigma_i \left[\lambda_{ri} e_{2i} + f_i + h_i - \lambda_{ri} e_{2i} + \ddot{q}_{di} - \hat{\bar{f}}_i - \hat{h}_i - \left(f_i^{\star\star} + h_i^\star + \alpha_{ri} \right) \ \mathrm{sgn}(\sigma_i) \right] \\
&= \sum_{i=1}^{n+3} \left[\sigma_i \left(\bar{f}_i - \hat{\bar{f}}_i \right) + \sigma_i \left(h_i - \hat{h}_i \right) - \left(f_i^{\star\star} + h_i^\star + \alpha_{ri} \right) |\sigma_i| \right] \\
&\leq \sum_{i=1}^{n+3} \left[\left(|\bar{f}_i - \hat{\bar{f}}_i| - f_i^{\star\star} \right) |\sigma_i| + \left(|h_i - \hat{h}_i| - h_i^\star \right) |\sigma_i| - \alpha_{ri} |\sigma_i| \right].
\end{aligned}
\tag{4.23}
$$

According to (4.20), $|\bar{f}_i - \hat{\bar{f}}_i| - f_i^{\star\star} \leq 0$ and $|h_i - \hat{h}_i| - h_i^\star < 0$. The substitution of these two equations into (4.23) proves that $\dot{V} \leq 0$. The equality holds only when the sliding mode is reached, i.e. $\boldsymbol{\sigma}(\boldsymbol{e}) = 0$. Therefore, the control law (4.22) ensures the convergence of system dynamics to the sliding surface.

Practically, FFSRs are always designed as light weight structures to save fuel consumption at launch and as such are flexible structures. The switching control law (4.22) involves extremely high control activity and may excite the unmodeled or high-frequency dynamics which induces uncontrolled vibration. To eliminate the undesirable chattering phenomenon, the boundary layer method is adopted. Subsequently, the controller is improved to,

$$
\tau_i^\star = -\lambda_{ri} e_{2i} + \ddot{q}_{di} - \hat{\bar{f}}_i - \hat{h}_i - \left(f_i^{\star\star} + h_i^\star + \alpha_{ri} \right) \ \mathrm{sat}(\sigma_i), \quad i = 1, 2, \cdots, n+3. \tag{4.24}
$$

The saturation function sat in (4.24) is defined as,

$$
\mathrm{sat}(\sigma_i) = \begin{cases} \mathrm{sgn}(\sigma_i) & \text{for } \sigma_i > \varepsilon_r, \\ \sigma_i / \varepsilon_r & \text{for } \sigma_i \leq \varepsilon_r, \end{cases} \tag{4.25}
$$

where ε_r is the boundary layer thickness. Actual torque $\boldsymbol{\tau}$ calculated by $\boldsymbol{\tau} = \hat{\boldsymbol{A}} \boldsymbol{\tau}^\star$ can definitely confirm system stability due to the accurate value of $\hat{\boldsymbol{A}}$.

4.4 Robust Adaptive Coordination Controller

Rapid spacecraft maneuver is very important. It can affect the overall performance of the on-board communication and power harvesting system; also, it is necessary to pick up a target in acquisition mode. The AVSC approach developed in [20] can converge the error states to zero in a fast robust manner whilst avoiding any overshoot. Thus, it is adopted in this section to produce fast settling times which is particularly advantageous in set-point regulation. The underlying theory behind the AVSC approach using a general second order dynamic system is presented in Section 4.4.1. Application of this method to the space robot model is then detailed in Section 4.4.2.

4.4.1 The Adaptive Variable Structure Control Method

This section presents the basic theory of the AVSC method based on Ref. [20].

Overall Description

Consider a typical second-order nonlinear system with uncertainties as follows:

$$\dot{x}_1 = x_2, \tag{4.26}$$

$$\dot{x}_2 = f(\boldsymbol{x}(t)) + g(\boldsymbol{x}(t))u + h(\boldsymbol{x}(t)), \tag{4.27}$$

where $\boldsymbol{x} = [x_1, x_2]^T$ represents the state vector; u denotes the control input; $f(\boldsymbol{x}(t))$ and $g(\boldsymbol{x}(t))$ are known and $g(\boldsymbol{x}(t)) \neq 0$; $h(\boldsymbol{x}(t))$ represents system uncertainties, which is not known but bounded, $\mid h(\boldsymbol{x}(t)) \mid \leq h_{\max}$.

Define an error state vector $\boldsymbol{e} = [e_1, e_2]^T$ to consider the error dynamics of the system, with

$$e_1 = x_1 - x_{1d}, \tag{4.28}$$

$$e_2 = x_2 - x_{2d}. \tag{4.29}$$

x_{1d} and x_{2d} denote the desired states.

Distinguished from SMC which restricts the error dynamics to a predetermined sliding manifold, the AVSC approach is able to update the control gain in real time and enforces the error states to the origin along a parabolic trajectory. Such a path is closer to the natural behaviour of the system [167]. As a result, the chattering effect is eliminated and the overall settling time is reduced. In addition, the AVSC method ensures robustness against system uncertainties and disturbances through gain adaptation.

The AVSC algorithm consists of three stages. In stage one, referred to as the *Reaching Phase*, the control law is designed to enforce the system to reach the condition $\bar{\sigma}(\boldsymbol{e}) = 0$. Once the error dynamics reaches $\bar{\sigma}(\boldsymbol{e}) = 0$, it enters the *Convergence Phase*. During the convergence phase, the error state converges to the origin of the error phase plane. When the error states arrive at the origin of error space, the *Constrained Phase* starts. In this final stage, an appropriate robust control approach, e.g. SMC, can be utilized to constrain the error at the origin in the error phase plane.

The equation of $\bar{\sigma}(\boldsymbol{e})$ which aids the control algorithm to switch from reaching phase to convergence phase, is defined as,

$$\bar{\sigma}(\boldsymbol{e}) = \begin{cases} \dot{e}_1 - |(-2\kappa e_1)^{0.5}| & \text{for } e_1 < 0, \\ \dot{e}_1 + |(2\kappa e_1)^{0.5}| & \text{otherwise.} \end{cases} \tag{4.30}$$

The value of parameter κ is selected based on the available control resources and system uncertainties and disturbances.

Reaching Phase Control Law

The first task of the controller is to drive the error states such that the system achieves $\bar{\sigma}(\boldsymbol{e}) = 0$ in finite time. To realize such condition, the control law can be represented by,

$$u = \frac{1}{g(\boldsymbol{x}(t))}[-f(\boldsymbol{x}(t)) + \dot{x}_{2d} - M_{\max} \operatorname{sgn}(\bar{\sigma}(\boldsymbol{e}))], \tag{4.31}$$

where the term $M_{\max}$ is selected such that $M_{\max} > h_{\max}$ with $\kappa = M_{\max} - h_{\max}$.

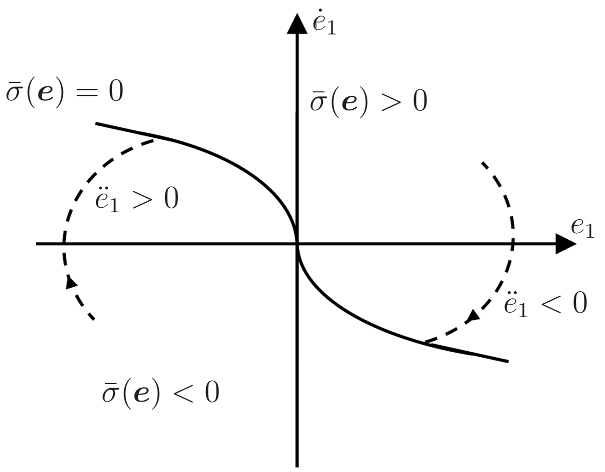

Figure 4.3: Reaching phase (dashed lines) of the error dynamics

Consider the following result obtained through twice differentiating (4.28),

$$\ddot{e}_1 = \dot{x}_2 - \dot{x}_{2d}. \tag{4.32}$$

Substituting (4.27) into (4.32) yields,

$$\ddot{e}_1 = f(\boldsymbol{x}(t)) + g(\boldsymbol{x}(t))u + h(\boldsymbol{x}(t)) - \dot{x}_{2d}. \tag{4.33}$$

Applying the control signal in (4.31) to (4.33) returns an expression for the acceleration of error state as,

$$\ddot{e}_1 = h(\boldsymbol{x}(t)) - M_{\max}\mathrm{sgn}(\bar{\sigma}(\boldsymbol{e})). \tag{4.34}$$

As $M_{\max} > h_{\max}$, the sign of $\ddot{e}_1$ in (4.34) is solely governed by $\mathrm{sgn}(\bar{\sigma}(\boldsymbol{e}))$. Hence, the error dynamics are now forced to evolve in a clockwise direction towards $\bar{\sigma}(\boldsymbol{e}) = 0$ as shown in Figure 4.3, under the influence of the control signal expressed in (4.31). The corresponding mathematical proof for finite time reaching can be found in [20].

Convergence Phase Control Law

On the first time the system reaches $\bar{\sigma}(\boldsymbol{e}) = 0$, the convergence phase starts and the control law switches to,

$$u = \frac{1}{g(\boldsymbol{x}(t))}[-f(\boldsymbol{x}(t)) + \dot{x}_{2d} + M(t)], \tag{4.35}$$

where $M(t)$ is the adaptive gain.

It is important to keep in mind that after entering the convergence phase, the control algorithm does not switch back to its previous stage until a new set-point is defined. In other words, the convergence phase control law is now responsible for driving the error states to the origin starting from their current position in the error phase plane.

Applying the control law in (4.35) to (4.33) returns,

$$\ddot{e}_1 = h(\boldsymbol{x}(t)) + M(t). \tag{4.36}$$

Set $t = 0$ when the convergence phase starts. Then for the convergence phase, the initial error states are $(e_1(0), \dot{e}_1(0))$ and the initial value of the gain is $M(0)$ determined as,

$$M(0) = \begin{cases} M_{\max} & \text{for } e_1(0) > 0, \\ -M_{\max} & \text{for } e_1(0) < 0. \end{cases} \tag{4.37}$$

Define the actual acceleration of the error state for a given sampling interval as,

$$\ddot{e}_1 = \kappa_m(t). \tag{4.38}$$

Therefore, the acceleration of the error state after the first sampling interval is

$$\ddot{e}_1 = \kappa_m(T), \tag{4.39}$$

where T is the sampling time. Accordingly, the following equation is obtained by integrating (4.39) twice with respect to time.

$$e_1(t) = \frac{\dot{e}_1^2(t)}{2\kappa_m(T)} - \frac{\dot{e}_1^2(0)}{2\kappa_m(T)} + e_1(0). \tag{4.40}$$

Substitution of the current coordinate of error states $(e_1(T), \dot{e}_1(T))$ into (4.40) produces the expression for $\kappa_m(T)$ as,

$$\kappa_m(T) = \frac{\dot{e}_1^2(T) - \dot{e}_1^2(0)}{2[e_1(T) - e_1(0)]}. \tag{4.41}$$

Using (4.36) and (4.39), $h(\boldsymbol{x}(t))|_{t=T}$ is given by,

$$h(\boldsymbol{x}(t))|_{t=T} = \kappa_m(T) - M(0). \tag{4.42}$$

Therefore, by substituting (4.41) into (4.42) $h(\boldsymbol{x}(t))$ can be estimated. This new result allows updating the control gain for the next cycle to accommodate system uncertainties and disturbances.

The controller is subsequently required to drive the error states from their current positions towards the origin in the error phase plane.

To define a parabola crossing the origin, the following equation can be used.

$$\dot{e}_1^2(t) = 2\kappa_c(t)e_1(t), \tag{4.43}$$

where $\kappa_c(t)$ denotes the acceleration of the error state. Therefore, the corresponding required value for $\kappa_c(t)$ which ensures convergence towards the origin becomes

$$\kappa_c(T) = \frac{\dot{e}_1^2(T)}{2e_1(T)}, \tag{4.44}$$

which is derived based on the current error states $(e_1(T), \dot{e}_1(T))$. It is also known that the value of $\kappa_c(T)$ is dependent on $h(\boldsymbol{x}(t))$ and $M(T)$ based on (4.36). Therefore, using the result obtained for $h(\boldsymbol{x}(t))|_{t=T}$ from (4.42) which is assumed not varying significantly for the next time interval, a second expression for $\kappa_c(T)$ can be derived as,

$$\kappa_c(T) = \kappa_m(T) - M(0) + M(T). \tag{4.45}$$

Hence, the adjusted gain $M(t)$ at $t = T$ that can enforce the system to achieve the acceleration of $\kappa_c(T)$ is obtained by rearranging (4.45) as,

$$M(T) = \kappa_c(T) - \kappa_m(T) + M(0). \tag{4.46}$$

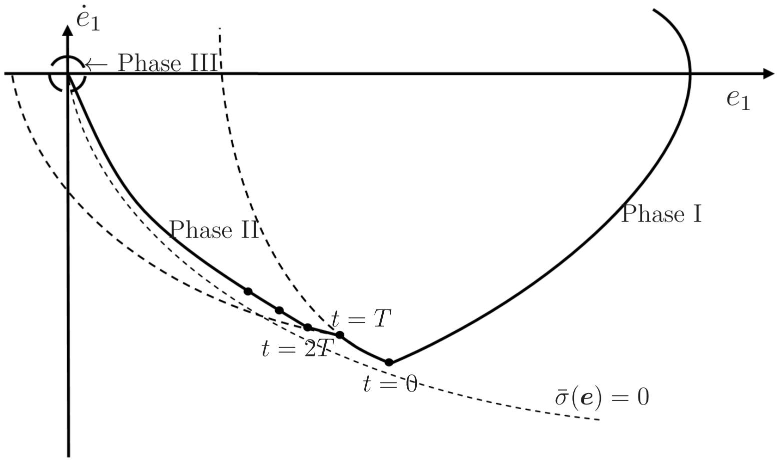

Figure 4.4: Gain adaptation mechanism during the convergence phase. The solid line represents the final path of the error states. [20]

This new gain $M(T)$ enforces the error states to the origin of error phase plane from its present position in a parabolic manner. As the value of $h(\boldsymbol{x}(t))$ varies with time, $M(t)$ is updated at each sampling time,

$$M(t) = \kappa_c(t) - \kappa_m(t) + M(t - T), \tag{4.47}$$

where, $t = kT$, $k \in \mathbb{Z}^+$,

$$\kappa_c(t) = \frac{\dot{e}_1^2(t)}{2e_1(t)}, \tag{4.48}$$

$$\kappa_m(t) = \frac{\dot{e}_1^2(t) - \dot{e}_1^2(t-T)}{2[e_1(t) - e_1(t-T)]}. \tag{4.49}$$

Now (4.37) and (4.47) to (4.49) successfully present the required values of the adaptive gain.

The control input presented in (4.35) enforces the error states to the origin of the error phase plane in finite time in a parabola-like path as shown in Figure 4.4. The dashed lines in Figure 4.4 depict possible trajectories of error dynamics if $M(t)$ is not adjusted to match the varying uncertainties. A continuous adjustment of $M(t)$ leads to a path similar to the solid line. The control methodology also restricts the system dynamics in the area bounded by $\bar{\sigma}(\boldsymbol{e}) = 0$ and the horizontal axis during the convergence phase as shown in Figure 4.4.

Once the error states arrive at the vicinity of the origin of error phase plane, a suitable robust control methodology can be applied to constrain the error states to the origin. To realize control of a space robot, the boundary SMC method is selected to hold the error states at the origin. Therefore, when system states satisfy the conditions $|e_1| < \mu_1$ and $|\dot{e}_1| < \mu_2$ (where μ_1 and μ_2 are small and positive), the control law switches to SMC to constrain the system to the origin of the error phase plane. Note that the switching should not cause any issue since the control torques calculated based on control laws for both phases are small due to small errors. The controller continues to operate in this stage until a set-point change occurs.

4.4.2 Application of the Controller to the Space Robot

The dynamic model of a space robot described in Section 4.2 has been successfully decoupled into $n+3$ separate subsystems by introducing a virtual control input vector $\boldsymbol{\tau}^\star$. Each resulting subsystem takes the form represented by (4.8) and (4.13), which makes the proposed adaptive variable structure algorithm directly applicable to both the spacecraft base and manipulator. Once the adaptive algorithm calculates the corresponding virtual control input vector $\boldsymbol{\tau}^\star$, the actual torque vector $\boldsymbol{\tau}$ can be unravelled by inverting the transformation of (4.12).

Let $\underline{\boldsymbol{f}}(\boldsymbol{e}, t)$ be the nominal system dynamics, i.e. $\underline{\boldsymbol{f}}(\boldsymbol{e}, t) = -\hat{\boldsymbol{A}}^{-1}\hat{\boldsymbol{B}}\,(\boldsymbol{e}_2 + \dot{\boldsymbol{q}}_d) - \ddot{\boldsymbol{q}}_d$, and $\underline{\boldsymbol{h}}(\boldsymbol{e}, t)$ be the overall uncertainties of the system. This transformation derives the i^{th} subsystem of the MIMO system represented by (4.50) and (4.51) of the same form as (4.26) and (4.27).

$$
\begin{aligned}
\dot{e}_{1i} &= e_{2i}, && (4.50)\\
\dot{e}_{2i} &= \underline{f}_i(\boldsymbol{e}, t) + \tau_i^\star + \underline{h}_i(\boldsymbol{e}, t). && (4.51)
\end{aligned}
$$

Similar to (4.30), set the corresponding expression for $\bar{\sigma}_i(\boldsymbol{e})$ be,

$$\bar{\sigma}_i(\boldsymbol{e}) = \begin{cases} \dot{e}_{1i} - |(-2\kappa_i e_{1i})^{0.5}| & \text{for } e_{1i} < 0, \\ \dot{e}_{1i} + |(2\kappa_i e_{1i})^{0.5}| & \text{otherwise.} \end{cases} \tag{4.52}$$

Control Law for Phase I

The controller will first impose the reaching phase control law on the system. Thus, the control law for Phase I takes the form,

$$\tau_i^\star = -\underline{f}_i - M_{\max_i}\ \mathrm{sgn}(\bar{\sigma}_i), \tag{4.53}$$

with,

$$\kappa_i = M_{\max_i} - \underline{h}_{\max_i}. \tag{4.54}$$

Theorem 4.3 Under the control law stated in (4.53), the system error dynamics reaches $\bar{\sigma}_i(\boldsymbol{e}) = 0$ in finite time.

Proof Substitution of (4.53) into (4.51) returns,

$$\ddot{e}_{1i} = \underline{h}_i - M_{\max_i}\mathrm{sgn}(\bar{\sigma}_i). \tag{4.55}$$

Combining (4.54) and (4.55), it can be concluded that,

$$\begin{cases} \ddot{e}_{1i} \leq -\kappa_i & \text{for } \sigma_i > 0, \\ \ddot{e}_{1i} \geq \kappa_i & \text{for } \sigma_i < 0. \end{cases} \tag{4.56}$$

Hence, for all initial conditions, the error states are forced to evolve in a clockwise direction in the error phase plane towards $\bar{\sigma}_i(\boldsymbol{e}) = 0$ with an acceleration of $|\ \ddot{e}_{1i}\ | \geq \kappa_i$ as shown in Figure 4.3. Once the system reaches $\bar{\sigma}_i(\boldsymbol{e}) = 0$, the control law switches to Phase II.

Control Law for Phase II

The control law for Phase II takes the form of

$$\tau_i^\star = -\underline{f}_i + M_i(t), \tag{4.57}$$

with

$$M_i(t) = \kappa_{ci}(t) - \kappa_{mi}(t) + M_i(t-T). \tag{4.58}$$

The values of $\kappa_{ci}(t)$ and $\kappa_{mi}(t)$ will be subjected to change based on (4.48) and (4.49).

Theorem 4.4 The control input presented in (4.57) drives the error states to the origin of the error phase plane.

Proof Set the Lyapunov candidate function as,

$$V = \frac{1}{2}e_{1i}^2 + \frac{1}{2}\dot{e}_{1i}^2. \tag{4.59}$$

Differentiating the Lyapunov function once yields,

$$\dot{V} = e_{1i}\dot{e}_{1i} + \dot{e}_{1i}\ddot{e}_{1i} = e_{1i}\dot{e}_{1i} + \dot{e}_{1i}\dot{e}_{2i}. \tag{4.60}$$

Substituting (4.51) into (4.60) returns,

$$\dot{V} = \dot{e}_{1i}[e_{1i} + \underline{f}_i + \tau_i^\star + \underline{h}_i]. \tag{4.61}$$

The following result can be obtained by substituting the convergence phase control law in (4.57) to (4.61).

$$\dot{V} = \dot{e}_{1i}[e_{1i} + \underline{h}_i + M_i(t)]. \tag{4.62}$$

As the control algorithm modifies its required acceleration $\kappa_{ci}(t)$ to match the estimated value of $\underline{h}_i(\boldsymbol{e}, t)$, (4.62) can be further simplified using (4.42) and (4.45) as,

$$\dot{V} = \dot{e}_{1i}[e_{1i} + \kappa_{ci}(t)]. \tag{4.63}$$

The value of $\kappa_{ci}(t)$ is modified at each sampling interval to satisfy (4.44). Thus, (4.63) can be rewritten as,

$$\begin{aligned}\dot{V} &= \dot{e}_{1i}(e_{1i} + \frac{\dot{e}_{1i}^2}{2e_{1i}}), \qquad (4.64)\\ \dot{V} &= \frac{\dot{e}_{1i}}{2e_{1i}}(2e_{1i}^2 + \dot{e}_{1i}^2). \qquad (4.65)\end{aligned}$$

As the convergence phase only occurs in the second or fourth quadrant of the error phase plane, the following equations

$$e_{1i}^2 > 0; \quad \dot{e}_{1i}^2 > 0; \quad \frac{\dot{e}_{1i}}{e_{1i}} < 0; \quad e_{1i} \neq 0, \qquad (4.66)$$

hold true for all $(e_{1i}, \dot{e}_{1i})$ in the second and fourth quadrants. Thus, according to Lyapunov stability theorem, $\dot{V} < 0$ is satisfied in the convergence phase, which leads to $e_{1i} \to 0$ and $\dot{e}_{1i} \to 0$ in finite time.

Control Law for Phase III

Once the error states are at the vicinity of the origin of error phase plane, the boundary layer SMC is utilized to constrain the error states. Thus, when system states are such that $|e_{1i}| < \mu_1$ and $|\dot{e}_{1i}| < \mu_2$, the following control input

$$\tau_i^\star = -\underline{f}_i - \underline{\lambda}_{ri}\dot{e}_{1i} - M_i \mathrm{sat}(\underline{\sigma}_i(\boldsymbol{e})), \qquad (4.67)$$

with $\underline{\sigma}_i(\boldsymbol{e}) = \underline{\lambda}_{ri}e_{1i} + \dot{e}_{1i}$ is applied to the system. The controller will continue to operate in Phase III until a new set-point is fed into the system. A new set-point would trigger the system back to Phase I and the relevant control laws would be applied again such that the system arrives at the desired states in a fast and robust manner. The control law presented in this section was aimed at controlling the i^{th} subsystem of the space robot. The same proposed algorithm with different control parameters can be utilized to expand the controller to all $n + 3$ subsystems.

It is worth to mention that the main advantage of the AVSC controller lies with individual set-point tracking. In the case of trajectory tracking, as the change of two adjacent desired states are really small, the proposed controller would continue to operate in Phase III. Thus, the controller would still be robust in trajectory tracking whereas the time advantages discussed cannot be seen since the set-point change is very small in trajectory tracking and the results will be similar to SMC.

4.5 Control in the Task Space

For many space missions, the desired hand trajectory is specified in the task space. Though the joint displacement can be uniquely determined by the desired hand position in the task space for a space robot system with an attitude controlled base, it cannot be accurately derived before the maneuvers, in that the mapping is dependent on system dynamic parameters which are not accurately known. That implies the performance of the end-effector's motion might be poor even the joints can follow their "desired" trajectory.

There are two methods that can better extend our controllers to the problems where control variables are specified in the task space. The first approach is to identify the unknown dynamic parameters and update the desired joint displacements intermittently. However, computational burden is increased due to system identification and two limitations arise, i.e. a persistent excitation function is required for the end-effector trajectory and the updating time is long [168].

As an alternative approach, the dynamic equation can be rewritten with respect to the end-effector motion and spacecraft attitude by involving system kinematics. Since the proposed control methods do not rely on parameter linearization which cannot be performed in the task space, the control laws can be consequently derived, provided that joint motions can be measured. The derived control laws, which take into account the difference between actual end-effector position and the desired end-effector trajectory, thus can guarantee the convergence of error states in the task space. The block diagrams of joint space control and task space control are illustrated in Figure 4.5 and Figure 4.6, respectively.

Next the dynamic model of a space robot in terms of motion in the task space is addressed in detail. Define a new control variable $\boldsymbol{X}$ to represent spacecraft attitude and space robot motion in the task space as $\boldsymbol{X} = [\boldsymbol{\Phi}_s^T, \boldsymbol{P}_e^T]^T$. The transformation

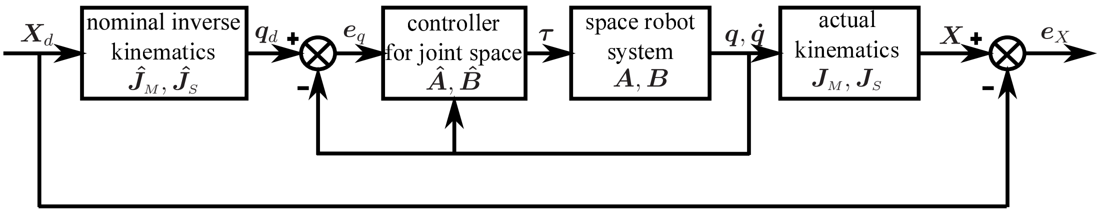

Figure 4.5: Block diagram of joint space control

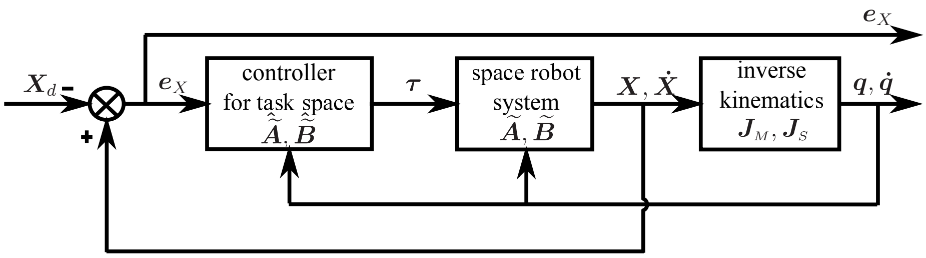

Figure 4.6: Block diagram of task space control

from $\boldsymbol{q}$ to $\boldsymbol{X}$ at velocity level can be obtained from (4.1) as,

$$\dot{\boldsymbol{X}} = \begin{bmatrix} \dot{\boldsymbol{\Phi}}_S \\ \dot{\boldsymbol{P}}_e \end{bmatrix} = \begin{bmatrix} \boldsymbol{O} & \boldsymbol{I} \\ \boldsymbol{J}_M & \boldsymbol{J}_S \end{bmatrix} \begin{bmatrix} \dot{\boldsymbol{\Phi}}_M \\ \dot{\boldsymbol{\Phi}}_S \end{bmatrix} = \widetilde{\boldsymbol{N}}\dot{\boldsymbol{q}}, \tag{4.68}$$

where $\boldsymbol{O} \in \mathbb{R}^{3\times n}$ is a zero matrix; $\boldsymbol{I} \in \mathbb{R}^{3\times 3}$ is an identity matrix; and

$$\widetilde{\boldsymbol{N}} = \begin{bmatrix} \boldsymbol{O} & \boldsymbol{I} \\ \boldsymbol{J}_M & \boldsymbol{J}_S \end{bmatrix}.$$

Differentiating (4.68) returns

$$\ddot{\boldsymbol{X}} = \dot{\widetilde{\boldsymbol{N}}}\dot{\boldsymbol{q}} + \widetilde{\boldsymbol{N}}\ddot{\boldsymbol{q}}. \tag{4.69}$$

Inverting (4.68) and (4.69) produces the transformation between the control variable in the joint space $\boldsymbol{q}$ and the control variable in the task space $\boldsymbol{X}$ at velocity level and acceleration level as follows:

$$\dot{\boldsymbol{q}} = \widetilde{\boldsymbol{N}}^{-1}\dot{\boldsymbol{X}}, \quad \ddot{\boldsymbol{q}} = \widetilde{\boldsymbol{N}}^{-1}\ddot{\boldsymbol{X}} - \widetilde{\boldsymbol{N}}^{-1}\dot{\widetilde{\boldsymbol{N}}}\widetilde{\boldsymbol{N}}^{-1}\dot{\boldsymbol{X}}. \tag{4.70}$$

Substituting (4.70) into (4.7) yields the dynamic equation with respect to the motion of the end-effector and spacecraft attitude as,

$$\boldsymbol{A}\widetilde{\boldsymbol{N}}^{-1}\ddot{\boldsymbol{X}} + \left(\boldsymbol{B}\widetilde{\boldsymbol{N}}^{-1} - \boldsymbol{A}\widetilde{\boldsymbol{N}}^{-1}\dot{\widetilde{\boldsymbol{N}}}\widetilde{\boldsymbol{N}}^{-1}\right)\dot{\boldsymbol{X}} = \boldsymbol{\tau}. \tag{4.71}$$

Let $\widetilde{\boldsymbol{A}} = \boldsymbol{A}\widetilde{\boldsymbol{N}}^{-1}$ and $\widetilde{\boldsymbol{B}} = \boldsymbol{B}\widetilde{\boldsymbol{N}}^{-1} - \boldsymbol{A}\widetilde{\boldsymbol{N}}^{-1}\dot{\widetilde{\boldsymbol{N}}}\widetilde{\boldsymbol{N}}^{-1}$. Equation (4.71) can be given by,

$$\widetilde{\boldsymbol{A}}\ddot{\boldsymbol{X}} + \widetilde{\boldsymbol{B}}\dot{\boldsymbol{X}} = \boldsymbol{\tau}. \tag{4.72}$$

Define a new error state vector $\widetilde{\boldsymbol{e}}$ as $\widetilde{\boldsymbol{e}}_1 = \boldsymbol{X} - \boldsymbol{X}_d,\ \widetilde{\boldsymbol{e}}_2 = \dot{\boldsymbol{X}} - \dot{\boldsymbol{X}}_d,\ \widetilde{\boldsymbol{e}} = [\widetilde{\boldsymbol{e}}_1^T, \widetilde{\boldsymbol{e}}_2^T]^T$, where $\boldsymbol{X}_d$ is the desired motion vector. Rearrange the dynamic equation (4.72) in state-space form as,

$$\dot{\widetilde{\boldsymbol{e}}}_1 = \widetilde{\boldsymbol{e}}_2, \tag{4.73}$$

$$\dot{\widetilde{\boldsymbol{e}}}_2 = -\widetilde{\boldsymbol{A}}^{-1}\widetilde{\boldsymbol{B}}\left(\widetilde{\boldsymbol{e}}_2 + \dot{\boldsymbol{X}}_d\right) - \ddot{\boldsymbol{X}}_d + \widetilde{\boldsymbol{A}}^{-1}\boldsymbol{\tau}. \tag{4.74}$$

The above dynamic equations prove to be of the same form as the dynamic model described in (4.8) and (4.9). Thus, the task space controller can be designed in the same way as the joint space controllers that have been presented in Section 4.3 and Section 4.4.

4.6 Simulation

The spacecraft carrying a three-link robotic manipulator with revolute joints as shown in Figure 4.7 is used in the simulations. The motion of the robotic manipulator causes spacecraft to deviate along roll, pitch and yaw axes in the body frame. Table 4.1 presents geometric parameters of the space robot system. The controller is aimed at controlling both manipulator motion and attitude of the spacecraft base whereas translation of the spacecraft base is left free.

The simulation mainly comprises three parts: 1) Comparison between set-point control performance of the system under three different controllers, i.e. smoothed SMC controller with constant gain M_i (CSMC), smoothed SMC controller with adaptive gain $\boldsymbol{k}_r = \boldsymbol{f}^{\star\star} + \boldsymbol{h}^{\star} + \boldsymbol{\alpha}_r$ (ASMC), and AVSC controller; 2) Comparison

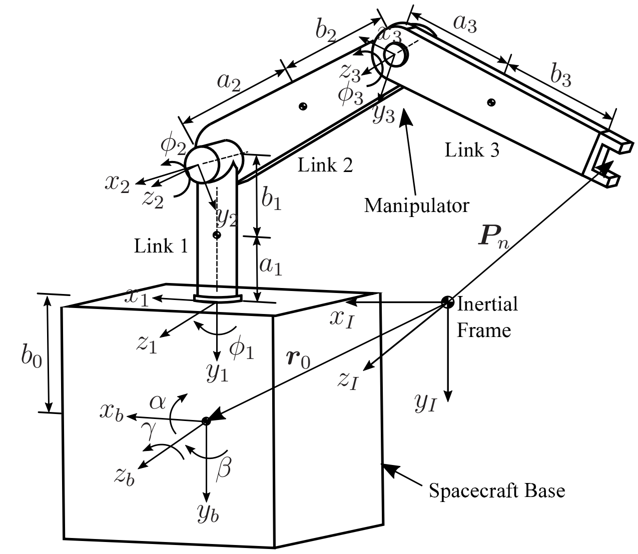

Figure 4.7: Space Robot: A three-link manipulator mounted on a spacecraft base

Table 4.1: Specifications of the three-link space robot

Body	Platform	Link1	Link2	Link3	RW
Mass(kg)	100	8	10	10	5
I_x(kg·m^2)	30	0.2	0.008	0.008	0.3
I_y(kg·m^2)	30	0.0064	0.8	0.8	0.3
I_z(kg·m^2)	30	0.2	0.8	0.8	0.3
a (m)	0.75	0.25	0.5	0.5	-
b (m)	0.75	0.25	0.5	0.5	-

Note: The specifications of RW represent the property of one reaction wheel and are same for roll, pitch and yaw axes.

between trajectory tracking control performance of the system under CSMC, ASMC and AVSC; 3) Comparison between indirect end-point control which is actually achieved by controlling joint motion (see Figure 4.5), and direct task space control (see Figure 4.6), with consideration of system uncertainties.

4.6.1 Set-Point Control

Suppose the space manipulator intends to perform a task which requires joint motion from $\mathbf{\Phi}_M(0) = [\phi_1(0), \phi_2(0), \phi_3(0)]^T = [50°, 65°, -105°]^T$ to $\mathbf{\Phi}_{Md} = [\phi_{1d}, \phi_{2d}, \phi_{3d}]^T = [60°, 60°, -120°]^T$. The space robot base with an initial attitude deviation $\mathbf{\Phi}_S(0) = [\alpha(0), \beta(0), \gamma(0)]^T = [-10°, 5°, 5°]^T$ is required to be re-oriented to the desired attitude $\mathbf{\Phi}_{Sd} = [0, 0, 0]^T$ and maintained there despite the disturbance generated by manipulator motion during the operation.

When selecting coefficients λ_{ri} for the sliding surfaces (4.10), small values are required in comparison to high frequencies of neglected dynamics in order to avoid exciting structural vibration. Based on the geometric features of a general error phase plane of SMC, it can be inferred that a larger λ_{ri} typically indicates shorter convergence phase to origin but longer reaching phase to the sliding surface. Define the settling condition such that the error states reach and remain within $|e_i| <= 0.05°, i = \alpha, \beta, \gamma, \phi_1, \phi_2, \phi_3$. The settling times of joint displacements and attitude angles based on different λ_{ri}s are shown in Figure 4.8. Such figures illustrate that with increasing value of λ_{ri}, all settling times (except settling time for joint 2, a larger extent of λ_{r2} results in the same trend) first decrease and then increase, in that with a smaller λ_{ri}, the time of convergence phase is dominant while the time of reaching phase becomes dominant with increasing λ_{ri}, leading to longer settling times.

It is worth mentioning that the strategy to save energy plays an important role in space missions. Thus total energy consumption of the system for this specific set-point regulation maneuver is calculated by $E_{\text{total}} = \int \sum_{i=1}^{3} (\tau_i \dot{\phi}_i + \tau_{wi} \dot{\phi}_{wi}) dt$ (efficiency of the motors is assumed to be same for system with different controllers and thus not included) and presented in Figure 4.9 in terms of different λ_{ri}s. The figure indicates that the total consumed energy first increases to its maximum value at $\mathbf{\Lambda}_r = \lambda_r \boldsymbol{I} = 2\ \boldsymbol{I}$ and then decreases. This variation is intuitively consistent with the trend of settling times presented in Figure 4.8 since shorter settling time typically implies more energy consumption. Practically, an appropriate value of $\mathbf{\Lambda}_r$ should lead to a trade-off between energy consumption and settling time under the premise that λ_{ri} is smaller than the frequency of unmodeled dynamics. In the following, to make a better comparison with the fast AVSC controller, λ_{ri} is determined to yield shortest settling times as $\lambda_{r1} = 4, \lambda_{r2} = 6, \lambda_{r3} = 4, \lambda_{r\alpha} = 2.5, \lambda_{r\beta} = 2.5, \lambda_{r\gamma} = 3.5$.

Robustness of the SMC controller with adaptive gains needs to be verified and the extent of uncertainty that could be accommodated by the proposed ASMC controller must be estimated since the adaptive gains are partially determined by

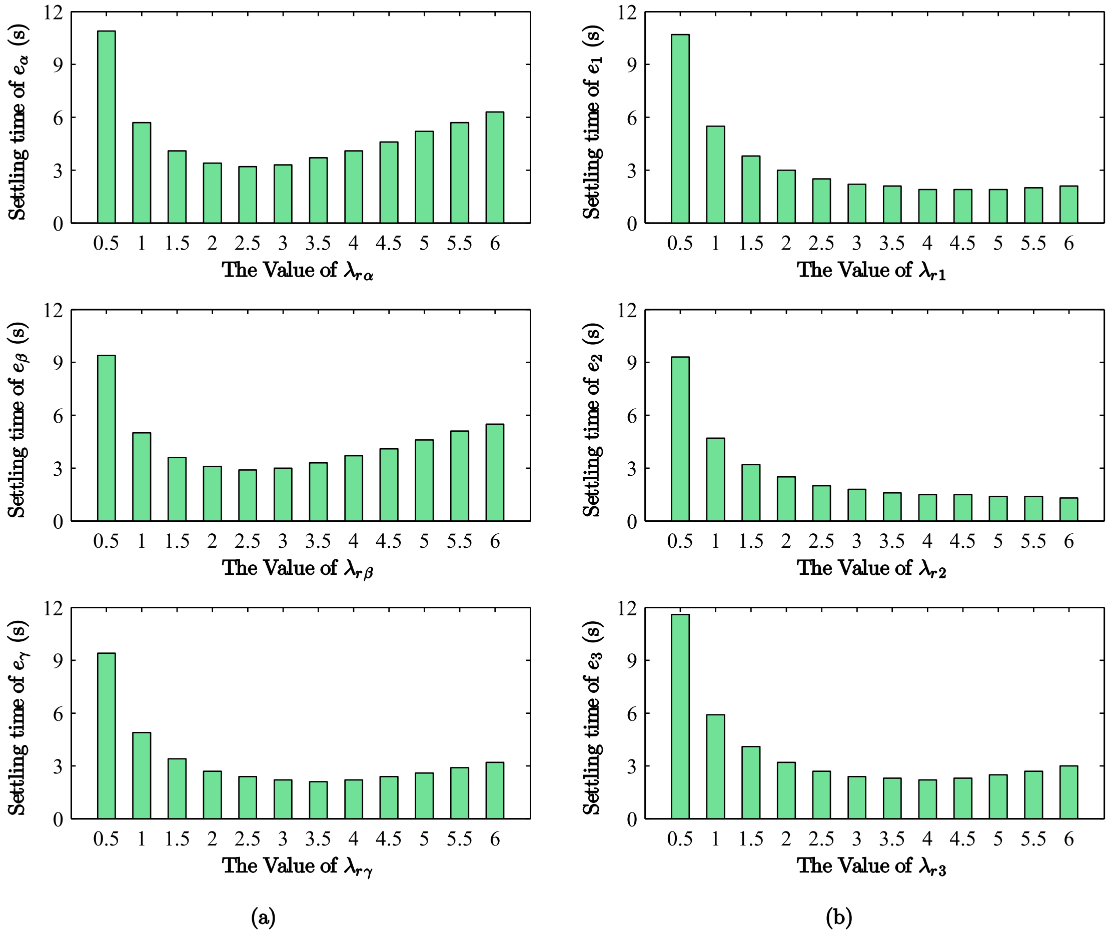

Figure 4.8: Settling time of the system under ASMC (SMC with adaptive gains) with different λ_{ri}s: (a) settling time of the spacecraft attitude and, (b) settling time of joint angles.

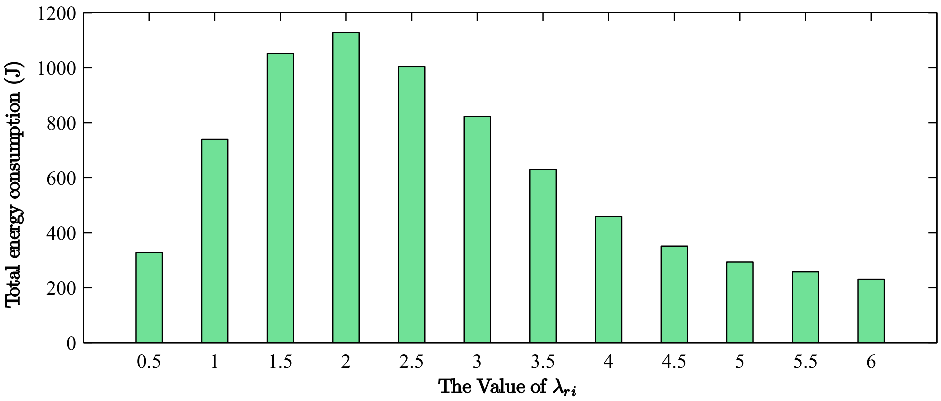

Figure 4.9: Total energy consumption

system uncertainties. In the controller of the simulation, nominal values of $\hat{\boldsymbol{A}}$ and $\hat{\boldsymbol{B}}$ were used. Actual matrices $\boldsymbol{A}$ and $\boldsymbol{B}$ used in the dynamic model of the simulation were set to several groups of values different from $\hat{\boldsymbol{A}}$ and $\hat{\boldsymbol{B}}$ to represent the system uncertainties. It turns out that when $\boldsymbol{\Delta A}$ (defined in (4.18)) and $\boldsymbol{\Delta B} = ||\boldsymbol{B}|| - ||\hat{\boldsymbol{B}}||$ are within $||\boldsymbol{\Delta A}|| \leq 0.13||\hat{\boldsymbol{A}}||$ and $||\boldsymbol{\Delta B}|| \leq 0.13||\hat{\boldsymbol{B}}||$ the system performance is convergent, which means 13% uncertainty can be accommodated. Set $\boldsymbol{A} = 1.1\hat{\boldsymbol{A}}$, $\boldsymbol{B} = -0.95\hat{\boldsymbol{B}}$, which has been proven that such setup of uncertainties can also be accommodated by AVSC.

Table 4.2: Control parameters for CSMC, ASMC and AVSC

Description	Parameter	Value
Constant gains for CSMC	$M_{\phi_1} = M_{\phi_2} = M_{\phi_3}$	0.25
	$M_\alpha = M_\beta = M_\gamma$	0.2
Positive scalar in k_{ri} of ASMC	$\alpha_{ri},\ i = \phi_1, \phi_2, \phi_3, \alpha, \beta, \gamma$	0.001
Maximum gains for AVSC	$M_{\max_{\phi_1}} = M_{\max_{\phi_2}} = M_{\max_{\phi_3}}$	0.2
	$M_{\max_\alpha} = M_{\max_\beta} = M_{\max_\gamma}$	0.15
Sliding manifold parameter	$\lambda_{c1} = \lambda_{r1} = \underline{\lambda}_{r1}$	4
CSMC: λ_{ci}	$\lambda_{c2} = \lambda_{r2} = \underline{\lambda}_{r2}$	6
ASMC: λ_{ri}	$\lambda_{c3} = \lambda_{r3} = \underline{\lambda}_{r3}$	4
AVSC: $\underline{\lambda}_{ri}$	$\lambda_{c\alpha} = \lambda_{r\alpha} = \underline{\lambda}_{r\alpha}$	2.5
	$\lambda_{c\beta} = \lambda_{r\beta} = \underline{\lambda}_{r\beta}$	2.5
	$\lambda_{c\gamma} = \lambda_{r\gamma} = \underline{\lambda}_{r\gamma}$	3.5
Positive scalar to define system bounds for ASMC	$\bar{\pi}$	0.1
	$\bar{a}_1 = \bar{b}_1 = \bar{c}_1$	0.9
	$\bar{a}_2 = \bar{b}_2 = \bar{c}_2$	1.1
Boundary layer thickness	$\varepsilon_{ri},\ i = \phi_1, \phi_2, \phi_3, \alpha, \beta, \gamma$	0.1

Next the system performance under different controllers, including CSMC, ASMC and AVSC, is investigated. The three controllers are applied to the same

Table 4.3: Comparison of settling times for CSMC, ASMC and AVSC

Error state	CSMC	ASMC	AVSC	time improvement of ASMC over CSMC	time improvement of AVSC over CSMC
e_α	3.68 s	3.20 s	2.42 s	13.04%	34.24%
e_β	2.54 s	2.86 s	1.68 s	-11.19%	33.86%
e_γ	2.40 s	2.08 s	1.74 s	13.33%	27.50%
e_1	3.54 s	1.90 s	2.40 s	46.33%	32.20%
e_2	2.52 s	1.24 s	1.82 s	50.79%	27.78%
e_3	4.68 s	2.14 s	2.68 s	54.27%	42.74%

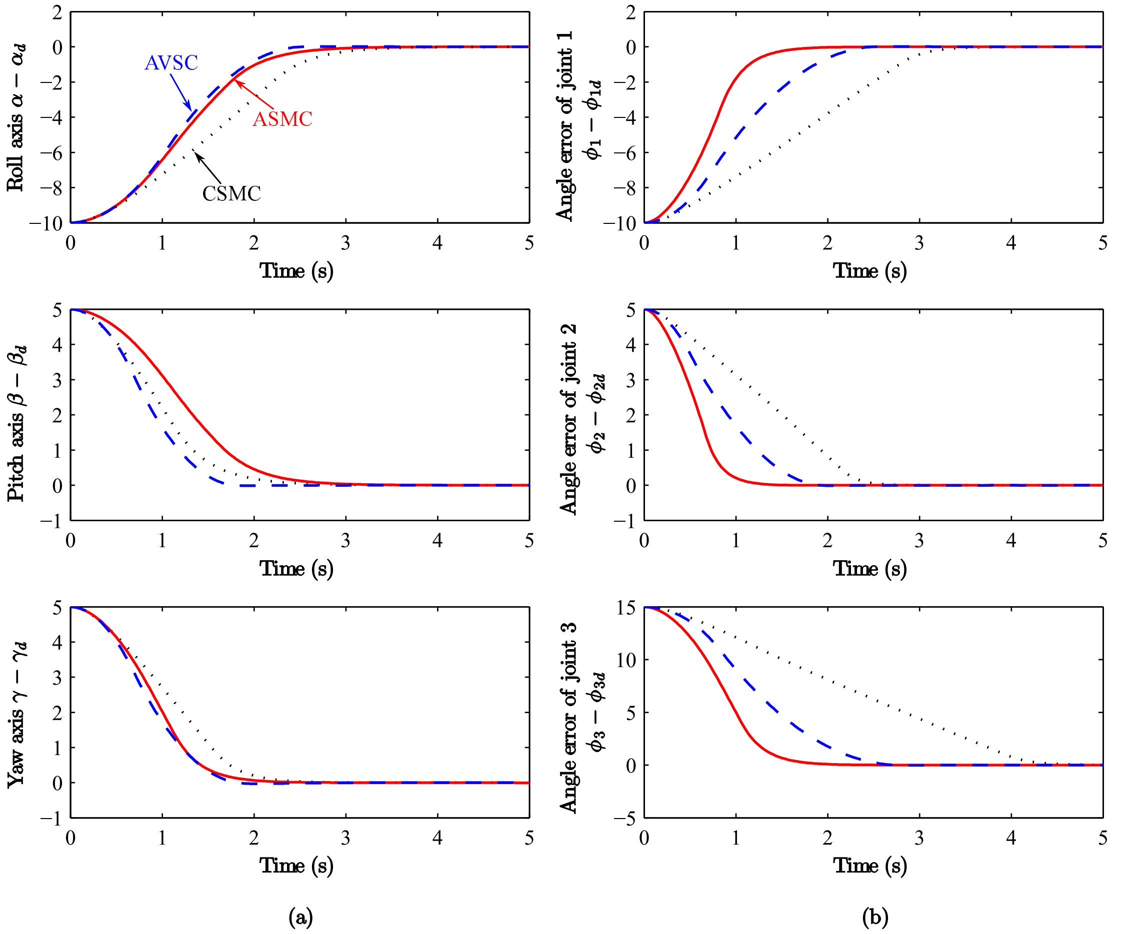

Figure 4.10: Stability of error states under CSMC (dotted lines), ASMC (solid lines) and AVSC (dashed lines): (a) spacecraft attitude regulation error and, (b) robot arm joint angle regulation error, all shown in degrees.

system under identical circumstances addressed in the first paragraph of this section. Specific control parameters utilized for the controllers are given in Table 4.2. It is important to note that the gradients of the sliding surfaces for CSMC and ASMC were selected such that they can deliver fastest possible settling times. The results are presented from Figure 4.10 to Figure 4.13.

Figure 4.10 depicts how the initial error states of the spacecraft attitude and robot manipulator joints settle to 0 under the application of CSMC, ASMC and AVSC so that the three approaches can be compared. In comparison to CSMC, ASMC and AVSC achieve to deliver faster convergence of the error states except for the pitch-axis channel. The deteriorated performance of settling time of e_β can be acceptable in that the extent of pitch-axis control torque under ASMC is smaller than that of CSMC. In fact, an exactly same extent of control torques in all channels is difficult to achieve since the system is strongly coupled. Table 4.3 presents the percentage time improvement for ASMC and AVSC in contrast to CSMC in each control channel.

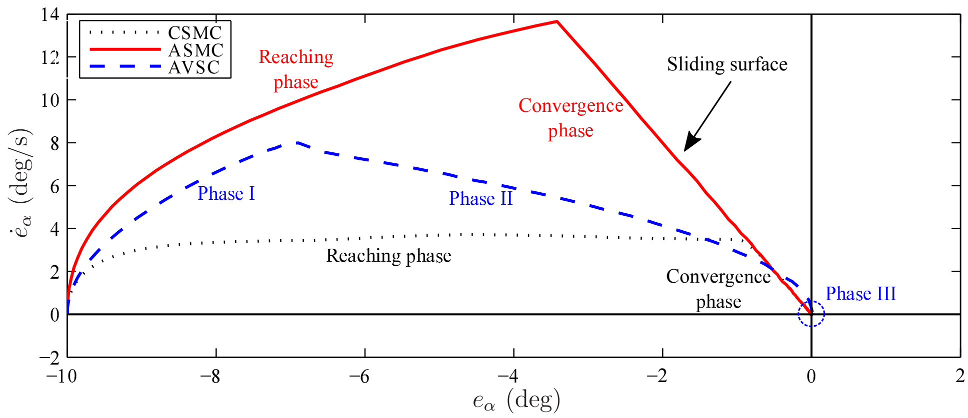

Figure 4.11: Error phase plane for spacecraft roll angle α under CSMC (dotted line), ASMC (solid line) and AVSC (dashed line)

Figure 4.11 illustrates how the error state for the spacecraft roll angle α evolves in the error phase plane under the three different methods. The CSMC and ASMC methods enforce the error state sliding on a same sliding surface. ASMC consumes more time for the convergence phase; however, a shorter reaching phase of ASMC which exceeds the extra time for its convergence phase finally leads to a shorter settling time than that of CSMC. The figure also illustrates that the AVSC method drives the error state in a natural parabola-like trajectory which results in improved convergence time.

Figure 4.12 depicts how the adaptive gain changes for the entire settling period. Different from CSMC which has a constant gain for each channel, the control gains of ASMC adapt according to the knowledge of system states and uncertainties. The AVSC controller first utilizes its maximum values of the control gains to reach the end of Phase I; once in Phase II the gains start to adapt to match system uncertainties so that the error states evolve in a parabolic manner.

The final control torque inputs to the system are presented in Figure 4.13. The torque values derived by the three control methods are kept within similar ranges by using the designated control parameters presented in Table 4.2. The torques

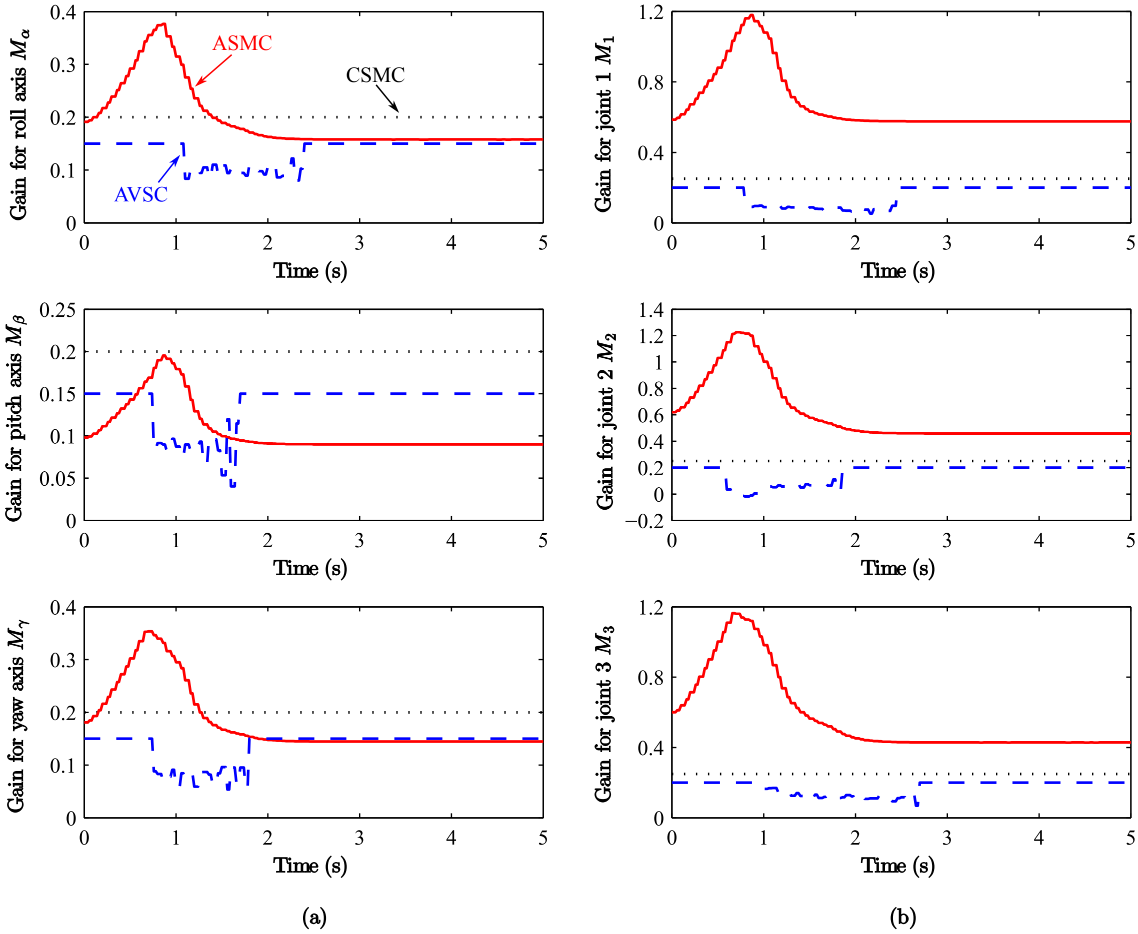

Figure 4.12: Gain variation under CSMC (dotted lines), ASMC (solid lines) and AVSC (dashed lines): (a) spacecraft attitude regulation gain and, (b) robot arm joint angle regulation gain.

under CSMC asymptotically go to zero as the system moves towards its desired values, whereas the control torques of ASMC tend to converge to a non-zero value initially and then react faster with a torque change than that of CSMC to damp the error states. For the AVSC methodology, it focuses on maintaining a constant torque (therefore a constant acceleration of error) throughout instead of reducing the torque to a smaller value as that of CSMC. Thus, compared with the conventional CSMC method, the proposed controllers are able to produce superior settling times.

4.6.2 Trajectory Tracking

In this section, the performance of the three-link space robot system for trajectory-tracking control in joint space is studied. The desired joint motions and

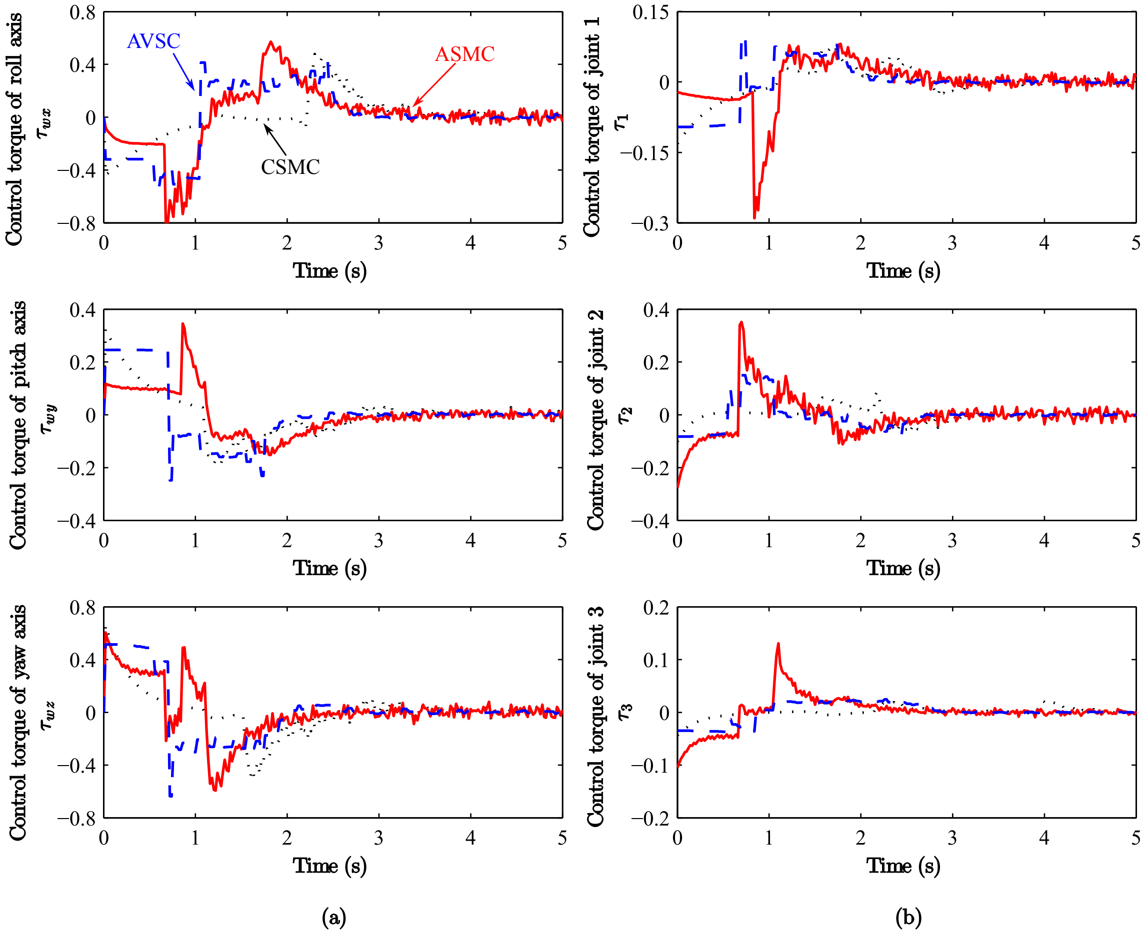

Figure 4.13: Control torque inputs for the six channels under CSMC (dotted lines), ASMC (solid lines) and AVSC (dashed lines): (a) reaction-wheel torques for attitude regulation along roll axis τ_{wx}, pitch axis τ_{wy} and yaw axis τ_{wz}, and (b) control torques of joint 1 τ_1, joint 2 τ_2 and joint 3 τ_3, all shown in N·m.

the desired attitude for the space robot are given in Figure 4.14. The trajectories of joint angles are chosen smooth in the sense that the maneuver can be implemented physically and the functions $\phi_{1d}(t)$, $\phi_{2d}(t)$, $\phi_{3d}(t)$ are twice differentiable. Referring to [169], a polynomial is introduced to describe the desired trajectory as,

$$\boldsymbol{q}_d(t) = \boldsymbol{q}_d(t_0) + \left(15t_n^4 - 6t_n^5 - 10t_n^3\right)\left(\boldsymbol{q}_d(t_0) - \boldsymbol{q}_d(t_f)\right), \tag{4.75}$$

where $\boldsymbol{q}_d(t_0)$ is the initial state and $\boldsymbol{q}_d(t_0) = \boldsymbol{q}(0) = [5^\circ, -5^\circ, 10^\circ, 0, 0, 0]^T$, $\boldsymbol{q}_d(t_f)$ represents the desired final configuration, $t_n = t/t_f$, t represents the elapsed time, t_f represents the total motion time and $t_f = 30$ s. The spacecraft is aimed at being controlled at its initial orientation despite the disturbance induced when the manipulator follows the desired joint trajectories.

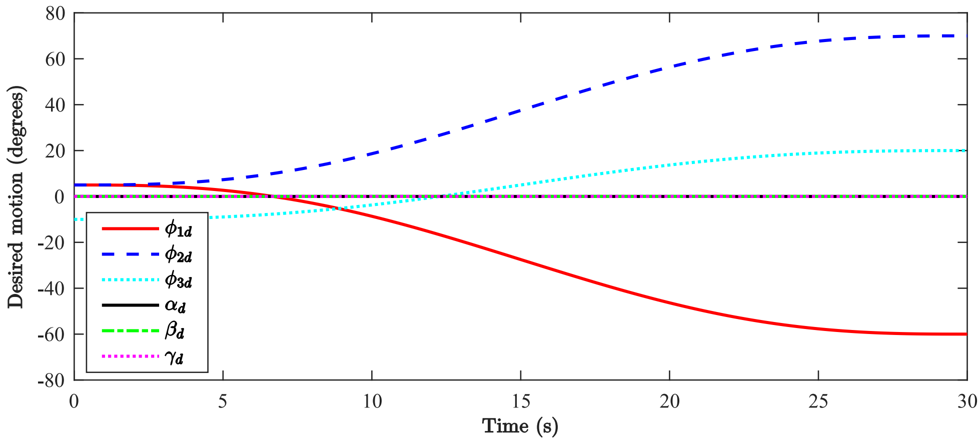

Figure 4.14: Desired motion of the space robot

In the simulation model, the values of $\boldsymbol{A}$ and $\boldsymbol{B}$ are set in the same conditions as addressed for the set-point control case to represent system uncertainties. Since the AVSC controller is constrained in Phase III in the case of trajectory tracking and as such performs in a same way as CSMC, the maximum gains of AVSC are determined with same values as those constant gains of CSMC, i.e. $M_{\phi_1} = M_{\phi_2} = M_{\phi_3} = M_{\max_{\phi_1}} = M_{\max_{\phi_2}} = M_{\max_{\phi_3}} = 0.25$, $M_\alpha = M_\beta = M_\gamma = M_{\max_\alpha} = M_{\max_\beta} = M_{\max_\gamma} = 0.15$. Other control parameters for CSMC, ASMC and AVSC remain same as presented in Table 4.2.

The simulated course of postural change of the three-link space robot under ASMC during the operation is illustrated in Figure 4.15. Specific simulation results of trajectory tracking under CSMC, ASMC and AVSC are presented from Figure 4.16 to Figure 4.18. The plots for CSMC and AVSC are overlapped which verifies the statement that AVSC delivers the same performance as CSMC because of the small change of the set points in trajectory tracking case.

Figure 4.16 depicts the change of the error state for each channel. The tracking errors of joint angles are maintained within small values and simultaneously, the spacecraft is controlled at the desired attitude with high accuracy (10^{-3}, 10^{-5}, and 10^{-2} in degrees for roll, pitch and yaw axes, respectively) under all the controllers. With similar extent of control outputs for each channel, the ASMC controller produces smaller tracking errors.

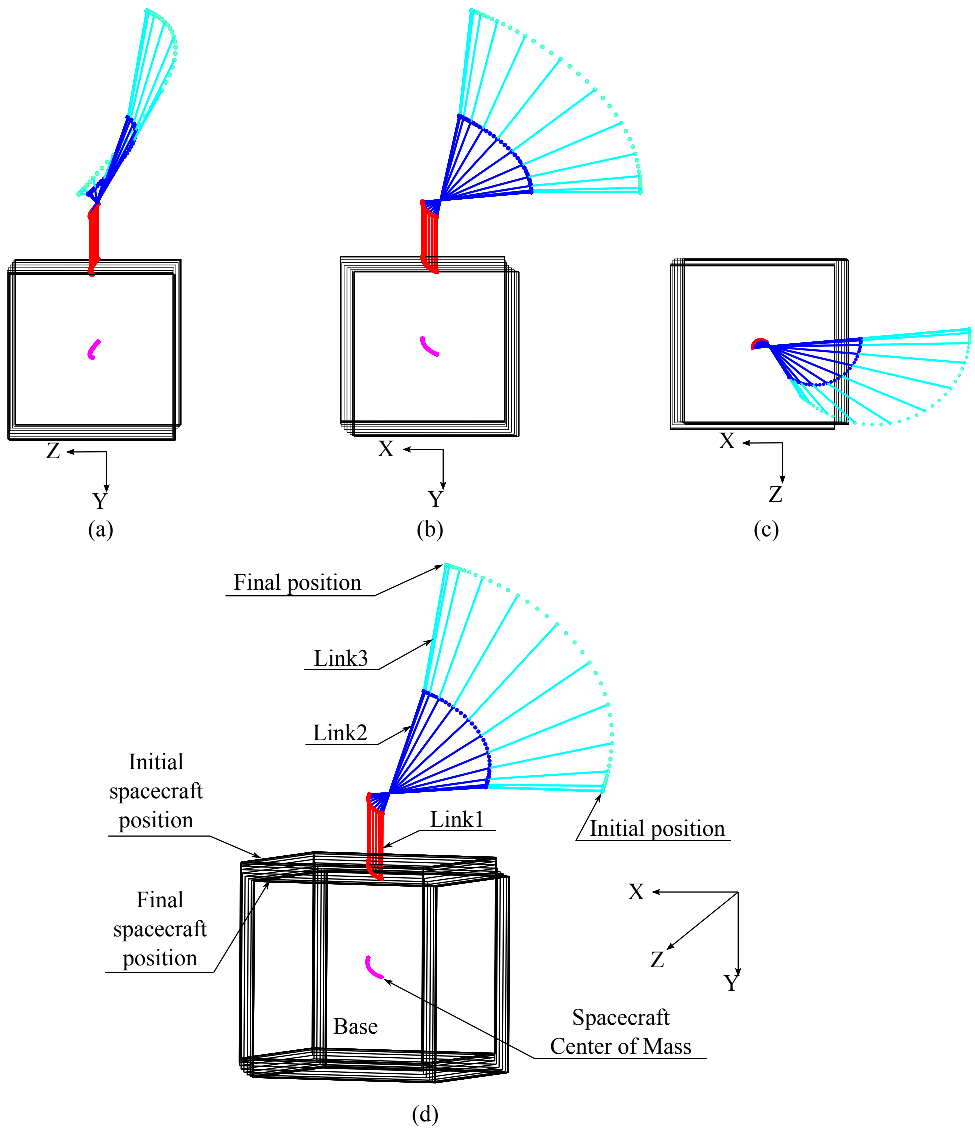

Figure 4.15: Course of postural change in different views: (a) Y-Z view, (b) X-Y view, (c) X-Z view and, (d) 3D view.

Figure 4.17 shows that the gains of ASMC adapt based on system states. However, the control outputs of ASMC trace same shapes as those of CSMC and AVSC in Figure 4.18 despite small difference when magnifying the plots, in that the magnitude of error states which determines the adaptive gains are kept within small range during the trajectory tracking operation.

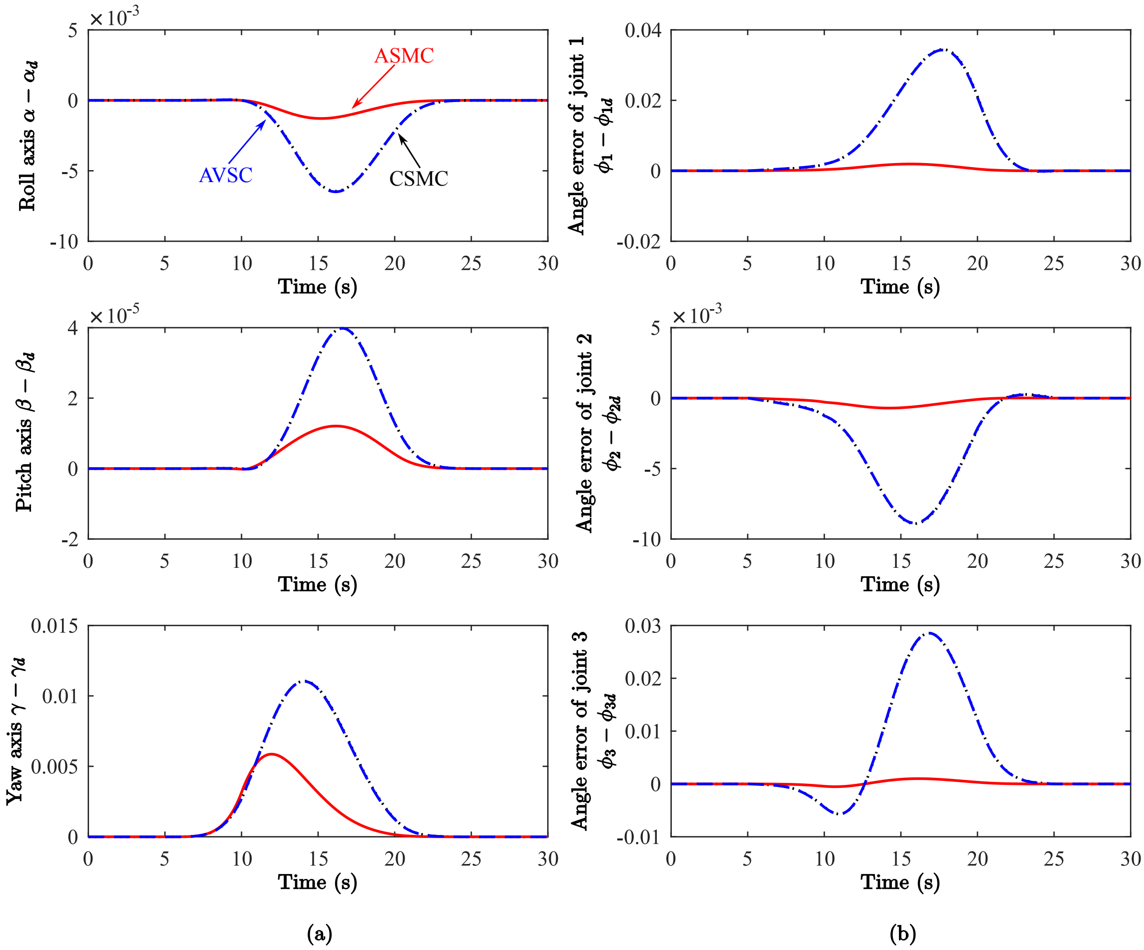

Figure 4.16: Stability of error states under CSMC (dotted lines), ASMC (solid lines) and AVSC (dashed lines): (a) spacecraft attitude regulation error and, (b) robot arm joint angle tracking error, all shown in degrees.

4.6.3 Task Space Control

The task space control methodology developed based on the dynamic equations (4.73) and (4.74) is verified in this section. This direct inertial-space control method, which utilizes the information of the error states of end-effector position (see Figure 4.6), is compared with the indirect end-point control method which assumes accurate system model and fulfils the task by controlling joint motions (see Figure 4.5). Two different kinds of scenarios are set to illustrate the comparison of system performance under direct and indirect end-point control methods: 1) the system model is actually known *a priori* or can be identified, and 2) system uncertainties are taken into account. It is worth noticing that the control laws take the form of CSMC to avoid inducing different conditions for the two

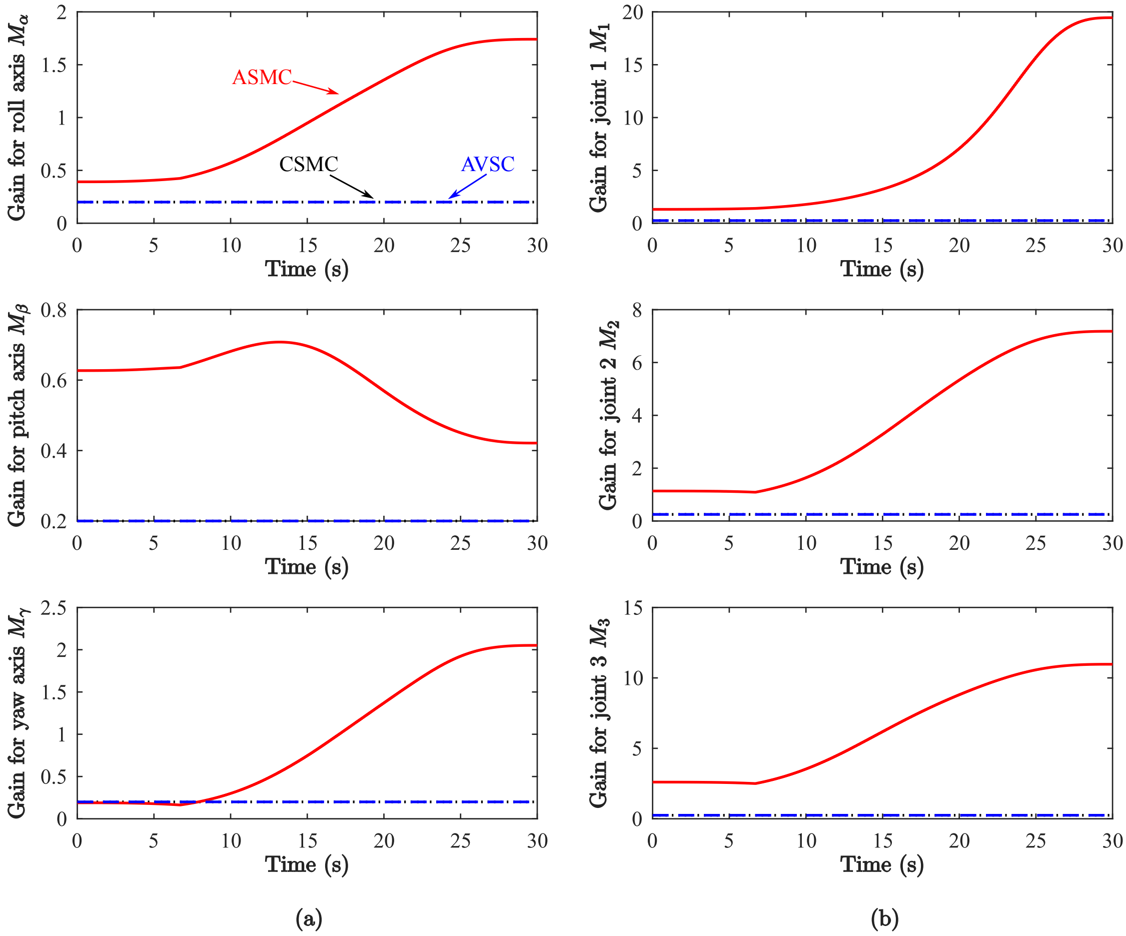

Figure 4.17: Gain variation under CSMC (dotted lines), ASMC (solid lines) and AVSC (dashed lines): (a) spacecraft attitude regulation gain and, (b) robot arm joint angle tracking gain.

control strategies and thus guarantee exactly identical conditions in each scenario. Specifications of the scenarios are given in Table 4.4. At the initial state, $\boldsymbol{\Phi}_M(0) = [5°, 5°, -10°]^T$, $\boldsymbol{\Phi}_S(0) = [0°, 0°, 0°]^T$ and $\boldsymbol{P}_e(0) = [-1.8297, -0.9854, 0.1601]^T$ m. The spacecraft is required to be maintained at its initial orientation while tracking a desired trajectory of the end-effector shown in Figure 4.19.

Figure 4.20 and Figure 4.21 present the attitude regulation error of the base and trajectory tracking error of the end-effector in terms of the two scenarios. Figure 4.20 shows that both control methods can precisely control the spacecraft attitude and end-effector position when the system model is accurate. However, when taking into account of system uncertainties, the indirect end-point control method leads to a large trajectory tracking error of the end-effector position with a magnitude

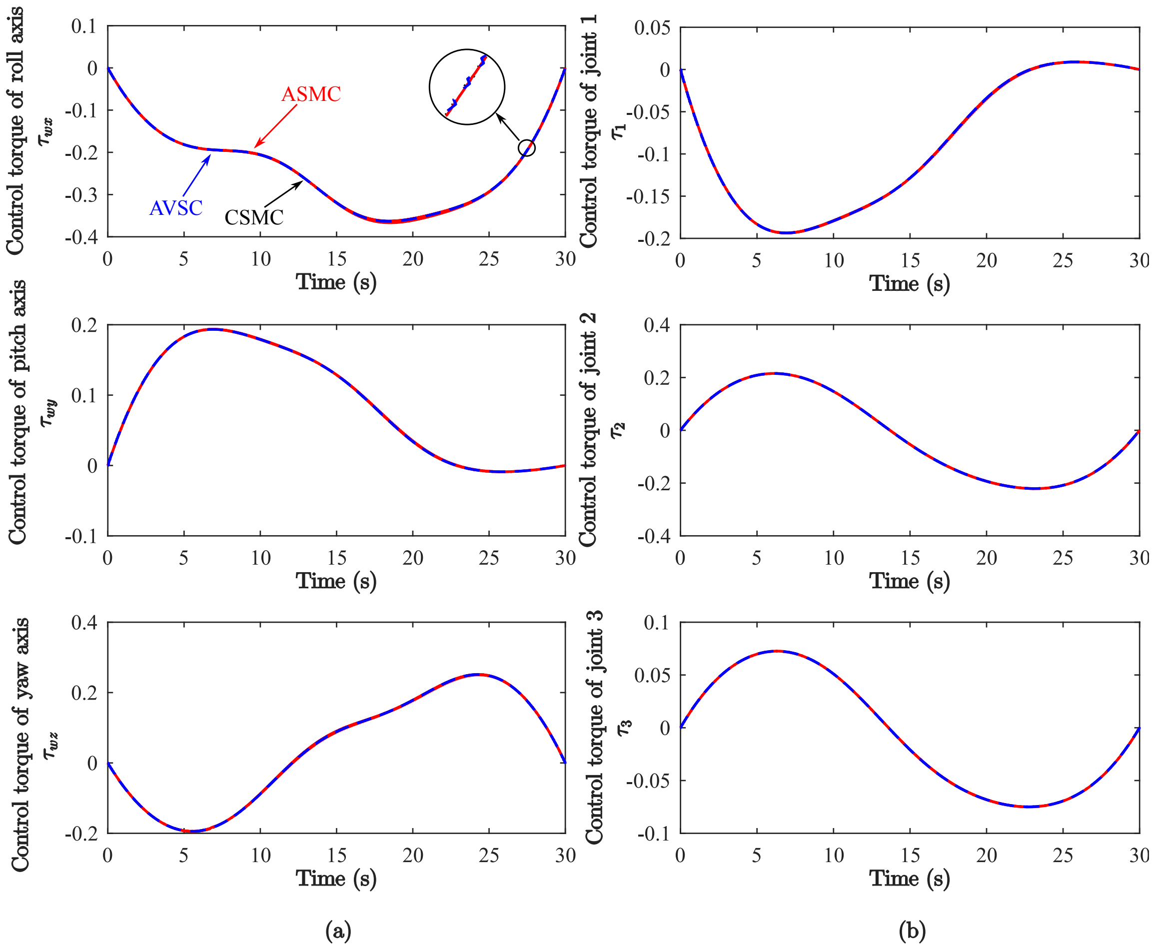

Figure 4.18: Control torque inputs for the six channels under CSMC (dotted lines), ASMC (solid lines) and AVSC (dashed lines): (a) reaction-wheel torques for attitude regulation along roll axis τ_{wx}, pitch axis τ_{wy} and yaw axis τ_{wz}, and (b) control torques of joint 1 τ_1, joint 2 τ_2 and joint 3 τ_3, all shown in N·m.

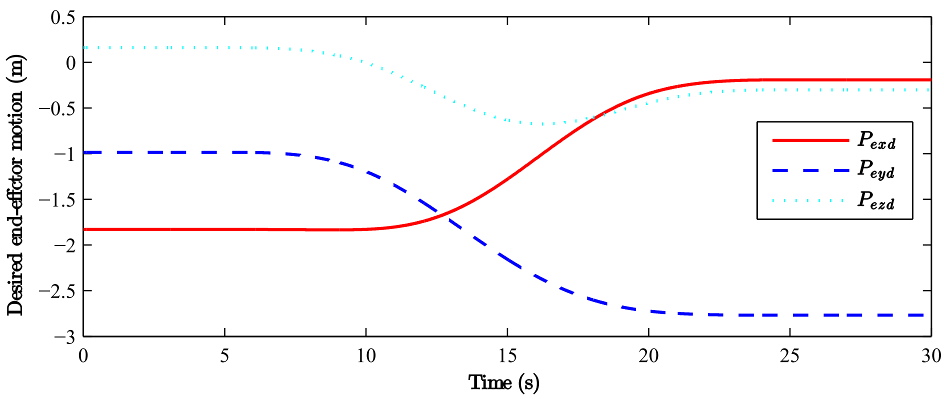

Figure 4.19: Desired trajectory of the end-effector

Table 4.4: Conditions of the scenarios

	Scenario 1 Accurate system model	Scenario 2 System with uncertainties
Inertia matrix (joint-space-based model)	$\boldsymbol{A} = \hat{\boldsymbol{A}}$	$\boldsymbol{A} = 1.03\hat{\boldsymbol{A}}$
Nonlinear terms (joint-space-based model)	$\boldsymbol{B} = \hat{\boldsymbol{B}}$	$\boldsymbol{B} = 1.03\hat{\boldsymbol{B}}$
Jacobian matrix	$\boldsymbol{J}_M = \hat{\boldsymbol{J}}_M,\ \boldsymbol{J}_S = \hat{\boldsymbol{J}}_S$	$\boldsymbol{J}_M = 1.03\hat{\boldsymbol{J}}_M,\ \boldsymbol{J}_S = 0.97\hat{\boldsymbol{J}}_S$
Coefficient matrix (inertial-space based model)	$\widetilde{\boldsymbol{A}} = \boldsymbol{A}\widetilde{\boldsymbol{N}}^{-1},\ \hat{\widetilde{\boldsymbol{A}}} = \hat{\boldsymbol{A}}\widetilde{\boldsymbol{N}}^{-1}$	
Nonlinear terms (inertial-space based model)	$\widetilde{\boldsymbol{B}} = \boldsymbol{B}\widetilde{\boldsymbol{N}}^{-1} - \boldsymbol{A}\widetilde{\boldsymbol{N}}^{-1}\dot{\widetilde{\boldsymbol{N}}}\widetilde{\boldsymbol{N}}^{-1}$ $\hat{\widetilde{\boldsymbol{B}}} = \hat{\boldsymbol{B}}\widetilde{\boldsymbol{N}}^{-1} - \hat{\boldsymbol{A}}\widetilde{\boldsymbol{N}}^{-1}\dot{\widetilde{\boldsymbol{N}}}\widetilde{\boldsymbol{N}}^{-1}$	

Note: The matrices with an over-hat sign $(\hat{\cdot})$ represent their nominal values and those without the sign represent the actual values.

of centre-meters as shown in Figure 4.21. To this end, direct inertial-space control is necessary if high accuracy end-effector control is required. The trajectory of the end-effector is illustrated in Figure 4.22.

4.7 Summary

This chapter has elaborated a dynamic model for a Free-Flying Space Robot (FFSR) with specifically designated actuators, i.e. Reaction Wheels (RWs), which includes the contribution of reaction-wheel momentum to the entire system. The derived Multiple-Input Multiple-Output system model was decoupled into multiple single-input subsystems using a diagonalization method. Different robust controllers that can coordinate the robot arm motions and the spacecraft attitude, including the Sliding Mode Control method with constant gains (CSMC), the Sliding Mode Control method with adaptive gains (ASMC) and the Adaptive Variable Structure Control (AVSC) method were developed. All the controllers were tested on a three-link space robot and the performance under each controller was compared. Numerical simulation results have illustrated that under the condition that the control torques are kept in similar ranges, ASMC and AVSC methods are able to reduce the settling times for the error states of the space robot in comparison to CSMC while ensuring robustness in set-point control. ASMC presents shorter settling times than CSMC and ASVC for the trajectory tracking case.

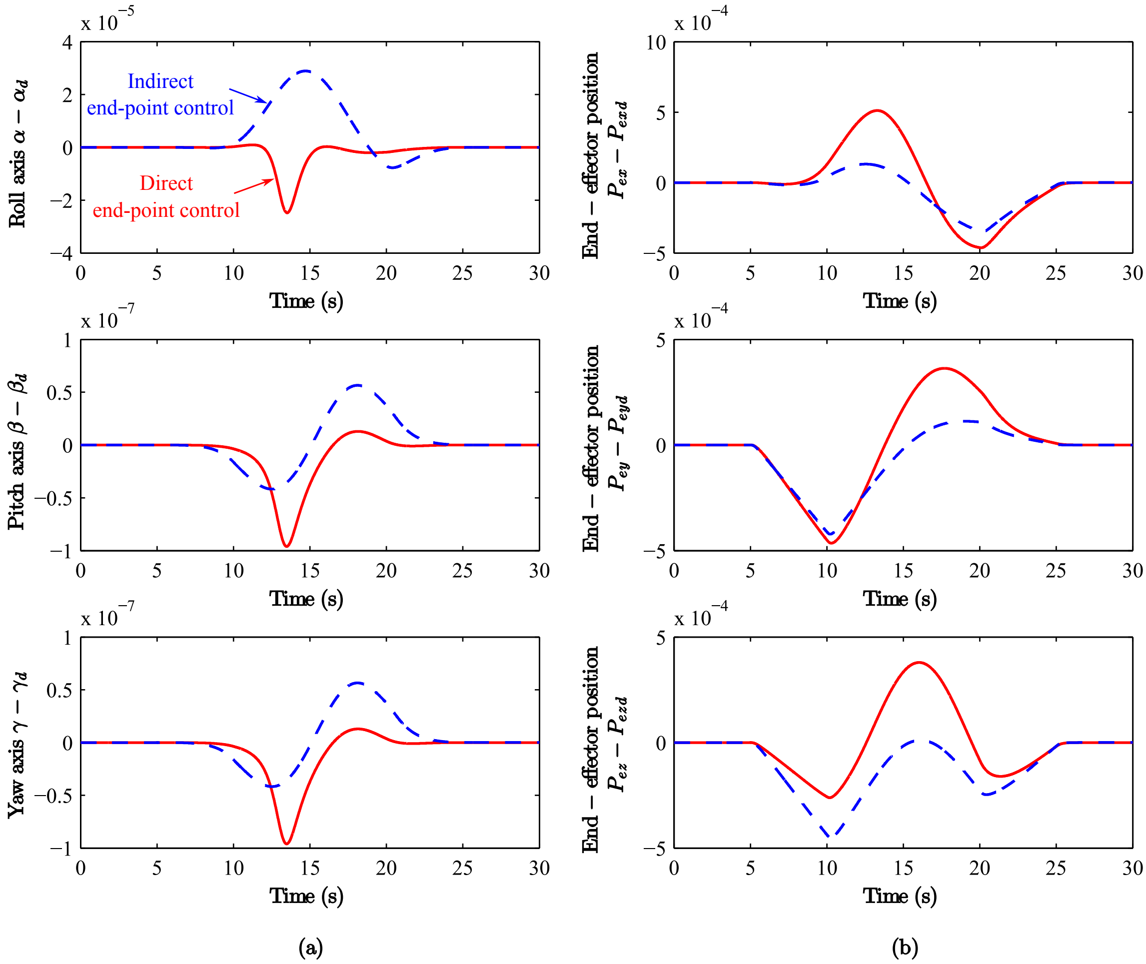

Figure 4.20: Trajectory tracking error of the space robot based on joint space control (dashed lines) and task space control (solid lines), with accurate dynamics (Scenario 1): (a) attitude regulation error shown in degrees, and (b) trajectory tracking error of the end-effector shown in meters.

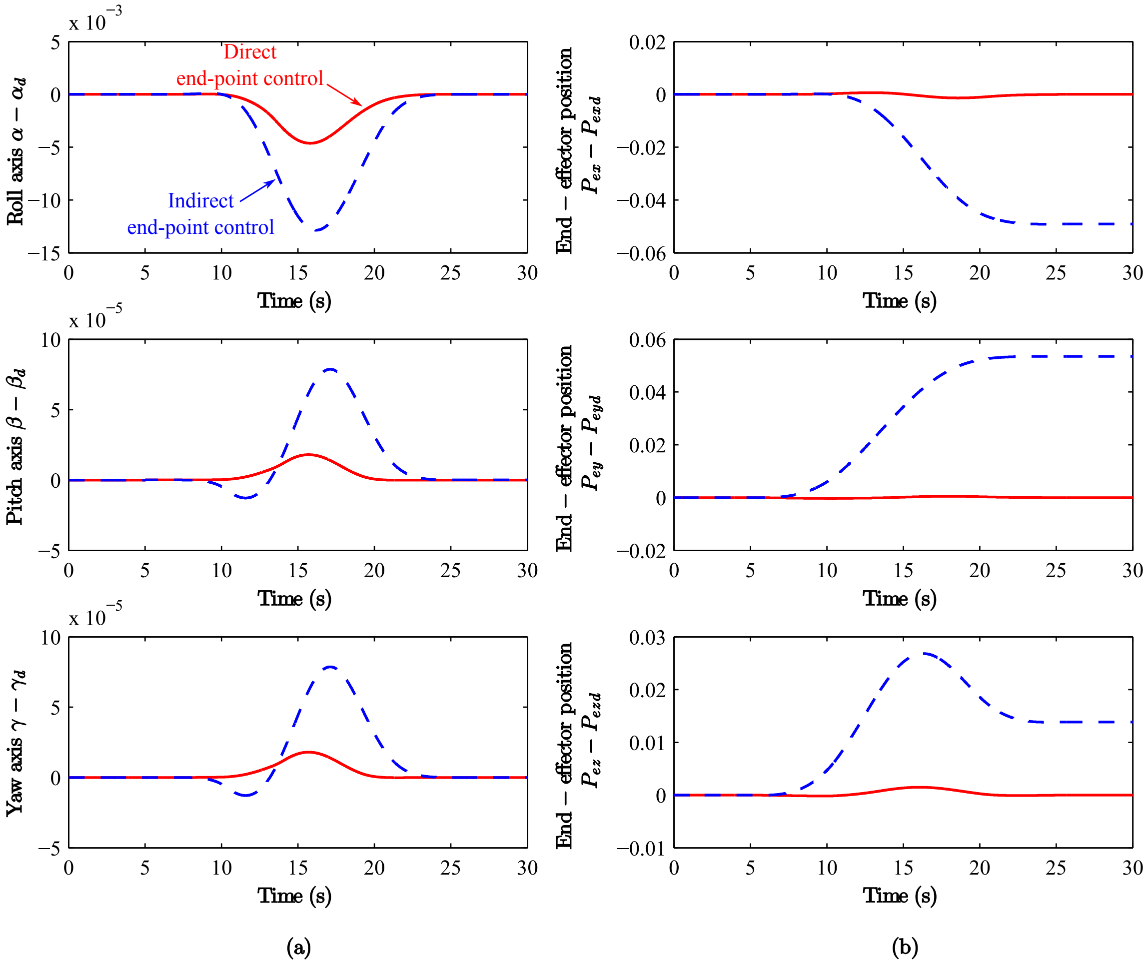

Figure 4.21: Trajectory tracking error of the space robot based on joint space control (dashed lines) and task space control (solid lines), with consideration of system uncertainties (Scenario 2): (a) attitude regulation error shown in degrees, and (b) trajectory tracking error of the end-effector shown in meters.

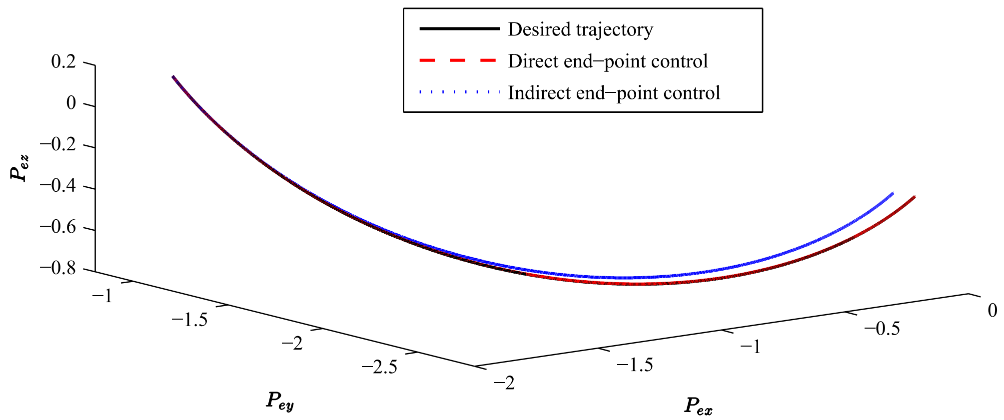

Figure 4.22: Trajectory of the end-effector

Chapter 5

Force Control of a Space Robot

5.1 Introduction

In an on-orbit assembly mission where Free-Flying Space Robots (FFSRs) are used to capture structural components and assemble them into a large space structure, physical contact between the FFSR's End-Effector (EE) and the target component is required. Two types of contact can be involved in a capture operation. One is the practiced *closed-contact* where the capture is achieved by forming a physical enclosure around a grapple fixture of the target before making contact. Such entrapping manner requires bulky infrastructure. To avoid orbiting bulky infrastructure which is very expensive, the target can be captured in an *open-contact* way such as using a gripper-link EE. In an open-contact capture operation, the generated contact forces have to be controlled so as to avoid losing the target or exerting excessive forces that may cause damage to the contacting bodies.

Chapter 4 has dealt with motion control of a space robot with no external forces for the approaching phase. In this chapter, a fundamental approach is taken to address the development of a control algorithm that can be applied to handle both the space robot motion and the contact forces for the capture phase when the space robot comes in open contact with a passive space object.

The majority of the work presented in the literature addressed maintaining of contact between the EE and a target. In this work the existing approaches are improved further by designing controllers that will not only maintain the contacts, but also will track the desired forces. The study can contribute to delicate space tasks, such as in-space screw-driving. By adopting the commonly used canonical-form dynamic model of a space robot as found in the literature, force tracking may be achieved, but a desired orientation of the spacecraft cannot be guaranteed. To solve this problem, the dynamic equations of the space manipulator and the spacecraft base are established separately to form basis for separate contact-force control and base attitude control. A hybrid controller, which incorporates the consistent motion between FFSR's EE and the tumbling floating target, is developed to track the designated motion of FFSR while ensuring a desired contact force. The spacecraft attitude is simultaneously regulated using Reaction Wheels (RWs). The Sliding Mode Control method developed in Chapter 4 is applied to the system to detumble the target and to stabilize the entire system for post-capture phase. Two examples, including an FFSR-Target contact example and a specific on-orbit screw-driving example are used to demonstrate effectiveness of the controllers by numerical simulations.

The chapter is organized with six sections. Section 5.2 details the contact scenario and introduces mathematical model of the system, including model of the floating target to be captured, model of the chaser FFSR and the contact dynamic model between the FFSR's EE and the target. A hybrid force and motion controller is proposed in Section 5.3. Also in the same section attitude control for the spacecraft base is addressed. Section 5.4 presents how to control the entire system in post-capture phase. Simulation results of a three-link planar FFSR in contact with a tumbling target and a four-link FFSR driving a screw into a floating target are presented in Section 5.5. Section 5.6 closes this chapter.

5.2 Model Description

In a scenario where a chaser FFSR interacts with a passive target, the FFSR and the target constitute the entire system. The system can be considered as a whole to take advantage of its conservation properties, since in such a way the contact forces/torques perform as internal forces/torques. Consequently, the inertial frame can be made to locate at the Center of Mass (CM) of the entire system (FFSR plus target) without translation throughout the contact operation. Such a definition for the inertial frame can simplify the representation of motion parameters.

However, in fact there is no fixed physical constraint between the FFSR's EE and the target for the contact operation prior to their rigid connection. Under the condition of maintaining a contact, the passive target has a trend to float away from the FFSR and may be tumbled due to the generated forces and/or torques. In addition, the disturbed spacecraft base due to manipulator's motion conversely affects EE's motion and subsequently the contact. Thus, the manipulator must be actively controlled to follow the target motion and to achieve an appropriate EE orientation to apply the interacting forces required for a specific assembly operation. To this end, construction of separate coordinate frames for the space robot and the target is necessary and transformation between the frames plays an essential role in motion analysis.

Therefore, in this section, frame description and some assumptions are clarified in 5.2.1 before proceeding with the presentation of system models, including model of the passive target presented in Section 5.2.2, model of the space robot presented in Section 5.2.3 and contact dynamic model presented in Section 5.2.4.

5.2.1 Coordinate Frames and Assumptions

The development of the methodology described in this chapter is based on following basic assumptions.

1. The FFSR consists of a spacecraft base and an open-chain manipulator mounted on it. The system is assumed to only include rigid bodies, as shown in Figure 5.1. Specific assumptions of the space robot hold same as detailed in Assumption 1 and Assumption 2 of Section 4.2.1.

2. Negligible external forces/torques exert on the entire system. Thrust jets are not fired during the operation, instead only RWs are utilized to regulate the attitude of the spacecraft base.

3. The operations are performed in close proximity after completion of the

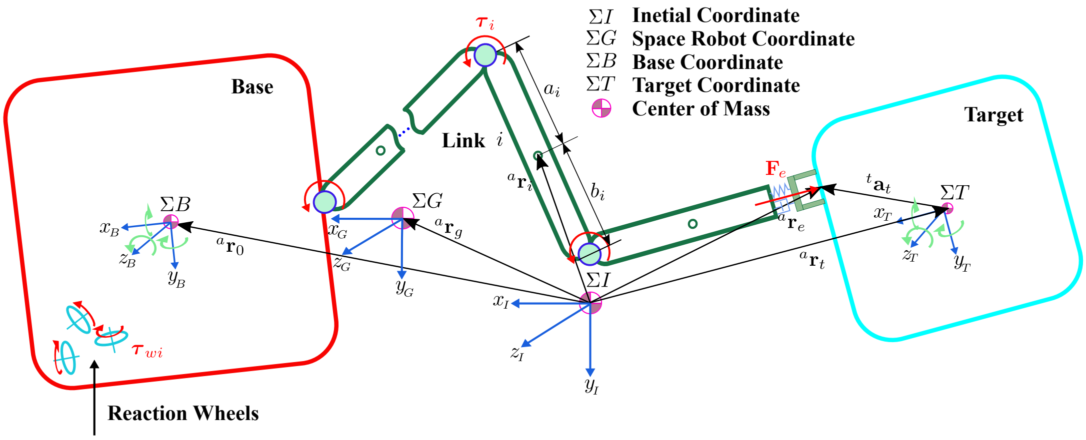

Figure 5.1: Model of an FFSR capturing a floating target

rendezvous process and thus orbital mechanics is neglected.

4. The target stays within the workspace of the FFSR by setting an appropriate initial configuration for the space robot and defining an achievable contact operation.

5. The properties of the target and its motion can be measured or estimated [170–173].

6. Initially, the FFSR's EE is positioned at the prescribed contact point in a proper orientation without exerting contact forces to the target. The entire system stays stationary before performing the contact operation.

7. The net contact force is assumed to localize at a contact point and can be measured using force/torque sensor mounted between the compliant wrist and the EE. The contact between the EE and the target is perfectly rigid except the compliance concentrated on the wrist. This assumption is to focus the research on robot control and to avoid dealing with sensory technique and complicated contact dynamics which belong to research areas that have been studied by many other researchers.

Throughout this chapter, ${}^t\{\cdot\}$ and ${}^a\{\cdot\}$ represent variables expressed in the target frame and in the inertial frame, respectively. The symbols appearing in Figure 5.1 are defined as follows:

${}^{a}\boldsymbol{r}_e \in \mathbb{R}^3$	position of the EE
${}^{a}\boldsymbol{r}_t \in \mathbb{R}^3$	position of CM of the target
${}^{t}\boldsymbol{a}_t \in \mathbb{R}^3$	constant position vector of the contact point located on the target surface with respect to (w.r.t.) the CM of the target
$\tau_i \in \mathbb{R}^1$	control torque of joint i
	generalized joint torques $\boldsymbol{\tau}_J = [\tau_1, \tau_2, \cdots, \tau_n]^T \in \mathbb{R}^n$
$\tau_{wi} \in \mathbb{R}^1$	control torque of the i^{th} RW
	attitude regulation torques $\boldsymbol{\tau}_w = [\tau_{wx}, \tau_{wy}, \tau_{wz}]^T \in \mathbb{R}^3$
$\boldsymbol{F}_e \in \mathbb{R}^3$	contact forces between the EE and the target
$\boldsymbol{\tau}_e \in \mathbb{R}^3$	external torques applied to the EE by the target

5.2.2 Target Model

The target is modeled as a single rigid body and its dynamic equation is developed based on the Newton-Euler method.

$$ {}^{t}\boldsymbol{I}_t \, {}^{t}\dot{\boldsymbol{\omega}}_t + {}^{t}\boldsymbol{\omega}_t \times {}^{t}\boldsymbol{I}_t \, {}^{t}\boldsymbol{\omega}_t = {}^{t}\boldsymbol{\tau}_t, \tag{5.1} $$

where ${}^{t}\boldsymbol{I}_t$ and ${}^{t}\boldsymbol{\omega}_t$ are the inertia matrix and inertial angular velocity of the target, respectively; ${}^{t}\boldsymbol{\tau}_t$ is the external torques applied on the target and ${}^{t}\boldsymbol{\tau}_t = {}^{t}\boldsymbol{\tau}_e + {}^{t}\boldsymbol{\tau}_{tf}$. ${}^{t}\boldsymbol{\tau}_{tf}$ represents the tumbling torques generated by a possible bias contact force and can be approximately calculated by ${}^{t}\boldsymbol{\tau}_{tf} = {}^{t}\boldsymbol{a}_t \times {}^{t}\boldsymbol{F}_e$ assuming that the contact point of $\boldsymbol{F}_e$ remains same during the operation. All variables in (5.1) are expressed in the target frame.

Quaternion parameters are adopted to represent attitude of the target to avoid singularity issues. The derivative of the quaternion vector relates to the angular acceleration by,

$$ \dot{\boldsymbol{q}}_t = \begin{bmatrix} \dot{\boldsymbol{\varepsilon}}_t \\ \dot{\eta}_t \end{bmatrix} = \frac{1}{2} \begin{bmatrix} \eta_t \boldsymbol{I} + \boldsymbol{S}(\boldsymbol{\varepsilon}_t) \\ -\boldsymbol{\varepsilon}_t^T \end{bmatrix} \dot{\boldsymbol{\omega}}_t, \tag{5.2} $$

where $\boldsymbol{q}_t$ denotes quaternion parameters of the target and $\boldsymbol{q}_t = [q_{t1}, q_{t2}, q_{t3}, q_{t4}]^T$; $\boldsymbol{\varepsilon}_t = [q_{t1}, q_{t2}, q_{t3}]^T$, $\eta_t = q_{t4}$ and $\boldsymbol{\varepsilon}_t^T \boldsymbol{\varepsilon}_t + \eta_t^2 = 1$; $\boldsymbol{I} \in \mathbb{R}^{3\times 3}$ is an identity matrix. The rotation matrix from the inertial frame to the target frame $\boldsymbol{R}_a^t$ can be expressed as,

$$\boldsymbol{R}_a^t = \boldsymbol{R}_a^t(\boldsymbol{q}_t) = \left(\eta_t^2 - \boldsymbol{\varepsilon}_t^T \boldsymbol{\varepsilon}_t\right) \boldsymbol{I} + 2\boldsymbol{\varepsilon}_t \boldsymbol{\varepsilon}_t^T - 2\eta_t \boldsymbol{S}(\boldsymbol{\varepsilon}_t), \tag{5.3}$$

and conversely the rotation matrix from the target frame to the inertial frame is $\boldsymbol{R}_t^a = (\boldsymbol{R}_a^t)^T$.

Based on Assumption 7, the directly measured contact force/torque is actually a value along a fixed vector in the target frame. Accordingly, ${}^t\boldsymbol{F}_e$ can be used to estimate translation of the target as,

$${}^a\boldsymbol{r}_t = \int_0^t \int_0^t \frac{{}^a\boldsymbol{F}_e}{m_t} dtdt = \int_0^t \int_0^t \frac{\boldsymbol{R}_t^a \; {}^t\boldsymbol{F}_e}{m_t} dtdt, \tag{5.4}$$

where m_t is the target mass.

5.2.3 Space Robot Model

Space Robot Kinematics

As addressed at the beginning of this section, origin of the inertial frame is fixed at CM of the entire system rather CM of the space robot. Therefore, when constructing the dynamic model for an FFSR, the motion of the entire system in the inertial frame needs to be considered, in that the contact forces/torques exerted at the EE are external forces/torques in terms of the FFSR and make the velocity of the entire system a non-zero value. However, it is not an easy task to compute the motion of the entire system by solely analyzing the FFSR dynamics due to the time-varying configuration of this multi-body system. Instead, a momentum conservation law under the premise of Assumption 2 can be applied to the entire system (FFSR plus target) to estimate the motion of the entire system by using target motion.

Angular momentum $\boldsymbol{H}_f$ or linear momentum $\boldsymbol{P}_f$ of the entire system, can be divided into two parts, i.e. momentum of the FFSR ($\boldsymbol{H}_{SR}$ for angular momentum or $\boldsymbol{P}_{SR}$ for linear momentum) and momentum of the target ($\boldsymbol{H}_t$ for angular momentum or $\boldsymbol{P}_t$ for linear momentum). The initial momentum of the entire system yields zero as stated in Assumption 6. $\boldsymbol{H}_f$ and $\boldsymbol{P}_f$ take the following form:

$$\begin{aligned}
\boldsymbol{H}_f &= \boldsymbol{H}_{SR} + \boldsymbol{H}_t = \sum_{i=0}^{n+3} ({}^a\boldsymbol{I}_i\ {}^a\boldsymbol{\omega}_i + {}^a\boldsymbol{r}_i \times m_i\ {}^a\boldsymbol{v}_i) + ({}^a\boldsymbol{I}_t\ {}^a\boldsymbol{\omega}_t + {}^a\boldsymbol{r}_t \times m_t\ {}^a\boldsymbol{v}_t) = \boldsymbol{0}, \\
\boldsymbol{P}_f &= \boldsymbol{P}_{SR} + \boldsymbol{P}_t = \sum_{i=0}^{n+3} m_i\ {}^a\boldsymbol{v}_g + m_t\ {}^a\boldsymbol{v}_t = \boldsymbol{0},
\end{aligned} \tag{5.5}$$

where all the angular momentums are defined with respect to the origin of the inertial coordinate; and m_i, ${}^a\boldsymbol{I}_i$, ${}^a\boldsymbol{\omega}_i$, ${}^a\boldsymbol{v}_i$, ${}^a\boldsymbol{r}_i$ denotes mass, inertia matrix, angular velocity, linear velocity and position vector of the robot base ($i = 0$), robot links ($i = 1, 2, \cdots, n$), RWs ($i = n+1, n+2, n+3$) and target ($i = t$), respectively. Assuming the motion of the robot links, spacecraft base and target can be measured or calculated, the motion of the entire system, including its linear velocity $\boldsymbol{v}_g$ and angular velocity $\boldsymbol{\omega}_g$ then can be deduced from (5.5) in combination with the expression of $\boldsymbol{v}_i$ and $\boldsymbol{\omega}_i$ as presented in (B.12) and (B.13).

Since both position and orientation of the EE are crucial for the capture phase, the linear velocity of the EE $\boldsymbol{v}_e$ and its angular velocity $\boldsymbol{\omega}_e$ are presented in the following based on joint motion of the manipulator, attitude of the spacecraft base and motion of the entire system as,

$$\boldsymbol{E}_e = \begin{bmatrix} \boldsymbol{v}_e \\ \boldsymbol{\omega}_e \end{bmatrix} = \boldsymbol{J}_E \dot{\boldsymbol{q}} + \begin{bmatrix} \boldsymbol{v}_g \\ \boldsymbol{\omega}_g \end{bmatrix} = \boldsymbol{J}_E \dot{\boldsymbol{q}} + \boldsymbol{E}_g, \tag{5.6}$$

where $\boldsymbol{E}_e = [\boldsymbol{v}_e^T, \boldsymbol{\omega}_e^T]^T \in \mathbb{R}^{6\times 1}$ is the velocity of the EE; $\boldsymbol{E}_g = [\boldsymbol{v}_g^T, \boldsymbol{\omega}_g^T]^T \in \mathbb{R}^{6\times 1}$ is the velocity of the entire system; $\boldsymbol{J}_E \in \mathbb{R}^{6\times(n+3)}$ denotes the Generalized Jacobian Matrix; $\boldsymbol{q} = [\boldsymbol{\Phi}_M^T, \boldsymbol{\Phi}_S^T]^T$, with $\boldsymbol{\Phi}_S = (\alpha, \beta, \gamma)^T$ representing the base attitude, $\boldsymbol{\Phi}_M = (\phi_1, \phi_2, \cdots, \phi_n)^T$ representing the joint angles. Detail derivation of (5.6) can be found in Appendix B.2.

Space Robot Dynamics

The conventional dynamic model of a space robot is of the following form:

$$\boldsymbol{A}_c \ddot{\boldsymbol{q}} + \boldsymbol{B}_c = \boldsymbol{\tau}_c - \boldsymbol{J}_c^T \boldsymbol{F}_c, \tag{5.7}$$

where $\boldsymbol{A}_c \in \mathbb{R}^{(n+3)\times(n+3)}$ is the inertia matrix with respect to the inertial frame; $\boldsymbol{B}_c \in \mathbb{R}^{(n+3)\times 1}$ contains the nonlinear terms; $\boldsymbol{\tau}_c \in \mathbb{R}^{(n+3)\times 1}$ is the control torques, including the joint torques and RW torques; $\boldsymbol{J}_c \in \mathbb{R}^{(n+3)\times 3}$ is Jacobian matrix; $\boldsymbol{F}_c$ represents the external forces applied on the EE. Note that possible external torques felt at the EE prior to the rigid connection can only be friction torques which depend on the contact forces and thus are expressed using $\boldsymbol{F}_c$ to avoid inducing coupling terms in (5.7).

By directly employing this model, the required input torques can be computed according to the desired EE motion and the desired contact force, as shown in Figure 5.2. However, such torques cannot ensure an appropriate spacecraft attitude. Therefore, instead of establishing the FFSR's model using Lagrangian formulation which takes the system as a whole, modeling of the spacecraft base and of the space robot manipulator are carried out separately using Newton-Euler method. The manipulator's motion, physically represented by reaction torques and constraint forces applied from the first articulate joint, is considered as a disturbance when establishing the base model. Accordingly, the joint torque controller can be designed based on the manipulator's model, which can track the desired EE motion and desired contact force with knowledge of current spacecraft attitude; while the RW torque controller is developed by solely analyzing the model of a single rigid base, which enforces desired spacecraft orientation. Control scheme based on separate models of the manipulator and the base is shown in Figure 5.3.

In the following, dynamic models of the space manipulator and the spacecraft base are established based on the Newton-Euler method. First, the manipulator dynamics is analyzed. For link i, $i = 1, \cdots, n-1$, the dynamic equations are

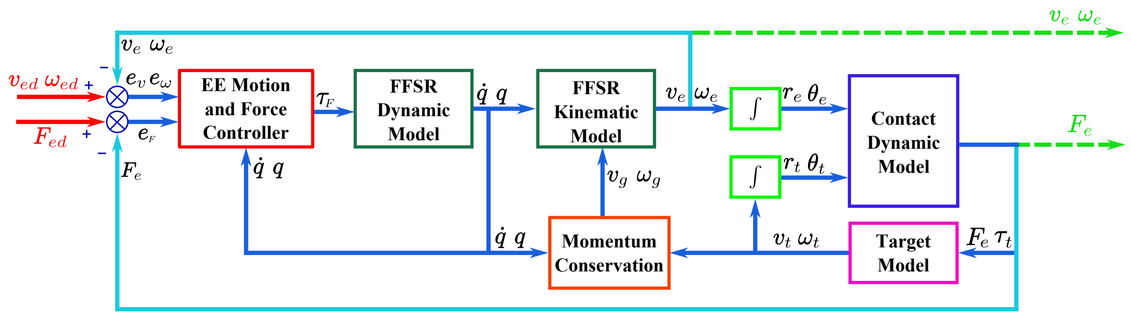

Figure 5.2: Control scheme based on conventional FFSR dynamic model

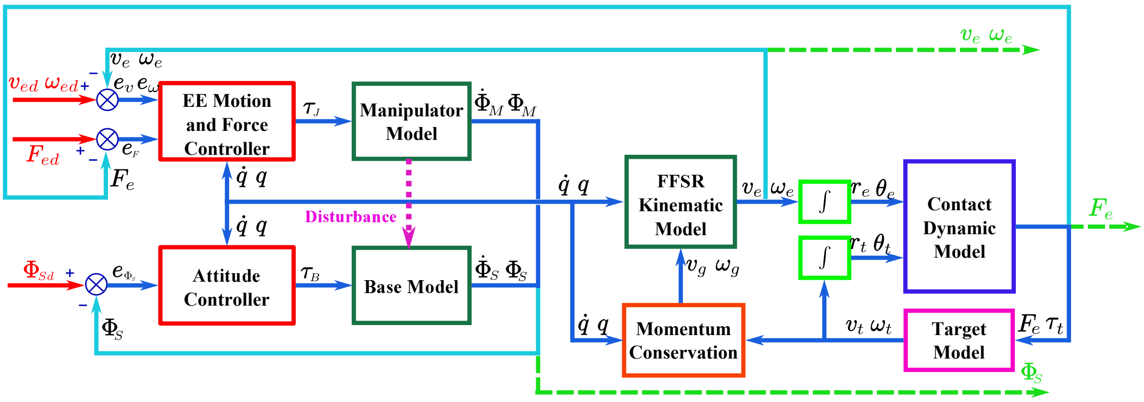

Figure 5.3: Control scheme based on separate manipulator model and base model

obtained as,

$$\begin{aligned} &\boldsymbol{f}_{i-1,i} + \boldsymbol{f}_{i+1,i} = m_i \dot{\boldsymbol{v}}_i \\ &\boldsymbol{\tau}_{i+1,i} + \boldsymbol{\tau}_{i-1,i} + (-\boldsymbol{a}_i) \times \boldsymbol{f}_{i-1,i} + \boldsymbol{b}_i \times \boldsymbol{f}_{i+1,i} = \dot{\boldsymbol{H}}_i. \end{aligned} \tag{5.8}$$

For link n, the dynamic equations are

$$\begin{aligned} &\boldsymbol{F} + \boldsymbol{f}_{n-1,n} = m_n \dot{\boldsymbol{v}}_n, \\ &\boldsymbol{\tau}_{n-1,n} + (-\boldsymbol{a}_n) \times \boldsymbol{f}_{n-1,n} + \boldsymbol{b}_n \times \boldsymbol{F} + \boldsymbol{\tau}_e = \dot{\boldsymbol{H}}_n, \end{aligned} \tag{5.9}$$

where $\boldsymbol{F} = -\boldsymbol{F}_e$ is the contact force felt at the EE; $\boldsymbol{f}_{i+1,i}$ and $\boldsymbol{\tau}_{i+1,i}$ are the force and torque applied by link $i+1$ on link i, respectively; $\boldsymbol{H}_i = \boldsymbol{I}_i \boldsymbol{\omega}_i$ is the angular momentum of link i; $\boldsymbol{a}_i$ is the position vector from joint i to CM of link i and $\boldsymbol{b}_i$ is the position vector from CM of link i to joint $i+1$. All parameters are expressed in the inertial frame.

Combining (5.8), (5.9) with the robot kinematic equations (B.12), (B.13), joint torques can be related to the contact force in a canonical form as,

$$\boldsymbol{A}_J\ddot{\boldsymbol{q}} + \boldsymbol{B}_J = \boldsymbol{\tau}_J - \boldsymbol{J}_{FJ}\boldsymbol{F}_e, \tag{5.10}$$

where $\boldsymbol{A}_J \in \mathbb{R}^{n\times(n+3)}$ is the coefficient matrix, $\boldsymbol{B}_J \in \mathbb{R}^{n\times 1}$ denotes nonlinear terms, $\boldsymbol{J}_{FJ} \in \mathbb{R}^{n\times 3}$ is the Jacobian transpose and $\boldsymbol{\tau}_J \in \mathbb{R}^{n\times 1}$ are joint torques.

Next, dynamic model of the spacecraft base is addressed. As RWs generate internal torques, the control torques are derived from RWs' momentum instead of simply defining an external torque as discussed in Chapter 3. The basic equation is

$$\dot{\widetilde{\boldsymbol{H}}}_B + \boldsymbol{\omega}_B \times \widetilde{\boldsymbol{H}}_B = \widetilde{\boldsymbol{T}}_B + \widetilde{\boldsymbol{D}}_B, \tag{5.11}$$

where $\boldsymbol{\omega}_B$ is the base angular velocity; $\widetilde{\boldsymbol{T}}_B$ is the external torque generated from manipulator motion and $\widetilde{\boldsymbol{T}}_B = -\boldsymbol{\tau}_1 + \boldsymbol{b}_0 \times \boldsymbol{f}_{1,0}$; $\boldsymbol{\tau}_1$ and $\boldsymbol{f}_{1,0}$ represent constraint torques and forces applied from joint 1 to the base; $\boldsymbol{b}_0$ represents the position vector of joint 1 w.r.t. base CM; $\widetilde{\boldsymbol{D}}_B$ represents reaction-wheel unloading torques and bounded environmental disturbances which are of negligible magnitude compared with $\widetilde{\boldsymbol{T}}_B$; $\widetilde{\boldsymbol{H}}_B$ is the total angular momentum of the spacecraft base with respect to the origin of the inertial coordinate, including angular momentum of the three RWs which are mounted on board orthogonally. In a similar way that has been done in (3.6) and (3.7), and assuming small attitude deviation ($\dot{\boldsymbol{\Phi}}_S \approx \boldsymbol{\omega}_B$), (5.11) is rewritten as,

$$\widetilde{\boldsymbol{J}}\ddot{\boldsymbol{\Phi}}_S + \dot{\boldsymbol{\Phi}}_S \times \widetilde{\boldsymbol{J}}\dot{\boldsymbol{\Phi}}_S = \widetilde{\boldsymbol{\tau}}_B + \widetilde{\boldsymbol{T}}_B + \widetilde{\boldsymbol{D}}_B, \tag{5.12}$$

where $\widetilde{\boldsymbol{J}}$ represents the inertia matrix of the spacecraft base; and

$$\widetilde{\boldsymbol{\tau}}_B = -\boldsymbol{\tau}_w - \boldsymbol{\omega}_B \times \int \boldsymbol{\tau}_w dt, \tag{5.13}$$

with $\boldsymbol{\tau}_w \in \mathbb{R}^{3\times 1}$ representing RW torques.

Since $\widetilde{\boldsymbol{T}}_B$ can be expressed as $\widetilde{\boldsymbol{T}}_B = \boldsymbol{g}(\boldsymbol{F}_e, \boldsymbol{q}, \dot{\boldsymbol{q}}, \ddot{\boldsymbol{q}}) = -\boldsymbol{J}_{FB}\boldsymbol{F}_e - \boldsymbol{A}_T\ddot{\boldsymbol{q}} + \widetilde{\boldsymbol{g}}(\boldsymbol{q}, \dot{\boldsymbol{q}})$, (5.12) is rearranged in the following form:

$$\widetilde{\boldsymbol{J}}\ddot{\boldsymbol{\Phi}}_S + \boldsymbol{A}_T\ddot{\boldsymbol{q}} + \dot{\boldsymbol{\Phi}}_S \times \widetilde{\boldsymbol{J}}\dot{\boldsymbol{\Phi}}_S - \widetilde{\boldsymbol{D}}_B - \widetilde{\boldsymbol{g}}(\boldsymbol{q}, \dot{\boldsymbol{q}}) = \widetilde{\boldsymbol{\tau}}_B - \boldsymbol{J}_{FB}\boldsymbol{F}_e. \tag{5.14}$$

The above equation can be rewritten in a similar form as the manipulator model presented in (5.10) as,

$$\boldsymbol{A}_B\ddot{\boldsymbol{q}} + \boldsymbol{B}_B = \widetilde{\boldsymbol{\tau}}_B - \boldsymbol{J}_{FB}\boldsymbol{F}_e, \tag{5.15}$$

where $\boldsymbol{A}_B \in \mathbb{R}^{3\times(n+3)}$ and $\boldsymbol{A}_B = [\boldsymbol{O}, \widetilde{\boldsymbol{J}}] + \boldsymbol{A}_T$, $\boldsymbol{O} \in \mathbb{R}^{3\times n}$ is a zero matrix; $\boldsymbol{B}_B \in \mathbb{R}^{3\times 1}$ contains nonlinear terms and $\boldsymbol{B}_B = \dot{\boldsymbol{\Phi}}_S \times \widetilde{\boldsymbol{J}}\dot{\boldsymbol{\Phi}}_S - \widetilde{\boldsymbol{D}}_B - \widetilde{\boldsymbol{g}}(\boldsymbol{q}, \dot{\boldsymbol{q}})$; $\boldsymbol{J}_{FB} \in \mathbb{R}^{3\times 3}$ is the Jacobian transpose. Thus, (5.10) and (5.12) can be integrated to express the complete dynamic model as,

$$\boldsymbol{A}_F\ddot{\boldsymbol{q}} + \boldsymbol{B}_F = \boldsymbol{\tau}_F - \boldsymbol{J}_F\boldsymbol{F}_e, \tag{5.16}$$

where $\boldsymbol{\tau}_F \in \mathbb{R}^{(n+3)\times 1}$ consists of joint torques and introduced virtual attitude control torques as $\boldsymbol{\tau}_F = [\boldsymbol{\tau}_J^T, \widetilde{\boldsymbol{\tau}}_B^T]^T$; and $\boldsymbol{A}_F = \left[\boldsymbol{A}_J^T, \boldsymbol{A}_B^T\right]^T \in \mathbb{R}^{(n+3)\times(n+3)}$, $\boldsymbol{B}_F = \left[\boldsymbol{B}_J^T, \boldsymbol{B}_B^T\right]^T \in \mathbb{R}^{(n+3)\times 1}$, $\boldsymbol{J}_F = \left[\boldsymbol{J}_{FJ}^T, \boldsymbol{J}_{FB}^T\right]^T \in \mathbb{R}^{(n+3)\times 3}$.

Note that this complete model is only used to simulate the model in Simulink and controller design will be dependent on separated models for the manipulator and the base which will be apparent in later sections.

5.2.4 Contact Dynamics

Contact dynamics is a critical issue for dynamic modeling of on-orbit servicing missions and is still an active research subject. In [174], a point contact scenario is assumed and the contact force is modeled as an impulse function. Ma proposed a general approach of contact dynamics modeling where multiple-contact and body flexibility are considered [175]. Ref. [176] presented two contact dynamics modeling techniques applied for space robotics applications: one for hard physical contact cases and one for contact with plastically deformable media. The simulation results obtained from multi-body dynamics simulation tools have been demonstrated to be helpful in terms of feasibility confirmation and system design. Uyama *et al.* used the coefficient of restitution and the contact duration as evaluating parameters, and performed experimental evaluation of the contact/impact dynamics between a space robot and a tumbling object [177].

A real contact is distributed determined by the features of the contact surfaces

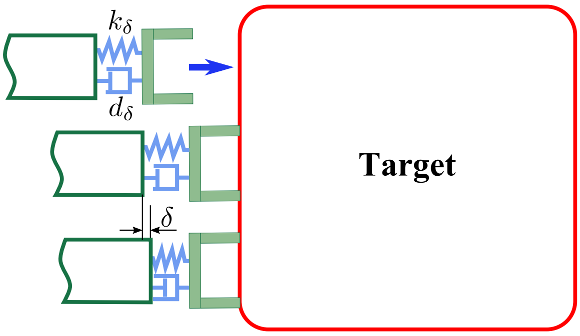

Figure 5.4: Spring-dashpot contact model

[121]. In the contact between the EE and the target, the contact force is assumed to concentrate on a central action point and frictional force is disregarded. Commonly used contact dynamic models to deal with contact dynamics of space manipulator include spring-dashpot model [178], Hertz's model [179] and nonlinear damping model [180]. Such models treat contact-impact phenomenon as continuous dynamics and define the normal contact force f_n as an explicit function of local indentation δ and its rate [181] as,

$$f_n = f_n(\delta, \dot{\delta}) = f_\delta(\delta) + f_{\dot{\delta}}(\dot{\delta}). \tag{5.17}$$

In the following, the spring-dashpot contact model is considered, which represents the contact with a linear damper (dashpot) in parallel with a linear spring, as shown in Figure 5.4. Based on this model, the contact force is formulated as,

$$f_n = k_\delta \delta + d_\delta \dot{\delta}, \tag{5.18}$$

where k_δ is the stiffness parameter and d_δ is the damping coefficient. Since the FFSR and the target are perfectly rigid except the compliance on the wrist, the damping term is neglected and a linear elastic model is applied to approximate the contact dynamics. As a result, the contact force depends only on the indentation as,

$$f_n = k_\delta \delta. \tag{5.19}$$

The indentation in the case of space manipulator interacting with a target can be computed by,

$$\delta = {}^t x_t - {}^t x_e, \tag{5.20}$$

where

$${}^t x_t = \boldsymbol{u}_n^T \ \boldsymbol{R}_a^t \ {}^a\boldsymbol{r}_e, \tag{5.21}$$

$${}^t x_e = \boldsymbol{u}_n^T \ \boldsymbol{R}_a^t \ {}^a\boldsymbol{r}_{tf}, \tag{5.22}$$

with ${}^a\boldsymbol{r}_{tf}$ denoting position vector of the reference point on the target surface and ${}^a\boldsymbol{r}_{tf} = {}^a\boldsymbol{r}_t + \boldsymbol{R}_t^a \ {}^t\boldsymbol{a}_t$; $\boldsymbol{u}_n \in \mathbb{R}^{3\times1}$ representing the unit normal vector of the target surface or the unit vector along the normal contact force direction. Therefore, the contact force vector is

$$\boldsymbol{F}_e = \boldsymbol{u}_n \ f_n. \tag{5.23}$$

By this point, a comprehensive description of system models, including the FFSR model, the passive target model and the contact dynamic model, have been addressed. Next, a controller which has the capacity to perform control of both EE pose and contact force is developed.

5.3 Hybrid Motion and Force Control

5.3.1 Basic Theory

Hybrid motion and force control has the ability to perform control of both EE pose and contact force. The control method analyzes force control and motion control independently on the basis of decomposition of task space. In a contact or manipulation situation by the manipulator's EE to an object, some directions are subject to EE motion constraints and belong to force-controlled subspace; other directions are subject to interaction force constraints and belong to motion-controlled subspace. Along those directions belonging to the motion-controlled subspace, the motion is unconstrained and the position reference is reached by EE; along those directions belonging to the force-controlled subspace, the motion is constrained and the force reference is reached. Next, basic ideas of how to design a hybrid motion and force controller is demonstrated using a ground manipulator example as follows. Note in this case, only EE translation and contact forces are taken into account. Details of controlling both EE linear velocity and its rotation motion are elaborated in the next section for the space robot.

By incorporating the kinematic equations, the conventional dynamic model of a ground manipulator which has n articulated links can be written based on its EE velocity as,

$$\boldsymbol{A}_G \dot{\boldsymbol{v}}_e + \boldsymbol{B}_G = \boldsymbol{\tau}_{GJ} - \boldsymbol{J}_G^T \boldsymbol{F}_e, \tag{5.24}$$

where $\boldsymbol{A}_G \in \mathbb{R}^{n\times 3}$ is the coefficient matrix; $\boldsymbol{B}_G \in \mathbb{R}^{n\times 1}$ contains nonlinear terms; $\boldsymbol{J}_G \in \mathbb{R}^{3\times n}$ is the Jacobian matrix; $\boldsymbol{\tau}_{GJ} \in \mathbb{R}^{n\times 1}$ represents joint torques.

Suppose the robot tries to apply a suitable contact force on a stationary object or the environment. The desired EE motion and interaction forces can be assigned into motion and force controlled subspaces using the so-called selection matrices by identifying the contact geometry. The decomposed form of EE velocity is,

$$\boldsymbol{v}_e = \boldsymbol{S}_v \boldsymbol{\nu} + \boldsymbol{C}\boldsymbol{S}_f \dot{\boldsymbol{\mu}}, \tag{5.25}$$

where $\boldsymbol{S}_v$ and $\boldsymbol{S}_f$ are selection matrices; $\boldsymbol{C}$ is a compliance matrix; $\boldsymbol{\nu}$ belongs to velocity-controlled subspace and $\boldsymbol{\nu} = \boldsymbol{S}_v^+ \boldsymbol{v}_e$; $\boldsymbol{\mu}$ belongs to force-controlled subspace and $\boldsymbol{\mu} = \boldsymbol{S}_f^+ \boldsymbol{F}_e$.

Adopt the inverse dynamics control law

$$\boldsymbol{\tau}_{GJ} = \boldsymbol{A}_G \boldsymbol{\alpha}_G + \boldsymbol{B}_G + \boldsymbol{J}_G^T \boldsymbol{F}_e, \tag{5.26}$$

with the choice of a new input [121]

$$\boldsymbol{\alpha}_G = \boldsymbol{S}_v \boldsymbol{\alpha}_v + \boldsymbol{C}\boldsymbol{S}_f \boldsymbol{\alpha}_f. \tag{5.27}$$

Substituting (5.26) into (5.24) returns $\dot{\boldsymbol{v}}_e = \boldsymbol{\alpha}_G$. Replace the left side of this equality by the derivative of (5.25) and replace the right side by (5.27). Note that $\boldsymbol{S}_v$ and

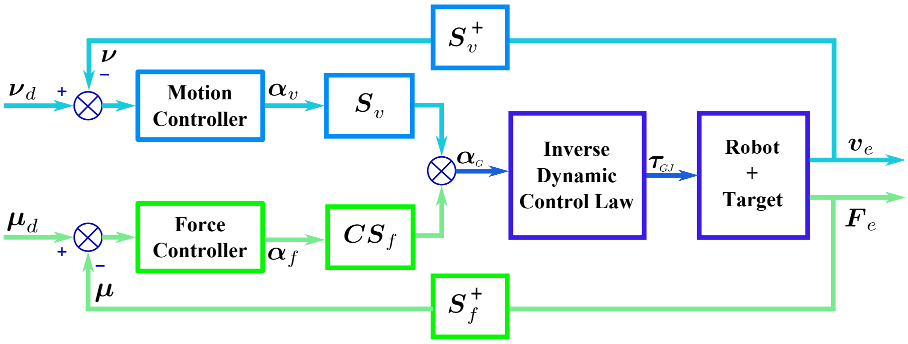

Figure 5.5: Block scheme of hybrid motion and force control

$\boldsymbol{S}_f$ are constant for the constraint frame. The equation becomes,

$$\boldsymbol{S}_v\dot{\boldsymbol{\nu}} + \boldsymbol{C}\boldsymbol{S}_f\ddot{\boldsymbol{\mu}} = \boldsymbol{S}_v\boldsymbol{\alpha}_v + \boldsymbol{C}\boldsymbol{S}_f\boldsymbol{\alpha}_f. \tag{5.28}$$

Let $\dot{\boldsymbol{\nu}} = \boldsymbol{\alpha}_v$ and $\ddot{\boldsymbol{\mu}} = \boldsymbol{\alpha}_f$. Then $\boldsymbol{\alpha}_v$ and $\boldsymbol{\alpha}_f$ can be designed separately to implement PID control for the EE motion and contact force. The block diagram of hybrid motion and force control is shown in Figure 5.5.

5.3.2 Manipulator Motion and Force Control

To design a hybrid motion and force controller for the space robot, it is necessary to rewrite (5.10) w.r.t. EE acceleration. Differentiating (5.6) returns the expression of joint accelerations as,

$$\ddot{\boldsymbol{q}} = \boldsymbol{J}_E^{-1}\left(\dot{\boldsymbol{E}}_e - \dot{\boldsymbol{E}}_g - \dot{\boldsymbol{J}}_E\dot{\boldsymbol{q}}\right). \tag{5.29}$$

Substituting above expression into (5.10), the dynamic equation is rewritten based on EE acceleration as,

$$\boldsymbol{A}_{EE}\dot{\boldsymbol{E}}_e + \boldsymbol{B}_{EE} = \boldsymbol{\tau}_J - \boldsymbol{J}_{FJ}\boldsymbol{F}_e, \tag{5.30}$$

where $\boldsymbol{A}_{EE} \in \mathbb{R}^{n\times 6}$ and $\boldsymbol{A}_{EE} = \boldsymbol{A}_J\boldsymbol{J}_E^{-1}$; $\boldsymbol{B}_{EE} \in \mathbb{R}^{n\times 1}$ and $\boldsymbol{B}_{EE} = -\boldsymbol{A}_J\boldsymbol{J}_E^{-1}\dot{\boldsymbol{E}}_g - \boldsymbol{A}_J\boldsymbol{J}_E^{-1}\dot{\boldsymbol{J}}_E\dot{\boldsymbol{q}} + \boldsymbol{B}_J$. Rewrite (5.30) into a form with separate terms for $\boldsymbol{v}_e$ and $\boldsymbol{\omega}_e$,

$$\boldsymbol{A}_{EV}\dot{\boldsymbol{v}}_e + \boldsymbol{A}_{E\omega}\dot{\boldsymbol{\omega}}_e + \boldsymbol{B}_{EE} = \boldsymbol{\tau}_J - \boldsymbol{J}_{FJ}\boldsymbol{F}_e, \tag{5.31}$$

where $\boldsymbol{A}_{EV} \in \mathbb{R}^{n\times 3}$ and $\boldsymbol{A}_{E\omega} \in \mathbb{R}^{n\times 3}$ are partitioned matrices of $\boldsymbol{A}_{EE}$. To analyze the translation and rotation of the EE separately, the conventional inverse dynamic control law (5.26) is adopted and improved by adding an additional term $\boldsymbol{A}_{E\omega}\boldsymbol{\beta}_{\omega}$ for orientation control and rate of rotation control of the EE, as follows:

$$\boldsymbol{\tau}_J = \boldsymbol{A}_{EV}\boldsymbol{\alpha}_v + \boldsymbol{A}_{E\omega}\boldsymbol{\beta}_{\omega} + \boldsymbol{B}_{EE} + \boldsymbol{J}_{FJ}\boldsymbol{F}_e, \tag{5.32}$$

where $\boldsymbol{\alpha}_v \in \mathbb{R}^{3\times 1}$ and $\boldsymbol{\beta}_{\omega} \in \mathbb{R}^{3\times 1}$ are introduced as new inputs.

To find specific expressions for $\boldsymbol{\alpha}_v$ and $\boldsymbol{\beta}_{\omega}$, the desired motion needs to be clarified and should be related to ${}^a\boldsymbol{v}_e$ and ${}^a\boldsymbol{\omega}_e$ included in (5.31). However, it is difficult to directly decompose ${}^a\boldsymbol{v}_e$ into motion or force subspace in the inertial frame due to the floating property of the target and the FFSR. As an approach, ${}^t\boldsymbol{v}_e$ can be first explicitly decomposed in the target frame according to contact geometry as follows:

$${}^t\boldsymbol{v}_e = {}^t\boldsymbol{S}_v\ {}^t\boldsymbol{\nu} + {}^t\boldsymbol{C}\ {}^t\boldsymbol{S}_f\ {}^t\dot{\boldsymbol{\mu}}, \tag{5.33}$$

where ${}^t\boldsymbol{S}_v$ and ${}^t\boldsymbol{S}_f$ are selection matrices determined by contact geometry and remain constant in the target frame; ${}^t\boldsymbol{\nu} = {}^t\boldsymbol{S}_v^+\ {}^t\boldsymbol{v}_e$ belongs to velocity-controlled subspace; ${}^t\boldsymbol{\mu} = {}^t\boldsymbol{S}_f^+\ {}^t\boldsymbol{F}_e$ belongs to force-controlled subspace; ${}^t\boldsymbol{C}$ denotes a compliance matrix defined as,

$${}^t\boldsymbol{C}_{ij} = \begin{cases} 1/k_\delta & \text{for } i = j = k,\ k \text{ satifies } {}^t\boldsymbol{S}_{fk} = 1, \\ 0 & \text{otherwise.} \end{cases} \tag{5.34}$$

Physically, ${}^t\boldsymbol{v}_e$ is defined as EE motion w.r.t. CM of the target and can be alternatively expressed as,

$${}^t\boldsymbol{v}_e = \boldsymbol{R}_a^t({}^a\boldsymbol{v}_e - {}^a\boldsymbol{v}_t). \tag{5.35}$$

Equivalence of (5.33) and (5.35) yields the relationship between ${}^a\boldsymbol{v}_e$ and ${}^t\boldsymbol{v}_e$ in the following form,

$${}^a\boldsymbol{v}_e = {}^a\boldsymbol{v}_t + \boldsymbol{R}_t^a\left({}^t\boldsymbol{S}_v\ {}^t\boldsymbol{\nu} + {}^t\boldsymbol{C}\ {}^t\boldsymbol{S}_f\ {}^t\boldsymbol{S}_f^+\ {}^t\dot{\boldsymbol{F}}_e\right). \tag{5.36}$$

Since a capture operation typically requires tracking a specific contact point, e.g. a grappling fixture on the target, the EE position components aligned with motion-controlled subspace, ${}^t\boldsymbol{r}_{ev}$, should be *constant* when expressed in the target frame. ${}^t\boldsymbol{r}_{ev}$ can be given by,

$$ {}^t\boldsymbol{r}_{ev} = {}^t\boldsymbol{S}_v^+ \; {}^t\boldsymbol{r}_e = {}^t\boldsymbol{S}_v^+ \; \boldsymbol{R}_a^t \left({}^a\boldsymbol{r}_e - {}^a\boldsymbol{r}_t\right). \tag{5.37} $$

Differentiate (5.37) to velocity level,

$$ \begin{aligned} {}^t\boldsymbol{v}_{ev} &= {}^t\dot{\boldsymbol{r}}_{ev} = {}^t\boldsymbol{S}_v^+ \; {}^t\dot{\boldsymbol{r}}_e \\ &= {}^t\boldsymbol{S}_v^+ \; \boldsymbol{R}_a^t \left({}^a\dot{\boldsymbol{r}}_e - {}^a\dot{\boldsymbol{r}}_t\right) + {}^t\boldsymbol{S}_v^+ \; \dot{\boldsymbol{R}}_a^t \left({}^a\boldsymbol{r}_e - {}^a\boldsymbol{r}_t\right) \\ &= {}^t\boldsymbol{S}_v^+ \; \boldsymbol{R}_a^t \left({}^a\boldsymbol{v}_e - {}^a\boldsymbol{v}_t\right) + {}^t\boldsymbol{S}_v^+ \; \dot{\boldsymbol{R}}_a^t \left({}^a\boldsymbol{r}_e - {}^a\boldsymbol{r}_t\right). \end{aligned} \tag{5.38} $$

Substituting (5.35) into (5.38) and adopting the definition ${}^t\boldsymbol{\nu} = {}^t\boldsymbol{S}_v^+ \; {}^t\boldsymbol{v}_e$, ${}^t\boldsymbol{\nu}$ is related to ${}^t\boldsymbol{v}_{ev}$ by,

$$ {}^t\boldsymbol{v}_{ev} = {}^t\boldsymbol{S}_v^+ \; {}^t\boldsymbol{v}_e + {}^t\boldsymbol{S}_v^+ \; \dot{\boldsymbol{R}}_a^t \left({}^a\boldsymbol{r}_e - {}^a\boldsymbol{r}_t\right) = {}^t\boldsymbol{\nu} + {}^t\boldsymbol{S}_v^+ \; \dot{\boldsymbol{R}}_a^t \left({}^a\boldsymbol{r}_e - {}^a\boldsymbol{r}_t\right), \tag{5.39} $$

or

$$ {}^t\boldsymbol{\nu} = {}^t\boldsymbol{v}_{ev} - {}^t\boldsymbol{S}_v^+ \; \dot{\boldsymbol{R}}_a^t \left({}^a\boldsymbol{r}_e - {}^a\boldsymbol{r}_t\right). \tag{5.40} $$

Then the substitution of (5.40) into (5.36) returns,

$$ \begin{aligned} {}^a\boldsymbol{v}_e =& {}^a\boldsymbol{v}_t + \boldsymbol{R}_t^a \; {}^t\boldsymbol{S}_v \left[{}^t\boldsymbol{v}_{ev} - {}^t\boldsymbol{S}_v^+ \; \dot{\boldsymbol{R}}_a^t \left({}^a\boldsymbol{r}_e - {}^a\boldsymbol{r}_t\right) \right] + \boldsymbol{R}_t^a \; {}^t\boldsymbol{C} \; {}^t\boldsymbol{S}_f \; {}^t\boldsymbol{S}_f^+ \; {}^t\dot{\boldsymbol{F}}_e \\ =& {}^a\boldsymbol{v}_t - \boldsymbol{R}_t^a \; {}^t\boldsymbol{S}_v \; {}^t\boldsymbol{S}_v^+ \; \dot{\boldsymbol{R}}_a^t \left({}^a\boldsymbol{r}_e - {}^a\boldsymbol{r}_t\right) + \boldsymbol{R}_t^a \; {}^t\boldsymbol{S}_v \; {}^t\boldsymbol{v}_{ev} + \boldsymbol{R}_t^a \; {}^t\boldsymbol{C} \; {}^t\boldsymbol{S}_f \; {}^t\boldsymbol{S}_f^+ \; {}^t\dot{\boldsymbol{F}}_e \\ =& \boldsymbol{h}_v + {}^a\boldsymbol{S}_v \; {}^t\boldsymbol{v}_{ev} + {}^a\boldsymbol{S}_f \; {}^t\dot{\boldsymbol{F}}_{ef}, \end{aligned} \tag{5.41} $$

where $\boldsymbol{h}_v = {}^a\boldsymbol{v}_t - \boldsymbol{R}_t^a \; {}^t\boldsymbol{S}_v \; {}^t\boldsymbol{S}_v^+ \; \dot{\boldsymbol{R}}_a^t \left({}^a\boldsymbol{r}_e - {}^a\boldsymbol{r}_t\right)$, ${}^a\boldsymbol{S}_v = \boldsymbol{R}_t^a \; {}^t\boldsymbol{S}_v$, ${}^a\boldsymbol{S}_f = \boldsymbol{R}_t^a \; {}^t\boldsymbol{C} \; {}^t\boldsymbol{S}_f$ and ${}^t\dot{\boldsymbol{F}}_{ef} = {}^t\boldsymbol{S}_f^+ \; {}^t\dot{\boldsymbol{F}}_e$. Equation (5.41) now represents the inertial EE linear velocity ${}^a\boldsymbol{v}_e$ with explicit control variables ${}^t\boldsymbol{v}_{ev}$ and ${}^t\boldsymbol{F}_{ef}$, where ${}^t\boldsymbol{v}_{ev}$ is the linear velocity belonging to motion-controlled subspace in the target frame which should be controlled at zero to follow the required contact point; ${}^t\boldsymbol{F}_{ef}$ is the actual contact force belonging to force-controlled subspace in the target frame which should be controlled as required to fulfil the capture task.

As mentioned above, the desired EE linear motion in motion-controlled subspace should be ${}^{t}\boldsymbol{r}_{evd} = constant$ and is ${}^{t}\boldsymbol{v}_{evd} = 0$ at velocity level. Define the desired force as ${}^{t}\boldsymbol{F}_{efd}$. Differentiate (5.41) to acceleration level,

$$ {}^{a}\dot{\boldsymbol{v}}_{e} = \dot{\boldsymbol{h}}_{v} + {}^{a}\dot{\boldsymbol{S}}_{v}\ {}^{t}\boldsymbol{v}_{ev} + {}^{a}\boldsymbol{S}_{v}\ {}^{t}\dot{\boldsymbol{v}}_{ev} + {}^{a}\dot{\boldsymbol{S}}_{f}\ \dot{\boldsymbol{F}}_{ef} + {}^{a}\boldsymbol{S}_{f}\ \ddot{\boldsymbol{F}}_{ef} = \dot{\boldsymbol{h}}_{v} + \boldsymbol{g}_{v} + \boldsymbol{g}_{f}, \tag{5.42} $$

where $\boldsymbol{g}_{v} = {}^{a}\dot{\boldsymbol{S}}_{v}\ {}^{t}\boldsymbol{v}_{ev} + {}^{a}\boldsymbol{S}_{v}\ {}^{t}\dot{\boldsymbol{v}}_{ev}$ and $\boldsymbol{g}_{f} = {}^{a}\dot{\boldsymbol{S}}_{f}\ {}^{t}\dot{\boldsymbol{F}}_{ef} + {}^{a}\boldsymbol{S}_{f}\ {}^{t}\ddot{\boldsymbol{F}}_{ef}$. Now the new input $\boldsymbol{\alpha}_{v}$ can be determined by the following form:

$$ \boldsymbol{\alpha}_{v} = \dot{\boldsymbol{h}}_{v} + \boldsymbol{\alpha}_{vs} + \boldsymbol{\alpha}_{fs}. \tag{5.43} $$

Set $\boldsymbol{\alpha}_{vs}$ and $\boldsymbol{\alpha}_{fs}$ as,

$$ \begin{aligned} \boldsymbol{\alpha}_{vs} =& {}^{a}\dot{\boldsymbol{S}}_{v}\ {}^{t}\boldsymbol{v}_{ev} + {}^{a}\boldsymbol{S}_{v}\ {}^{t}\dot{\boldsymbol{v}}_{evd} - \boldsymbol{K}_{Pv}\ {}^{a}\boldsymbol{S}_{v}\left({}^{t}\boldsymbol{v}_{ev} - {}^{t}\boldsymbol{v}_{evd}\right) - \boldsymbol{K}_{Iv}\ {}^{a}\boldsymbol{S}_{v}\int_{0}^{\tau}\left({}^{t}\boldsymbol{v}_{ev} - {}^{t}\boldsymbol{v}_{evd}\right)dt, \\ \boldsymbol{\alpha}_{fs} =& {}^{a}\dot{\boldsymbol{S}}_{f}\ {}^{t}\dot{\boldsymbol{F}}_{ef} + {}^{a}\boldsymbol{S}_{f}\ {}^{t}\ddot{\boldsymbol{F}}_{efd} - \boldsymbol{K}_{Df}\ {}^{a}\boldsymbol{S}_{f}\left({}^{t}\dot{\boldsymbol{F}}_{ef} - {}^{t}\dot{\boldsymbol{F}}_{efd}\right) - \boldsymbol{K}_{Pf}\ {}^{a}\boldsymbol{S}_{f}\left({}^{t}\boldsymbol{F}_{ef} - {}^{t}\boldsymbol{F}_{efd}\right), \end{aligned} \tag{5.44} $$

where $\boldsymbol{K}_{Pv}$, $\boldsymbol{K}_{Iv}$, $\boldsymbol{K}_{Df}$ and $\boldsymbol{K}_{Pf}$ are control gain matrices. To avoid using the derivative of noisy force feedback, ${}^{t}\dot{\boldsymbol{F}}_{e}$ is replaced by ${}^{t}\boldsymbol{K}\left({}^{t}\boldsymbol{v}_{e} - {}^{t}\dot{\boldsymbol{r}}_{tf}\right)$, where ${}^{t}\boldsymbol{K}$ is a stiffness matrix and has the elements

$$ {}^{t}\boldsymbol{K}_{ij} = \begin{cases} k_{\delta} & \text{for } i = j = k,\ k \text{ satifies } {}^{t}\boldsymbol{S}_{fk} = 1, \\ 0 & \text{otherwise.} \end{cases} \tag{5.45} $$

To control EE orientation, $\boldsymbol{\beta}_{\omega}$ is defined as,

$$ \boldsymbol{\beta}_{\omega} = \dot{\boldsymbol{\omega}}_{ed} - \boldsymbol{K}_{P\omega}(\boldsymbol{\omega}_{e} - \boldsymbol{\omega}_{ed}) - \boldsymbol{K}_{I\omega}\int_{0}^{\tau}(\boldsymbol{\omega}_{e} - \boldsymbol{\omega}_{ed})dt, \tag{5.46} $$

where $\boldsymbol{K}_{P\omega}$ and $\boldsymbol{K}_{I\omega}$ are also control gain matrices. By using control law (5.32), (5.43), (5.44), and (5.46), the EE motion tracking error $\boldsymbol{e}_{v} = {}^{t}\boldsymbol{v}_{ev} - {}^{t}\boldsymbol{v}_{evd}$, $\boldsymbol{e}_{\omega} = \boldsymbol{\omega}_{e} - \boldsymbol{\omega}_{ed}$ and force tracking error $\boldsymbol{e}_{f} = {}^{t}\boldsymbol{F}_{ef} - {}^{t}\boldsymbol{F}_{efd}$ are guaranteed to converge to zero.

5.3.3 Spacecraft Attitude Control

The disturbance induced by the manipulator's motion to the base must be compensated by the spacecraft attitude control system. Such disturbance is physically represented by the constraint forces or torques and exerted by the first articulated joint to the base, denoted by $\widetilde{\boldsymbol{T}}_B$ in (5.12). Rearrange (5.12) as,

$$\widetilde{\boldsymbol{J}}\ddot{\boldsymbol{\Phi}}_S + \boldsymbol{\Upsilon}_B = \widetilde{\boldsymbol{\tau}}_B, \tag{5.47}$$

where $\boldsymbol{\Upsilon}_B = \dot{\boldsymbol{\Phi}}_S \times \widetilde{\boldsymbol{J}}\dot{\boldsymbol{\Phi}}_S - \widetilde{\boldsymbol{T}}_B - \widetilde{\boldsymbol{D}}_B$. Adopt the feedback-linearization control law,

$$\widetilde{\boldsymbol{\tau}}_B = \boldsymbol{\Upsilon}_B + \widetilde{\boldsymbol{J}}\left[\ddot{\boldsymbol{\Phi}}_{Sd} - \boldsymbol{K}_{BD}(\dot{\boldsymbol{\Phi}}_S - \dot{\boldsymbol{\Phi}}_{Sd}) - \boldsymbol{K}_{BP}(\boldsymbol{\Phi}_S - \boldsymbol{\Phi}_{Sd})\right], \tag{5.48}$$

where $\boldsymbol{\Phi}_{Sd}$ is the desired spacecraft attitude; $\boldsymbol{K}_{BD}$ and $\boldsymbol{K}_{BP}$ are control gain matrices. It is apparent that this control law is able to enforce the attitude error $\boldsymbol{e}_{\boldsymbol{\Phi}_S} = \boldsymbol{\Phi}_S - \boldsymbol{\Phi}_{Sd}$ to zero. The actual required RW torques $\boldsymbol{\tau}_w$ then can be derived from $\widetilde{\boldsymbol{\tau}}_B$ according to (5.13). Control and magnetic unloading of the RWs have been detailed in Section 3.3.2 and Section 3.3.3 and thus are not restated in this chapter.

5.4 Post Capture Control

Due to the floating nature and conservation property of the entire system, in an open-contact capture operation, the target will tend to drift away from FFSR and the robot base will move in an opposite direction. The EE has to follow the target motion during the capture phase to maintain the contact and avoid losing the target. Suppose that an on-board mechanism is activated and can firmly fasten the target with the EE to complete the capture task and thus proceed the mission to post-capture phase.

In post-capture phase, the inherited "stretching" motion of the robot arm will finally lead to a singular configuration for the robot arm without effectively controlling the system motion. Besides, the target is tumbled due to the contact forces and is required to be detumbled to prepare next assembly task. Therefore, post-capture control plays an crucial role in carrying out successful space mission.

Since the initial momentum of the entire system is assumed to be zero, the desired final state is set to be a fully stationary system with a desired spacecraft attitude maintained right throughout the time. For a case where the initial momentum of the entire system is not zero, the overall momentum can be absorbed by rotating momentum exchange devices and/or counteracted by firing thrusters.

In that the captured target has been rigidly connected with the EE, the FFSR model holds a same form as the model established in Section 4.2 for an FFSR in the approaching phase. Assume the dynamics of the space robot incorporating the captured target can be updated using system identification as,

$$\boldsymbol{A}'(\boldsymbol{q})\ddot{\boldsymbol{q}} + \boldsymbol{B}'(\boldsymbol{q}, \dot{\boldsymbol{q}})\dot{\boldsymbol{q}} = \boldsymbol{\tau}, \tag{5.49}$$

where $\boldsymbol{A}'$ and $\boldsymbol{B}'$ represent the updated inertial matrix and nonlinear terms, respectively. Set error state vector $\boldsymbol{e}_1 = \boldsymbol{q} - \boldsymbol{q}_d$, $\boldsymbol{e}_2 = \dot{\boldsymbol{q}} - \dot{\boldsymbol{q}}_d$, where $\boldsymbol{q}_d$ and $\dot{\boldsymbol{q}}_d$ denote the desired FFSR's motion. Rewrite (5.49) in state-space form as,

$$\begin{aligned} \dot{\boldsymbol{e}}_1 &= \boldsymbol{e}_2, \\ \dot{\boldsymbol{e}}_2 &= -\boldsymbol{A}'^{-1}(\boldsymbol{e})\boldsymbol{B}'(\boldsymbol{e})\left(\boldsymbol{e}_2 + \dot{\boldsymbol{q}}_d\right) - \ddot{\boldsymbol{q}}_d + \boldsymbol{A}'^{-1}(\boldsymbol{e})\boldsymbol{\tau}. \end{aligned} \tag{5.50}$$

Despite the updating dynamic model, a coordination controller based on boundary layer Sliding Mode Control (SMC) method developed in Section 4.3 can be adopted to securely control the motion of a space robot which may deal with different loads in a complicated on-orbit assembly mission. Application of the derived smoothed SMC control law in (4.24) to the model described in (5.50) returns,

$$\tau_i^\star = -\lambda_i e_{2i} + \ddot{q}_{di} - \hat{\hat{f}}_i' - \hat{h}_i' - (f_i^{\star\star\prime} + h_i^{\star\prime} + \alpha_i)\mathrm{sat}(\sigma_i), \qquad i = 1, 2, \cdots, n+3, \tag{5.51}$$

where $\tau_i^\star$, λ_i, $\hat{\hat{f}}_i'$, $f_i^{\star\star\prime}$, $\hat{h}_i'$, $h_i^{\star\prime}$, α_i and σ_i can be derived in a similar way as those symbols in Section 4.3.

5.5 Simulation

To demonstrate effectiveness of the proposed control laws, two examples are presented in this section. First a case where a three-link planar FFSR is utilized to implement capture of a floating target is investigated, and next another case where a four-link FFSR is used to drive a screw into a floating target is analyzed. Conditions and assumptions shared by these two examples are introduced as follows:

1. At the initial state of the capture phase, the entire system, including the space robot and the target, is stationary and the EE (or the clamped screw) has been positioned at the contact point. Such settings are realizable and can be achieved in approaching phase by adopting the motion control method proposed in Chapter 4.

2. For the capture phase, the FFSR are required to control its EE motion so as to exert an appropriate contact force to the target and follow a designated contact point despite the intrinsic floating feature of the system. Meanwhile, the spacecraft base is expected to be regulated and maintained at a desired orientation regardless of its translation.

3. A one-second time interval is set between the capture operation and post-capture phase, as the controller for capture operation requires some time to achieve its desired motion (also the initial condition for post-capture phase) as well as to activate and complete the establishment of a rigid contact between the EE and the target.

4. For the post-capture phase, the target is manipulated by the FFSR and is required to be detumbled. Specifically, the desired final state can be depicted as zero joint rate ($\dot{\phi}_{id} = 0$) and zero attitude error ($\boldsymbol{\Phi}_{Sd} = \boldsymbol{0}$), regardless of the FFSR's final configuration.

5. To demonstrate robustness of the control methods, external disturbances and parametric uncertainties are considered in the simulation. The disturbance is represented by applying an external torque $\boldsymbol{D} = [0, 0, 0.1]^T$ Nm to the base. In the controller of the simulation, nominal values of $\hat{\boldsymbol{A}}_F(\hat{\boldsymbol{A}}')$ and $\hat{\boldsymbol{B}}_F(\hat{\boldsymbol{B}}')$ are

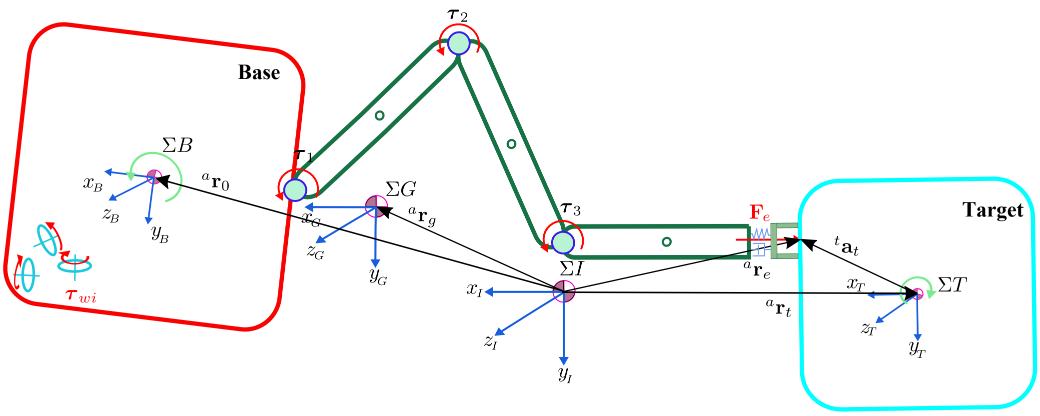

Figure 5.6: Model of a 3-link space robot contacting with a floating target

used; actual matrices $\boldsymbol{A}_F(\boldsymbol{A}')$ and $\boldsymbol{B}_F(\boldsymbol{B}')$ used in the dynamic model of the simulation are set as $\boldsymbol{A}_F = 1.1\hat{\boldsymbol{A}}_F(\boldsymbol{A}' = 1.1\hat{\boldsymbol{A}}')$ and $\boldsymbol{B}_F = 0.9\hat{\boldsymbol{B}}_F(\boldsymbol{B}' = 0.9\hat{\boldsymbol{B}}')$ to represent system uncertainties (see Section 4.6.1).

In contrast to the three-link robot capture case, an external friction torque is inevitably induced and applied at the EE by the floating target in the screw-driving example, which extends the control objectives to a more complicated three-dimensional case. Besides, the rotation of the fourth link has to be controlled to implement a desired screw-driving operation. Details of the screw-driving scenario will be illustrated in Section 5.5.2.

5.5.1 Target Capture

Operation Scenario

Table 5.1: Specifications of the 3-link space robot and the target

Body		Base	Link 1	Link 2	Link 3	RW	Target
Mass(kg)		100	10	10	10	5	80
Inertia (kg·m^2)	I_x	30	0.016	0.016	0.016	0.1	25
	I_y	30	1.6	1.6	1.6	0.1	25
	I_z	30	1.6	1.6	1.6	0.1	25
a (m)		1.25	1	1	1	-	1
b (m)		1.25	1	1	1	-	1

In this example, a three-link planar FFSR is used to fulfil capture of a floating target, as shown in Figure 5.6. Kinematic and dynamic parameters of the space robot and the target are listed in Table 5.1. The figure illustrates the initial state of the contact scenario which can be elaborated as follows: the target frame is aligned with the inertial frame; the EE has been positioned at the designated contact point where a grapple fixture is assumed to be located and presents an orientation perpendicular to the contact target surface; the location of the contact point is set in a condition where the generated contact force does not pass through the CM of the target and a tumbling torque will be induced by the contact force. Initial values listed in Table 5.2 facilitates such a scenario.

Table 5.2: Initial conditions of the capture operation

Description		Symbol	Value	Unit
Position	EE	${}^{a}\boldsymbol{r}_{e}$	$[-2.4433, -0.0046, 0]^T$	m
	Contact point	${}^{a}\boldsymbol{r}_{tf}$	$[-2.4433, -0.0046, 0]^T$	m
	FFSR	${}^{a}\boldsymbol{r}_{g}$	$[2.1190, -0.3048, 0]^T$	m
	Base	${}^{a}\boldsymbol{r}_{0}$	$[2.7877, -0.2217, 0]^T$	m
	Target	${}^{a}\boldsymbol{r}_{t}$	$[-3.4433, 0.4954, 0]^T$	m
Attitude/ Angles	Joint	$\boldsymbol{\Phi}_{M}$	$[70, -120, 60]^T$	$\circ$
	Base	$\boldsymbol{\Phi}_{S}$	$[0, 0, -10]^T$	$\circ$
	Target	$\boldsymbol{q}_{t}$	$[0, 0, 0, 1]^T$	—
Linear velocity	FFSR	$\boldsymbol{v}_{g}$	$\mathbf{0}$	m/s
	Target	$\boldsymbol{v}_{t}$	$\mathbf{0}$	m/s
Angular velocity	Joint	$\dot{\boldsymbol{\Phi}}_{M}$	$\mathbf{0}$	rad/s
	FFSR	$\boldsymbol{\omega}_{g}$	$\mathbf{0}$	rad/s
	Base	$\boldsymbol{\omega}_{B}$	$\mathbf{0}$	rad/s
	Target	$\boldsymbol{\omega}_{t}$	$\mathbf{0}$	rad/s

Under the premise of above conditions, the motion of the system will be constrained to $x_I - y_I$ plane in the capture phase. The initial relative posture between the EE and the target shown in Figure 5.6 is required to be maintained throughout the contact operation so as to always generate a normal contact force. Therefore, the EE needs to follow the target motion along y_T axis which belongs to motion-controlled subspace and apply a contact force along x_T axis which belongs to force-controlled subspace. Note that the contact force arises only when the EE pushes against the target surface and not when it tends to recede away.

A desired pushing force defined by a smooth sinusoidal function of maximum amplitude 2N is given in Figure 5.8. Such a continuous and differentiable function is selected since the derivative of the desired contact force is used in the controller. Also the force is set to last a certain period (5 seconds) with an appropriate magnitude to avoid inducing singularity problems for the space robot.

Based on above settings, the contact phase lasts 5 seconds from $t = 0$s to $t = 5$s, during which period the hybrid controller and the base attitude controller proposed in Section 5.3 are applied. Thereafter, a time interval from $t = 5$s to $t = 6$s allows rigid connection between the chaser FFSR and the client target, during which the hybrid controller is continuously used to make the EE to follow the target. At $t = 6$s, the control mode switches from capture-phase control to post-capture control. The post-capture phase starts from $t = 6$s and proceeds afterwards, during which period the post-capture controller proposed in Section 5.4 is adopted.

Control parameters used in the simulation are listed in Table 5.3. For the contact model, the stiffness k_δ is dominantly dependent on the compliance on the wrist; $\boldsymbol{a}_t$ represents position of the reference point located on the target surface and remains constant throughout in the target frame. For capture control phase, the selection matrices $\boldsymbol{S}_v$ and $\boldsymbol{S}_t$ are determined by the contact geometry presented in Figure 5.6 and remain constant throughout in the target frame. For both phases, torque constraints are considered for joint actuators and RW motors. Other parameters are determined in a same way as discussed in Chapter 4.

Simulation Results

To intuitively demonstrate system response throughout contact operation, the contact scenario corresponding to Figure 5.6 is sketched based on simulation data and presented in Figure 5.7. The figure shows that the EE successfully holds a perpendicular configuration w.r.t. the contact target surface despite a tumbling motion of the target. Meanwhile, the spacecraft base is reoriented from an initial error to the desired orientation. A penetration between the EE tip and the target surface implies a generated contact force. Also, it is evident that the spacecraft base and the target move in an opposite direction along x_I axis due to momentum conservation property of the entire system.

Table 5.3: Parameters in the simulation

Module	Parameter	Value	Unit	Parameter	Value	Unit
Contact dynamics	k_δ	50	N/m	${}^t\boldsymbol{a}_t$	$[1, -0.5, 0]^T$	m
Capture control	γ_d	0	rad	v_{evd}	0	m/s
	${}^t\boldsymbol{S}_v$	$[0, 1, 0]^T$	—	${}^t\boldsymbol{S}_f$	$[1, 0, 0]^T$	—
	K_{Pv}	16	—	K_{Iv}	64	—
	K_{Df}	16	—	K_{Pf}	64	—
	$K_{P\omega}$	16	—	$K_{I\omega}$	64	—
	K_{BD}	10	—	K_{BP}	25	—
Post-capture control	γ_d	0	rad	$\dot{\phi}_{id}$	0	rad/s
	λ_i	3	—	α_i	0.01	—
	ε_i	0.1	—	$\bar{\pi}$	0.1	—
	$\bar{a}_1$	0.9	—	$\bar{a}_2$	1.1	—
	$\bar{b}_1$	0.9	—	$\bar{b}_2$	1.1	—
	$\bar{c}_1$	0.9	—	$\bar{c}_2$	1.1	—
	$\boldsymbol{\tau}_{J\max i}$	10	Nm	$\boldsymbol{\tau}_{w\max i}$	5	Nm

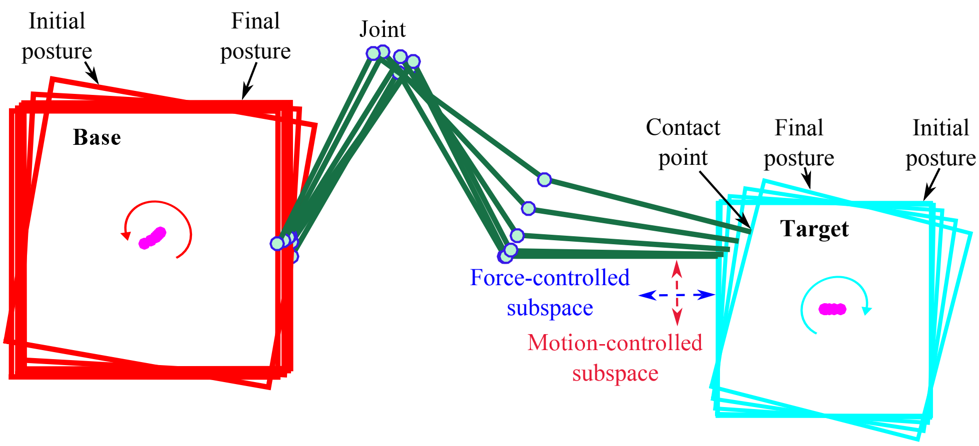

Figure 5.7: Scenario of a three-link robot contacting with a floating target

Figure 5.8 presents the generated contact force. The negative actual force (along x_T axis) implies that the space robot keeps pushing the target and thus does not lose contact. Comparison between the actual contact force and the desired contact force indicates that the system achieves good force tracking performance. The force error is restricted within 3% of the amplitude of the desired force. Also the EE position tracking error along y_T axis illustrated in Figure 5.9 is of negligible magnitude

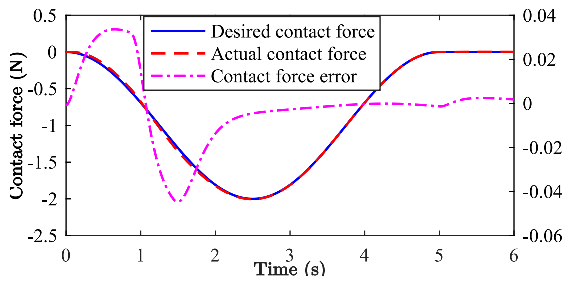

Figure 5.8: Contact force

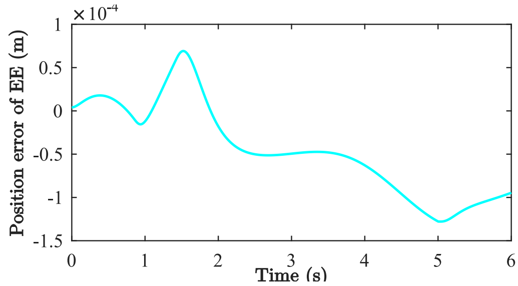

Figure 5.9: Position tracking error of EE

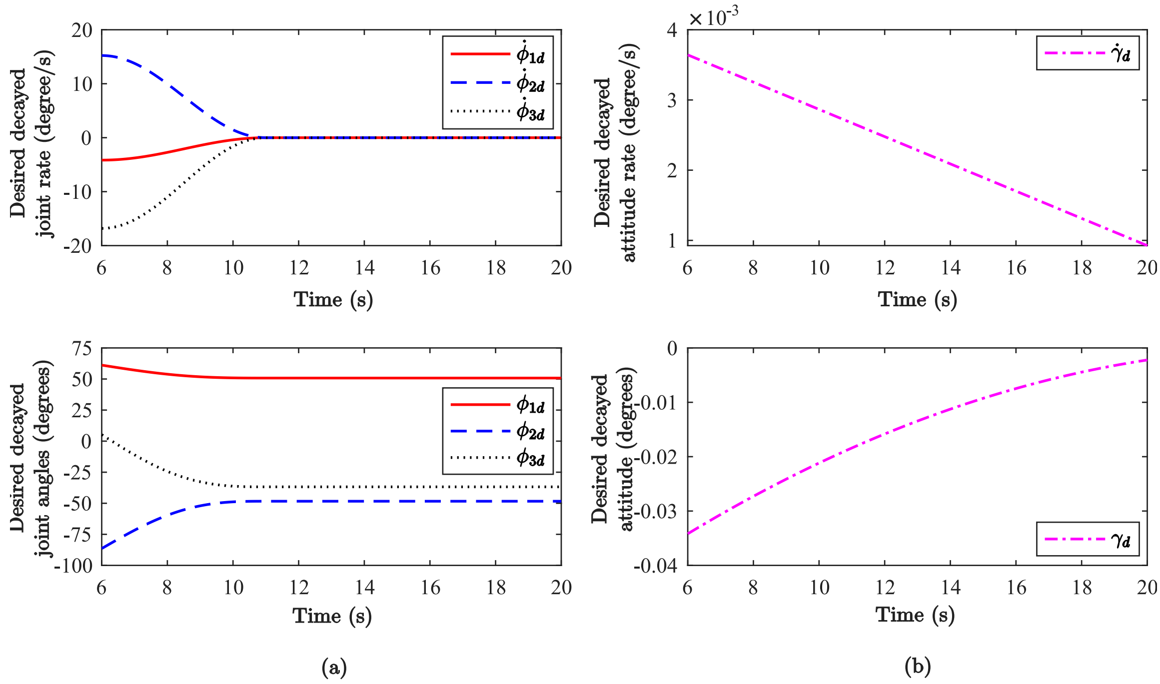

Figure 5.10: Desired FFSR motion for post-capture phase: (a) desired joint motion and, (b) desired base motion.

(10^{-4}m). This demonstrates that the controller can enforce the EE to follow a fixture to be grasped and thus exert a force at the designated contact point.

Next, post-capture scenario is addressed. The initial state of post-capture phase is actually the final state of capture phase, i.e. t_0 (post-capture) $= t_f$ (capture)$=$ 6s (rigid connection interval is included). As mentioned in Condition 4 at the beginning of this section, the desired final state for the space robot in post-capture phase can be specifically depicted as zero joint rate ($\dot{\phi}_{id} = 0, i = 1, 2, 3$) and zero attitude error ($\gamma_d = 0$), regardless of its final configuration. To formulate the desired post-capture motion for the space manipulator as well as for the spacecraft base, trajectories of joint rate and of base angular velocity are first determined according to their

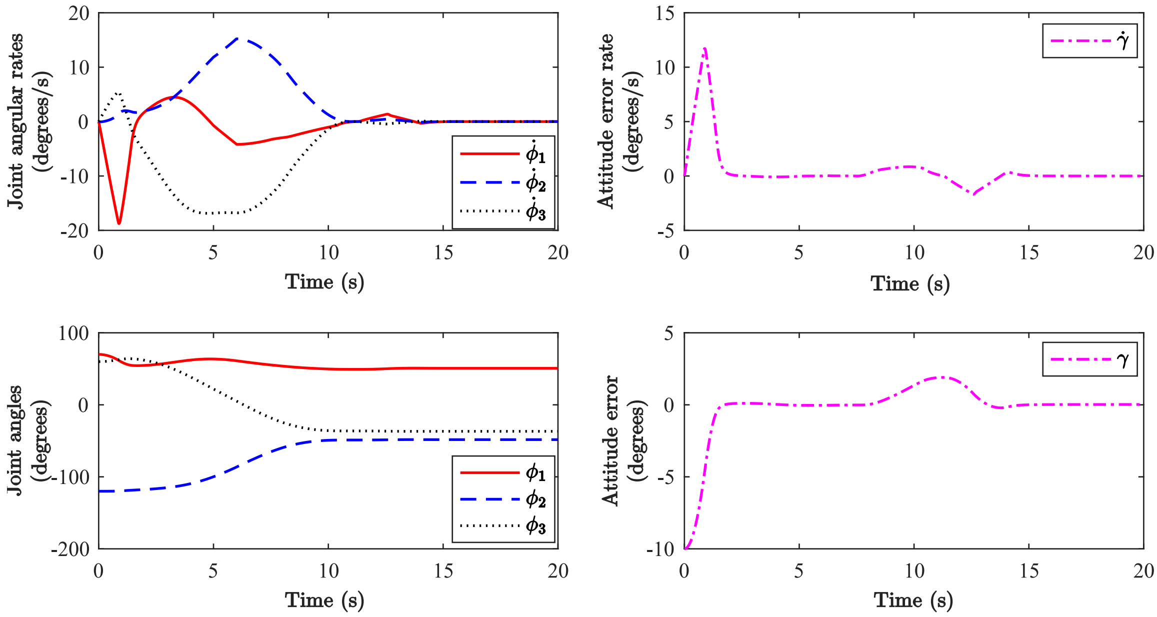

(a) (b)

Figure 5.11: Actual FFSR motion throughout capture phase and post-capture phase: (a) joint motion and, (b) base motion.

initial states and referenced final states. Then the velocity-level quantities can be integrated to deduce the designated joint angles and base attitude. Determination of desired post-capture motion is detailed as follows:

Set $\dot{\phi}_i$ decaying along a smooth cosine function from its initial value $\dot{\phi}_i$ $(t = 6\text{s})$ to zero at $t = 11\text{s}$. Note that no specific manipulator configuration is required and this condition can result in an arbitrary manipulator configuration. Distinguish from joint motion, the spacecraft base is required to be finally oriented at $\gamma_d = 0$ with zero rotation rate $\dot{\gamma}_d = 0$. Hence, the desired angle rate is set to decay along a slope function, of which the function slope k_i is determined by initial base rotation rate $(\dot{\gamma}(t = 6\text{s}))$ and initial attitude error $(\gamma(t = 6\text{s}))$ as $k_i = 2\gamma(t = 6\text{s})/\dot{\gamma}(t = 6\text{s})$. In accordance with such conditions, the desired FFSR motion for post-capture phase is presented in Figure 5.10. Note that with a longer simulation time the desired base attitude rate will reach zero and the desired attitude error converges to $\gamma_d = 0$.

The manipulator's motion, throughout capture and post-capture phases, is illustrated in Figure 5.11 (a). As shown in the figure, for the first 5 seconds, the joints move to achieve their desired motion for capture operation; from $t = 5\text{s}$ to $t = 6\text{s}$, the joints' motion allows the EE to smoothly follow the tumbling target

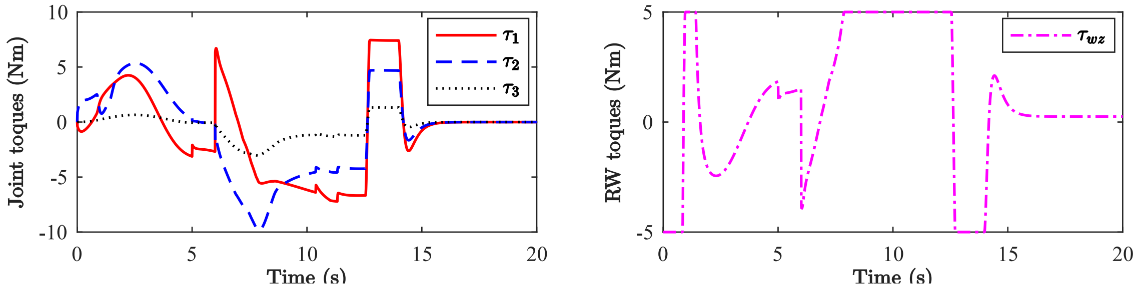

Figure 5.12: Control torques

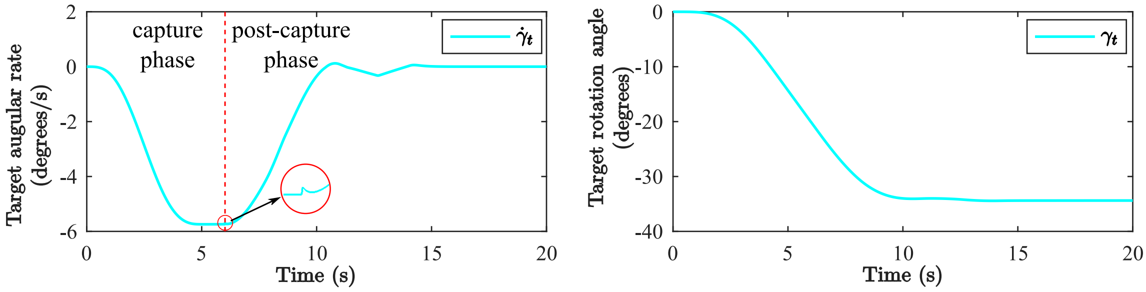

Figure 5.13: Rotation of the target

so as to establish the rigid connection; for the post-capture phase which starts from t=6s, the angular rates of all joints decrease to zero following their predefined trajectories (Figure 5.10 (a)) and thus the joint angles remain constant afterwards. This indicates that the space manipulator will maintain this configuration.

Figure 5.11 (b) demonstrates that the spacecraft attitude error is able to converge from its initial value $\gamma(0) = -10°$ to zero around $t = 2$s, despite the disturbance induced by manipulator's motion. Even after the space robot is rigidly connected with the tumbling bulky target, the robust SMC controller successfully constrains the base attitude error within an acceptable extent since the target angular momentum is transferred to onboard RWs.

Figure 5.12 presents the corresponding output joint torques and RW torques, which are restricted within practical limits. The figure indicates that the output torques suddenly increase to large values at $t = 6$s in order to detumble the added load.

Figure 5.13 depicts the target motion. Since the contact force does not pass its CM, the target is tumbled during the contact operation (from $t = 0$s to $t = 5$s) and then gradually stops rotating (from $t = 6$s) after connected with the EE. It can be seen that despite a one-second interval existing before implementing post-capture control, a small gap of rotation rate between the EE and the target exists. This is practically acceptable and can be relieved if extending the time interval.

5.5.2 Screw-Driving Operation

In this section, a potential screw-driving operation by an FFSR that may be required in future on-orbit assembly missions is addressed to evidence effectiveness of the proposed controllers. First contact dynamics of a screw-driving operation which is extended from Section 5.2.4 is introduced, followed by elaboration of the screw-driving scenario. Finally, numerical simulation results are presented.

Contact Model

Since friction torques arise during the screw-driving operation, the floating target will tumble around the screw axis. Relative rotation angle between the clamped screw (motion defined as EE tip) and the nut (motion defined as target reference point) along this specific axis is

$$\Delta\theta = {}^t\theta_e - {}^t\theta_t, \tag{5.52}$$

where ${}^t\theta_e$ denotes EE rotation vector component along screw's axis and ${}^t\theta_t$ denotes target rotation vector component along the same axis. The insertion displacement h relates to $\Delta\theta$ by,

$$h = \frac{\Delta\theta}{2\pi} p, \tag{5.53}$$

where p is the screw pitch.

Local indentation δ in this example is given by (Figure 5.14)

$$\delta = h - ({}^t x_t - {}^t x_e), \tag{5.54}$$

where ${}^t x_t$ and ${}^t x_e$ have been defined in (5.21) and (5.22). ${}^a\boldsymbol{r}_{tf}$ in (5.21) and (5.22) denotes position vector of the reference point which is fixed at the center of the

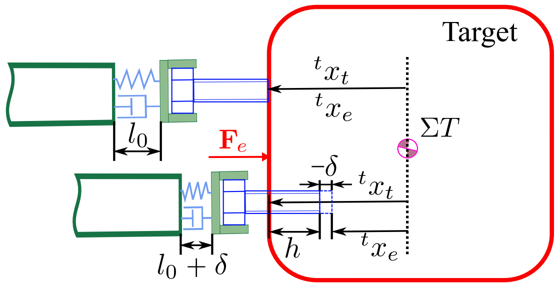

Figure 5.14: Contact Force

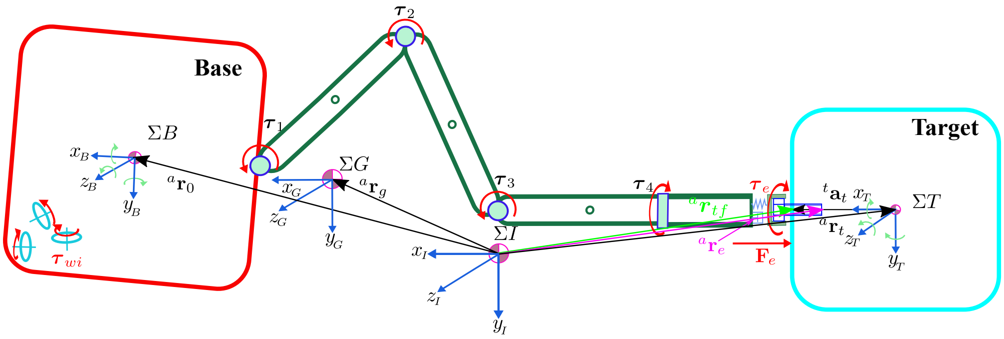

Figure 5.15: Model of screw-driving operation by a 4-link space robot

threaded hole on the target surface. Substitution of (5.53), (5.54) into (5.19) returns,

$$f_n = k_\delta \left[h - ({}^t x_t - {}^t x_e)\right] = k_\delta \left[\frac{\Delta\theta}{2\pi} p - ({}^t x_t - {}^t x_e)\right]. \tag{5.55}$$

Friction torque generated by inserted portion of the screw has to be included when analyzing the system which takes the following form:

$${}^t\boldsymbol{T}_e = c\ d\ {}^t\boldsymbol{F}_e = k_t {}^t\boldsymbol{F}_e, \tag{5.56}$$

where c is the coefficient of friction; d is the nominal screw diameter; $k_t = c\ d$.

Operation Scenario

As shown in Figure 5.15, a four-link FFSR is used to drive a screw into a floating target. Kinematic and dynamic parameters of the space robot and the target are listed in Table 5.4. Initially, the target frame is aligned with the inertial frame. The screw attached to the EE is positioned at the center of the threaded hole, in such a manner that the contact force passes through the CM of the target and no tumbling

Table 5.4: Specifications of the 4-link space robot and the target

Body		Base	Link 1	Link 2	Link 3	Link 4	RW	Target
Mass(kg)		100	7.5	7.5	7.5	5	5	80
Inertia ($\text{kg}\cdot\text{m}^2$)	I_x	30	0.012	0.012	0.012	0.8	0.1	25
	I_y	30	1.2	1.2	1.2	0.8	0.1	25
	I_z	30	1.2	1.2	1.2	0.008	0.1	25
a (m)		1.25	0.75	0.75	0.75	0.5	-	1
b (m)		1.25	0.75	0.75	0.75	0.5	-	1

torques will be induced by this contact force. Also, the axis of the screw, which aligns with x-axis of the EE frame is perpendicular to the contact target surface. Initial values listed in Table 5.5 satisfy conditions of such a scenario.

Table 5.5: Initial conditions of the screw-driving operation

Description		Symbol	Value	Unit
Position	EE	${}^a\boldsymbol{r}_e$	$[-2.2060, 0.1139, 0]^T$	m
	Contact point	${}^a\boldsymbol{r}_{tf}$	$[-2.2060, 0.1139, 0]^T$	m
	FFSR	${}^a\boldsymbol{r}_g$	$[2.0116, -0.0715, 0]^T$	m
	Base	${}^a\boldsymbol{r}_0$	$[2.5632, -0.0167, 0]^T$	m
	Target	${}^a\boldsymbol{r}_t$	$[-3.2060, 0.1139, 0]^T$	m
Attitude/ Angles	Joint	$\boldsymbol{\Phi}_M$	$[76, -140, 70, 0]^T$	$\circ$
	Base	$\boldsymbol{\Phi}_S$	$[0, 0, -6]^T$	$\circ$
	Target	$\boldsymbol{q}_t$	$[0, 0, 0, 1]^T$	—
Linear velocity	FFSR	$\boldsymbol{v}_g$	$\boldsymbol{0}$	m/s
	Target	$\boldsymbol{v}_t$	$\boldsymbol{0}$	m/s
Angular velocity	Joint	$\dot{\boldsymbol{\Phi}}_M$	$\boldsymbol{0}$	rad/s
	FFSR	$\boldsymbol{\omega}_g$	$\boldsymbol{0}$	rad/s
	Base	$\boldsymbol{\omega}_B$	$\boldsymbol{0}$	rad/s
	Target	$\boldsymbol{\omega}_t$	$\boldsymbol{0}$	rad/s

The screw-driving task is aimed to be achieved by controlling EE motion and applying an appropriate pushing force. Note that practically either a pushing axial force or a pulling axial force will work though it should be a pushing force initially. The later indicates that the space robot first stretches its arm to exert a pushing force on the target but retracts its arm when the screw has been inserted to a safe threshold. For the screw-driving model presented in Figure 5.15, the space manipulator motion will be constrained to a plane perpendicular to the operating target surface. Actually, this plane should be $x_I - y_I$ plane if the base attitude is successfully regulated. By configuring the first three articulated links, the EE can be controlled at an arbitrary orientation in the operating plane, while the fourth link applies the turning torque. Assume no off-plane net force is generated during the operation.

Figure 5.16 presents the desired axial force f_{nd} which is same as that of the 3-link FFSR example. Suppose a 30mm insertion displacement needs to be accomplished between $t = 0$s and $t = 5$s, which derives a desired relative rotation rate $\Delta\dot{\theta}_d$ defined by the same-type smooth sinusoidal function of the desired force with amplitude 1440°/s. With a faster rotation speed along the screw's axis, the EE keeps an orientation in alignment with the target frame. As a result, the desired EE angular velocity used in (5.46) becomes ${}^a\boldsymbol{\omega}_{ed} = \boldsymbol{R}_t^a\ {}^t\boldsymbol{\omega}_{ed} = \boldsymbol{R}_t^a \left({}^t\boldsymbol{\omega}_t + \boldsymbol{u}_n\ \Delta\dot{\theta}_d\right)$. Control parameters used in the simulation are listed in Table 5.6, which are determined in a similar way as those of Table 5.3.

Simulation Results

As presented in (5.55), the contact force relates to the relative rotation angle $\Delta\theta$ with k_δ. Since both the insertion displacement and the contact force are supposed to be controlled, their variation w.r.t. different contact stiffness k_δ is investigated. As illustrated by Figure 5.16, the maximum force tracking error increases from 1.8% to 3.7% of the desired force's amplitude when k_δ increases from 200N/m to 400N/m. Nevertheless, though a smaller stiffness improves the force tracking performance, an undesirable overshoot of the insertion displacement is induced as shown in Figure 5.17. Therefore, to avoid undesirable unscrewing during assembly, $k = 400$N/m is practically preferred and applied to simulate the model. EE position tracking error is demonstrated in Figure 5.18, which is of negligible magnitude and should be acceptable in practice.

The screw-driving scenario is sketched in Figure 5.19 based on the simulation results. It shows that the EE holds a perpendicular configuration w.r.t. the contact target surface throughout the operation. At the same time, the spacecraft base is reoriented from an initial error to the desired orientation. A penetration between the

Table 5.6: Parameters in the simulation

Module	Parameter	Value	Parameter	Value
Contact dynamics	k_δ	400 N/m	${}^t\boldsymbol{a}_t$	$[1,0,0]^T$ m
	p	1.5 mm	${}^t\boldsymbol{u}_n$	$[1,0,0]^T$
	c	0.2	d	20 mm
Capture control	$\boldsymbol{\Phi}_{Sd}$	$\boldsymbol{0}$ rad	$\boldsymbol{v}_{evd}$	$[0,0]^T$ m/s
	${}^t\boldsymbol{S}_v$	$\begin{bmatrix} 0 & 1 & 0 \\ 0 & 0 & 1 \end{bmatrix}^T$	${}^t\boldsymbol{S}_f$	$[1,0,0]^T$
	$\boldsymbol{K}_{Pv}$, $\boldsymbol{K}_{Df}$, $\boldsymbol{K}_{P\omega}$	$\begin{bmatrix} 30 & & \\ & 30 & \\ & & 30 \end{bmatrix}$	$\boldsymbol{K}_{Iv}$, $\boldsymbol{K}_{Pf}$, $\boldsymbol{K}_{I\omega}$	$\begin{bmatrix} 225 & & \\ & 225 & \\ & & 225 \end{bmatrix}$
	$\boldsymbol{K}_{BD}$	$\begin{bmatrix} 4 & & \\ & 4 & \\ & & 4 \end{bmatrix}$	$\boldsymbol{K}_{BP}$	$\begin{bmatrix} 4 & & \\ & 4 & \\ & & 4 \end{bmatrix}$
Post-capture control	$\boldsymbol{\Phi}_{Sd}$	$\boldsymbol{0}$ rad	$\dot{\phi}_{id}$	0 rad/s
	λ_i	3	α_i	0.01
	ε_i	0.1	$\bar{\pi}$	0.1
	$\bar{a}_1$	0.9	$\bar{a}_2$	1.1
	$\bar{b}_1$	0.9	$\bar{b}_2$	1.1
	$\bar{c}_1$	0.9	$\bar{c}_2$	1.1
	$\boldsymbol{\tau}_{J\max i}$	10 Nm	$\boldsymbol{\tau}_{w\max i}$	5 Nm

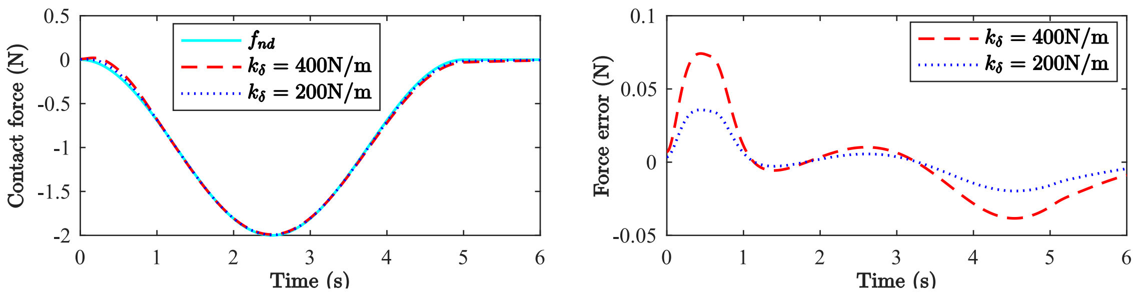

Figure 5.16: Contact force

EE tip and the target surface implies a combination of the insertion displacement and axial force. Note that Figure 5.19 omits rotation off $x_I - y_I$ plane which is demonstrated in later specific results.

The desired post-capture motion for the screw-driving operation can be obtained in a similar way as that of the capture example and is depicted in Figure 5.20.

Figure 5.21 (a) illustrates the FFSR motion throughout screw-driving operation

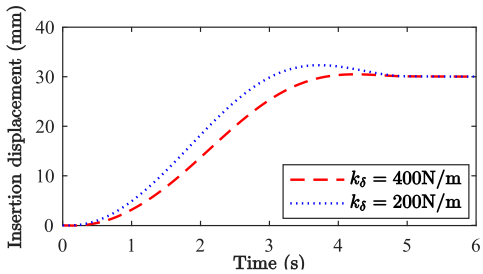

Figure 5.17: Insertion displacement

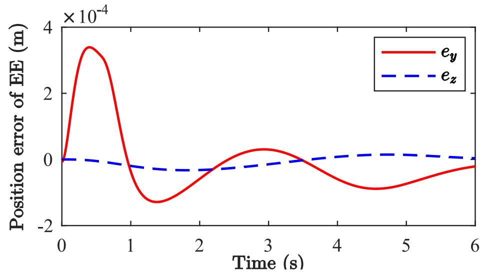

Figure 5.18: Position tracking error of EE

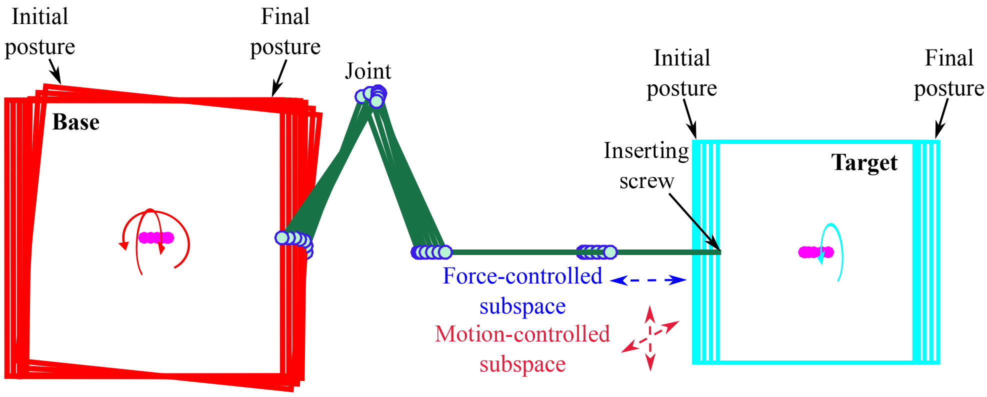

Figure 5.19: Scenario of a four-link FFSR driving a screw into a floating target

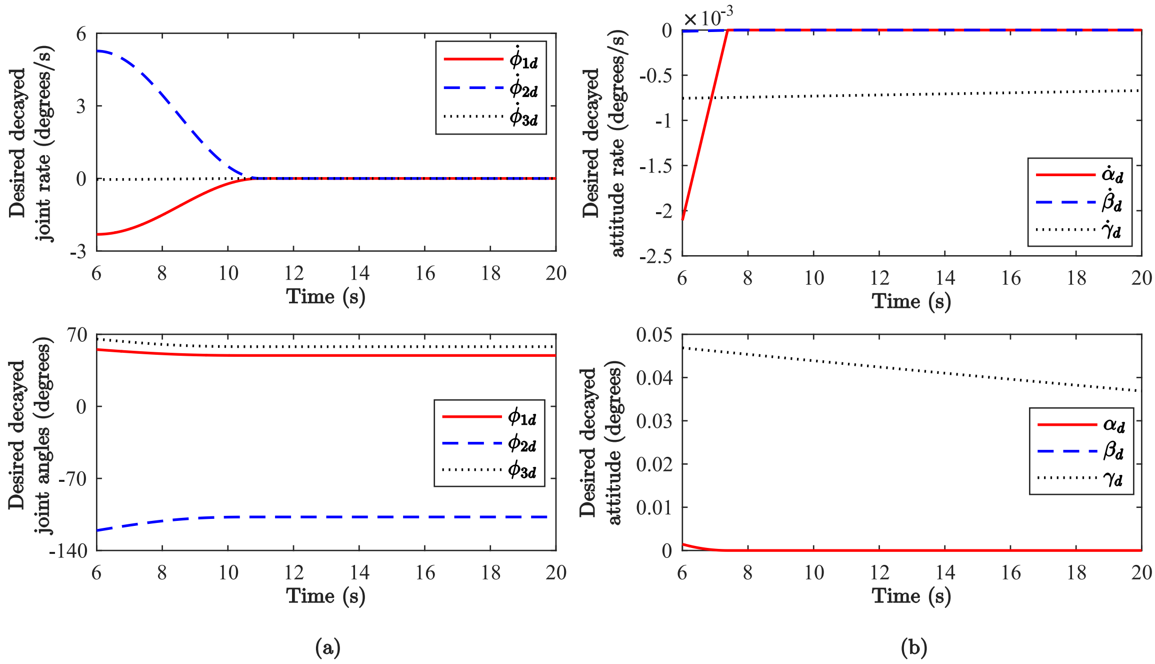

Figure 5.20: Desired FFSR motion for post-capture phase: (a) desired joint motion and, (b) desired base motion.

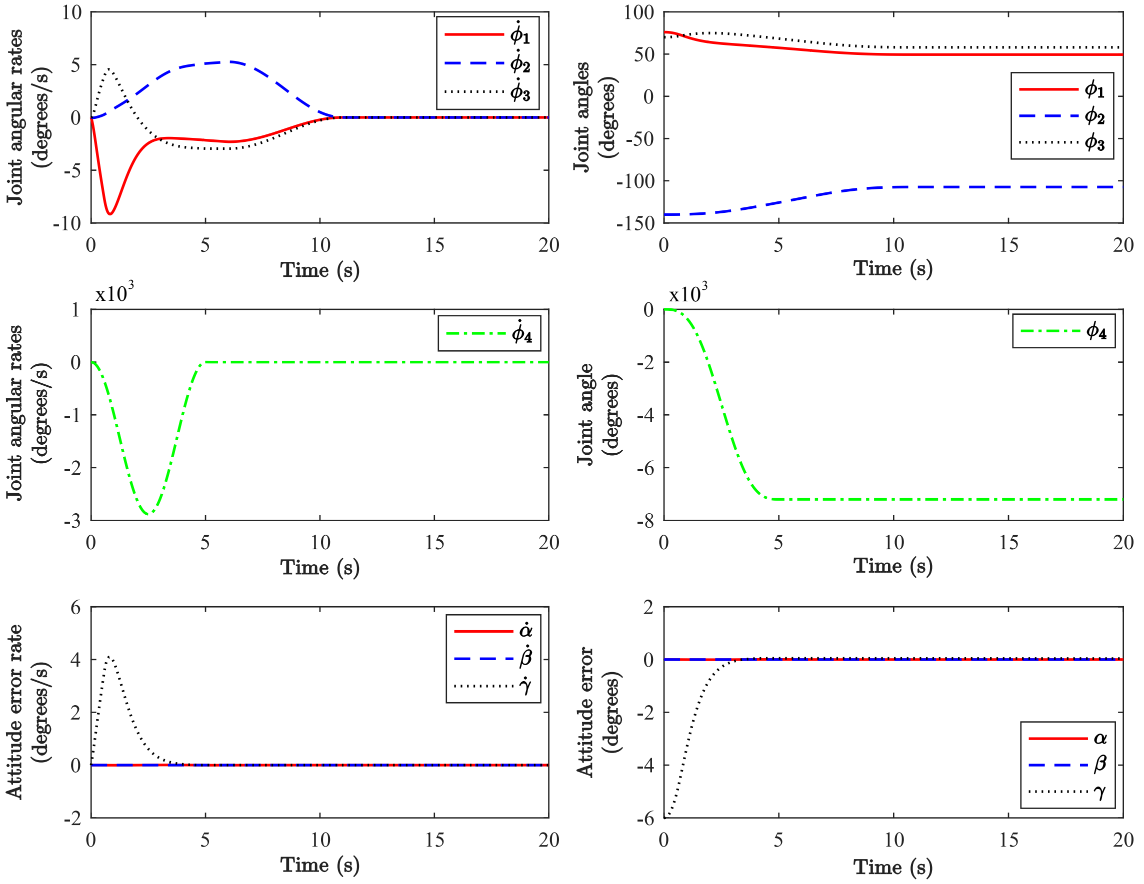

(a) (b)

Figure 5.21: Actual FFSR motion throughout capture phase and post-capture phase: (a) angular rate and, (b) rotation angle.

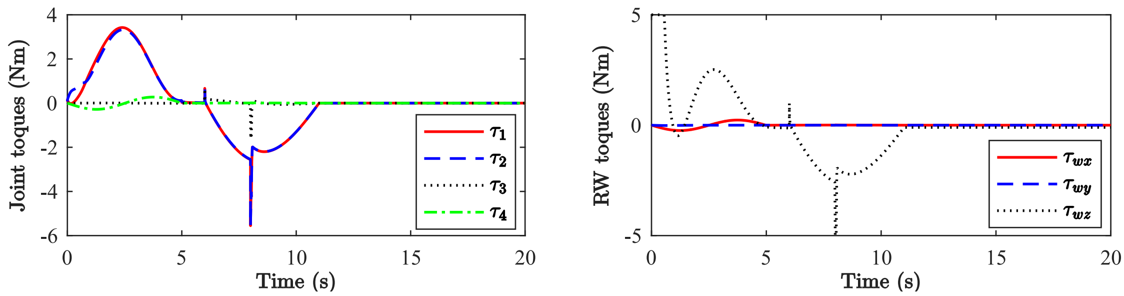

Figure 5.22: Control torques

and post-screw phase. For the first 5 seconds, the first joints move to maintain a desired EE position and orientation w.r.t. the target; while the fourth joint rotates with high speed to drive the screw into the threaded hole and stops rotating when the inserted displacement reaches 30mm. From t = 5s to t = 6s, the joints (joint 1-3) move to allow the EE to follow the moving target. For the post-capture phase,

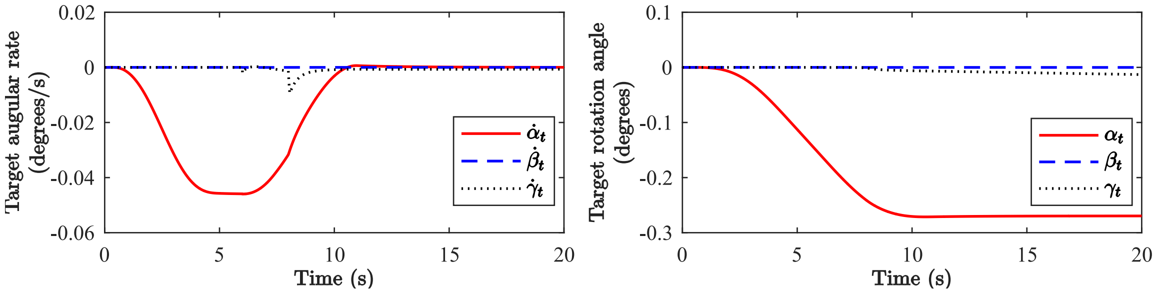

Figure 5.23: Rotation of the target

the angular rates of all joints decrease to zero following their predefined trajectory (Figure 5.20) and afterwards the space manipulator maintains this configuration.

Figure 5.21 (b) shows that the spacecraft attitude error converges to zero and reaches within an acceptable extent even when detumbling the bulky target. Corresponding output joint torques and RW torques are presented in Figure 5.22, which are smooth and kept within practical limits. The first spike in the torques is due to the switching from the control law for the capture phase to the control law for the post capture phase, and the second spike is caused by the slope change of the desired decayed attitude in the roll axis as shown in Figure 5.20.

Figure 5.23 depicts the target motion. The target rotates along x_T axis due to the friction torque, and then gradually stops rotating (from $t = 6$s) after rigidly connecting with the EE since the rotation rate of the EE is controlled to decease to zero. The yaw angle γ_t keeps decreasing for post-capture phase, in that the prescribed base attitude rate $\dot{\gamma}_d$ has not reached zero, implying the manipulator and the captured target passively follow their moving base. With a longer simulation time, $\dot{\gamma}_t$ will decrease to zero and γ_t will eventually flatten.

5.6 Summary

This chapter presents a control strategy to maintain accurate End-Effector (EE) contact forces (and torques) during a compliant motion task enabling the successful capture of a space object. First, the modeling of a Free-Flying Space Robot (FFSR) is completed by establishing separate models for the space manipulator and the spacecraft base. Such modeling scheme enables separate design for force controller and attitude controller which can maintain the desired spacecraft attitude while tracking a predefined contact force trajectory. As the core content, the hybrid force and motion controller is then developed based on the space manipulator model by first analyzing the capture motion in the target frame and then transforming it to the inertial frame. Also robust control of the post-capture operations including space robot stabilization and de-tumbling of the space object is addressed. The capture and post-capture operation in the presence of external disturbances and system uncertainties are verified through two simulation examples. The results demonstrate that the controllers can enforce accurate force tracking performance and attitude regulation for the capture phase, and the system can be stabilized for the post-capture phase.

Chapter 6

Conclusions and Future Work

6.1 Conclusions

The focus of this thesis is to develop systematic modeling and control methods for spacecraft, which can provide a theoretical basis for carrying out potential on-orbit assembly tasks. In this final chapter, principal contributions of the research and potential future work are presented. The first part claims and evaluates the main outcomes of this thesis. Further, some recommendations are then given regarding directions of future work.

The main contributions of this thesis can be highlighted as follows.

- A robust attitude controller for a deploying spacecraft which represents a simple specific on-orbit assembly case was developed. The modeling approach proposed for the deploying spacecraft allows a concise model and thus benefits development of the control algorithm. It has been shown that the proposed Twisting-algorithm -based SMC (TASMC) controller is able to accommodate substantial inertia change of the spacecraft resulting from its structural reconfiguration. Also, the controller derives smooth control torques which are ideally suitable to Reaction Wheels (RWs). Such an advantage facilitates on-board fuel savings and precise operations using electrically-powered RWs instead of firing thrusters. It was shown further through numerical simulations that the controller has the capability to steer the satellite to the desired orientation with small settling time in comparison to SQC2S. The proposed control method can therefore be used to implement fast and high-accuracy tracking operations.

- The dynamic equations of a Free-Flying Space Robot (FFSR) with actuating RWs were reformulated. Previous derivations of the model for an FFSR addressed the system by assuming external attitude control torques. Much to the contrary, the application of RWs is discussed specifically in this research and the model developed takes into account the contribution of RWs to the angular momentum of the entire system. Such a comprehensive model is theoretically more accurate than the conventional space robot model but results in loss of advantageous properties of the conventional space robot model, i.e. the coefficient matrix is neither symmetric nor positive definite. The adopted diagonalization method successfully transformed the strongly coupled problem into multiple single-input problems by introducing virtual torques, which provides valuable insight into application of conventional control methods to complicated nonlinear systems.

- Two robust controllers, i.e. the Sliding Mode Controller with adaptive gains (ASMC) and the Adaptive Variable Structure Controller (AVSC), that can coordinate the robot arm motions and the spacecraft attitude were developed. The controllers have been demonstrated to be effective for both approaching and post-capture phases in the presence of system uncertainties. It has been shown that for the set-point control case, the proposed controllers are able to reduce settling times in comparison to the popular Sliding Mode Control method with constant gains (CSMC), indicating the resulting system can quickly orient the spacecraft to the desired attitude and approach the end-effector to a target by utilizing the full potential of harnessing solar energy. This advantage has a significant effect on a space vehicle which has electrically powered actuators, as in the presented system where all joint motors and RWs are electrically powered. For the path tracking case, the ASMC controller is shown to produce smaller tracking errors compared with AVSC and CSMC, under the condition of holding the control outputs in similar extent. Therefore, the ASMC controller allows the spacecraft to maintain communication links with ground stations with minimal disruptions and/or degradation of signal quality, and to efficiently implement space tasks along specific paths, such as capturing a structural component while avoiding collision with obstacles.

- A novel control-oriented modeling framework of an FFSR subject to external forces was proposed. Such a framework contributes to establishment of separate models for the manipulator and for the spacecraft base. Thereby, by solely analyzing the manipulator model, required joint torques are derived to meet contact force specifications. On the other hand, considering the reaction torques/forces from the first articulated joint to the base as a disturbance, required RW torques are derived to satisfy attitude specifications. As such, the model structure facilitates controller design which achieves simultaneous contact force control and active attitude control, overcoming the disadvantage of the conventional unified model for an FFSR which can only implement force control but without a guarantee of desired spacecraft attitude.

- A control strategy to maintain accurate end-effector contact forces during a compliant motion task enabling the successful capture of a space object was developed. The hybrid controller presented in this research extends the powerful concept of hybrid control to the realm of free-flying space robot. Such a controller incorporates the consistent motion between FFSR's end-effector and the tumbling floating target. The presented methodologies are substantially different to the currently practiced methods such as entrapping the space objects using bulky infrastructure of which the launching and orbiting are expensive. The novelty of this controller also reflects in achieving force trajectory tracking performance for open-contact space operations in contrast to impedance controllers proposed in the previous literature which tried to maintain a contact. The work presented provides a theoretical basis for promising robotic/tele-robotic in-space screw-driving operations, which can be extended to any on-orbit servicing task requiring simultaneous force-torque exertion.

6.2 Future Work

Suggestions of future work directions are addressed as below.

- Improvement of space robot model incorporating its flexible properties. Space robots are always designed as light weight structures to save fuel consumption at launch and as such are flexible structures. The intrinsic flexibility of the space robot has an influence on the exact end-effector motion and may excite undesirable vibrations which can result in instability of the system. This aspect needs to be taken into account to build more realistic space robot model and thereby develop control laws to suppress the vibration.

- The performance of different controllers has been demonstrated and compared using simulations in Matlab and Simulink. In addition to this, a validation of dynamic modeling for a space robotic system using a commercial multibody software, such as MSC Adams, will strengthen the contribution.

- Experimental validation. The presented work depicts the theoretical establishment of the spacecraft model and demonstrates the developed control algorithms by numerical simulations. Validation of the proposed controllers through hardware experiments needs to be performed which can give insight of practical issues.

This thesis provides a theoretical basis of modeling and control for potential on-orbit assembly tasks. From a practical point of view, other important issues, such as control of space robots with multiple manipulators or of cooperative space robots, sensing techniques and comprehensive contact dynamics also need to be investigated.

References

[1] C. Sallaberger, "Canadian space robotic activities," *Acta Astronautica*, vol. 41, no. 4, pp. 239–246, 1997.

[2] J. Sasiadek, "Space robotics and its challenges," in *Aerospace Robotics*, pp. 1–8, Springer, 1 ed., 2013.

[3] M. Oda, "Experiences and lessons learned from the ETS-VII robot satellite," in *Proceedings of the 2000 IEEE International Conference on Robotics and Automation*, (San Francisco, CA), pp. 914–919, 2000.

[4] A. Ogilvie, J. Allport, M. Hannah, and J. Lymer, "Autonomous satellite servicing using the orbital express demonstration manipulator system," in *Proceedings of the 9th International Symposium on Artificial Intelligence, Robotics and Automation in Space (i-SAIRAS'08)*, pp. 25–29, 2008.

[5] D. Reintsema, J. Thaeter, A. Rathke, W. Naumann, P. Rank, and J. Sommer, "DEOS - the German robotics approach to secure and de-orbit malfunctioned satellites from low earth orbits," in *International Symposium on Artificial Intelligence, Robotics and Automation in Space*, (Sapporo,Japan), pp. 244–251, 2010.

[6] B. B. Reed, R. C. Smith, B. Naasz, J. Pellegrino, and C. Bacon, "The Restore-L Servicing Mission," *URL: https://www.nasa.gov/sites/default/files/atomsfiles/reed_restorel_tagged.pdf*, 2016.

[7] D. Barnhart, B. R. Sullivan, R. Hunter, J. Bruhn, E. Fowler, L. Hoag, S. Chappie, G. Henshaw, B. Kelm, T. Kennedy, M. Mook, and K. Vincent,

"Phoenix project status," in *Proceedings of the AIAA SPACE Conference and Exposition*, (San Diego, CA), 2013.

[8] G. Hausmann, M. Wieser, R. Haarmann, A. Brito, and J.-c. Meyer, "E.Deorbit Mission: OHB debris removal concepts," in *ASTRA 2015 - 13th Symposium on Advanced Space Technologies in Robotics and Automation*, (Noordwijk, Netherlands), 2015.

[9] A. Flores-Abad, Z. Wei, O. Ma, and K. Pham, "Optimal control of a space robot to approach a tumbling object for capture with uncertainties in the boundary conditions," *Journal of Guidance, Control, and Dynamics*, vol. 37, no. 6, pp. 2014–2017, 2014.

[10] Y. Xu and H.-y. Shum, "Dynamic control of a space robot system with no thrust jets controlled base," tech. rep., Carnegie Mellon University, Pittsburgh, Pennsylvania, 1991.

[11] K. Senda, H. Nagoaka, and Y. Murotsu, "Adaptive control of free-flying space robot with position/attitude control system," *Journal of Guidance, Control, and Dynamics*, vol. 22, no. 3, pp. 488–490, 1999.

[12] W.-H. Zhu and J. D. Schutter, "Adaptive control of electrically driven space robots based on virtual decomposition," *Journal of Guidance, Control, and Dynamics*, vol. 22, no. 2, pp. 329–339, 1999.

[13] K. D. Bilimoria and B. Wiet, "Time-optimal three-axis reorientation of a rigid spacecraft," *Journal of Guidance Control and Dynamics*, vol. 16, no. 3, pp. 446–452, 1993.

[14] X. Bai and J. L. Junkins, "New results for time-optimal three-axis reorientation of a rigid spacecraft," *Journal of Guidance, Control, and Dynamics*, vol. 32, no. 4, pp. 1071–1076, 2009.

[15] H. Zhou, D. Wang, B. Wu, and E. K. Poh, "Time-optimal reorientation for rigid satellite with reaction wheels," *International Journal of Control*, vol. 85, no. 10, pp. 1452–1463, 2012.

[16] S. Arimoto, H.-Y. Han, C. C. Cheah, and S. Kawamura, "Extension of impedance matching to nonlinear dynamics of robotic tasks," *Systems and Control Letters*, vol. 36, no. 2, pp. 109–119, 1999.

[17] K. Yoshida, H. Nakanishi, H. Ueno, N. Inaba, T. Nishimaki, and M. Oda, "Dynamics, control and impedance matching for robotic capture of a non-cooperative satellite," *Advanced Robotics*, vol. 18, no. 2, pp. 175–198, 2004.

[18] N. Uyama, D. Hirano, H. Nakanishi, K. Nagaoka, and K. Yoshida, "Impedance-based contact control of a free-flying space robot with respect to coefficient of restitution," in *2011 IEEE/SICE International Symposium on System Integration*, (Kyoto, Japan), pp. 1196–1201, 2011.

[19] N. Uyama, H. Nakanishi, K. Nagaoka, and K. Yoshida, "Impedance-based contact control of a free-flying space robot with a compliant wrist for non-cooperative satellite capture," in *IEEE/RSJ International Conference on Intelligent Robots and Systems*, (Algarve, Portugal), pp. 4477–4482, 2012.

[20] H. Jayakody and J. Katupitiya, "A gain adaptive variable structure control methodology for second order nonlinear dynamic systems," in *53rd IEEE Conference on Decision and Control*, (Los Angeles, USA), pp. 4391–4397, 2014.

[21] I. Newton, D. Bernoulli, C. MacLaurin, and L. Euler, *Philosophiae Naturalis Principia Mathematica*. 1833.

[22] J. L. Lagrange, *Mécanique analytique*, vol. 1. Mallet-Bachelier, 1853.

[23] T. R. Kane and C. F. Wang, "On the derivation of equations of motion," *Journal of the Society for Industrial and Applied Mathematics*, vol. 13, no. 2, pp. 487–492, 1965.

[24] S. Dubowsky and E. Papadopoulos, "The kinematics, dynamics, and control of free-flying and free-floating space robotic systems," *IEEE Transactions on Robotics and Automation*, vol. 9, no. 5, pp. 531–543, 1993.

[25] J. L. R. d'Alembert, *Traité de dynamique.* 1743.

[26] W. Hamilton, "Second essay on a general method in dynamics," *Philosophical Transactions of the Royal Society of London*, 1835.

[27] L. Boltzmann, "Über die form der lagrangeschen gleichungen fr nichtholonome, generalisierte coordinaten," *Sitzungsberichte der Kaiserlichen Akademie der Wissenschaften*, pp. 1603–1614, 1902.

[28] J. W. Gibbs, "On the fundamental formulae of dynamics," *American Journal of Mathematics*, vol. 2, no. 1, pp. 49–64, 1879.

[29] T. R. Kane and D. a. Levinson, "Formulation of equations of motion for complex spacecraft," *Journal of Guidance, Control, and Dynamics*, vol. 3, no. 2, pp. 99–112, 1980.

[30] W. Hooker and G. Margulies, "The dynamical attitude equations for n-body satellite," *Journal of the Astronautical Sciences*, vol. 12, p. 123, 1965.

[31] R. E. Roberson and J. Wittenburg, "A dynamical formalism for an arbitrary number of interconnected rigid bodies, with reference to the problem of satellite attitude control," in *Proceedings of IFAC Congress*, (London), 1966.

[32] J. Wittenburg, *Dynamics of systems of rigid bodies*, vol. 33. Springer-Verlag, 2013.

[33] J. M. Hollerbach, "A recursive Lagrangian formulation of maniputator dynamics and a comparative study of dynamics formulation complexity," *IEEE Transactions on Systems, Man, and Cybernetics*, vol. 10, no. 11, pp. 730–736, 1980.

[34] S. A. A. Moosavian and E. Papadopoulos, "Explicit dynamics of space free-flyers with multiple manipulators via SPACEMAPLE," *Advanced Robotics*, vol. 18, no. 2, pp. 223–244, 2004.

[35] W. W. Hooker, "A set of r dynamical attitude equations for an arbitrary n-body satellite having r rotational degrees of freedom," *AIAA Journal*, vol. 8, no. 7, pp. 1205–1207, 1970.

[36] T. R. Kane, "Dynamics of nonholonomic systems," *Journal of Applied Mechanics*, vol. 28, no. 4, pp. 574–578, 1961.

[37] M. Asme, "Impulsive Motions," *Journal of Applied Mechanics*, vol. 29, no. 4, pp. 715–718, 1962.

[38] R. W. Longman, R. E. Lindberg, and M. F. Zedd, "Satellite mounted robot manipulators - new kinematics and reaction moment compensation," *International Journal of Robotics Research*, vol. 6, no. 3, pp. 87–103, 1987.

[39] Y. Umetani and K. Yoshida, "Resolved motion rate control of space robotic manipulators with Generalized Jacobian Matrix," *IEEE Transactions on Robotics and Automation*, vol. 5, no. 3, pp. 303–314, 1989.

[40] Y. Umetani and K. Yoshida, "Unfettered behavior of space robot," in *Proceedings of 3rd International Conference on Advanced Robotics*, vol. 103, p. 114, 1987.

[41] Y. Umetani and K. Yoshida, "Continuous path control of space manipulators mounted on OMV," *Acta Astronautica*, vol. 15, no. 12, pp. 981–986, 1987.

[42] E. Papadopoulos and S. Dubowsky, "Dynamic singularities in free- floating space manipulators," *Journal of Dynamic Systems, Measurement and Control*, vol. 115, no. 1, pp. 44–52, 1993.

[43] D. Nenchev, Y. Umetani, and K. Yoshida, "Analysis of a redundant free-flying spacecraft/manipulator system," *IEEE Transactions on Robotics and Automation*, vol. 8, no. 1, pp. 1–6, 1992.

[44] Z. Vafa and S. Dubowsky, "On the dynamics of manipulators in space using the virtual manipulator approach," in *1987 IEEE International Conference on Robotics and Automation*, pp. 579–585, 1987.

[45] Z. Vafa and S. Dubowsky, "The kinematics and dynamics of space manipulators: The virtual manipulator approach," *International Journal of Robotics Research*, vol. 9, no. 4, pp. 3–21, 1990.

[46] A. Flores-Abad, O. Ma, K. Pham, and S. Ulrich, “A review of space robotics technologies for on-orbit servicing,” *Progress in Aerospace Sciences*, vol. 68, pp. 1–26, 2014.

[47] B. Liang, “Mapping a space manipulator to a dynamically equivalent manipulator,” *Journal of Dynamic Systems, Measurement and Control*, vol. 120, no. 1, pp. 1–7, 1998.

[48] A. Ellery, “An engineering approach to the dynamic control of space robotic on-orbit servicers,” *Proceedings of the Institution of Mechanical Engineers, Part G: Journal of Aerospace Engineering*, vol. 218, no. 2, pp. 79–98, 2004.

[49] Z. Vafa and S. Dubowsky, “On the dynamics of space manipulators using the virtual manipulator, with applications to path planning,” in *Space Robotics: Dynamics and Control*, pp. 45–76, Springer, 1993.

[50] S. Dubowsky and M. A. Torres, “Path planning for space manipulators to minimize spacecraft attitude disturbances,” *IEEE International Conference on Robotics and Automation*, vol. 3, no. April, pp. 2522–2528, 1991.

[51] D. N. Nenchev, K. Yoshida, P. Vichitkulsawat, and M. Uchiyama, “Reaction null-space control of flexible structure mounted manipulator systems,” *IEEE Transactions on Robotics and Automation*, vol. 15, no. 6, pp. 1011–1023, 1999.

[52] D. Nenchev, K. Yoshida, and Y. Umetani, “Analysis, design and control of free-flying space robots using fixed-attitude-restricted jacobian matrix,” in *The fifth international symposium on Robotics research*, pp. 251–258, MIT Press, 1991.

[53] D. N. Nenchev, “A controller for a redundant free-flying space robot with spacecraft attitude/manipulator motion coordination,” in *Proceedings of the 1993 IEEE/RSJ International Conference on Intelligent Robots and Systems*, pp. 2108–2114, 1993.

[54] Y. Fukazu, N. Hara, Y. Kanamiya, and D. Sato, “Reactionless resolved acceleration control with vibration suppression capability for JEMRMS/SFA,”

in *International Conference on Robotics and Biomimetics*, pp. 1359–1364, IEEE, 2009.

[55] Y. Xu and H.-y. Shum, "Dynamic control and coupling of a free-flying space robot system," *Journal of Robotic Systems*, vol. 11, no. 7, pp. 573–589, 1994.

[56] R. D. Quinn, J. L. Chen, and C. Lawrence, "Base reaction control for space-based robots operating in microgravity environment," *Journal of Guidance, Control, and Dynamics*, vol. 17, no. 2, pp. 263–270, 1994.

[57] S. Cocuzza, I. Pretto, and S. Debei, "Least-squares-based reaction control of space manipulators," *Journal of Guidance, Control, and Dynamics*, vol. 35, no. 3, pp. 976–986, 2012.

[58] W. Xu, Y. Liu, and Y. Xu, "The coordinated motion planning of a dual-arm space robot for target capturing," *Robotica*, vol. 30, no. 05, pp. 755–771, 2012.

[59] Y. Masutani, F. Miyazaki, and S. Arimoto, "Sensory feedback control for space manipulators," in *1989 IEEE International Conference on Robotics and Automation*, (Scottsdale, Arizona), pp. 1346–1351, 1989.

[60] M. Oda and Y. Ohkami, "Coordinated control of spacecraft attitude and space manipulators," *Control Engineering Practice*, vol. 5, no. 1, pp. 11–21, 1997.

[61] Z. Li, H. Liu, and B. Wang, "Motion planning and coordination control of space robot using methods of calculated momentum," in *Proceeding of the IEEE International Conference on Robotics and Biomimetics (ROBIO)*, (Shenzhen, China), pp. 1151–1156, 2013.

[62] T. Oki, H. Nakanishi, and K. Yoshida, "Time-optimal manipulator control of a free-floating space robot with constraint on reaction torque," in *2008 IEEE/RSJ International Conference on Intelligent Robots and Systems, IROS*, (Nice, France), pp. 2828–2833, 2008.

[63] K. Nanos and E. Papadopoulos, "On the use of free-floating space robots in the presence of angular momentum," *Intelligent Service Robotics*, vol. 4, no. 1, pp. 3–15, 2011.

[64] Y. Murotsu, S. Tsujio, and K. Senda, "Dynamics and positioning control of space robot with flexible manipulators," in *AIAA Guidance, Navigation and Control Conference*, (AIAA 90-3397-CP, Portland, OR), pp. 735–742, 1990.

[65] E. Papadopoulos and S. Dubowsky, "Coordinated manipulator/spacecraft motion control for space robotic systems," in *Proceedings of the 1991 IEEE International Conference on Robotics and Automation*, (Sacramento, California), pp. 1696–1701, 1991.

[66] S. Moosavian and E. Papadopoulos, "Control of space free-flyers using the modified transpose Jacobian algorithm," in *Proceedings of the 1997 IEEE/RSJ International Conference on Intelligent Robot and Systems (IROS)*, (Grenoble, France), pp. 1500–1505, 1997.

[67] K. Senda, Y. Murotsu, H. Nagaoka, and A. Mitsuya, "Attitude control for free-flying space robot with CMG," in *Proceedings of the AIAA Guidance, Navigation and Control Conference*, (AIAA-95-3336-CP), pp. 1494–1502, 1995.

[68] Y. Chen and L. Meirovitch, "Control of a flexible space robot executing a docking maneuver," *Journal of Guidance, Control, and Dynamics*, vol. 18, no. 4, pp. 756–766, 1995.

[69] P. Gasbarri and A. Pisculli, "Dynamic/control interactions between flexible orbiting space-robot during grasping, docking and post-docking manoeuvres," *Acta Astronautica*, vol. 110, pp. 225–238, 2015.

[70] Y. Xu and H.-y. Shum, "Adaptive control of space robot system with an attitude controlled base," tech. rep., The Robotics Institute, Carnegie- Mellon University, 1991.

[71] Y. H. Jia, Q. Hu, and S. J. Xu, "Dynamics and adaptive control of a dual-arm space robot with closed-loop constraints and uncertain inertial parameters," *Acta Mechanica Sinica*, vol. 30, no. 1, pp. 112–124, 2014.

[72] M. W. Walker and L. B. Wee, "Adaptive control of space-based robot manipulators," *IEEE Transactions on Robotics and Automation*, vol. 7, no. 6, pp. 828–835, 1991.

[73] O. Parlaktuna and M. Ozkan, "Adaptive control of free-floating space manipulators using dynamically equivalent manipulator model," *Robotics and Autonomous Systems*, vol. 46, no. 3, pp. 185–193, 2004.

[74] N. Kumar, V. Panwar, J.-H. Borm, J. Chai, and J. Yoon, "Adaptive neural controller for space robot system with an attitude controlled base," *Neural Computing and Applications*, vol. 23, no. 7-8, pp. 2333–2340, 2013.

[75] S. Ulrich and J. Z. Sasiadek, "Modified simple adaptive control for a two-link space robot," in *American Control Conference (ACC)*, (Marriott Waterfront, Baltimore, MD, USA), pp. 3654–3659, 2010.

[76] S. Ulrich, J. Z. Sasiadek, and I. Barkana, "Nonlinear adaptive output feedback control of flexible-joint space manipulators with joint stiffness uncertainties," *Journal of Guidance, Control, and Dynamics*, vol. 37, no. 6, pp. 1961–1975, 2014.

[77] S. Tsuda and T. Kobayashi, "Space robot control for unknown target handling," in *Lecture Notes in Electrical Engineering*, pp. 11–24, Springer Science & Business Media, Dec 2011.

[78] A. Arisoy, M. K. Bayrakceken, and S. Basturk, "High order sliding mode control of a space robot manipulator," in *2011 International Conference on IEEE Recent Advances in Space Technologies (RAST)*, (Istanbul, Turkey), pp. 833–838, 2011.

[79] B. Wie, H. Weiss, and a. Arapostathis, "Quarternion feedback regulator for spacecraft eigenaxis rotations," *Journal of Guidance, Control, and Dynamics*, vol. 12, no. 3, pp. 375–380, 1989.

[80] R. Newton and Y. Xu, "Neural network control of a space manipulator," *IEEE Control Systems*, vol. 13, no. 6, pp. 14–22, 1993.

[81] D. Gorinevsky, "Radial basis function network architecture for nonholonomic motion planning and control of free-flying manipulators," *IEEE Transactions on Robotics*, vol. 12, no. 3, pp. 491–496, 1996.

[82] E. N. Sanchez and M. Bernal, "Adaptive recurrent neural control for nonlinear system tracking," *IEEE Transactions on Systems, Man, and Cybernetics*, vol. 30, no. 6, pp. 886–889, 2000.

[83] Z. Wenhui, F. Yamin, and Y. Xiaoping, "Adaptive neural network robust control for space robot with uncertainty," *Telecommunication Computing Electronics and Control*, vol. 11, no. 3, pp. 513–520, 2013.

[84] Y. Fang, W. Zhang, and X. Ye, "Variable structure control for space robots based on neural networks," *International Journal of Advanced Robotic Systems*, vol. 11, no. 35, pp. 1–7, 2014.

[85] N. Inaba and M. Oda, "Autonomous satellite capture by a space robot," in *Proceedings of 2000 IEEE International Conference on Robotics and Automation*, vol. 2, (San Francisco, CA), pp. 1169–1174, 2000.

[86] A. Ogilvie, J. Allport, M. Hannah, and J. Lymer, "Autonomous robotic operations for on-orbit satellite servicing," in *SPIE Defense and Security Symposium* (R. T. Howard and P. Motaghedi, eds.), vol. 6958, pp. 1–12, Apr. 2008.

[87] L. Shi, H. S. Jayakody, N. Kinkaid, and J. Katupitiya, "Attitude regulation of a free-flying space robot during contact operations," in *IEEE Aerospace Conference*, (Big Sky, USA), 2016.

[88] K. Yoshida, R. Kurazumet, N. Sashida, and Y. Umetani, "Modeling of collision dynamics for free-floating links with extended generalized inertia tensor," in *Proceedings of the 1992 IEEE International Conference on Robotics and Automation*, (Nice, France), pp. 899–904, 1992.

[89] K. Yoshida and N. Sashida, "Modeling of impact dynamics and impulse

minimization," in *Proceedings of the 1993 IEEE/RSJ International Conference on Intelligent Robots and Systems*, (Yokohama, Japan), pp. 2064–2069, 1993.

[90] D. N. Nenchev and K. Yoshida, "Impact analysis and post-impact motion control issues of a free-floating space robot subject to a force impulse," *IEEE Transactions on Robotics and Automation*, vol. 15, no. 3, pp. 548–557, 1999.

[91] K. Yoshida and D. N. Nenchev, "Space robot impact analysis and satellite-base impulse minimization using reaction null-space," in *ICRA*, pp. 1271–1277, 1995.

[92] K. Yoshida, D. Dimitrov, and H. Nakanishi, "On the capture of tumbling satellite by a space robot," in *2006 IEEE/RSJ International Conference on Intelligent Robots and Systems*, (Beijing, China), pp. 4127–4132, 2006.

[93] D. Dimitrov and K. Yoshida, "Momentum distribution in a space manipulator for facilitating the post-impact control," in *2004 IEEE/RSJ International Conference on Intelligent Robots and Systems (IROS)*, vol. 4, (Sendai, Japan), pp. 3345–3350, 2004.

[94] L. B. Wee and M. W. Walker, "On the dynamics of contact between space robots and configuration control for impact minimization," *IEEE Transactions on Robotics and Automation*, vol. 9, no. 5, pp. 581–591, 1993.

[95] P. Huang, Y. Xu, and B. Liang, "Dynamic balance control of multi-arm free-floating space robots," *International Journal of Advanced Robotic Systems*, vol. 2, no. 2, pp. 117–124, 2005.

[96] P. Huang, J. Yuan, Y. Xu, and R. Liu, "Approach trajectory planning of space robot for impact minimization," *Proceedings of IEEE International Conference on Information Acquisition*, pp. 382–387, 2006.

[97] Evangelos, Papadopoulos and Paraskevas, Iosif, "Design and configuration control of space robots undergoing impact," in *Proceedings of 6th International ESA Conference on Guidance, Navigation and Control Systems*, 2005.

[98] P. Huang, W. Xu, B. Liang, and Y. Xu, "Configuration control of space robots for impact minimization," *2006 IEEE International Conference on Robotics and Biomimetics, ROBIO 2006*, pp. 357–362, 2006.

[99] S. Matunaga, T. Kanzawa, and Y. Ohkami, "Rotational motion-damper for the capture of an uncontrolled floating satellite," *Control Engineering Practice*, vol. 9, no. 2, pp. 199–205, 2001.

[100] S. Yoshikawa and K. Yamada, "Impulsive control for angular momentum management of tumbling spacecraft," *Acta Astronautica*, vol. 60, no. 10-11, pp. 810–819, 2007.

[101] M. Shibli, "Unified modeling approach of kinematics, dynamics and control of a free-flying space robot interacting with a target satellite," *Intelligent Control and Automation*, vol. 02, pp. 8–23, 2011.

[102] M. M. Al-Shibli, *Modeling and control of a free-flying space robot interacting with a target satellite*. PhD thesis, Concordia University, 2005.

[103] J. K. Salisbury, "Active stiffness control of a manipulator in cartesian coordinates," in *19th IEEE Conference on Decision and Control including the Symposium on Adaptive Processes*, pp. 95–100, IEEE, 1980.

[104] D. E. Whitney, "Historical perspective and state of the art in robot force control," *The International Journal of Robotics Research*, vol. 6, no. 1, pp. 3–14, 1987.

[105] N. Hogan, "Impedance control: An approach to manipulation," *Journal of Dynamic Systems, Measurement and Control*, vol. 107, no. 1, pp. 1–24, 1985.

[106] D. E. Whitney, "Force feedback control of manipulator fine motions," *Journal of Dynamic Systems, Measurement, and Control*, vol. 99, no. 2, pp. 91–97, 1977.

[107] J. J. Raibert, M. H., and Craig, "Hybrid position / force control of manipulators," *Journal of Dynamic Systems, Measurement and Control*, vol. 126, no. 2, pp. 126–133, 1981.

[108] R. Volpe and P. Khosla, "A theoretical and experimental investigation of explicit force control strategies for manipulators," *IEEE Transactions on Automatic Control*, vol. 38, no. 11, pp. 1634–1650, 1993.

[109] G. Zeng and A. Hemami, "An overview of robot force control," *Robotica*, vol. 15, no. 5, pp. 473–482, 1997.

[110] R. Carelli, R. Kelly, and R. Ortega, "Adaptive force control of robot manipulators," *International Journal of Control*, vol. 52, no. 1, pp. 37–54, 1990.

[111] S. K. Singh and D. O. Popa, "An analysis of some fundamental problems in adaptive control of force and impedance behavior: Theory and experiments," *IEEE Transactions on Robotics and Automation*, vol. 11, no. 6, pp. 912–921, 1995.

[112] R. Colbaugh, H. Seraji, and K. Glass, "Direct adaptive impedance control of robot manipulators," *Journal of Robotic Systems*, vol. 10, no. 2, pp. 217–248, 1993.

[113] H. Seraji, "Adaptive force and position control of manipulators," *Journal of robotic systems*, vol. 4, no. 4, pp. 551–578, 1987.

[114] Y. Chen and S. Pandey, "Robust hybrid control of robot manipulators," in *Proceedings of 1989 IEEE International Conference on Robotics and Automation*, pp. 236–241, IEEE, 1989.

[115] D. Shusterman and G. R. Widmann, "Force control of robotic manipulators with structured uncertainties using variable structure control," *Robotics and Computer-Integrated Manufacturing*, vol. 9, no. 2, pp. 169–180, 1992.

[116] B. Yao and M. Tomizuka, "Robust adaptive motion and force control of robot manipulators in unknown stiffness environments," in *1993 Proceedings of the 32nd IEEE Conference on Decision and Control*, pp. 142–147, IEEE, 1993.

[117] D. Dawson, F. Lewis, and J. Dorsey, "Robust force control of a robot manipulator," *The International journal of robotics research*, vol. 11, no. 4, pp. 312–319, 1992.

[118] D. Jeon and M. Tomizuka, "Learning hybrid force and position control of robot manipulators," *IEEE Transactions on Robotics and Automation*, vol. 9, no. 4, pp. 423–431, 1993.

[119] P. Lucibello, "A learning algorithm for hybrid force control of robot arms," in *Proceedings of 1993 IEEE International Conference on Robotics and Automation*, pp. 654–658, IEEE, 1993.

[120] S. R. Pandian and S. Kawamura, "Hybrid force/position control for robot manipulators based on a d-type learning law," *Robotica*, vol. 14, no. 01, pp. 51–59, 1996.

[121] B. Siciliano, L. Sciavicco, L. Villani, and G. Oriolo, *Robotics: Modelling, Planning and Control*. Springer Science & Business Media, 2009.

[122] S. A. Schneider and R. H. Cannon, "Object impedance control for cooperative manipulation - theory and experimental results," *IEEE Transactions on Robotics and Automation*, vol. 8, no. 3, pp. 383–394, 1992.

[123] S. A. A. Moosavian and E. Papadopoulos, "Free-flying robots in space : An overview of dynamics modeling, planning and control," *Robotica*, vol. 25, no. 5, pp. 537–547, 2007.

[124] S. Moosavian and E. Papadopoulos, "Multiple impedance control for object manipulation," in *Proceedings of 1998 IEEE/RSJ International Conference on Intelligent Robots and Systems*, pp. 461–466, 1998.

[125] R. Bonitz and T. Hsia, "Internal force-based impedance control for cooperating manipulators," *IEEE Transactions on Robotics and Automation*, vol. 12, no. 1, pp. 78–89, 1996.

[126] F. Caccavale and L. Villani, "An impedance control strategy for cooperative manipulation," in *Proceedings of 2001 IEEE/ASME International Conference on Advanced Intelligent Mechatronics*, no. 1, pp. 343–348, 2001.

[127] C.-C. Cheah and D. Wang, "Learning impedance control for robotic manipulators," *IEEE Transactions on Robotics and Automation*, vol. 14, no. 3, pp. 452–465, 1998.

[128] S. Jung and T. Hsia, "Stability and convergence analysis of robust adaptive force tracking impedance control of robot manipulators," in *Proceedings of 1999 IEEE/RSJ International Conference on Intelligent Robots and Systems*, pp. 635–640, 1999.

[129] A. Goldenberg, "Implementation of force and impedance control in robot manipulators," in *Proceedings of 1988 IEEE International Conference on Robotics and Automation*, pp. 1626–1632, 1988.

[130] T. Hsia, "Neural network impedance force control of robot manipulator," *IEEE Transactions on Industrial Electronics*, vol. 45, no. 3, pp. 451–461, 1998.

[131] S. Jung, T. C. Hsia, and R. G. Bonitz, "Force tracking impedance control for robot manipulators with an unknown environment: theory, simulation, and experiment," *The International Journal of Robotics Research*, vol. 20, no. 9, pp. 765–774, 2001.

[132] S. Jung, T. C. Hsia, and R. G. Bonitz, "Force tracking impedance control of robot manipulators under unknown environment," *IEEE Transactions on Control Systems Technology*, vol. 12, no. 3, pp. 474–483, 2004.

[133] M.-C. Chien and A.-C. Huang, "Adaptive impedance control of robot manipulators based on function approximation technique," *Robotica*, vol. 22, no. 4, pp. 395–403, 2004.

[134] W. He, Y. Dong, and C. Sun, "Adaptive neural impedance control of a robotic manipulator with input saturation," *IEEE Transactions on Systems, Man, and Cybernetics: Systems*, vol. 46, no. 3, pp. 334–344, 2016.

[135] S. A. A. Moosavian, R. Rastegari, and E. Papadopoulos, "Multiple impedance control for space free-flying robots," *Journal of Guidance, Control, and Dynamics*, vol. 28, no. 5, pp. 939–947, 2005.

[136] A. K. Swain and A. S. Morris, "Dynamic control of multi-arm co-operating manipulator systems," *Robotica*, vol. 22, no. 03, pp. 271–283, 2004.

[137] R. Rastegari and S. A. A. Moosavian, "Multiple impedance control of space free-flying robots using virtual object grasp," in *2006 IEEE/RSJ International Conference on Intelligent Robots and Systems*, pp. 3125–3130, IEEE, 2006.

[138] S. A. A. Moosavian and R. Rastegari, "Force tracking in multiple impedance control of space free-flyers," in *Proceedings of 2000 IEEE/RSJ International Conference on Intelligent Robots and Systems*, vol. 3, pp. 1646–1651, IEEE, 2000.

[139] M. J. Sidi, *Spacecraft Dynamics and Control: A Practical Engineering Approach*, vol. 7. Cambridge University Press, 1997.

[140] H. Nakanishi and K. Yoshida, "Impedance control for free-flying space robots -basic equations and applications-," in *2006 IEEE/RSJ International Conference on Intelligent Robots and Systems*, (Beijing, China), pp. 3137–3142, 2006.

[141] S. Hayati, "Hybrid position/force control of multi-arm cooperating robots," *Proceedings of 1986 IEEE International Conference on Robotics and Automation*, vol. 3, pp. 82–89, 1986.

[142] W. Gueaieb, S. Member, and F. Karray, "A robust hybrid intelligent position / force control scheme for cooperative manipulators," *IEEE/ASME Transactions on Mechatronics*, vol. 12, no. 2, pp. 109–125, 2007.

[143] T. Yoshikawa and A. Sudou, "Dynamic hybrid position/force control of robot manipulators-on-line estimation of unknown constraint," *IEEE Transactions on Robotics and Automation*, vol. 9, no. 2, 1993.

[144] S. Kilicaslan, M. K. Ozgoren, and S. K. Ider, "Hybrid force and motion control of robots with flexible links," *Mechanism and Machine Theory*, vol. 45, no. 1, pp. 91–105, 2010.

[145] C. M. Kwan, "Hybrid force/position control for manipulators with motor dynamics using a sliding-adaptive approach," *IEEE Transactions on Automatic Control*, vol. 40, no. 5, pp. 963–968, 1995.

[146] L. L. Whitcomb, S. Arimoto, T. Naniwa, and F. Ozaki, "Adaptive model-based hybrid control of geometrically constrained robot arms," *IEEE Transactions on Robotics and Automation*, vol. 13, no. 1, pp. 105–116, 1997.

[147] N. Kumar, V. Panwar, N. Sukavanam, S. P. Sharma, and J. H. Borm, "Neural network based hybrid force/position control for robot manipulators," *International Journal of Precision Engineering and Manufacturing*, vol. 12, no. 3, pp. 419–426, 2011.

[148] V. Rutkovsky, V. Sukhanov, and V. Glumov, "Free-flying manipulation robot using for in-orbit assembly of large space structures," in *2011 5th International Conference on Recent Advances in Space Technologies (RAST)*, pp. 808–813, 2011.

[149] S. R. Tsitas and G. Constantinos, "Garada SAR formation flying requirements, space system baseline and spacecraft structural design," tech. rep.

[150] D. Simpson, "The "Snapdragon" family," in *Proceedings of the European Conference on Spacecraft Structures, Materials and Mechanical Testing*, pp. 337–346, 2000.

[151] C. Pukdeboon, A. S. I. Zinober, and M.-W. L. Thein, "Quasi-continuous higher order sliding-mode controllers for spacecraft-attitude-tracking maneuvers," *IEEE Transactions on Industrial Electronics*, vol. 57, no. 4, pp. 1436–1444, 2010.

[152] M. D. Shuster, "A survey of attitude representations," *The Journal of the Astronautical Science*, vol. 41, no. 4, pp. 439–517, 1993.

[153] F. S. Holberg, "Optimal attitude control of a double cubesat using magnetorquers," tech. rep., Norwegian University of Science and Technology, Trondheim, 2011.

[154] A. Tavakkoli, M. Kabganian, and M. Shahravi, "Modeling of attitude control actuator for a flexible spacecraft using an extended simulation environment," *2005 International Conference on Control and Automation*, pp. 147–152, 2005.

[155] A. H. De Ruiter, C. Damaren, and J. R. Forbes, *Spacecraft Dynamics and Control: An Introduction*. John Wiley & Sons, 2012.

[156] H. B. Hablani, "Sun-tracking commands and reaction wheel sizing with configuration optimization," *Journal of Guidance, Control, and Dynamics*, vol. 17, no. 4, pp. 805–814, 1994.

[157] C.-H. Won, "Comparative study of various control methods for attitude control of a LEO satellite," *Aerospace Science and Technology*, vol. 3, no. 5, pp. 323–333, 1999.

[158] P. Pillay and R. Krishnan, "Modeling, simulation, and analysis of permanent-magnet motor drives. ii. the brushless dc motor drive," *IEEE Transactions on Industry Applications*, vol. 25, no. 2, pp. 274–279, 1989.

[159] R. J. McElvain, "Satellite angular momentum removal utilizing the Earths magnetic field," *Torques and Attitude Sensing in Earth Satellites*, pp. 137–158, 1964.

[160] W. Perruquetti and J.-P. Barbot, *Sliding Mode Control in Engineering*. CRC Press, 2002.

[161] V. Utkin, J. Guldner, and J. Shi, *Sliding Mode Control in Electro-Mechanical Systems*. CRC press, 2009.

[162] S.-C. Lo and Y.-P. Chen, "Smooth sliding-mode control for spacecraft attitude tracking maneuvers," *Journal of Guidance, Control, and Dynamics*, vol. 18, no. 6, pp. 1345–1349, 1995.

[163] A. Levant, "Quasi-continuous higher order sliding-mode controllers," *IEEE Transactions on Automatic Control*, vol. 50, no. 11, pp. 1812–1816, 2005.

[164] S. Dubowsky and P. Boning, "The coordinated control of space robot teams for the on-orbit construction of large flexible space structures," in *IEEE International Conference on Robotics and Automation*, 2007.

[165] J. Slotine and W. Li, *Applied Nonlinear Control*. Prentice Hall, 1 ed., 1991.

[166] R. DeCarlo, S. Zak, and G. Matthews, "Variable structure control of nonlinear multivariable systems : A tutorial," in *Proceedings of the IEEE*, vol. 76, pp. 212–232, 1988.

[167] G. Bartolini, A. Ferrara, and E. Usai, "Applications of a sub-optimal discontinuous control algorithm for uncertain second order systems," *International Journal of Robust and Nonlinear Control*, vol. 7, no. 4, pp. 299–319, 1997.

[168] Y. Xu and H.-y. Shum, "Adaptive control of space robot system with an attitude controlled base," tech. rep., The Robotics Institute, Carnegie- Mellon University, 1991.

[169] T. Yamawaki and M. Yashima, "Arm trajectory planning by controlling the direction of end-point position error caused by disturbance," in *IEEE/ASME International Conference on Advanced Intelligent Mechatronics*, pp. 1120–1125, 2008.

[170] B. E. Tweddle and A. Saenz-Otero, "Relative computer vision-based navigation for small inspection spacecraft," *Journal of Guidance, Control, and Dynamics*, vol. 38, no. 5, pp. 969–978, 2015.

[171] M. O'Connor and B. Tweddle, "Visual-inertial estimation and control for inspection of a tumbling spacecraft: Experimental results from the international space station," in *AIAA Guidance, Navigation, and Control Conference*, 2012.

[172] U. Hillenbrand and R. Lampariello, "Motion and parameter estimation of a free-floating space object from range data for motion prediction," in *Proceedings of i-SAIRAS*, 2005.

[173] M. Lichter and S. Dubowsky, "State, shape, and parameter estimation of space objects from range images," in *IEEE International Conference on Robotics and Automation*, pp. 2974–2979, 2004.

[174] M. Walker, "On the dynamics of contact between space robots and configuration control for impact minimization," *IEEE Transactions on Robotics and Automation*, vol. 9, no. 5, pp. 581–591, 1993.

[175] O. Ma, "Contact dynamics modelling for the simulation of the Space Station manipulators handling payloads," *Proceedings of 1995 IEEE International Conference on Robotics and Automation*, vol. 2, pp. 1252–1258, 1995.

[176] R. Krenn and G. Hirzinger, "Contact Dynamics Simulation for Space Robotics Applications," in *Proceedings of IROS*, 2008.

[177] N. Uyama, Y. Fujii, K. Nagaoka, and K. Yoshida, "Experimental evaluation of contact-impact dynamics between a space robot with compliant wrist and a free-flying object," in *International Symposium on Artificial Intelligence, Robotics and Automation in Space*, (Turin, Italy), 2012.

[178] W. Goldsmith and J. Frasier, "Impact: The theory and physical behavior of colliding solids," *Journal of Applied Mechanics*, vol. 28, p. 639, 1961.

[179] H. Hertz, *Miscellaneous papers*. Macmillan, 1896.

[180] K. H. Hunt and F. R. E. Crossley, "Coefficient of restitution interpreted as damping in vibroimpact," *Journal of Applied Mechanics*, vol. 42, no. 2, p. 440, 1975.

[181] G. Gilardi and I. Sharf, "Literature survey of contact dynamics modelling," *Mechanism and Machine Theory*, vol. 37, no. 10, pp. 1213–1239, 2002.

Appendix A

A.1 Introduction

The purpose of Appendix A is to introduce mathematical details of how to derive the actual inertia matrix of a deploying satellite and the disturbance torques which depend on spacecraft configuration. Section A.2 shows calculation details of the inertia matrix for a deploying satellite in body frame based on its geometric features. Section A.3 derives the aerodynamic disturbance torques suffered by the deploying satellite.

A.2 Inertia of a Deploying Satellite

The simplified geometrics feature of a deploying satellite are used to estimate its inertia change, as shown in Figure A.1. The deploying angle is $\bar{\delta}_s$. $\bar{a}$ and $\bar{b}$ denote length and height of a half clamshell (assume same size for the two halves). The "reference" half and the trailing half of the satellite are named as B_1 and B_2, respectively. Suppose the deploying angular rate is always perpendicular to the orbit plane, which means CM of B_1, B_2 and the entire spacecraft stays in $XOZ-$ plane of the orbit frame or their coordinate along Y_O- (Y_B-) axis is always 0. Therefore, the geometric calculations in the $XOZ-$ plane are performed. In Figure A.1, the coordinate of CM of B_2 (O_{B2}) w.r.t. CM of B_1 (O_{B1}) is

$$\begin{aligned} {}^1x_{b2} &= -\left[\frac{\bar{a}}{2} - \left(\frac{\bar{a}}{2} - \frac{\bar{b}}{2}\tan\bar{\delta}_s\right)\cos\bar{\delta}_s\right], \\ {}^1z_{b2} &= \frac{\bar{b}}{2} + \frac{\bar{b}}{2\cos\bar{\delta}_s} + \left(\frac{\bar{a}}{2} - \frac{\bar{b}}{2}\tan\bar{\delta}_s\right)\sin\bar{\delta}_s. \end{aligned} \tag{A.1}$$

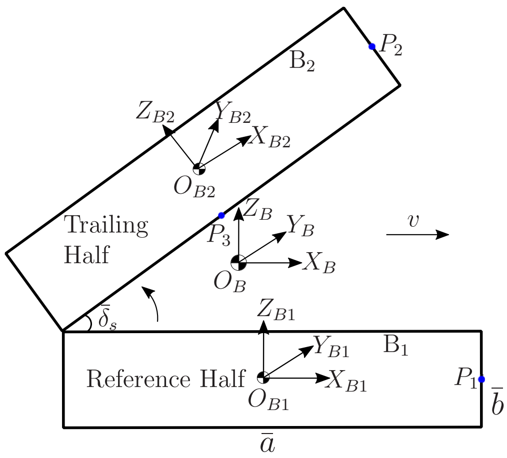

Figure A.1: Coordinate systems for a deploying satellite.

Note symbols with superscript ${}^1\{\cdot\}$,${}^2\{\cdot\}$ and ${}^b\{\cdot\}$ represent variables expressed in the "reference" half coordinate frame (ΣB_1), the opening half coordinate frame (ΣB_2) and the body frame (ΣB), respectively. The coordinate of CM of the entire spacecraft O_B w.r.t. O_{B1} is

$$ {}^1x_b = \frac{1}{2}{}^1x_{b2}, {}^1z_b = \frac{1}{2}{}^1z_{b2}. \tag{A.2}$$

So perpendicular distance between the axes Y_B and Y_{B1} or Y_B and Y_{B2} is

$$ \bar{d} = \sqrt{{}^1x_b^2 + {}^1z_b^2} = \frac{1}{2}\sqrt{{}^1x_{b2}^2 + {}^1z_{b2}^2}. \tag{A.3}$$

Then the inertia matrix of each half w.r.t. the body frame can be obtained by using Parallel Axis Theorem followed by coordinate frame transformation

$$ {}^b\boldsymbol{I}_1 = {}^1\boldsymbol{I}_1 + m_1\bar{d}^2, {}^{b'}\boldsymbol{I}_2 = {}^2\boldsymbol{I}_2 + m_2\bar{d}^2, {}^b\boldsymbol{I}_2 = {}^b\boldsymbol{R}_{b'}{}^{b'}\boldsymbol{I}_2{}^b\boldsymbol{R}_{b'}^T, \tag{A.4}$$

where m_1 and m_2 are the mass of B$_1$ and B$_2$, respectively; ${}^1\boldsymbol{I}_1$ and ${}^2\boldsymbol{I}_2$ represent inertia of B$_1$ and B$_2$ in their body fixed frame ΣB_1 and ΣB_2, respectively; ${}^{b'}\boldsymbol{I}_2$ is the inertia matrix of B$_2$ w.r.t. a frame $\Sigma B'$ which has its origin located at the origin of ΣB with axes aligned with ΣB_2; ${}^b\boldsymbol{R}_{b'}$ represents the rotation matrix from this frame to the body frame ΣB and

$$^{b}\boldsymbol{R}_{b'} = \begin{bmatrix} \cos\bar{\delta}_s & 0 & -\sin\bar{\delta}_s \\ 0 & 1 & 0 \\ \sin\bar{\delta}_s & 0 & \cos\bar{\delta}_s \end{bmatrix}.$$

Finally the inertia of the entire spacecraft expressed in the body frame is

$$\boldsymbol{J} = {}^{b}\boldsymbol{I}_1 + {}^{b}\boldsymbol{I}_2. \tag{A.5}$$

A.3 Aerodynamic Disturbance

The aerodynamic disturbance torque suffered by the deploying satellite depends on the configuration of the spacecraft and is also calculated based on the simplified geometric feature shown in Figure A.1. To derive the aerodynamic disturbance torque $\boldsymbol{\tau}_a$, we need to find the aerodynamic forces subject by the spacecraft and their acting points. According to Figure A.1, the coordinates of the center of three windward surfaces (or the force acting point for each surface with the assumption of same density of the atmosphere), P_1, P_2, P_3 w.r.t. the CM of the spacecraft body are

$$\begin{aligned}
\boldsymbol{\rho}_1 &= \left[\frac{\bar{a}}{2} - \frac{x_{b2}}{2}, 0, -\frac{z_{b2}}{2}\right]^T, \\
\boldsymbol{\rho}_2 &= \left[\frac{x_{b2}}{2} + \frac{\bar{a}}{2}\cos\bar{\delta}_s, 0, \frac{z_{b2}}{2} + \bar{a}\,\sin\frac{\bar{\delta}_s}{2}\right]^T, \\
\boldsymbol{\rho}_3 &= \left[\frac{x_{b2}}{2} + \frac{\bar{b}}{2}\sin\bar{\delta}_s, 0, \frac{z_{b2}}{2} - \frac{\bar{b}}{2}\cos\bar{\delta}_s\right]^T.
\end{aligned}$$

Accordingly, the total aerodynamic force applied on the spacecraft windward surfaces is

$$\boldsymbol{F}_a = -\rho_a v^2 \hat{\boldsymbol{v}} \int_{swa} \boldsymbol{n} \cdot \boldsymbol{v}\ \mathrm{d}\boldsymbol{S} = -\rho_a v^2 \left(\bar{b}\bar{l} + \bar{b}\bar{l}\,\cos\bar{\delta}_s + \bar{a}\bar{l}\,\sin\bar{\delta}_s\right)\hat{\boldsymbol{v}}, \tag{A.6}$$

where $\bar{l}$ is the width of a half clamshell. The equivalent pressure center of $\boldsymbol{F}_a$ can be expressed by

$$\boldsymbol{C}_{pa} = \frac{\int_{swa} \boldsymbol{\rho}\,(\boldsymbol{n}\cdot\boldsymbol{v})\ \mathrm{d}\boldsymbol{S}}{\int_{swa} (\boldsymbol{n}\cdot\boldsymbol{v})\ \mathrm{d}\boldsymbol{S}} = \frac{\bar{b}\bar{l}\boldsymbol{\rho}_1 + \bar{b}\bar{l}\boldsymbol{\rho}_2\ \cos\bar{\delta}_s + \bar{a}\bar{l}\boldsymbol{\rho}_3\ \sin\bar{\delta}_s}{\bar{b}\bar{l} + \bar{b}\bar{l}\ \cos\bar{\delta}_s + \bar{a}\bar{l}\ \sin\bar{\delta}_s}. \tag{A.7}$$

The orbital velocity of the spacecraft is $\bar{\boldsymbol{v}} = {}^{b}\boldsymbol{R}_o{}^{o}\boldsymbol{v}_o$, where ${}^{o}\boldsymbol{v}_o = [v_0, 0, 0]^T = [\omega_o R, 0, 0]^T$ with R as the orbit radius.

Appendix B

B.1 Introduction

This appendix provides detailed derivation of kinematics and dynamics for a space robot. The space robot consists of a mobile base and n rigid links connected by revolute joints, as shown in Figure B.1. Section B.2 establishes the relationship between the motion rate of the end-effector and that of spacecraft attitude angles and joint angles in a linearized form based on geometric features of the space robot model. Section B.3 first formulates the kinetic energy of the system and then derives the space robot dynamic equation by Lagrangian dynamics.

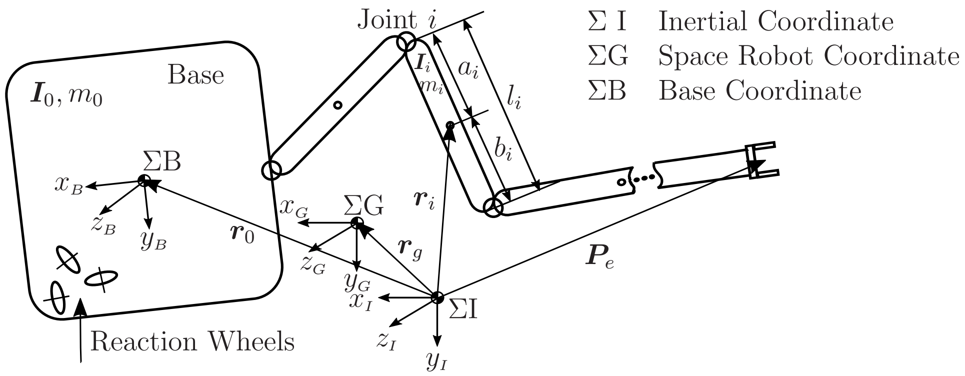

Figure B.1: Space robot model

B.2 Space Robot Kinematics

This section is based on the treatment of Umetani and Yoshida [39]. Basic equations originated from geometric features of the system, as illustrated in Figure B.1, are described as follows:

$$\begin{aligned} &\boldsymbol{r}_{i+1} = \boldsymbol{r}_i + {}^a\boldsymbol{A}_i\ {}^i\boldsymbol{b}_i + {}^a\boldsymbol{A}_{i+1}\ {}^{i+1}\boldsymbol{a}_{i+1}, \quad i = 0, 1, \cdots, n-1, \\ &\sum_{i=0}^{n} m_i \boldsymbol{r}_i = \boldsymbol{r}_g \sum_{i=0}^{n} m_i, \end{aligned} \tag{B.8}$$

where ${}^i\boldsymbol{a}_i$ and ${}^i\boldsymbol{b}_i$ are the length vector of the i^{th} link expressed in the link frame Σ_i; ${}^a\boldsymbol{A}_i$ denotes transformation matrix from the link frame Σ_i to the inertial frame. Based on (B.8), position vector of the base and each link can be expressed by,

$$\boldsymbol{r}_i = \sum_{j=1}^{n} k_{ij} \left({}^a\boldsymbol{A}_j\ {}^j\boldsymbol{a}_j + {}^a\boldsymbol{A}_{j-1}\ {}^{j-1}\boldsymbol{b}_{j-1} \right) + \boldsymbol{r}_g, \tag{B.9}$$

with

$$k_{ij} = \begin{cases} \left(\sum\limits_{l=0}^{j-1} m_l \right) / m_g & (j \leq i) \\ -\left(\sum\limits_{l=j}^{n} m_l \right) / m_g & (j > i) \end{cases}, \tag{B.10}$$

where $m_g = \sum\limits_{i=0}^{n} m_i$ is total mass of the entire system. Differentiate the position vector to get inertial velocity.

$$\boldsymbol{v}_i = \dot{\boldsymbol{r}}_i = \sum_{j=1}^{n} k_{ij} \left({}^a\dot{\boldsymbol{A}}_j\ {}^j\boldsymbol{a}_j + {}^a\dot{\boldsymbol{A}}_{j-1}\ {}^{j-1}\boldsymbol{b}_{j-1} \right) + \dot{\boldsymbol{r}}_g, \tag{B.11}$$

where ${}^a\dot{\boldsymbol{A}}_j = \sum\limits_{k=0}^{j} \dfrac{\partial\ {}^a\boldsymbol{A}_j}{\partial \phi_k} \dot{\phi}_k$ with ϕ_k representing spacecraft attitude angles ($k = 0$) and joint angles ($k = 1, \cdots, n$). Substituting this expression of ${}^a\dot{\boldsymbol{A}}_j$ into (B.11) returns

$$\boldsymbol{v}_i = \sum_{j=0}^{n} \boldsymbol{v}_{ij} \dot{\phi}_j + \boldsymbol{v}_g, \tag{B.12}$$

where $\boldsymbol{v}_{ij} = \sum\limits_{k=j}^{n} k_{ik} (\dfrac{\partial\ {}^a\boldsymbol{A}_k}{\partial \phi_j}\ {}^k\boldsymbol{a}_k + \dfrac{\partial\ {}^a\boldsymbol{A}_{k-1}}{\partial \phi_j}\ {}^{k-1}\boldsymbol{b}_{k-1})$ and $\boldsymbol{v}_g = \dot{\boldsymbol{r}}_g$.

The angular velocity of each link is of the similar form as its linear velocity,

$$\boldsymbol{\omega}_i = \sum_{j=0}^{i} {}^a\boldsymbol{A}_j\ {}^j\boldsymbol{\omega}_j = \sum_{j=0}^{i} {}^a\boldsymbol{A}_j\ {}^j\boldsymbol{u}_j \dot{\phi}_j + \boldsymbol{\omega}_g, \tag{B.13}$$

where ${}^{j}\boldsymbol{u}_j$ denotes unit vector of the j^{th} joint axis; $\boldsymbol{v}_g$ and $\boldsymbol{\omega}_g$ represent linear velocity and angular velocity of the entire system.

Accordingly, velocity of the end-effector can be expressed by,

$$\begin{aligned}\boldsymbol{v}_e &= \boldsymbol{v}_{n\alpha}\dot{\alpha} + \boldsymbol{v}_{n\beta}\dot{\beta} + \boldsymbol{v}_{n\gamma}\dot{\gamma} + \sum_{i=1}^{n}\boldsymbol{v}_{ni}\dot{\phi}_i + \boldsymbol{v}_g,\\ \boldsymbol{\omega}_e &= {}^{a}\boldsymbol{A}_{\alpha}\,{}^{\alpha}\boldsymbol{u}_{\alpha}\dot{\alpha} + {}^{a}\boldsymbol{A}_{\beta}\,{}^{\beta}\boldsymbol{u}_{\beta}\dot{\beta} + {}^{a}\boldsymbol{A}_{\gamma}\,{}^{\gamma}\boldsymbol{u}_{\gamma}\dot{\gamma} + \sum_{i=1}^{n}{}^{a}\boldsymbol{A}_{i}\,{}^{i}\boldsymbol{u}_{i}\dot{\phi}_i + \boldsymbol{\omega}_g.\end{aligned} \tag{B.14}$$

Equation (B.14) can be rearranged as,

$$\begin{aligned}\boldsymbol{E}_e = \begin{bmatrix}\boldsymbol{v}_e\\ \boldsymbol{\omega}_e\end{bmatrix} &= \begin{bmatrix}\boldsymbol{v}_{n\alpha} & \boldsymbol{v}_{n\beta} & \boldsymbol{v}_{n\gamma}\\ {}^{a}\boldsymbol{A}_{\alpha}\,{}^{\alpha}\boldsymbol{u}_{\alpha} & {}^{a}\boldsymbol{A}_{\beta}\,{}^{\beta}\boldsymbol{u}_{\beta} & {}^{a}\boldsymbol{A}_{\gamma}\,{}^{\gamma}\boldsymbol{u}_{\gamma}\end{bmatrix}\begin{bmatrix}\dot{\alpha}\\ \dot{\beta}\\ \dot{\gamma}\end{bmatrix}\\ &\quad + \begin{bmatrix}\boldsymbol{v}_{n1} & \cdots & \boldsymbol{v}_{nn}\\ {}^{a}\boldsymbol{A}_{1}\,{}^{1}\boldsymbol{u}_{1} & \cdots & {}^{a}\boldsymbol{A}_{n}\,{}^{n}\boldsymbol{u}_{n}\end{bmatrix}\begin{bmatrix}\dot{\phi}_1\\ \vdots\\ \dot{\phi}_n\end{bmatrix} + \begin{bmatrix}\boldsymbol{v}_g\\ \boldsymbol{\omega}_g\end{bmatrix}\\ &= \boldsymbol{J}_{ES}\dot{\boldsymbol{\Phi}}_{S} + \boldsymbol{J}_{EM}\dot{\boldsymbol{\Phi}}_{M} + \boldsymbol{E}_g\\ &= \boldsymbol{J}_{E}\dot{\boldsymbol{q}} + \boldsymbol{E}_g,\end{aligned} \tag{B.15}$$

where $\boldsymbol{\Phi}_S = [\alpha, \beta, \gamma]^T$ represents the spacecraft attitude; $\boldsymbol{\Phi}_M = [\phi_1, \phi_2, \cdots, \phi_n]^T$ is a vector composed of joint angles; $\boldsymbol{q} = \left[\boldsymbol{\Phi}_M^T, \boldsymbol{\Phi}_S^T\right]^T$; $\boldsymbol{E}_g = \left[\boldsymbol{v}_g^T, \boldsymbol{\omega}_g^T\right]^T$ is the velocity of the space robot centroid; $\boldsymbol{J}_{ES}$ and $\boldsymbol{J}_{EM}$ are quasi-Jacobian matrices corresponding to the spacecraft base part and the manipulator part with the following expression:

$$\begin{aligned}\boldsymbol{J}_{ES} &= \begin{bmatrix}\boldsymbol{v}_{n\alpha} & \boldsymbol{v}_{n\beta} & \boldsymbol{v}_{n\gamma}\\ {}^{a}\boldsymbol{A}_{\alpha}\,{}^{\alpha}\boldsymbol{u}_{\alpha} & {}^{a}\boldsymbol{A}_{\beta}\,{}^{\beta}\boldsymbol{u}_{\beta} & {}^{a}\boldsymbol{A}_{\gamma}\,{}^{\gamma}\boldsymbol{u}_{\gamma}\end{bmatrix},\\ \boldsymbol{J}_{EM} &= \begin{bmatrix}\boldsymbol{v}_{n1} & \boldsymbol{v}_{n2} & \cdots & \boldsymbol{v}_{nn}\\ {}^{a}\boldsymbol{A}_{1}\,{}^{1}\boldsymbol{u}_{1} & {}^{a}\boldsymbol{A}_{2}\,{}^{2}\boldsymbol{u}_{2} & \cdots & {}^{a}\boldsymbol{A}_{n}\,{}^{n}\boldsymbol{u}_{n}\end{bmatrix},\\ \boldsymbol{J}_{E} &= \left[\boldsymbol{J}_{EM}, \boldsymbol{J}_{ES}\right].\end{aligned}$$

B.3 Space Robot Dynamics

In Section 4.2.3, according to angular momentum conservation law, the base attitude rate can be expressed using joint angle rate and RW rate as,

$$\dot{\boldsymbol{\Phi}}_S = \boldsymbol{H}_{ms}\dot{\boldsymbol{\Phi}}_M + \boldsymbol{H}_{ws}\dot{\boldsymbol{\Phi}}_W. \tag{B.16}$$

Assumption of stationary initial state makes $\boldsymbol{v}_g = \boldsymbol{\omega}_g \equiv \boldsymbol{0}$. Replacing the attitude rate using the above expression, (B.12) and (B.13) are rewritten as,

$$\begin{aligned}
\boldsymbol{v}_i &= \boldsymbol{V}_{iS}\dot{\boldsymbol{\Phi}}_S + \boldsymbol{V}_{iM}\dot{\boldsymbol{\Phi}}_M + \boldsymbol{v}_g = \boldsymbol{V}_{iS}\left(\boldsymbol{H}_{ms}\dot{\boldsymbol{\Phi}}_M + \boldsymbol{H}_{ws}\dot{\boldsymbol{\Phi}}_W\right) + \boldsymbol{V}_{iM}\dot{\boldsymbol{\Phi}}_M \\
&= \left(\boldsymbol{V}_{iS}\boldsymbol{H}_{ms} + \boldsymbol{V}_{iM}\right)\dot{\boldsymbol{\Phi}}_M + \boldsymbol{V}_{iS}\boldsymbol{H}_{ws}\dot{\boldsymbol{\Phi}}_W + \boldsymbol{v}_g = \boldsymbol{H}_{iv}\dot{\boldsymbol{\Phi}}, \\
\boldsymbol{\omega}_i &= \boldsymbol{\Omega}_{iS}\dot{\boldsymbol{\Phi}}_S + \boldsymbol{\Omega}_{iM}\dot{\boldsymbol{\Phi}}_M + \boldsymbol{\omega}_g = \boldsymbol{\Omega}_{iS}\left(\boldsymbol{H}_{ms}\dot{\boldsymbol{\Phi}}_M + \boldsymbol{H}_{ws}\dot{\boldsymbol{\Phi}}_W\right) + \boldsymbol{\Omega}_{iM}\dot{\boldsymbol{\Phi}}_M \\
&= \left(\boldsymbol{\Omega}_{iS}\boldsymbol{H}_{ms} + \boldsymbol{\Omega}_{iM}\right)\dot{\boldsymbol{\Phi}}_M + \boldsymbol{\Omega}_{iS}\boldsymbol{H}_{ws}\dot{\boldsymbol{\Phi}}_W + \boldsymbol{\omega}_g = \boldsymbol{H}_{i\omega}\dot{\boldsymbol{\Phi}},
\end{aligned} \tag{B.17}$$

where

$$\dot{\boldsymbol{\Phi}} = \left[\dot{\boldsymbol{\Phi}}_M^T, \dot{\boldsymbol{\Phi}}_W^T\right]^T,$$

$$\boldsymbol{H}_{iv} = \left[\boldsymbol{V}_{iS}\boldsymbol{H}_{ms} + \boldsymbol{V}_{iM}, \boldsymbol{V}_{iS}\boldsymbol{H}_{ws}\right],$$

$$\boldsymbol{H}_{i\omega} = \left[\boldsymbol{\Omega}_{iS}\boldsymbol{H}_{ms} + \boldsymbol{\Omega}_{iM}, \boldsymbol{\Omega}_{iS}\boldsymbol{H}_{ws}\right],$$

$$\boldsymbol{V}_{iS} = \left[\begin{array}{ccc} \boldsymbol{v}_{i\alpha}, & \boldsymbol{v}_{i\beta}, & \boldsymbol{v}_{i\gamma} \end{array}\right],\ \boldsymbol{V}_{iM} = \left[\begin{array}{ccc} \boldsymbol{v}_{i1}, & \cdots, & \boldsymbol{v}_{in} \end{array}\right],$$

$$\boldsymbol{\Omega}_{iS} = \left[{}^a\boldsymbol{A}_\alpha, {}^a\boldsymbol{A}_\beta, {}^a\boldsymbol{A}_\gamma\right],\ \boldsymbol{\Omega}_{iM} = \left[{}^a\boldsymbol{A}_1, \cdots, {}^a\boldsymbol{A}_i, 0, \cdots, 0\right]_{3\times n}.$$

The RWs have same linear velocity as that of the spacecraft base as,

$$\boldsymbol{v}_{wi} = \boldsymbol{v}_0 = \boldsymbol{H}_{0v}\dot{\boldsymbol{\Phi}},\ i = 1, 2, 3. \tag{B.18}$$

The angular velocities of the RWs are given by,

$$\begin{aligned}
\boldsymbol{\omega}_{wi} &= \boldsymbol{\omega}_0 + \boldsymbol{R}_{wi}^b\dot{\boldsymbol{\Phi}}_{wi} = \boldsymbol{\omega}_0 + \boldsymbol{R}_{wi}^b\boldsymbol{u}_{wi}\dot{\boldsymbol{\Phi}}_W \\
&= \boldsymbol{H}_{0\omega}\dot{\boldsymbol{\Phi}} + \boldsymbol{R}_{wi}^b\boldsymbol{u}_{wi}\left[\begin{array}{cc} \boldsymbol{O}_{3\times n} & \boldsymbol{I}_{3\times 3} \end{array}\right]\left[\begin{array}{c} \dot{\boldsymbol{\Phi}}_M \\ \dot{\boldsymbol{\Phi}}_W \end{array}\right] = \boldsymbol{H}_{wi}\dot{\boldsymbol{\Phi}},
\end{aligned} \tag{B.19}$$

where $\boldsymbol{v}_0$ and $\boldsymbol{\omega}_0$ are the linear velocity and angular velocity of the spacecraft base, respectively; $\dot{\boldsymbol{\Phi}}_{wi}$ is the angular velocity of i^{th} RW w.r.t. the spacecraft base expressed in the reaction-wheel frame and $\dot{\boldsymbol{\Phi}}_{wi} = \boldsymbol{u}_{wi}\dot{\boldsymbol{\Phi}}_W$; $\boldsymbol{u}_{wi} \in \mathbb{R}^{3\times 3}$ has a form of $u_{wi}(i,i) = 1$ and zero for other components; $\boldsymbol{R}^b_{wi}$ denotes the transformation matrix from the i^{th} reaction-wheel frame to the base frame; $\boldsymbol{O}_{3\times n}$ is a zero matrix and $\boldsymbol{I}_{3\times 3}$ is an identity matrix; $\boldsymbol{H}_{wi} = \boldsymbol{H}_{0\omega} + \boldsymbol{R}^b_{wi}\boldsymbol{u}_{wi}\begin{bmatrix} \boldsymbol{O}_{3\times n} & \boldsymbol{I}_{3\times 3} \end{bmatrix}$.

The total kinetic energy of the space robot system is represented by,

$$T = \frac{1}{2}\sum_{i=0}^{n}\left(\boldsymbol{v}_i^T m_i \boldsymbol{v}_i + \boldsymbol{\omega}_i^T \, {}^a\boldsymbol{I}_i \, \boldsymbol{\omega}_i\right) + \frac{1}{2}\sum_{i=1}^{3}\left(\boldsymbol{v}_{wi}^T m_{wi} \boldsymbol{v}_{wi} + \boldsymbol{\omega}_{wi}^T \, {}^a\boldsymbol{I}_{wi} \, \boldsymbol{\omega}_{wi}\right). \tag{B.20}$$

Inertia transformation from the link frame Σ_i or the i^{th} reaction-wheel frame Σ_{wi} to the inertial frame takes the form as,

$${}^a\boldsymbol{I}_i = {}^a\boldsymbol{A}_i \, {}^i\boldsymbol{I}_i \, ({}^a\boldsymbol{A}_i)^T, \quad {}^a\boldsymbol{I}_{wi} = {}^a\boldsymbol{A}_{wi} \, {}^{wi}\boldsymbol{I}_{wi} \, ({}^a\boldsymbol{A}_{wi})^T. \tag{B.21}$$

Substituting (B.17), (B.18), (B.19) and (B.21) into (B.20), the translational energy is

$$\begin{aligned}
T_v &= \frac{1}{2}\sum_{i=0}^{n}\left(\boldsymbol{v}_i^T m_i \boldsymbol{v}_i\right) + \frac{1}{2}\sum_{i=1}^{3}\left(\boldsymbol{v}_{wi}^T m_{wi} \boldsymbol{v}_{wi}\right) \\
&= \frac{1}{2}\sum_{i=0}^{n}\left[\left(\boldsymbol{H}_{iv}\dot{\boldsymbol{\Phi}}\right)^T m_i \left(\boldsymbol{H}_{iv}\dot{\boldsymbol{\Phi}}\right)\right] + \frac{1}{2}\sum_{i=1}^{3}\left[\left(\boldsymbol{H}_{0v}\dot{\boldsymbol{\Phi}}\right)^T m_{wi} \left(\boldsymbol{H}_{0v}\dot{\boldsymbol{\Phi}}\right)\right] \\
&= \frac{1}{2}\dot{\boldsymbol{\Phi}}^T\left[\sum_{i=0}^{n}\left(\boldsymbol{H}_{iv}^T \, m_i \, \boldsymbol{H}_{iv}\right) + \sum_{i=1}^{3}\left(\boldsymbol{H}_{0v}^T \, m_{wi} \, \boldsymbol{H}_{0v}\right)\right]\dot{\boldsymbol{\Phi}} \\
&= \frac{1}{2}\dot{\boldsymbol{\Phi}}^T \underline{\boldsymbol{H}}_V \dot{\boldsymbol{\Phi}},
\end{aligned} \tag{B.22}$$

and the rotational energy is

$$
\begin{aligned}
T_\omega =& \frac{1}{2}\sum_{i=0}^{n}\left(\boldsymbol{\omega}_i^T\ {}^a\boldsymbol{I}_i\ \boldsymbol{\omega}_i\right) + \frac{1}{2}\sum_{i=1}^{3}\left(\boldsymbol{\omega}_{wi}^T\ {}^a\boldsymbol{I}_{wi}\ \boldsymbol{\omega}_{wi}\right)\\
=& \frac{1}{2}\sum_{i=0}^{n}\left[\left(\boldsymbol{H}_{i\omega}\dot{\boldsymbol{\Phi}}\right)^T\left({}^a\boldsymbol{A}_i\ {}^i\boldsymbol{I}_i\ {}^a\boldsymbol{A}_i^T\right)\left(\boldsymbol{H}_{i\omega}\dot{\boldsymbol{\Phi}}\right)\right]\\
&+\frac{1}{2}\sum_{i=1}^{3}\left[\left(\boldsymbol{H}_{wi}\dot{\boldsymbol{\Phi}}\right)^T\left({}^a\boldsymbol{A}_{wi}\ {}^{wi}\boldsymbol{I}_{wi}\ {}^a\boldsymbol{A}_{wi}^T\right)\left(\boldsymbol{H}_{wi}\dot{\boldsymbol{\Phi}}\right)\right]\\
=& \frac{1}{2}\dot{\boldsymbol{\Phi}}^T\left[\sum_{i=0}^{n}\left({}^a\boldsymbol{A}_i^T\boldsymbol{H}_{i\omega}\right)^T\ {}^i\boldsymbol{I}_i\ \left({}^a\boldsymbol{A}_i^T\boldsymbol{H}_{i\omega}\right)\right.\\
&\left.+\sum_{i=1}^{3}\left({}^a\boldsymbol{A}_{wi}^T\boldsymbol{H}_{wi}\right)^T\ {}^{wi}\boldsymbol{I}_{wi}\ \left({}^a\boldsymbol{A}_{wi}^T\boldsymbol{H}_{wi}\right)\right]\dot{\boldsymbol{\Phi}}\\
=& \frac{1}{2}\dot{\boldsymbol{\Phi}}^T\underline{\boldsymbol{H}}_\Omega\dot{\boldsymbol{\Phi}},
\end{aligned}
\tag{B.23}
$$

where $\underline{\boldsymbol{H}}_V = \sum_{i=0}^{n}\left(\boldsymbol{H}_{iv}^T\ m_i\ \boldsymbol{H}_{iv}\right) + \sum_{i=1}^{3}\left(\boldsymbol{H}_{0v}^T\ m_{wi}\ \boldsymbol{H}_{0v}\right)$ and $\underline{\boldsymbol{H}}_\Omega = \sum_{i=0}^{n}\left({}^a\boldsymbol{A}_i^T\boldsymbol{H}_{i\omega}\right)^T\ {}^i\boldsymbol{I}_i\ \left({}^a\boldsymbol{A}_i^T\boldsymbol{H}_{i\omega}\right) + \sum_{i=1}^{3}\left({}^a\boldsymbol{A}_{wi}^T\boldsymbol{H}_{wi}\right)^T\ {}^{wi}\boldsymbol{I}_{wi}\ \left({}^a\boldsymbol{A}_{wi}^T\boldsymbol{H}_{wi}\right)$.

Since the spacecraft is cruising in a micro-gravity environment and only rigid bodies are included, its potential energy is taken equal to zero. As a result, the Lagrangian is

$$
\mathscr{L} = T = \frac{1}{2}\dot{\boldsymbol{\Phi}}^T\left(\underline{\boldsymbol{H}}_V + \underline{\boldsymbol{H}}_\Omega\right)\dot{\boldsymbol{\Phi}} = \frac{1}{2}\dot{\boldsymbol{\Phi}}^T\boldsymbol{H}\dot{\boldsymbol{\Phi}},
\tag{B.24}
$$

where $\boldsymbol{H} = \underline{\boldsymbol{H}}_V + \underline{\boldsymbol{H}}_\Omega$ which proves to be a symmetric and positive definite matrix.

According to the Lagrangian formulation, the generalized torques are given by,

$$
\frac{d}{dt}\left(\frac{\partial\mathscr{L}}{\partial\dot{\boldsymbol{\Phi}}}\right) - \frac{\partial\mathscr{L}}{\partial\boldsymbol{\Phi}} = \boldsymbol{\tau},
\tag{B.25}
$$

which yields the dynamic equation of the following form,

$$
\boldsymbol{H}\ddot{\boldsymbol{\Phi}} + \boldsymbol{C}\dot{\boldsymbol{\Phi}} = \boldsymbol{\tau},
\tag{B.26}
$$

where $\boldsymbol{C}\dot{\boldsymbol{\Phi}} = \dot{\boldsymbol{H}}\dot{\boldsymbol{\Phi}} - \dfrac{\partial}{\partial\boldsymbol{\Phi}}\left(\dfrac{1}{2}\dot{\boldsymbol{\Phi}}^T\boldsymbol{H}\dot{\boldsymbol{\Phi}}\right)$; $\boldsymbol{\tau} = [\tau_1, \cdots, \tau_n, \tau_{w1}, \tau_{w2}, \tau_{w3}]^T$ with $\tau_i, i = 1, 2, \cdots, n$ denoting joint torques and $\tau_{w1}, \tau_{w2}, \tau_{w3}$ denoting RW torques.